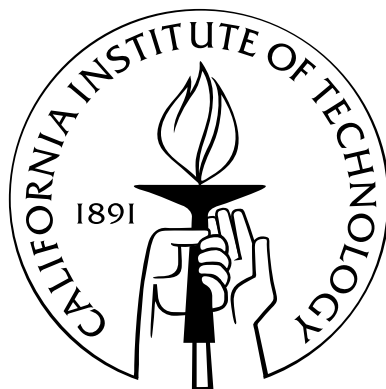


High-Temperature Transport in Lanthanum Telluride and Other Modern Thermoelectric Materials

Thesis by
Andrew F. May

In Partial Fulfillment of the Requirements
for the Degree of
Doctor of Philosophy



California Institute of Technology
Pasadena, California

2010
(Defended April 29, 2010)

Acknowledgements

I would like to begin by thanking Nicole, my wife, for putting up with me while I was a graduate student. Without her, this work would be of little meaning to me.

My research advisor, Jeff Snyder, has been a pleasure to work with. I thank him for the perfect mix of knowledge, motivation, and fun during my time at Caltech. We have enjoyed had many detailed discussions about electrical transport in solids, as well as many regarding life in general (be it in a place like Pasadena or Buffalo).

I have been fortunate to interact with many intelligent scientists while working toward my doctorate. Specifically, I would like to thank Sossina Haile for advice regarding teaching and professional development, as well as interesting discussions regarding society and science. Eric Toberer and I have enjoyed many conversations, about science and otherwise, and we have shared many successful collaborations for which I am grateful. I would also like to Teruyuki Ikeda for his role as my initial mentor, and then the numerous trips to the electron probe for chemical analysis of samples.

I have enjoyed working at the Jet Propulsion Laboratory and would like to thank Jean-Pierre Fleurial for working closely with me during my initial years of study, as well as for providing the funding that allowed me to pursue some more basic scientific questions in the materials of interest. This work was sponsored by a NASA grant through the Jet Propulsion Laboratory, and for that I am very grateful. I would like to thank Thierry Caillat for useful interactions and discussions, as well as L. Danny Zoltan for facilitating Seebeck coefficient measurements and providing an unmistakable presence in the Lab. Also, George Nakatsukasa deserves credit for keeping the JPL lab running smoothly; in particular, for taking care of the ball mills and hot presses that allowed numerous samples to be produced. I would like to thank Ali Saramat for his time performing synthesis on the Ba-Ga-Ge system; I am also grateful for Lloyd MacPherson's (Netzsch) collection of specific heat data for the same system. I am also very grateful for Kathy Bubash's assistance with various aspects of life as a graduate student in Chemical Engineering at Caltech.

Collaboration with several non-Caltech scientists also complemented this dissertation research. David Singh of Oak Ridge National Lab performed first principles calculations on lanthanum telluride, which proved critical in our understanding of its electrical transport, and I am grateful for his input in this research and his kind demeanor. I have also enjoyed working with theorist Espen Flage-Larsen of the University of Oslo, and I am grateful for the many conversations we have had. I would like to acknowledge Olivier Delaire

and Michael McGuire of Oak Ridge National Laboratory for an experimental collaboration studying the vibration properties of lanthanum telluride; W. D. Porter should also be acknowledged for his significant efforts to obtain high-temperature heat capacity during this collaboration.

Finally, my friends and family need to be acknowledged. Of course, my parents and siblings all deserve significant thanks for their endless encouragement and ability to put things in perspective. My brother Steve's knowledge of the graduate student life and the difficulties encountered in scientific research have made his words particularly meaningful. I would also like to thank the great friends I made while attending Penn State; put simply, our gatherings always make life's difficulties fade away. I have made some good friends at Caltech, and my only regret is not devoting more time to them. I also thank those who provided the calories to get me through these years, Ernie and the ladies—lunch will never be the same.

Abstract

This manuscript discusses the materials physics of thermal and electrical transport in the solid state. In particular, the focus is on thermoelectric materials, which enable the direct conversion between thermal and electrical energy. The ability of simple approximations and semiclassical models to describe transport is explored in a variety of systems. In some cases, the traditional models provide a very accurate description of the transport for the compositions of interest to thermoelectric applications. This is the case for *n*-type $\text{Ba}_8\text{Ga}_{16-x}\text{Ge}_{30+x}$, where a single, parabolic band model captures the electrical transport and thus allows the accurate prediction of optimal composition for energy conversion. This is not found to be true in $\text{La}_{3-x}\text{Te}_4$, and more than one parabolic conduction band is required to describe the electrical transport. In this case, the use of *ab initio* electronic band structure calculations provided critical knowledge for physical models to be developed. The influence of structure on thermal transport is also examined in detail. The compounds considered typically possess low lattice thermal conductivity, with values often being less than or equal to 1 W/m/K at 300 K. This can generally be associated with large unit cells, where the high number of atoms per unit cell results in a large number of optical modes, which carry little heat due to their low group velocities. Phonon scattering is also considered, and the cation vacancies in $\text{La}_{3-x}\text{Te}_4$ are found to reduce the lattice thermal conductivity by over 100% at room temperature. Finally, the resulting thermoelectric efficiency is discussed, where leg efficiencies near 20% of the Carnot efficiency are predicted in segmented legs. The work detailed here has led to the continued development of $\text{La}_{3-x}\text{Te}_4$ by the Jet Propulsion Laboratory, where it is a top candidate for future use in deep-space power-generation systems.

Contents

Acknowledgements	iii
Abstract	v
List of Figures	ix
List of Tables	xii
List of Symbols and Notation	xiv
1 Introduction	1
1.1 Summary	1
1.2 Thermoelectric Energy Conversion	1
1.3 Thermoelectric Figure of Merit	4
1.4 Optimizing Thermoelectric Efficiency	6
1.5 Pertinent Materials	11
1.5.1 $\text{La}_{3-x}\text{Te}_4$	11
1.5.2 $\text{Ba}_8\text{Ga}_{16-x}\text{Ge}_{30+x}$	14
1.5.3 SrZnSb_2 and SrZn_2Sb_2	15
1.6 Summary of Research	17
2 Experimental Methods	19
2.1 Summary	19
2.2 Synthesis of Inorganic Solids	19
2.2.1 $\text{La}_{3-x}\text{Te}_4$	20
2.2.2 $\text{Ba}_8\text{Ga}_{16-x}\text{Ge}_{30+x}$	23
2.2.3 SrZnSb_2 and SrZn_2Sb_2	23
2.3 Characterization	24
2.3.1 Chemical Characterization	24
2.3.2 Characterization of Transport Properties	25

2.4	Analysis of Transport Properties	26
2.5	Density Functional Calculations	27
3	Chemical and Structural Results	29
3.1	Summary	29
3.2	$\text{La}_{3-x}\text{Te}_4$ and Subsystems	29
3.3	$\text{Ba}_8\text{Ga}_{16-x}\text{Ge}_{30+x}$	33
3.4	SrZnSb_2 and SrZn_2Sb_2	34
4	Electrical Transport	36
4.1	Summary	36
4.2	Electrical Transport Theory	37
4.2.1	Introduction	37
4.2.2	Relaxation Times and Carrier Scattering	40
4.2.3	Carrier Concentration and Hall Coefficient	41
4.2.4	Electrical Conductivity and Mobility	43
4.2.5	Seebeck Coefficient	45
4.2.6	Mixed Conduction	48
4.2.7	Estimation of the Band Gap	49
4.2.8	Electronic Contribution to the Thermal Conductivity	50
4.3	$\text{La}_{3-x}\text{Te}_4$	52
4.3.1	Heavily Doped $\text{La}_{3-x}\text{Te}_4$	52
4.3.2	Near-Insulating $\text{La}_{3-x}\text{Te}_4$	60
4.3.3	$\text{La}_{3-x-y}\text{Yb}_y\text{Te}_4$	62
4.3.4	$\text{La}_{3-x}\text{Te}_{4-z}\text{Sb}_z$ and $\text{La}_{3-x}\text{Te}_{4-z}\text{Bi}_z$	64
4.4	$\text{Ba}_8\text{Ga}_{16-x}\text{Ge}_{30+x}$	73
4.5	SrZnSb_2 and SrZn_2Sb_2	78
5	Thermal Transport	81
5.1	Summary	81
5.2	Thermal Transport Theory	82
5.2.1	Lattice Thermal Conductivity	82
5.2.2	Minimum Lattice Thermal Conductivity	85
5.2.3	Electronic Contribution to the Thermal Conductivity	85
5.3	$\text{La}_{3-x}\text{Te}_4$	87
5.3.1	$\text{La}_{3-x-y}\text{Yb}_y\text{Te}_4$	90
5.3.2	$\text{La}_{3-x}\text{Te}_{4-z}\text{Sb}_z$ and $\text{La}_{3-x}\text{Te}_{4-z}\text{Bi}_z$	90

5.4	$\text{Ba}_8\text{Ga}_{16-x}\text{Ge}_{30+x}$	94
5.5	SrZnSb_2 and SrZn_2Sb_2	98
6	Thermoelectric Efficiency	102
6.1	Summary	102
6.2	Review of Thermoelectric Efficiency	102
6.3	$\text{La}_{3-x}\text{Te}_4$	104
6.4	$\text{Ba}_8\text{Ga}_{16-x}\text{Ge}_{30+x}$	106
6.5	SrZnSb_2 and SrZn_2Sb_2	109
6.6	Thermoelectric Compatibility and Device Efficiency	110
6.6.1	Overview of Device Efficiency	110
6.6.2	Efficiency in $\text{La}_{3-x}\text{Te}_4$ and Subsystems	111
7	Future Studies	114
A	Minority Carrier Properties and Transport	116
A.1	General Trends	116
A.2	Experimental Hall Carrier Concentration and Mobility	118
B	Pressure-Assisted Sintering	120
C	Thermal Stability in $\text{Ba}_8\text{Ga}_{16-x}\text{Ge}_{30+x}$	122
D	Transport Coefficients in Single Scattering Limit	124
E	The Mott Relation	125
F	Degenerate Limit of the Seebeck Coefficient	129
F.1	From the Boltzmann Transport Equation	129
F.2	From the Mott Relation	130
G	Sound Velocity: Measurement and Use	132
H	The Transport Integral	134
	Bibliography	136

List of Figures

1.1	A schematic representation of the Seebeck effect, and the optimization of carrier concentration to provide the maximum thermoelectric power factor.	3
1.2	The temperature-dependent figure of merit for state-of-the-art thermoelectric materials at the onset of this work.	5
1.3	Simulation of the temperature-dependent electrical resistivity and Seebeck coefficient in heavily-doped semiconductors.	7
1.4	The Hall mobility and Lorenz number are simulated versus temperature for a variety of extrinsic doping levels.	8
1.5	Typical behavior of the thermal conductivity in semiconductors, with both the lattice and electronic contributions considered.	8
1.6	The dependence of the thermoelectric figure of merit on temperature and carrier concentration in a typical semiconductor.	10
1.7	The crystal structure of La_3Te_4 highlighting the coordination of La around Te.	12
1.8	Crystal structures of SrZnSb_2 and SrZn_2Sb_2 , with the primitive unit cells outlined.	16
2.1	The lanthanum-tellurium phase diagram.	21
3.1	X-ray diffraction scans for two lanthanum telluride samples.	30
3.2	Electronprobe micrographs for two lanthanum telluride samples.	30
3.3	X-ray diffraction scan and electronprobe micrograph for nominal composition $\text{La}_{2.375}\text{Yb}_{0.55}\text{Te}_4$	31
3.4	A representative x-ray diffraction scan and compositional data for the samples of nominal composition $\text{La}_3\text{Te}_{4-z}\text{Sb}_z$	33
3.5	X-ray diffraction scan of $\text{Ba}_8\text{Ga}_{16-x}\text{Ge}_{30+x}$ with a close examination of the region that reveals the common impurity.	34
3.6	X-ray diffraction scans for SrZnSb_2 and SrZn_2Sb_2	35
4.1	Simulation of the Hall factor versus electrochemical potential and carrier density for various scattering mechanisms.	43
4.2	Normalized values of the Hall mobility versus reduced electrochemical potential and Hall carrier density.	44

4.3	The dependence of the Seebeck coefficient on electrochemical potential, carrier density, and carrier scattering mechanism in the parabolic band model.	47
4.4	Lorenz number as a function of electrochemical potential, carrier density, and carrier scattering mechanism.	51
4.5	The experimental Hall carrier density at 300 K for a variety of $\text{La}_{3-x}\text{Te}_4$ compositions, as well as the temperature-dependent Hall number for a single sample.	53
4.6	The temperature-dependent Hall mobility in heavily doped $\text{La}_{3-x}\text{Te}_4$ samples.	53
4.7	The room temperature Hall mobility in $\text{La}_{3-x}\text{Te}_4$ is fit to a model that assumes acoustic phonon scattering limits the mobility.	54
4.8	Temperature dependence of the electrical conductivity and Seebeck coefficient in $\text{La}_{3-x}\text{Te}_4$	55
4.9	Seebeck coefficient versus Hall carrier density in $\text{La}_{3-x}\text{Te}_4$	55
4.10	The calculated single-band effective masses in $\text{La}_{3-x}\text{Te}_4$	56
4.11	The calculated band structure in La_3Te_4 examined in both large and small energy ranges.	57
4.12	The projected density of states calculated for La_3Te_4	57
4.13	The calculated Hall carrier density as a function of Fermi energy and the chemical carrier concentration in $\text{La}_{3-x}\text{Te}_4$	58
4.14	The temperature-dependent Seebeck coefficients calculated from the first principles band structure of La_3Te_4	59
4.15	The theoretical dependence of Seebeck coefficient on Hall carrier density in $\text{La}_{3-x}\text{Te}_4$ is compared to experimental data.	60
4.16	Electrical conductivity of near-insulating lanthanum telluride samples in an Arrhenius plot, and the corresponding Seebeck coefficient versus temperature.	61
4.17	Chemical compositions obtained from wavelength dispersive spectroscopy are presented along with the room temperature Hall carrier concentrations for $\text{La}_{3-x-y}\text{Yb}_y\text{Te}_4$	62
4.18	The temperature-dependent electrical resistivity and Seebeck coefficient in $\text{La}_{3-x-y}\text{Yb}_y\text{Te}_4$	63
4.19	The electrical transport properties at 1000 K in $\text{La}_{3-x-y}\text{Yb}_y\text{Te}_4$ and $\text{La}_{3-x}\text{Te}_4$	63
4.20	The experimental Hall carrier density at 300 K is plotted versus the theoretical carrier density obtained from charge counting for nominal $\text{La}_3\text{Te}_{4-z}\text{Sb}_z$ and $\text{La}_3\text{Te}_{4-z}\text{Bi}_z$	66
4.21	Temperature dependence of Seebeck coefficients for nominal $\text{La}_3\text{Te}_{4-z}\text{Sb}_z$ and $\text{La}_3\text{Te}_{4-z}\text{Bi}_z$	67
4.22	The dependence of Seebeck coefficient at 1000 K on the electrical conductivity and the room temperature Hall carrier concentration is compared in $\text{La}_3\text{Te}_{4-z}\text{Sb}_z$, $\text{La}_3\text{Te}_{4-z}\text{Bi}_z$, and $\text{La}_{3-x}\text{Te}_4$ samples.	67
4.23	The calculated electronic structures of La_3Te_4 , $\text{La}_3\text{Te}_3\text{Sb}$, and $\text{La}_3\text{Te}_3\text{Bi}$	68
4.24	The projected density of states for La_3Te_4 , $\text{La}_3\text{Te}_3\text{Sb}$, and $\text{La}_3\text{Te}_3\text{Bi}$	69
4.25	The temperature-dependent electrical resistivity in $\text{La}_3\text{Te}_{4-z}\text{Sb}_z$ and $\text{La}_3\text{Te}_{4-z}\text{Bi}_z$	70

4.26	Temperature dependence of the Hall carrier concentration and Hall mobility for the sample of nominal composition $\text{La}_3\text{Te}_{3.2}\text{Sb}_{0.8}$	71
4.27	Room temperature Hall density in $\text{Ba}_8\text{Ga}_{16-x}\text{Ge}_{30+x}$ as a function of the experimentally characterized chemical composition.	74
4.28	Temperature and carrier density dependence of the Hall mobility in $\text{Ba}_8\text{Ga}_{16-x}\text{Ge}_{30+x}$	75
4.29	Electrical resistivity and Seebeck coefficient versus temperature in $\text{Ba}_8\text{Ga}_{16-x}\text{Ge}_{30+x}$	76
4.30	The temperature dependence of the electrical resistivity of near-insulating $\text{Ba}_8\text{Ga}_{16-x}\text{Ge}_{30+x}$	77
4.31	Seebeck coefficient versus Hall carrier density in n -type $\text{Ba}_8\text{Ga}_{16-x}\text{Ge}_{30+x}$	78
4.32	The temperature-dependent Hall carrier concentration and mobility in SrZnSb_2 and SrZn_2Sb_2	79
4.33	Temperature-dependent electrical resistivity and Seebeck coefficient in SrZnSb_2 and SrZn_2Sb_2	80
5.1	Temperature dependence of the experimental thermal diffusivity and calculated heat capacity in $\text{La}_{3-x}\text{Te}_4$	88
5.2	Temperature dependence of the total and lattice thermal conductivity in $\text{La}_{3-x}\text{Te}_4$	88
5.3	Temperature dependence of the calculated Lorenz number in $\text{La}_{3-x}\text{Te}_4$	89
5.4	Temperature dependence of the thermal diffusivity and conductivity in $\text{La}_{3-x-y}\text{Yb}_y\text{Te}_4$	91
5.5	The dependence of thermal conductivity at 1000 K on room temperature Hall carrier density in $\text{La}_{3-x-y}\text{Yb}_y\text{Te}_4$ and $\text{La}_{3-x}\text{Te}_4$	91
5.6	The temperature-dependent thermal diffusivity and conductivity in nominal $\text{La}_3\text{Te}_{4-z}\text{Sb}_z$ and $\text{La}_3\text{Te}_{4-z}\text{Bi}_z$ are compared to that in $\text{La}_{3-x}\text{Te}_4$	92
5.7	Examining phonon group velocity and scattering via the lattice thermal conductivity versus electrical conductivity and temperature in nominal $\text{La}_3\text{Te}_{4-z}\text{Sb}_z$, $\text{La}_3\text{Te}_{4-z}\text{Bi}_z$, and $\text{La}_{3-x}\text{Te}_4$	93
5.8	Temperature-dependent thermal diffusivity and heat capacity in n -type $\text{Ba}_8\text{Ga}_{16-x}\text{Ge}_{30+x}$	95
5.9	The total thermal conductivity and lattice thermal conductivity versus temperature in n -type $\text{Ba}_8\text{Ga}_{16-x}\text{Ge}_{30+x}$	96
5.10	The calculated Lorenz numbers versus temperature in $\text{Ba}_8\text{Ga}_{16-x}\text{Ge}_{30+x}$	97
5.11	Temperature dependence of the total and lattice thermal conductivity in SrZnSb_2 and SrZn_2Sb_2	99
6.1	The temperature-dependent zT in $\text{La}_{3-x}\text{Te}_4$ and its subsystems.	105
6.2	The carrier density dependence of zT for $\text{La}_{3-x}\text{Te}_4$ and its subsystems at 1000 K	106
6.3	The theoretical relationship between electrochemical potential and carrier concentration in $\text{La}_{3-x}\text{Te}_4$ at various temperatures.	107
6.4	The temperature and carrier concentration dependence of zT in n -type $\text{Ba}_8\text{Ga}_{16-x}\text{Ge}_{30+x}$	108
6.5	Examination of the figure of merit in SrZnSb_2 and SrZn_2Sb_2	110
6.6	Theoretical conversion efficiency for single-leg systems operating under various temperature gradients.	112
6.7	The temperature-dependent thermoelectric compatibility factor of various materials.	113

A.1	The influence of minority carrier band properties and energy gap on the electrical resistivity and the Seebeck coefficient as a function of temperature.	117
A.2	The influence of minority carrier band properties and energy gap on the temperature-dependent electronic contribution to the thermal conductivity and the thermoelectric figure of merit. . . .	117
A.3	The influence of minority carrier band properties and energy gap on the maximum zT obtained at the optimum carrier density, both of which are functions of temperature.	118
A.4	The influence of minority carrier properties and energy gap on the electrochemical potential . . .	118
A.5	Demonstration of the variation in Hall properties obtained using a single band assumption when minority carrier properties change.	119
B.1	Representative heating/pressure profiles for the sintering of samples considered in this thesis. .	120
C.1	Temperature dependence of electrical resistivity for $\text{Ba}_8\text{Ga}_{16-x}\text{Ge}_{30+x}$ upon repeated heat treatments.	123
C.2	The temperature dependence of Hall effect data taken between consecutive measurements of $\text{Ba}_8\text{Ga}_{16-x}\text{Ge}_{30+x}$ to high temperatures.	123
G.1	Longitudinal and transverse response in an ultrasonic pulse/response experiment.	133

List of Tables

1.1	Cation radii for eightfold coordination	14
2.1	Standards and detector settings commonly utilized during wavelength dispersive spectroscopy	24
2.2	Calculated lattice parameters for the relaxed La_3Te_4 , $\text{La}_3\text{Te}_3\text{Sb}$, and $\text{La}_3\text{Te}_3\text{Bi}$ cells	27
3.1	Summary of compositional data for $\text{La}_{3-x}\text{Te}_4$ and subsystems	32
3.2	Atomic composition of $\text{Ba}_8\text{Ga}_{16-x}\text{Ge}_{30+x}$ samples assessed via wavelength dispersive spectroscopy	34
4.1	Summary of energy and effective mass dependence of the carrier relaxation time due to various scattering mechanisms for carriers in a parabolic band	41
4.2	Nominal composition and corresponding electrical transport properties for nominal $\text{La}_3\text{Te}_{4-z}\text{Sb}_z$ and $\text{La}_3\text{Te}_{4-z}\text{Bi}_z$	65
4.3	Room temperature electrical transport properties of n -type $\text{Ba}_8\text{Ga}_{16-x}\text{Ge}_{30+x}$	74
5.1	Room temperature ultrasonic data and calculated properties of $\text{Ba}_8\text{Ga}_{16-x}\text{Ge}_{30+x}$ samples . .	97
5.2	Properties of SrZnSb_2 and SrZn_2Sb_2 that are related to thermal transport	101
6.1	Parameters for the theoretical zT versus carrier density in $\text{Ba}_8\text{Ga}_{16-x}\text{Ge}_{30+x}$ at 600 K	109
6.2	Parameters for theoretical zT versus carrier density in SrZnSb_2 and SrZn_2Sb_2	110
B.1	Programming details for the sintering of selected compounds.	121

List of Symbols and Notation

Fundamental Constants

e	magnitude of charge of an electron or hole
h	Planck constant
k	Boltzmann constant
m_e	rest mass of electron
ϵ_0	permittivity of free space
\hbar	$= h/2\pi$

Transport Properties

C_{ac}	specific heat of acoustic phonons ($= C_P/N_a$)
C_P	specific heat capacity at constant pressure
D_T	thermal diffusivity
v_{ac}	velocity of acoustic phonons (typically $= v_m$)
v_l	longitudinal speed of sound
v_m	mean sound velocity
v_t	transverse speed of sound
n	carrier density
n_H	Hall carrier density ($= 1/R_H e$)
R_H	Hall coefficient
zT	thermoelectric figure of merit (dimensionless)
α	Seebeck coefficient
κ	thermal conductivity
κ_b	bipolar contribution to thermal conductivity
κ_e	electronic contribution to thermal conductivity
κ_L	lattice or phonon contribution to thermal conductivity
μ_H	Hall mobility
μ_d	Drift mobility
μ	carrier mobility
ρ	electrical resistivity

σ	electrical conductivity
τ	relaxation time (for a charge carrier or phonon)

Analysis Variables and Symbols

E	particle energy
E_{def}	deformation potential
f	Fermi distribution function
F_j	Fermi integral of order j
L	Lorenz number
m^*	carrier effective mass (in parabolic band models)
$N(E)$	Density of states
N_i	concentration of impurity ions
r_H	Hall factor ($= n/n_H = \mu/\mu_H$)
Z	effective charge
ϵ	reduced particle energy ($= E/kT$)
γ	Grüneisen parameter
ζ	electrochemical potential
η	reduced electrochemical potential ($= \zeta/kT$)
Θ_D	Debye temperature
χ	dimensionless or relative permittivity

Common Abbreviations

CRTA	Constant relaxation time approximation
DFT	density functional theory
DSC	differential scanning calorimetry
EDS	energy dispersive spectroscopy
EPMA	electron probe microanalysis
JPL	Jet Propulsion Laboratory
LAPW	Linearized augmented planewave
LFA	laser flash analysis
SEM	scanning electron microscope (microscopy)
SPB	single parabolic band
VASP	Vienna ab initio simulation package
WDS	wavelength dispersive spectroscopy

Other Symbols

D_M	mass diffusion coefficient
l_D	diffusion length
\bar{M}	average molar mass

N_a	atoms per primitive unit cell
Q_A	activation energy (generic)
T	absolute temperature
t_D	equilibrium diffusion time
V	volume per atom
ε	electric field

Chapter 1

Introduction

1.1 Summary

This chapter begins with a discussion of the fundamentals of thermoelectricity. The evolution of a thermally-induced voltage and the materials properties required to exploit such a voltage are discussed in detail. These material properties are combined to form the thermoelectric figure of merit, zT , which is a dimensionless number on the order of unity in good, modern thermoelectrics. The zT of state-of-the-art materials is shown, along with some discussion of how to obtain a large zT .

The optimization of zT in a typical thermoelectric material is considered. These materials tend to be semiconductors, and the importance of controlling the majority carrier concentration is highlighted by simulation of temperature-dependent transport properties. The influence of the minority carrier on thermoelectric properties is also highlighted. This discussion concludes with plots of zT versus temperature T and majority carrier concentration n , the latter of which demonstrates the optimization of zT as a function of n .

The remainder of the chapter discusses background information on the materials considered: $\text{La}_{3-x}\text{Te}_4$, $\text{Ba}_8\text{Ga}_{16-x}\text{Ge}_{30+x}$, and SrZnSb_2 and SrZn_2Sb_2 . Of particular importance is the discussion of charge counting in $\text{La}_{3-x}\text{Te}_4$, which can be utilized to understand the electronic properties of this material. A historical perspective is also given for $\text{La}_{3-x}\text{Te}_4$ to highlight the need for a simple synthesis procedure. The introduction for $\text{Ba}_8\text{Ga}_{16-x}\text{Ge}_{30+x}$ also discusses the importance of valence-counting, as well as the motivation for this work. Finally, the discussion of the Sr-Zn-Sb compounds briefly touches on some of the reasons these “Zintl” materials are of interest to thermoelectric research.

1.2 Thermoelectric Energy Conversion

Thermoelectric devices convert between thermal and electrical energy via the solid state. This phenomenon exists because charge carriers move in response to a temperature gradient, and thermoelectric generators can be viewed as heat engines where the electronic gas is the working fluid. As such, the overall conversion efficiency is limited to the Carnot efficiency, and typical devices achieve only a fraction of this value.

Thermoelectric devices possess the desirable characteristics of being highly reliable, silent, and scalable. In heating and cooling applications, thermoelectrics provide impressive temperature control because both heating and cooling is performed by the same module (depending solely on the direction of current flow). For stability reasons, thermoelectric devices have been utilized to produce power for deep-space missions, with power generation continuing after 30 years in the case of Voyager I[1]. Despite these reliable characteristics, thermoelectrics are not commonly employed due to their low efficiency[2]. Much of the efficiency loss occurs due to poor thermal transport between reservoir and device, but another significant loss arises due to poor performance at the material level. The majority of thermoelectric research conducted at universities focuses on obtaining large performance at the material level.

The property that characterizes the response of a charge carrier to a thermal gradient is known as the Seebeck coefficient α ; specifically, $\alpha = \frac{V}{\Delta T}$ is the proportionality between the measured voltage V and ΔT when ΔT is small. Understanding the Seebeck effect requires some effort, and the interested reader is referred to references [2–9]. The evolution of a thermally induced voltage is probably best visualized by analogy to a gas-filled tube in a temperature gradient. The gas at the hot end of the closed tube has greater thermal energy and diffuses to the cold side (the hot gas expands and the cold side gas contracts). A similar effect is observed for electrons and holes (the electron's positively charged counterpart), and the buildup of these charge carriers on one side of the sample produces a voltage (see Figure 1.1a). The Seebeck coefficient is negative when conduction is dominated by electrons, and it is positive when conduction is dominated by holes.

When both electrons and holes are present in a material, the thermoelectric voltage is reduced because both species diffuse from hot to cold. The energy gap in semiconductors helps eliminate this “compensation” of $|\alpha|$ (at moderate T), and semiconductors tend to be the best thermoelectric materials. Both n -type (electron conducting) and p -type (hole conducting) materials are necessary to form an efficiency device, and the matching of mechanical properties in these materials is critical for device development. A thermoelectric device is produced by connecting these thermoelectric materials (legs) in series electrically and thermally in parallel so that a large total voltage can be produced.

At open circuit, the buildup of charge continues until the flux caused by the temperature gradient is equal to the flux associated with the induced voltage (V_{th}). This voltage is generated due to the difference across ∇T in the electrons' electrochemical potential, $\zeta = \xi - e\phi$ where ξ is chemical potential and ϕ is the electrostatic potential. It is common to use proportionality coefficients L_{ij} to relate forces to fluxes; the field of Irreversible Thermodynamics is called on for the complete discussion and employs slightly different representations[6, 10]. For the generic one-directional case, the total flux of current in the x direction is given by[11]

$$J_e = L_{11} \frac{-1}{e} \frac{d\zeta}{dx} + L_{12} \frac{-dT}{dx}. \quad (1.1)$$

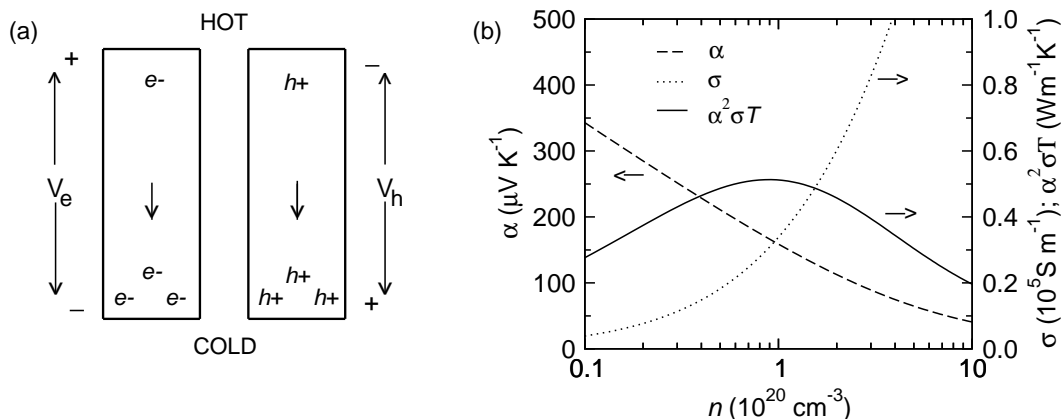


Figure 1.1. (a) A schematic representation of the Seebeck effect, where charge carriers diffuse in response to a temperature gradient until the resulting voltage counterbalances the flux associated with ΔT . (b) The optimization of the thermoelectric power factor ($\alpha^2 \sigma T$) reveals the need to control carrier density n such that reasonable values of both α and σ are obtained. The data are compiled from the simulations (at 600 K) shown in Section 1.4.

When $\nabla T = 0$, this expression reveals that $J_e = L_{11} \varepsilon$ because $\varepsilon_x = \frac{d\phi}{dx}$, assuming no change in ξ with x (no change in carrier density). Thus, the electrical conductivity is found to be $\sigma = L_{11}$ by recalling that $J_e = \sigma \varepsilon$ in an isothermal medium (Ohm's Law). The functional forms of L_{ij} can be found in Section 4.2 where the theory of electrical transport is discussed, and a more exact representation is given in Appendix E.

When a temperature gradient exists, but current is not allowed to flow, Equation 1.1 gives

$$\frac{-1}{e} \frac{d\xi}{dx} = \frac{L_{12}}{L_{11}}, \quad (1.2)$$

which leaves the definition of the Seebeck coefficient α ,

$$\frac{V_{th}}{\Delta T} = \frac{L_{12}}{L_{11}} \equiv \alpha. \quad (1.3)$$

The thermoelectric effect is therefore a fundamental response of conductive materials to a temperature gradient. Combining Equation 1.1 for electric flux with a similar expression for the entropy flux, it is found that the Seebeck coefficient gives the entropy transported per unit charge[6]:

$$\alpha = \left(\frac{\text{entropy flux via electrons}}{\text{current density}} \right)_{\nabla T=0}. \quad (1.4)$$

Thermoelectric devices require materials with large Seebeck coefficients (α) so that a large voltage may be obtained from a temperature gradient, or vice versa. The power output of a solid state generator is V^2/R , where R is the total resistance. Thus, at the materials level, low electrical resistivity ρ or large electrical conductivity $\sigma = 1/\rho$ is desired.

High thermoelectric efficiency is most readily achieved in semiconductors, where the free carrier concentration can be manipulated readily and the detrimental effects of minority carriers can be avoided. A typical

optimization of performance is illustrated in Figure 1.1b, where the balance between the Seebeck coefficient α and electrical conductivity σ leads to large $\alpha^2\sigma$ (known as the thermoelectric *power factor*). It is common to multiple the power factor by T to obtain units of thermal conductivity, as in Figure 1.1b. The complete optimization of thermoelectric efficiency is heavily influenced by the optimization of the power factor, but the thermal conductivity must also be considered in detail.

The flow of thermal energy is required for the production of electricity in a thermoelectric generator. Fourier's law gives the heat flux as $q = -\kappa\nabla T$, where κ is the thermal conductivity. Therefore, small κ is desired so that a large ΔT is achieved from a given thermal flux thereby allowing a large voltage to be produced from the thermoelectric effect.

In summary, good thermoelectric materials are those that possess a small thermal conductivity, a large electrical conductivity, and a large Seebeck coefficient (more specifically, large $|\alpha|$ which is sometimes referred to as the *thermopower*). Obtaining this combination of material properties is particularly difficult because large σ corresponds to low α and vice versa (see Figure 1.1b). Large σ also corresponds to large κ due to the conduction of heat by charge carriers; the electronic contribution κ_e is often estimated by the Wiedemann-Franz relationship $\kappa_e = L\sigma T$, where L is an energy dependent proportionality known as the Lorenz number (see Sections 4.2.8 and 5.2.3).

1.3 Thermoelectric Figure of Merit

The thermoelectric conversion efficiency η of a thermoelectric device is limited by the Carnot efficiency η_C [3, 10]. Typical thermoelectric generators only achieve a fraction of this efficiency, say approximately $\eta_C/6$. The loss of efficiency can be characterized by a reduced efficiency η_r , which approaches unity as the material parameter zT approaches infinity ($\eta = \eta_C\eta_r$). Thermoelectric materials research thus focuses on improving zT , so as to improve the more complex, device level efficiency. While characterizing zT is not easy, it is much simpler than examining improvements in device efficiency as the materials change. The nature of zT makes physical sense in light of the discussion in the previous Section (large power output and large ΔT are desired).

$$zT = \frac{\alpha^2\sigma T}{\kappa}. \quad (1.5)$$

The values of zT in state-of-the art materials, at the onset of this thesis work, are shown in Figure 1.2. The figure of merit zT generally increases with increasing T at 'moderate' temperatures, and a maximum is observed at high T due to minority carrier effects. Good thermoelectric materials have zT near unity at the desired operating temperature. The highest zT values are typically observed in doped semiconductors, where reasonable balance between large α and large σ is achieved. There is no theoretical bound on zT [10], though experimentally $zT > 2$ is rarely reported. Note that, for a particular semiconductor, the declaration of 'high

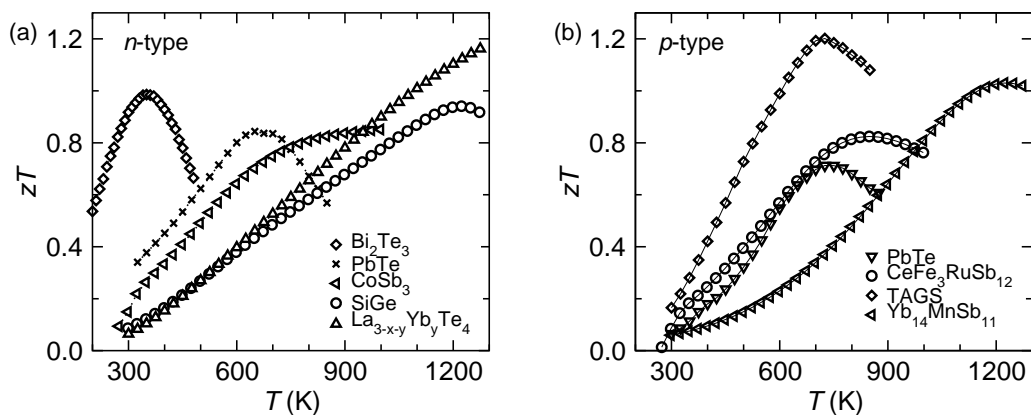


Figure 1.2. The temperature-dependent zT values for state-of-the-art thermoelectric materials at the onset of this work; panel (a) shows n -type materials and (b) shows p -type. The $\text{La}_{3-x-y}\text{Yb}_y\text{Te}_4$ data were taken from this thesis, and all other curves are from Reference [13]. TAGS stands for $(\text{GeTe})_{1-x}(\text{AgSbTe}_2)_x$.

T^* is generally given by the size of the band gap E_g with E_g at least $6\text{--}10 kT_{Hot}$ required in a thermoelectric material operating with a hot-side temperature of T_{Hot} [12].

It is insightful to recall that the thermal conductivity has two primary contributions, a lattice conductivity κ_L and an electronic contribution κ_e :

$$zT = \frac{\alpha^2 \sigma T}{\kappa_e + \kappa_L}. \quad (1.6)$$

The value of κ_e is proportional to σ , and thus thermoelectric research typically attempts to reduce κ_L . Minimizing κ_L while maintaining large σ can be very difficult because many of the obstacles that scatter phonons also scatter charge carriers. Furthermore, large carrier mobility μ is typically found in materials with large κ (covalent semiconductors with stiff bonds). Traditionally, improvements in zT were achieved via alloying, such as in $\text{Si}_{1-x}\text{Ge}_x$ [14, 15], where phonon transport is affected more significantly than carrier transport.

Modern technologies have allowed the design of systems with nanometer scale features which allow the inherent connection between κ_L and μ to be manipulated. This is possible because the characteristic mean free path of electrons is generally much smaller than that of phonons. Introducing scattering centers at length scales larger than the carrier mean free path but smaller than the phonon mean free path therefore allows an increase in the quantity μ/κ_L to be achieved[16]. A number of good review articles discuss the influence of this type of nanoengineering on κ_L [16–19].

Large enhancements in zT have been achieved by producing *nanobulk* Si, SiGe, and Bi_2Te_3 via mechanical alloying[20–23]; nanobulk refers to a bulk specimen composed of nanoscale crystals/grains. Other phonon inhibiting structures include superlattices[24], bulk materials with nanometer scale precipitates[25], and lamellar structures at scales as large as 300 nm[26]. The latter two approaches can often be achieved through traditional heat treatments and exploitation of the phase diagram (temperature-dependent solubility, invariant reactions). Another approach to reduce κ_L focuses on the selection of complex materials with

inherently low κ_L , as discussed in References [9, 27].

In the limit $\kappa_L = 0$, the figure of merit is given by

$$zT = \frac{\alpha^2}{L}, \quad (1.7)$$

and the Lorenz number L is a function of energy that relates σ to κ_e (see Section 4.2.8). This representation of zT is useful in that it provides an immediate guideline for the values of α required for large zT . In this limit, zT of 1 requires $\alpha \sim 150\mu\text{V}/\text{K}$, and finite κ_L necessitates even larger α . Indeed, it is common for $\kappa_L \approx \kappa_e$ in thermoelectric materials, which requires $\alpha \sim 210\mu\text{V}/\text{K}$ for $zT \sim 1$.

As discussed above, significant efforts to reduce κ_L have been made. Much less work has been done on manipulating the electrical transport properties to obtain large $\alpha^2\sigma$. Yet the need for large α is clearly demonstrated by Equation 1.7. As discussed in Section 4.2 and shown in Figure 1.1b, the values of σ and α are intimately linked and it is very difficult to obtain significant improvement in the power factor ($\alpha^2\sigma$). Large α is obtained when σ has a large energy dependence around the electrochemical potential (σ is highly asymmetric about ζ)[28, 29]. Such behavior is promoted by highly energy-dependent density of states $N(E)$ or carrier relaxation times τ .

The manipulation of $N(E)$ for increased zT was demonstrated by doping PbTe with Tl, where a change to the majority carrier mass led to an $\sim 100\%$ increase in zT while shifting the peak to higher T [30]. Also, large α may be obtained in low-dimensional materials due to a sharp electronic density of states associated with reduced dimensionality[31]. A change to the relaxation time is believed to be possible via *electron filtering*, where the low energy electrons are excluded from the conduction process via energy barriers (designed using superlattices or precipitates)[32–35].

1.4 Optimizing Thermoelectric Efficiency

For a given set of material parameters, such as the carrier's effective mass m^* and mobility μ and the crystal's lattice thermal conductivity κ_L , the thermoelectric figure of merit zT optimizes as a function of carrier concentration n . Thermoelectric efficiency generally optimizes in the range $10^{19}\text{cm}^{-3} \leq n_{opt} \leq 10^{21}\text{cm}^{-3}$. This is primarily the result of a balance between the Seebeck coefficient α and the electrical conductivity σ (see Figure 1.1), though the thermal conductivity also plays a role in this optimization. Furthermore, the ability to reduce κ_L and thus shift n_{opt} (to lower n_{opt}) must also be considered[9].

The requirements for optimization typically lead to the observation of large zT in semiconductors, where the carrier density can be tuned to a desired level and the suppression of α due to bipolar conduction (the presence of multiple carrier types) can be avoided via the band gap E_g . The carrier concentration in such a system is generally independent of temperature, as these free carriers result from an imbalance in the valence electron count and not activation of electron-hole pairs across the energy gap (generally referred to as an

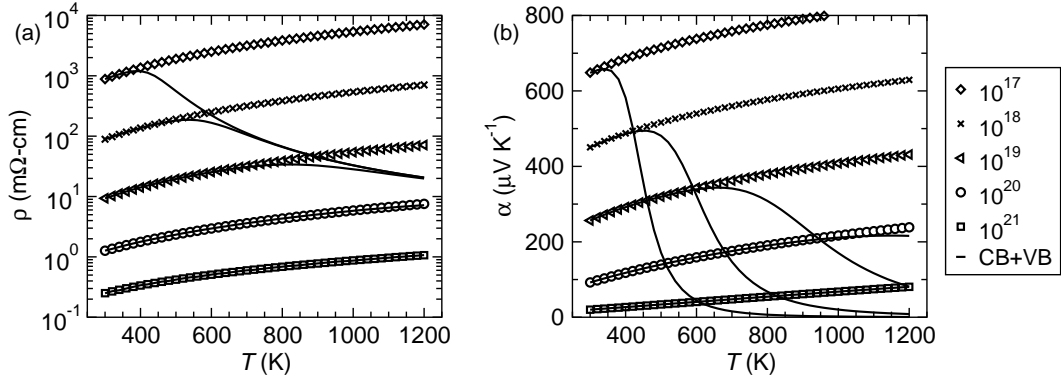


Figure 1.3. The temperature-dependent (a) electrical resistivity and (b) Seebeck coefficient in materials with extrinsic carrier density given in the key (units of cm^{-3}); it is assumed acoustic phonon scattering limits the carrier mobility. Data markers represent a single, parabolic band model and the solid curves represent a semiconductor with a band gap of 0.5 eV and equal characteristics for holes and electrons. In the multiband case, minority carrier effects lead to reduced ρ and α at high T ; the notation CB+VB = implies a conduction band and a valence band.

extrinsic semiconductor)[27]. At high T , however, the activation of carriers generally occurs because the extrinsic carrier concentration cannot be too large if high zT is to be achieved. The term *heavily doped semiconductor* is often utilized to describe a material with this type of $n \neq n(T)$. The following phrase is then, in turn, utilized to describe transport in typical thermoelectric materials: “the transport properties behave as expected for a heavily doped semiconductor.”

Before discussion transport, let us first clarify the nomenclature associated with these semiconductors. A material that possesses a high carrier density is often said to be *degenerate*, which is synonymous with heavily doped semiconductor to some scientists. This is not entirely true (to a physicist), as the level of degeneracy (of the electron gas) is not determined by the value of n , but rather by the corresponding value of the electrochemical potential ζ , often discussed in terms of the reduced potential $\eta = \zeta/kT$. For this reason, degeneracy is determined by a combination of n , T , and m^* .

An electron gas is *highly degenerate* when the electrochemical potential is well above the band edge. In this case, approximations for the Fermi statistics or necessary integrals can be utilized to simplify the transport coefficients and the electronic properties are generally well described by the theory of metals. An electron gas is *mildly degenerate* when η is within a few k_bT of the band edge, and Fermi-Dirac statistics must be utilized. Finally, a *nondegenerate* electron gas is defined as one that obeys Boltzmann statistics, and this generally occurs when η is more than a few k_bT below the band edge (into the band gap). Thus, the term *degenerate* is often applied to any electron gas that does not obey Boltzmann statistics. In a chemical sense, the term degenerate is often used to imply that a crystal has a high level of impurity atoms (dopants) which are all ionized. A higher concentration of impurity atoms generally results in a lower ionization energy due to the formation of an impurity band as opposed to impurity states.

This section demonstrates the transport properties of heavily doped semiconductors with the goal of

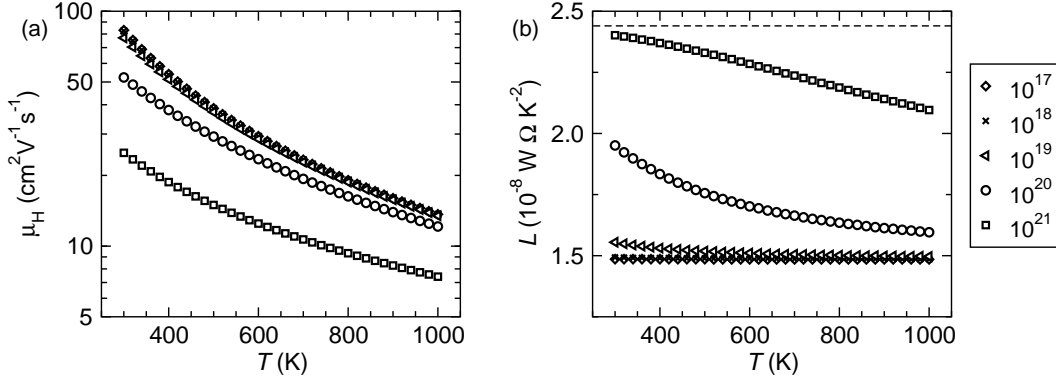


Figure 1.4. The temperature-dependent (a) Hall mobility and (b) Lorenz number for a variety of extrinsic doping levels (see key, units of cm^{-3}) when the mobility is limited by acoustic phonon scattering. These properties are similar in samples with low n as because the nondegenerate limit is approached. The Lorenz number is consistently lower than the metallic limit (dashed line) commonly utilized in data analysis.

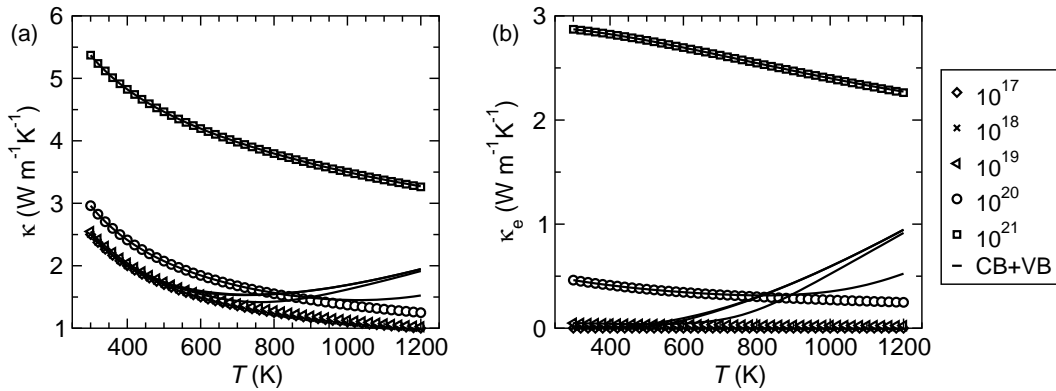


Figure 1.5. The (a) total thermal conductivity and (b) its electronic contribution versus temperature for a variety of extrinsic levels (indicated by the key in units of cm^{-3}). The lattice contribution is taken to be $\kappa_L = 600/T + 0.5$ (in W/m/K), which is represented by the single band models (open markers) with $n < 10^{20} \text{ cm}^{-3}$. The effect of minority carriers in an ideal semiconductor is shown by the solid curve, which reveals the relatively large bipolar contribution at high T and low n .

revealing the ‘expected behavior’ as well as why zT optimizes as a function of n . Two sets of data are shown in the various plots to provide insight into this behavior. The data represented by markers are for the case of an infinite band gap (single band), and the solid curves represent the case of $E_g=0.5 \text{ eV}$ in a semiconductor where the electrons’ and holes’ effective mass and limiting mobility are equal. The effect of the minority carrier’s properties on the net transport properties is significant and is examined in more detail in Appendix A. The equations utilized to generate these plots are provided in Section 4.2. It is assumed that conduction occurs in a parabolic band and that acoustic phonons limit the carriers’ mobility. The pertinent material parameters were selected arbitrarily, though they are reasonable for materials with modest zT : a deformation potential of 3 eV, longitudinal sound velocity of 3000 m/s, density of 6 g/cm^3 , and a lattice thermal conductivity of $\kappa_L = 600/T + 0.5$ in W/m/K were utilized for these simulations.

When the carrier density is independent of T , the electrical resistivity ρ increases with increasing T (Fig-

ure 1.3a) because lattice vibrations (phonons) disrupt the movement of the charge carriers. This is observed as a decrease in the carrier mobility μ (Figure 1.4a) and is the behavior typically observed in metals at high T (itinerant conduction with constant n). At low temperatures, localization, impurity scattering, or carrier activation (ionization) effects are observed and a different temperature-dependence is expected. Typically, this leads to an exponential rise in either μ and/or n with increasing T at low temperatures.

The Seebeck coefficient increases with increasing T , as shown in Figure 1.3b. This is because η decreases with increasing T in materials with temperature independent n . The linear increase with T is exemplified by the metallic limit expression for α (Eqn. 1.8), which also reveals the desire for low carrier density (more specifically, low η). Derivations of Equation 1.8 are given in Appendix F. As T increases, the level of degeneracy decreases (because η decreases) and the increase in α slows (even in an infinite band gap material). Finally, at high T , the activation of electron-hole pairs across the energy gap results in reduced ρ and α , as observed by the solid curves representing a material with $E_g=0.5$ eV in Figure 1.3.

$$\alpha = \frac{\pi^2 k_b^2 T m^*}{3eh^2} \left(\frac{\pi}{3n} \right)^{2/3} \quad (1.8)$$

The total thermal conductivity κ generally decreases with increasing T , as demonstrated in Figure 1.5a. This behavior is caused by a decrease in the lattice thermal conductivity κ_L , which generally decays as T^{-1} at high T in crystalline materials due to phonon-phonon scattering[29, 36, 37]. κ_L does not approach zero, though, and κ_L tends to a minimum value at high T . Therefore, a simple model for κ_L suggests $\kappa_L = A/T + \kappa_{min}$, where A is a constant. However, when other scattering mechanisms become important, κ_L has less temperature-dependence and approaches a temperature independent value in the limit of extremely high scattering rates. The values of κ and κ_L are equal in Figure 1.5a for $n \leq 10^{19} \text{ cm}^{-3}$ in the single band model because the electronic contribution κ_e is essentially equal to zero.

At high T , the thermal activation of charge carriers can lead to a large increase κ_e due to the bipolar thermal conductivity κ_b . The single band approximation does not account for this rise in κ associated with the thermal activation of electron-hole pairs. At high T , the use of a single band model thus introduces error due to the presence of κ_b , and an overestimation of κ_L results from such data analysis (often observed as an increase in κ_L as T increases). A more detailed discussion of the electronic contribution in real semiconductors can be found in Appendix A and in Section 5.2. Note that the single band Lorenz number (Figure 1.4b) decreases with increasing T due to decreasing η , and is almost always less than the metallic limit (dashed line) of $2.45 \times 10^{-8} \text{ W}\Omega\text{K}^{-2}$. Using this metallic limit of L is discouraged, and can even result in negative values for κ_L [38].

The net result of this heavily doped semiconductor behavior is an increase in the figure of merit zT with increasing T at moderate T . zT increases with increasing T for all doping levels in the single band case, which is likely the case for materials with band gap E_g on the order of 1 eV (up to ~ 1200 K). Materials with small E_g , however, would experience the detrimental effects of minority carriers, and $zT(T)$ would display

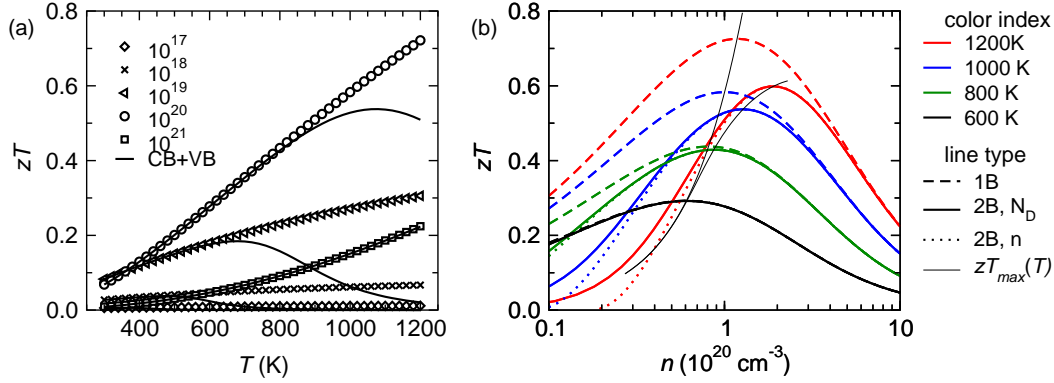


Figure 1.6. (a) The temperature-dependent zT increases with increasing T , and a maximum is observed in the case when both valence and conduction band are considered (solid curve, $E_g=0.5$ eV). The key contains the extrinsic carrier concentration in units of cm $^{-3}$. (b) The optimization of zT reveals increasing optimum n as T increases, an effect that is more severe when the influence of minority carriers is taken into account (solid curves). The thin black curves represent zT_{max} versus n_{opt} and increasing n corresponds to increasing T ; these curves are parametric plots of Figures A.3a,b in Appendix A. In the legend, ‘1B’ stands for one parabolic band, ‘2B’ for the case of a valence and conduction band separated by 0.5 eV, and ‘ N_D ’ stands for the extrinsic carrier concentration while n stands for the true carrier concentration (extrinsic plus intrinsic).

a maximum at high T ; this effect is estimated for a material with $E_g = 0.5$ eV by the solid curves.

The figure of merit optimizes near $n = 1 \times 10^{20}$ cm $^{-3}$ for the material properties simulated here. This optimization is typical of semiconductors, and controlling n is of the utmost importance in thermoelectrics. When n is too large, small zT results due to large κ_e and small α ; zT is small due to small σ when n is too small. This is the inherent difficulty in obtaining large zT . Note that the maximum in zT does not correspond to the maximum in $\alpha^2\sigma$ (as a function of n) due to the influence of thermal conductivity[3, 9].

The maximum (optimized) zT and corresponding optimum carrier density n_{opt} increases with increasing T . The thin solid curves in Figure 1.6b trace zT_{max} versus n_{opt} with the influence of T implied by increasing zT_{max} . This behavior is consistent with simple theories, as discussed in Section 6.2. A more significant shift to higher n_{opt} with increasing T occurs when the effect of minority carriers is considered because a higher majority carrier concentration corresponds to a lower minority carrier concentration. For the two band (2B) models in Figure 1.6b, the solid curve is plotted as a function of the extrinsic doping level (N_D) which is always slightly less than the total carrier concentration n (extrinsic plus intrinsic). However, near zT_{max} , the carrier concentration is dictated by the extrinsic level because the intrinsic carriers must be avoided (as much as possible) for large zT to be achieved.

The characteristics of the minority carrier play an important role in determining the high T transport properties in real semiconductors. The effect of these properties and the band gap is examined in Appendix A. It is clear, however, that multiple carrier types lead to reduced zT at high T , and thus a large band gap is desired. This feature has been discussed by several authors, and a general rule of E_g at least $6-10)kT_{op}$ is accepted, where T_{op} is the desired operating temperature[7, 8, 12].

The increase in n_{opt} with increasing T has significant implications for device development, as does the

general behavior of $zT(T)$. Thermoelectric generators operate in a temperature gradient, and larger ΔT allows a higher efficiency to be achieved. The optimum carrier density therefore changes across the thermoelectric material, and segmenting different materials together is a common method to achieve large, average zT [39]. Maintaining a variation of n across an individual thermoelectric material (a *graded* material) is difficult due to diffusion at high T over the long lifetime of a thermoelectric device.

1.5 Pertinent Materials

1.5.1 $\text{La}_{3-x}\text{Te}_4$

This section is an adapted reproduction, with permission, from *Phys. Rev. B*, **78** 125205 (2008) and *Phys. Rev. B*, **81**, 125205 (2010). Copyright 2008 and 2010, American Physical Society. Reprinted, in part, with permission from *Chem. Mater* **22**, 2995 (2010). Copyright 2010 American Chemical Society.

Lanthanum telluride is one of many rare earth (RE) chalcogenides ($\text{RE}_{3-x}\text{Ch}_4$, Ch=chalcogen) that possess relatively large thermoelectric efficiency at high-temperature[38, 40–44], as well as superconductivity at low temperature[45, 46].

These materials adopt the body centered cubic Th_3P_4 structure type (space group $\bar{I}43d$, No. 220), the crystal structure of which is shown in Figure 1.7. Up to one-ninth of the cations can be vacant ($0 \leq x \leq \frac{1}{3}$), which corresponds to a phase width of roughly three atomic percent. This can be observed in the phase diagram, which is presented in Figure 2.1 (Section 2.2.1).

In $\text{La}_{3-x}\text{Te}_4$, tellurium atoms sit on the phosphorus site and experience sixfold coordination by lanthanum via a distorted-octahedron (the shaded polyhedron in Figure 1.7). The lanthanum atoms are eightfold coordinated by Te, which can be considered to sit on the corners of two inverted and distorted tetrahedra. Details of the crystallography in $\text{La}_{2.667}\text{Te}_4$ can be found in Reference [47], and a nice overview of the lattice parameters and phases present in various $\text{RE}_{3-x}\text{Ch}_4$ is found in Reference [48]. Note that $\text{La}_{3-x}\text{Te}_4$ only exists in the Th_3P_4 structure type, whereas other $\text{RE}_{3-x}\text{Ch}_4$ possess multiple crystal structures; as a consequence of this phase stability, $\text{La}_{3-x}\text{Te}_4$ is attractive for device development.

To first order, the electronic behavior of $\text{La}_{3-x}\text{Te}_4$ and other rare-earth chalcogenides possessing the Th_3P_4 structure type is easily understood in terms of sample stoichiometry[7, 49, 50]. For $x < \frac{1}{3}$, $\text{La}_{3-x}\text{Te}_4$ can be considered like a heavily doped semiconductor, or a metal with an underlying ionic structure (but, this is unlike metals which typically possess cation cores underneath the electron cloud). Each La donates three electrons (the $5d^1$ and $6s^2$ electrons) to the crystal to become La^{3+} , and tellurium utilizes two of these to complete valence and is thus Te^{2-} (both ions possess the electronic configuration of xenon). The insulating composition is therefore represented by the stoichiometry La_2Te_3 , though this composition exists as $\text{La}_{3-x}\text{Te}_4$ with $x = \frac{1}{3}$. When $x < \frac{1}{3}$, the electrons released by La that are not necessary to fulfill Te valence begin to fill the conduction band, and the relationship between free electron concentration and composition

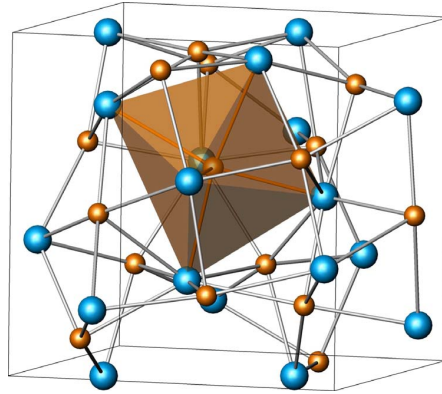
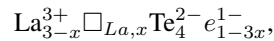


Figure 1.7. The structure of La_3Te_4 with blue spheres representing La and brown spheres representing Te. The shaded polyhedron shows the octahedron-like coordination around Te. Reprinted with permission from *Phys. Rev. B*, **78** 125205 (2008). Copyright 2008, American Physical Society.

is obtained by combining simple valence counting with crystallographic data. By analogy to simple ionic compounds, one expects the (filled) anionic Te states to reside mostly in the valence band while the (empty) cationic La states make up the conduction band. This was verified during this thesis work[51].

The chemical environment in $\text{La}_{3-x}\text{Te}_4$ can be represented by



where $\square_{La,x}$ represents a La vacancy and e^{-1} an electron. The free electron concentration in $\text{La}_{3-x}\text{Te}_4$ is therefore easily calculated as $n = n_{max}(1 - 3x)$, where $n_{max} \sim 4.5 \times 10^{21} \text{cm}^{-3}$ corresponds to $x = 0$, or one free electron per formula unit. While the value of n is typically utilized in this thesis, prior publications on these compounds have utilized the reduced carrier concentration $n^* = n/n_{max} = (1-3x)$.

A metal-insulator transition is observed as x changes from zero to one-third. For small values of x , the carrier concentration is large and the transport properties are similar to those of metals or heavily doped semiconductors. This behavior is maintained for most of the solid solution; it is only when $x \rightarrow \frac{1}{3}$ that the carrier concentration is reduced enough for non-degenerate semiconductor behavior to be observed at moderate temperatures. In this limit, the conductivity is also expected to switch from itinerant to hopping conduction, as discussed by Cutler and Mott in work describing the low temperature transport in $\text{Ce}_{3-x}\text{S}_4$ samples with large x [52].

Despite extensive investigations in the 1980s, the thermoelectric properties of lanthanum telluride have been difficult to reproducibly confirm for a particular stoichiometry. Previous investigations utilized solid-state diffusion, melt synthesis, or a combination of the two[53–56]. Studies employing melt synthesis required the use of pressure sealed tungsten or tantalum crucibles, and temperatures reached between 2080 and 2280 K[40]. These high-temperature techniques are time consuming and often result in inhomogeneous samples or, at a minimum, a lack of stoichiometric reproducibility. High-temperature syntheses are complicated by several factors: (i) vapor phase loss of tellurium (Te melts at 722 K and boils at 1261 K), (i) high melting

temperature of $\text{La}_{3-x}\text{Te}_4$ and LaTe (1992 K), (iii) severe reactivity with oxygen for $\text{La}_{3-x}\text{Te}_4$ and elemental lanthanum, especially at elevated temperatures, and (iv) the presence of a liquid/solid two-phase region above the $\text{La}_{3-x}\text{Te}_4$ solidus curve, as well as a neighboring eutectic reaction.

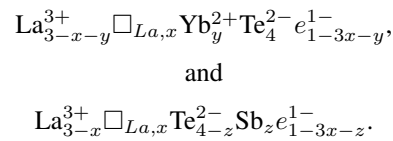
Previous work sponsored by the Jet Propulsion Laboratory and performed at ThermoElectron Corporation was able to overcome the difficulties associated with high-temperature synthesis, and thermoelectric transport was investigated on a series of single phase samples with a varying composition[40, 41]. These studies concluded that relatively high thermoelectric efficiency was achievable in $\text{La}_{3-x}\text{Te}_4$, with $zT \sim 1.2$ obtained at 1273 K. Despite synthetic difficulties, it was suggested that the optimal composition corresponded to $x \sim 0.26$ [40, 41], though it appeared as though larger n may be desirable.

The continued development of $\text{La}_{3-x}\text{Te}_4$ was hampered not only by synthetic difficulties, but also by the lack of a complementary p -type material. $\text{La}_{3-x}\text{Te}_4$ does not produce p -type conduction, and thus a different material system is required for the development of a thermoelectric generator. Traditionally, SiGe was utilized for high-temperature thermoelectric generators, and p -type SiGe has lower thermoelectric efficiency than n -type SiGe[15]. The net gain associated with replacing n -type SiGe by $\text{La}_{3-x}\text{Te}_4$ would be limited by the poor performance of p -type SiGe, not to mention the mechanical issues that would arise due to poor matching of the thermal expansion coefficients. However, the desire to develop $\text{La}_{3-x}\text{Te}_4$ regained a sense of urgency with the discovery that $\text{Yb}_{14}\text{MnSb}_{11}$ could serve as a p -type leg[57].

The primary goal of this work was to obtain single phase samples of $\text{La}_{3-x}\text{Te}_4$ and demonstrate reproducible control over composition and thermoelectric transport. After this initial task was fulfilled, the characterization of a series of compositions was to be performed. The next step in this research and development project was to model the thermoelectric transport and investigate methods for optimizing efficiency. This requires understanding the physics governing thermoelectric transport.

The analysis of transport data is, in general, complicated by a variety of factors. For $\text{La}_{3-x}\text{Te}_4$, the materials physics governing thermoelectric efficiency is difficult to isolate due to the inherent link between structural defects (vacancies) and carrier concentration. Two approaches were utilized to separate the influence of the vacancy and carrier concentrations on the various transport properties: (i) first-principles calculations of the electronic structure and (ii) chemical manipulation. The former task was accomplished through collaborations with theorists David Singh of Oak Ridge National Laboratory and Espen Flage-Larsen of the University of Oslo. These calculations were performed on ideal structures and thus provide an approximate model to investigate the influence of electronic structure on the thermoelectric transport.

The following describes the local environments in the most successful elemental substitutions:



In the case of a divalent cation substitution, such as that shown above for the substitution of La^{3+} by Yb^{2+} ,

Table 1.1. Cation radii for eightfold coordination reveals similar ionic size in Yb^{2+} and La^{3+} [59].

ion	radii (Å)
La^{3+}	1.16
Yb^{2+}	1.14
Na^{1+}	1.18
Ca^{2+}	1.12
Sr^{2+}	1.26
Ba^{2+}	1.42
Pb^{2+}	1.43
K^{1+}	1.51

the theoretical carrier density can thus be expressed as $n = n_{max}(1 - 3x - y)$. Similarly, in the case of anionic substitutions for Te^{2-} , such as by Sb^{3-} or Bi^{3-} , the expected carrier density is expressed in terms of the Sb or Bi content as $n = n_{max}(1 - 3x - z)$. In both types of substitutions, the carrier density and vacancy concentration are no longer interdependent, and the physics governing phonon and charge carrier transport can be probed more explicitly.

The non-isoelectronic substitutions thus provide finer control over carrier density than can be achieved in $\text{La}_{3-x}\text{Te}_4$. In $\text{La}_{3-x}\text{Te}_4$, the chemical control of carrier density is limited by the formal valence of lanthanum (III). The tuning of Yb content y or Sb(Bi) content z should render a threefold finer control of n compared to that achieved by changing the La vacancy concentration x .

A variety of cationic substitutions can be envisioned, though the anionic substitutions are limited and to our knowledge these studies represent the first of their kind. The selection of a substitutional element is relatively simple. According to the Hume-Rothery rules for solubility in solid solutions[58], high solubility is promoted by similarity in ionic (atomic) radii. Based on the data in Table 1.1[59], Yb is very promising for substitution on a La site.

Yb is typically a divalent cation in Te compounds[60]. This is exemplified by the formation of only YbTe in the Yb-Te phase diagram[61], which is an insulating phase with divalent Yb[62, 63]. Divalent Yb is stabilized due to the full $4f$ shell, such as in elemental Yb[63], where the $4f$ states lie at binding energies between 1.3 and 2.5 eV[64]. This reasoning is also consistent with the formation of divalent Yb in $\text{Yb}_4\text{Bi}_2\text{Te}$ [65], which possesses the anti- Th_3P_4 structure type. Also, divalent Yb has been suggested in $\text{Pb}_{1-x}\text{Yb}_x\text{Te}$ from lattice parameter data[66], as well as x-ray photoemission spectroscopy[67]. This is contrary to $\text{Pb}_{1-x}\text{Yb}_x\text{S}$ where mixed Yb valency is observed[67], and is expected to be the case for Yb substitution in $\text{La}_{3-x}\text{S}_4$. Thus, it is believed that Te is not electronegative enough to promote significant concentrations of Yb^{3+} and Yb can be regarded as predominantly Yb^{2+} in the lanthanum telluride matrix.

1.5.2 $\text{Ba}_8\text{Ga}_{16-x}\text{Ge}_{30+x}$

This section is an adapted reproduction, with permission, from *Phys. Rev. B*, **80**, 125205 (2009). Copyright 2009, American Physical Society.

The clathrate structure types contain three-dimensional, covalently bound frameworks with voids (*cages*) where guest atoms (*fillers*) can reside. The $\text{Ba}_8\text{Ga}_{16-x}\text{Ge}_{30+x}$ compound discussed here has the Type I clathrate structure (cubic, space group $Pm\bar{3}n$, No. 223)[68], which possesses two types of cages formed by the Ga-Ge framework and the Ba atoms reside within these cages; a nice overview of the crystal structure is found in Reference [69].

The composition $\text{Ba}_8\text{Ga}_{16}\text{Ge}_{30}$ is valence balanced, as each Ba donates two electrons and every Ga utilizes one of these electrons for bonding within the framework. Deviation from this stoichiometry results in valence imbalance and thus doped semiconductor behavior, with excess Ge giving *n*-type samples and excess Ga resulting in *p*-type behavior[27, 70–72].

At high-temperature, the clathrates have shown to possess thermoelectric efficiency equivalent to state of the art materials, such as PbTe and SiGe[73–75]. Specifically, the clathrates possess $zT \sim 1$ near 900 K due to the combination of relatively low κ_L and large $\mu m^{*3/2}$, where μ is the electron mobility and m^* is its effective mass.

A large number of investigations on the low temperature thermal conductivity of clathrates have been performed[76–84]. The main purpose of these studies was to reveal the role of the filler atom, with filler atom-phonon and filler atom-framework interactions of primary interest. Many clathrates have glass-like thermal conductivity (κ_L independent of T at high T), and similar behavior has been observed in *p*-type $\text{Ba}_8\text{Ga}_{16-x}\text{Ge}_{30+x}$. Interestingly, *n*-type $\text{Ba}_8\text{Ga}_{16-x}\text{Ge}_{30+x}$ has crystalline-like thermal conductivity ($\kappa_L \propto T^{-1}$ at high T).

While many studies continue to investigate the coupling between chemical composition and thermoelectric properties in $\text{Ba}_8\text{Ga}_{16-x}\text{Ge}_{30+x}$ -based compounds[85–88], the transport features in $\text{Ba}_8\text{Ga}_{16-x}\text{Ge}_{30+x}$ have not been completely characterized and analyzed for the compositions of interest to thermoelectric application (for *n*-type $15 \leq x \leq 16$). One objective of this thesis is to provide a thorough study of the high-temperature transport in polycrystalline $\text{Ba}_8\text{Ga}_{16-x}\text{Ge}_{30+x}$, and address the claim of surprisingly large n_{opt} made in Reference [89].

1.5.3 SrZnSb_2 and SrZn_2Sb_2

This section is an adapted reproduction, with permission, from *J. Appl. Phys.*, **106** 013706 (2009). Copyright 2009, American Institute of Physics.

The search for high efficiency thermoelectric materials encompasses many classes of semiconductors. While most conventional thermoelectric materials employ tellurium, its low natural abundance suggests the discovery of Te-free thermoelectric materials may be required for widespread application. A large variety of uncharacterized materials exists, and the trick is to predict which compounds will possess large zT . One class of promising compounds are termed Zintl compounds, which are valence balanced (semiconducting) materials that possess both ionic and covalent bonding in a single compound[9, 27, 90]. The term Zintl compound is used loosely here to include compositions that have a valence imbalance.

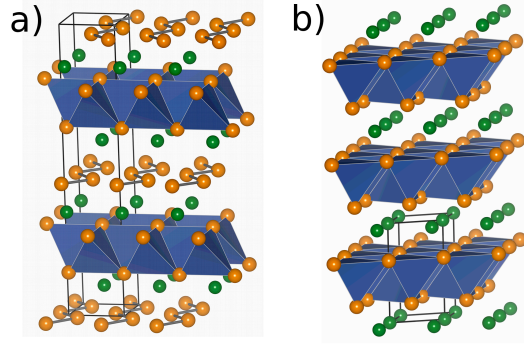


Figure 1.8. Crystal structures of (a) SrZnSb_2 and (b) SrZn_2Sb_2 . Green spheres represent Sr, gold sphere represent Sb, and Zn is located within the tetrahedra. The solid black lines trace the edges of the primitive unit cells. Reprinted with permission from *J. Appl. Phys.*, **106** 013706 (2009). Copyright 2009, American Institute of Physics.

Zintl compounds are attractive for thermoelectric application because their valence-precise nature frequently results in tunable semiconductors[27, 38, 91]. Also, Zintl compounds are often composed of discrete structural units (layers, cages, channels, polyanionic groups) that promote low κ_L [9, 92–94]. Many material systems can be understood using Zintl chemistry[9], including high performance thermoelectric materials like $\text{Yb}_{14}\text{MnSb}_{11}$, $\text{La}_{3-x}\text{Te}_4$, and $\text{Ba}_8\text{Ga}_{16}\text{Ge}_{30}$. However, the transport properties of many Zintl compounds remain uncharacterized.

This thesis examines transport in polycrystalline SrZnSb_2 and SrZn_2Sb_2 between room temperature and 725 K. A variety of AZn_2Sb_2 ($A = \text{Ca}, \text{Yb}, \text{Sr}, \text{Eu}$) compounds exist[95–97], and their transport properties were discussed in detail in a recent article[97]. This discussion focuses mainly on the variation of κ_L between SrZnSb_2 and SrZn_2Sb_2 .

SrZnSb_2 was predicted to be a semimetal by *ab initio* calculations that predicted a maximum zT of 0.14 (0.21) for p -type (n -type) conduction at 300 K; slightly lower zT was predicted for SrZn_2Sb_2 [98]. The crystal structure of SrZnSb_2 (orthorhombic, $Pnma$; Fig.1.8a) is derived from the ThCr_2Si_2 structure (tetragonal, $I4/mmm$), where anionic slabs of edge sharing tetrahedra are separated by square monolayers of cations. In SrZnSb_2 , every other $(\text{Zn}_2\text{Sb}_2)^{2-}$ slab is replaced by a monolayer consisting of $(\text{Sb}_2)^{2-}$ zigzag chains.

The AZn_2Sb_2 compounds have been shown to possess moderate thermoelectric performance, with $0.5 \leq zT \leq 1$ at 750 K[95, 96]. As shown in Fig. 1.8, the AZn_2Sb_2 compounds ($P\bar{3}m$ CaAl_2Si_2 parent compound) have structural features similar to SrZnSb_2 , but the unit cell of SrZnSb_2 is larger due to the layer of $(\text{Sb}_2)^{2-}$ zigzag chains. The AZn_2Sb_2 ($A = \text{Ca}, \text{Yb}, \text{Sr}, \text{Eu}$) compounds are composed of trigonal monolayers of A^{2+} cations separating $(\text{Zn}_2\text{Sb}_2)^{2-}$ slabs. The anionic slabs can be viewed as two puckered graphitic Sb-Zn layers that have been brought into contact[99].

1.6 Summary of Research

This thesis addresses the ability of traditional solid-state models to describe transport in modern thermoelectric materials. The models of interest are solutions to the Boltzmann transport equation combined with theories of the electronic relaxation times associated with various scattering mechanisms. The simplest model utilizes a parabolic dispersion relationship (free electron behavior), while more complex models combine multiple parabolic bands. The analysis and modeling of temperature T and carrier concentration n dependent transport properties is the primary concern.

The compound $\text{La}_{3-x}\text{Te}_4$ is considered for much of this work, and is in some ways an ideal compound to study due to the explicit link between the free carrier concentration n and the vacancy count x ($n \propto (1 - 3x)$). This system was known to have large thermoelectric performance,[40, 41] but synthetic difficulties inhibited detailed studies. Therefore, the initial goal of this research was to circumvent downfalls of the high-temperature synthesis (the compound melts near 1775 K) by utilizing a low-temperature, solid-state synthesis technique. This was achieved via mechanical alloying, or ball milling, which resulted in the reproducible synthesis of single-phase samples.[38, 100] Characterization of the transport properties as a function of composition x led to confirmation of large thermoelectric efficiency near $x = 0.26$.[38]

With a reliable set of data, the materials physics governing transport in $\text{La}_{3-x}\text{Te}_4$ was investigated. The electronic properties were considered within the single, parabolic band model. The model did not describe the core thermoelectric property, the Seebeck coefficient α , for all compositions.[38, 51] Specifically, lower-than-expected α was observed at large x (low n). Thus, this analysis suggested that a fundamental material property changed as various carrier concentrations were probed.

Two hypotheses were examined regarding the failure of the initial model: (i) the scattering of electrons by La vacancies influences α at large x , and (ii) the electronic structure depends on n and/or x . Hypothesis (i) was quickly eliminated by examining the T and n dependent carrier mobility, which is well described by a theory for the scattering of electrons by phonons (even at large x). Also, unusual scattering mechanisms tend to enhance α (relative to phonon scattering), which is opposite to what was observed here.

Collaboration with David Singh of Oak Ridge National Laboratory (ORNL) investigates hypothesis (ii). A first-principles calculation on vacancy-free La_3Te_4 was performed, and this revealed that multiple bands contribute to electron conduction for the energy ranges (the n, T values) of interest. Specifically, a *light* band was found in the energy range corresponding to small n (large x), which provided a qualitative description of the experimental α data.[51] Also, a collaboration with Olivier Delaire of ORNL investigated the vibrational characteristics of $\text{La}_{3-x}\text{Te}_4$ via calorimetry and inelastic neutron scattering. This work confirmed the existence of a light band at large x , and also found a significant stiffening of the phonon density of states at large x due to the reduction in ion core screening as n decreases. The pertinent results of this study are called on during the discussion of thermal transport, and the interested reader should see Reference [101] for the detailed publication.

With the general picture of transport in $\text{La}_{3-x}\text{Te}_4$ developed, attempts to manipulate and optimize the thermoelectric efficiency were conducted. The incorporation of Yb by substitution on the La site revealed no significant changes in transport, but the difference in formal valence between these two rare earth elements facilitated the optimization of efficiency and an optimum was identified at $n \sim 3 \times 10^{20} \text{cm}^{-3}$, [102] which is smaller than previously identified. [38, 40, 41] The substitutions of Sb or Bi for Te in nominally vacancy free samples were utilized to examine the electron and phonon scattering mechanisms in detail. [103] These substitutions resulted in changes in the transport properties, with a transition from itinerant to activated conduction observed as Sb(Bi) content increased. Also, a reduction of the energy gap was observed and confirmed via first-principles calculations by Espen Flage-Larsen of the University of Oslo. An increase in both the carrier mobility and lattice thermal conductivity was observed at high Sb (Bi) content, likely due to the reduced La vacancy concentration, which resulted in a small increase in zT at high T .

The work on $\text{La}_{3-x}\text{Te}_4$ taught me the basics of thermoelectric research, from synthesis to theoretical considerations. As such, it enabled my role in the investigations of several other compounds. [91, 97, 104–107] Much of this work is discussed in a recent review article. [27]

In addition to the core work on $\text{La}_{3-x}\text{Te}_4$, this thesis discusses the transport in $\text{Ba}_8\text{Ga}_{16-x}\text{Ge}_{30+x}$ and the $\text{SrZnSb}_2/\text{SrZn}_2\text{Sb}_2$ systems. The work discussed here corresponds to the publications in which I was first author. [104, 105] After much effort obtaining reproducible data in the $\text{Ba}_8\text{Ga}_{16-x}\text{Ge}_{30+x}$ system, [107] the parabolic band model was utilized to optimize performance with $x = 0.25$ identified as the most promising n -type composition. [104] A collaborative effort with Bo Iversen's group at the University of Aarhus is currently underway in an attempt to understand an anomalous transition event that was observed.

The $\text{SrZnSb}_2/\text{SrZn}_2\text{Sb}_2$ materials were examined to investigate the influence of atomic structure on transport. It was found that the high number of atoms per unit cell in SrZnSb_2 corresponds to a low lattice thermal conductivity, whereas the smaller unit cell of SrZn_2Sb_2 possesses a higher lattice thermal conductivity. This is believed to be due to the direct relationship between atoms per cell and the number of optical phonons, which generally have low group velocities and thus promote low lattice thermal conductivity. The nano/micro-structure of these compounds is currently being examined via transmission electron microscopy by Øystein Prytz of the University of Oslo.

Chapter 2

Experimental Methods

2.1 Summary

This chapter discusses the synthesis and characterization of inorganic, crystalline materials. It begins with an introduction to solid-state synthesis, in which case mass diffusion limits the reaction time. The essential tools to overcome this kinetic barrier are discussed in relation to the basic forms for the diffusion coefficient. After establishing the basic principles for the synthesis of crystalline solids, the procedures utilized to obtain the compounds discussed in this text are given in detail.

In the case of $\text{La}_{3-x}\text{Te}_4$, direct milling (high-energy ball milling) of the elements was utilized to obtain single-phase samples near room temperature; the importance of this is discussed in relation to the phase diagram. $\text{Ba}_8\text{Ga}_{16-x}\text{Ge}_{30+x}$ samples were prepared by a combination of melting/quench and ball milling. For the Sr-Zn-Sb compounds, melting of the elements was followed by a short anneal at elevated temperatures then ball milling. In all cases, pressure-assisted sintering was utilized to transform the fine powder product into a dense cylinder. The chapter also contains the pertinent details for characterizing the chemical and transport properties of these compounds, as well as some computational details provided by the theoretical collaborators performing density functional theory calculations.

2.2 Synthesis of Inorganic Solids

The synthesis of inorganic, crystalline solids is generally limited by mass diffusion. That is, the phase diagram reveals which compounds are thermodynamically accessible, and the goal is then to overcome kinetic barriers for forming the desired phase. The primary goal during synthesis is thus to reduce the time for diffusion to occur. In general, the diffusion time (t_D) scales as l_D^2/D_M , where l_D is the diffusion length and D_M is the mass diffusion coefficient.

In solids, the diffusion coefficient has activated behavior, $D_M = D_{0,M} \text{Exp}[-Q_a/kT]$, where Q_a is the activation energy for diffusion[108, 109]. Therefore, synthesis often employs high-temperatures, which results in relatively large diffusion coefficients. Upon melting, D_M increases by several orders of magnitude

and l_D decreases dramatically[109], and thus procedures involving melting are often employed. Alternatively, one can reduce l_D and thus greatly reduce t_D .

The synthesis of a single phase material from a high-temperature melt procedure can be very difficult. The pertinent phase diagram(s) should always be consulted before attempting such a synthesis. However, phase diagrams are not available for many systems, and in such cases trial and error typically leads to the most-successful synthesis procedure. Often times, solidification must be avoided due to the presence of a peritectic reaction or other phase diagram feature that leads to the formation of undesired phase(s). In these cases, lower temperature, solid-state synthesis is often employed.

The classic ‘shake and bake’ procedure can often be applied: elements are combined and held at an elevated temperature for a long period of time to allow diffusion to occur. The mixture is cooled, the system is ground, and the procedure is repeated until the desired phase is obtained. This technique has the disadvantage of taking a long time to complete, and the high number of cycles provides ample opportunity for contaminants (such as oxygen) to enter the system or for the experimentalist to make an error. The sublimation or boiling of volatile elements can also complicate high-temperature synthesis, leading to a system with an undesired stoichiometry that may or may not result in the formation of an undesired phase(s).

The work discussed in this thesis has employed high energy mechanical grinding (*mechanical alloying*, *high-energy ball milling*) to reduce l_D and promote the synthesis of homogenous, single phase samples in a short period of time. In some cases, as in the $\text{La}_{3-x}\text{Te}_4$ system, mechanical alloying alone has been utilized to form the desired phase. In other cases, such as in $\text{Ba}_8\text{Ga}_{16-x}\text{Ge}_{30+x}$ or SrZnSb_2 , the mixture is first melted and quenched, and then ball milled. Sometimes the best synthesis involves slow cooling upon solidification, while quenching may be required elsewhere. The postmilled mixture is often single phase, but small quantities of impurities may be present. In particular, this procedure can result in grain boundary oxidation, as the resulting grains are typically small. Thus, it is important to perform all tasks that expose the sample in an inert atmosphere.

The final synthetic step is the sintering of powders to produce dense samples that can be characterized by a variety of techniques. The samples discussed in this work were sintered via pressure-assisted sintering, or *hot pressing*. Pertinent details for this technique can be found in Appendix B. The combination of fine grains resulting from milling and high-temperature sintering is believed to reduce the inhomogeneity within a single phase region, and likely promotes single phase samples through a macroscopic reflection of the microscopic mixing. After dense cylinders (roughly 0.5–1.5 cm tall, 1.2 cm in diameter) were obtained from hot pressing, the samples were cut using a low-speed diamond saw and non-aqueous lubricant. The characterized specimens were roughly 1–2mm in thickness.

2.2.1 $\text{La}_{3-x}\text{Te}_4$

The synthesis of $\text{La}_{3-x}\text{Te}_4$ is complicated by the lanthanum-tellurium phase diagram, which is shown in Figure 2.1[54]. The compositions of interest are $\text{La}_{3-x}\text{Te}_4$ with $0 \leq x \leq \frac{1}{3}$, which possess the Th_3P_4 struc-

ture type; the end-member compositions can be represented by La_3Te_4 and La_2Te_3 . As observed in Figure 2.1, the compositions of interest melt near 1773 K and both peritectic and eutectic reactions are observed to occur with end-member compositions and the appropriate neighboring phase. The melting temperature of $\text{La}_{3-x}\text{Te}_4$ is above the boiling point of tellurium (Te melts at 722 K and boils at 1261 K), and thus tellurium evaporation/sublimation is a significant concern.

Solidification of a particular composition (x value) results in changing tellurium content within a particular grain (due to liquid/solid two phase regions) and long annealing times are required to homogenize such a sample. For samples with less than approximately 58 at.% Te, the proximity of the eutectic reaction with LaTe necessitates large quenching rates during solidification and only a small stoichiometric window exists. Together with the high vapor pressure of tellurium, this makes producing high resistance/semi-insulating samples ($x = \frac{1}{3}$) especially difficult. Finally, the sensitivity of lanthanum to oxygen provides an additional complication. Despite these difficulties, prior work sponsored by the Jet Propulsion Laboratory was successful in generating single phase samples of lanthanum telluride via a melt and anneal procedure that utilized tungsten crucibles. However, the process was slow and obtaining single phase (and homogeneous) samples was not systematic. Therefore, the initial goal of this work was to produce single phase, homogenous samples of $\text{La}_{3-x}\text{Te}_4$ in which the stoichiometry could be reproducibly controlled.

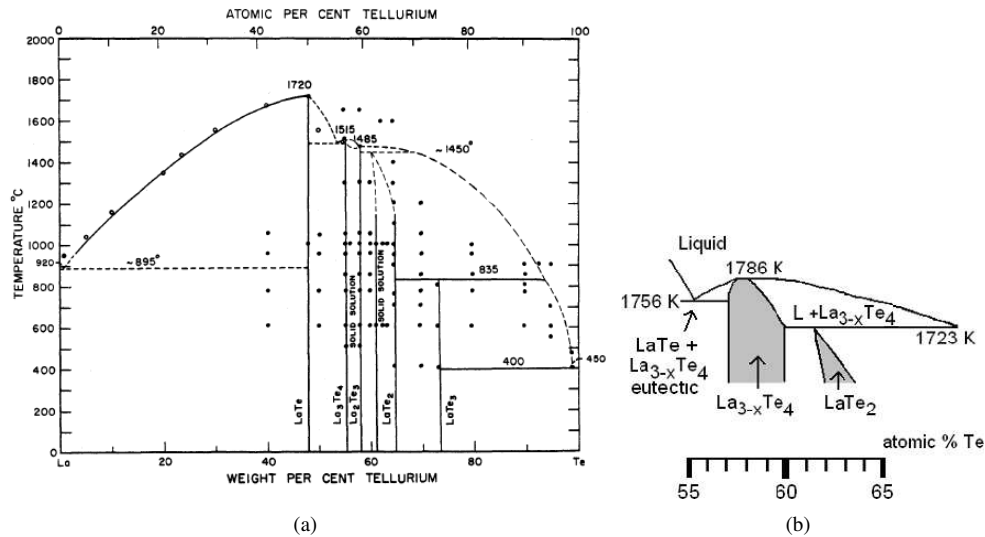


Figure 2.1. The lanthanum-tellurium phase diagram[54]. The melting point of $\text{La}_{3-x}\text{Te}_4$ is higher than the boiling point of elemental Te, and the presence of a peritectic and eutectic reaction with the neighboring LaTe_2 and LaTe binaries complicate traditional melt synthesis. (b) Close examination of the pertinent region of the phase diagram. Panel (a) is reprinted with permission from *Inorg. Chem.* **4**, 1154 (1965). Copyright 1965, American Chemical Society. Panel (b) is reprinted with permission from *Phys. Rev. B*, **78** 125205 (2008). Copyright 2008, American Physical Society.

The synthesis of lanthanum telluride is accomplished near room temperature by mechanical alloying. The production of the desired $\text{La}_{3-x}\text{Te}_4$ phase near room temperature increases sample homogeneity and

reproducibility by two distinct routes: (i) avoiding solidification reduces concerns about the production of inhomogeneous grains, and (ii) reducing elemental tellurium to the Te^{2-} state (via reaction with La) stabilizes tellurium with respect to vapor phase losses. Mechanical alloying also allows multiple samples to be produced in a short time period, and is therefore an ideal tool for studying the relationship between the thermoelectric properties and composition in $\text{La}_{3-x}\text{Te}_4$.

Mechanical alloying occurred as follows: A total of ten grams of the raw elements are combined in a stainless steel vial with two half-inch stainless balls (purchased from SPEX). The vial is placed into a SPEX 8000 Series Mixer/Mill and is milled for a total of eight hours, using a procedure of one hour of milling followed by one hour of cooling to minimize damage to the motor and keep the metallic phases from becoming overly ductile. The amount of milling time required has not been investigated thoroughly; the goal for this study was to obtain single phase, homogenous samples, thereby allowing the thermoelectric efficiency to be investigated.

For a successful synthesis, elemental lanthanum must be cut to 2-3 mm pieces. Elemental species were obtained from Alfa Aesar; lanthanum and tellurium chunks with metals basis purity 99.9% and 99.999%, respectively, were utilized. The size of the tellurium starting material has little impact on the final product because tellurium is very brittle and grinds quickly. Lanthanum, on the other hand, is ductile and if the initial pieces are too large the lanthanum will stick to the walls or corners of the vial and prevent the formation of single phase samples. A similar effect is observed if too much material is placed into the vial and complete reaction is inhibited due to this ‘caking’ (compaction of material into the corners of the vial).

The lanthanum obtained from Alfa Aesar comes packaged under mineral oil, which is removed via d-limonene; after cleaning the metal it must be stored in an inert atmosphere. The surface of the lanthanum ingots (roughly 1 cm^2 in size, enough for two samples) must be polished to remove all oxygen contamination. Along with polishing, the lanthanum ingots are cut to the appropriate size just prior to the onset of mechanical alloying to ensure minimal surface contamination. A two foot bolt cutter followed by an eight inch bolt cutter was found to be the best method for obtaining the necessary particle size in a reasonable amount of time (~ 1 hr per sample). All steps are performed in an argon dry box. The synthesis has been attempted with powder lanthanum, however this approach was not successful, presumably due to oxidation of the La grains.

A fine grain, homogenous powder results from the mechanical alloying. This powder is believed to contain only the desired $\text{La}_{3-x}\text{Te}_4$ phase. The powder is recovered from the vial using a curved bearing scraper obtained from McMaster-Carr, which enables yields greater than 95%. The powder is densified using pressure assisted sintering, or *hot pressing*, where the powder is sintered at elevated temperatures while under uniaxial pressure. See Appendix B for further details regarding hot pressing; the use of a graphoil liner was not found to be critical in the sintering of $\text{La}_{3-x}\text{Te}_4$, but was employed to avoid cross contamination.

Samples with large x are more difficult to sinter than those with low x . This is likely due to a combination of effects. Samples with low x are metallic, and are thus more ductile than those with large x . The nature (effective composition) of the sample can be observed after milling, because the low x samples tend to

stick to the vial, while large x or oxidized samples are easy to remove and produce very high yields. Also, samples with large x are more readily oxidized to $\text{La}_2\text{O}_2\text{Te}$ and the presence of this compound likely inhibits sintering. Many different press profiles were utilized, with none providing the high density observed in the more metallic samples. The best profile ($\sim 90\%$ theoretical density) involved changing the vacuum conditions, suggesting Te loss may have caused additional problems. The large x samples do not possess the optimal thermoelectric performance and are thus of little technological interest.

2.2.2 $\text{Ba}_8\text{Ga}_{16-x}\text{Ge}_{30+x}$

This section is an adapted reproduction, with permission, from *Phys. Rev. B*, **80**, 125205 (2009). Copyright 2009, American Physical Society.

Polycrystalline samples of the Type I clathrate $\text{Ba}_8\text{Ga}_{16-x}\text{Ge}_{30+x}$ were synthesized using a melt, quench, ball mill, hot-press procedure [104, 107]. The work performed on $\text{Ba}_8\text{Ga}_{16-x}\text{Ge}_{30+x}$ was a collaborative effort, with the synthesis responsibilities falling primarily on Ali Saramat after a procedure was decided upon. The samples discussed here were synthesized by a direct reaction of the elements in pyrolytic boron nitride crucibles sealed within evacuated (2×10^{-5} torr) quartz ampoules. High purity Ga (99.99% metals basis, Aldrich), Ge (99.9999% metals basis, Alfa Aesar) and Ba (distilled, dendritic 99+% metals basis, Aldrich) were utilized, and a slight excess of Ba was employed to compensate for possible oxidation—nominal compositions were $\text{Ba}_{8.2}\text{Ga}_{16-x}\text{Ge}_{30+x}$ [107].

Mixtures of the elements were heated to 1325 K at 100 K/hr, where the melts were held for 2 hr prior to quenching in air. The resulting ingots were ground under argon in a SPEX SamplePrep 8000 Series Mixer/Mill for a minimum of 1 hr and maximum of 4 hr inside stainless steel vials with two half-inch, stainless steel balls. Fine, homogeneous powders from the high energy milling were hot pressed in high density graphite dies (POCO) utilizing roughly 1.1 metric tons of force over a 12 mm diameter at 1100 K. Hot pressing took place over 1 hr in an argon atmosphere, and was followed by 1 hr of stress free anneal under vacuum. Further details of the sintering procedure can be found in Appendix B.

2.2.3 SrZnSb_2 and SrZn_2Sb_2

This section is an adapted reproduction, with permission, from *J. Appl. Phys.*, **106** 013706 (2009). Copyright 2009, American Institute of Physics.

Stoichiometric amounts of the elements (at least 99.9% metals basis purity) were combined in a pyrolytic BN crucible, which was sealed in a quartz tube evacuated to 1×10^{-5} torr. Samples were slowly heated from 575 to 1225 K, and the resulting melt was held at 1225 K for 30 min. The melt was cooled to 825 K in 2.5 hr, and the sample was annealed at 825 K for 2.5 hr. The resulting ingot was ball milled under argon for 15 min in the high energy SPEX 8000 Series Mixer/Mill utilizing stainless steel vial and balls. The fine grain, homogenous powder obtained from milling was hot pressed (see Appendix B) in a high-density

graphite die (POCO) at 825 K, for approximately 3 hr, while roughly 1.4 metric tons of force was placed on a 12 mm diameter surface. The dense ingots obtained from hot-pressing were cut using a slow cut saw with non-aqueous lubricant, and the resulting wafers were $\sim 1\text{--}2$ mm thick.

2.3 Characterization

2.3.1 Chemical Characterization

Phase purity was addressed using powder x-ray diffraction, electron probe microanalysis (EPMA), and scanning electron microscopy (SEM). To address composition and homogeneity, wavelength dispersive spectroscopy (WDS) and energy dispersive spectroscopy (EDS) were performed during EPMA and SEM, respectively. X-ray diffraction was the primary tool utilized to identify the phases contained within a sample. A Philip's X'Pert Plus diffractometer with Cu radiation (K_α) was employed under a current of 40 mA with a voltage of 45 kV. A JOEL JXA-8200 electron microprobe was utilized in the back-scattered electron mode to create compositional contrast images. Images were taken at magnifications up to $1000\times$, however, the images taken at $200\times$ provide the same evidence of single-phase samples with near theoretical density.

Table 2.1. Standards and detector settings commonly utilized during wavelength dispersive spectroscopy (WDS).

Element	Standard	Detection Crystal	Radiation Type	Background Position
Te	Te	PETH	L_α	(+3,-3.4)
Sb	Sb	PETJ	L_α	(+3.0,-2.9)
Bi	Bi	PETJ	M_α	(+5.0,-3.0)
La	LaPO ₄	PETL	L_α	(+4.0,-2.0)
Yb	YbPO ₄	LIF	L_α	(+5,-5)
Ba	BaTiSi ₃ O ₉ (benitoite)	PETH	L_α	(+5.0,-3.0)
Ga	GaAs	LIF	K_α	(+5.0,-5.0)
Ge	Ge	Tap	L_α	(+3.0,-5.0)

The JEOL JXA-8200 was also employed for WDS where an electric potential of 15 kV is utilized and a ZAF matrix correction is employed to account for atomic number, absorption and fluorescence effects. The EPMA was performed by Teruyuki Ikeda, with some assistance from Chi Ma, in Caltech's Division of Geology and Planetary Sciences. WDS is generally considered to be a more accurate probe of elemental composition due to the use of standards. The standards employed are shown in Table 2.1. Also shown in Table 2.1 are the typical settings utilized during WDS. Specific background positions are selected to avoid peak overlap.

For $\text{La}_{3-x}\text{Te}_4$, a NETZSCH Dilatometer (DIL 402C) measured the coefficient of thermal expansion to 1225 K, in an argon forming gas of 7% H_2 , at 2 K/min[100, 101]. Vilupanur A. Ravi and Samad A. Firdosy performed these measurements at JPL. Also, a NETZSCH STA 449C simultaneously performed thermogravimetry and differential thermal analysis (TG-DTA); this was performed by J. Paik of JPL to estimate the

rate of sublimation as this is a candidate material for deepspace power generation. The TG-DTA data were obtained between room temperature and 1375 K at 20 K/min, under argon flow with an alumina crucible as reference.

2.3.2 Characterization of Transport Properties

Transport properties were characterized from room temperature to a temperature specified by the material of interest. All measurements were performed under dynamic vacuum; a pressure of less than 5×10^{-4} torr is desirable.

Electrical transport was characterized via Hall coefficient, electrical resistivity, and Seebeck coefficient measurements. The Hall coefficient and electrical resistivity were obtained using the Van der Pauw method. Hall coefficients (R_H) were measured on two separate systems. High-temperature measurements ($T > 673$ K) were performed at the Jet Propulsion Laboratory using a magnetic field of ~ 1 T. Lower temperature Hall effect measurements were generally performed at Caltech to take advantage of the ~ 2 T magnetic field (signal \propto field). The Seebeck coefficient (α) was obtained at room temperature using Cu/constantan thermocouples by accounting for the Cu voltage. High-temperature α measurements employed W/Nb thermocouples and utilized the differential light pipe method discussed in Reference [110]; a $\Delta T \sim 5$ K was employed for all temperatures. The electrical resistivity and Seebeck coefficients for lanthanum telluride-based materials and the $\text{Ba}_8\text{Ga}_{16-x}\text{Ge}_{30+x}$ samples were collected at the Jet Propulsion Laboratory; ‘System 1’ was typically employed using the software written by G. J. Snyder. Data for SrZnSb_2 and SrZn_2Sb_2 were collected at Caltech.

Thermal conductivity (κ) was determined via $\kappa = D_T C_P d$, where D_T is the thermal diffusivity, C_P the heat capacity, and d the geometric density. The value of D_T was obtained via a NETZSCH Laser Flash Analysis (LFA) 457. The JPL and Caltech NETZSCH LFA 457 systems were found to provide indistinguishable data, and thus measurements from both systems can be accurately compared and reported simultaneously. The LFA measurements were generally performed under vacuum pulled by a turbo pump after purging the system multiple times with industrial argon.

For $\text{La}_{3-x}\text{Te}_4$ -based samples, the heat capacity initially reported [38] was obtained from the NETZSCH LFA 457 using a pyroceram 9606 standard. This heat capacity was lower than expected at room temperature and more recent publications have utilized an updated version obtained during a collaboration with scientists at Oak Ridge National Laboratory[101]. These later measurements were performed at ORNL by W. D. Porter on a NETZSCH 404c differential scanning calorimeter (DSC). The results were found to be in better agreement with the value expected from the Dulong-Petit limit of $3R/\bar{M}$, where \bar{M} is the mean molecular weight of the crystal. The high-temperature data were collected for a highly metallic sample with nominal composition La_3Te_4 . To utilize these data for the wide compositional range, the data is manipulated to estimate the electronic contribution and account for the reduced electronic contribution as x increases.

The high-temperature DSC measurements performed at ORNL utilized Pt crucibles with alumina liners

under an ultrapure Ar purge gas cycled through a Ti gettering furnace. The scans were performed after a careful evacuation of the sample chamber. The temperature scan rate was 20 K/min. Low temperature heat capacity was also collected, for which a Quantum Design physical property measurement system (PPMS) was employed. Data were collected between 1.85 and 300 K in zero applied magnetic field for all samples. Data for the highly metallic La_3Te_4 sample were also collected over the temperature range of 1.86 to 10 K in an applied field of 12 T to suppress the superconducting transition[101].

For $\text{Ba}_8\text{Ga}_{16-x}\text{Ge}_{30+x}$ samples, high-temperature heat capacity data were collected from the LFA 457 by utilizing a pyroceram 9606 standard. A NETZSCH 200 series DSC also obtained C_P to roughly 775 K using a sapphire standard and a heating rate of 20 K/min with Pt crucibles and Al_2O_3 liners. Thermogravimetry (TGA) data were obtained in a NETZSCH TG 209 F3 from 300 to 1025 K at 20 K/min under nitrogen; the purpose of this was to confirm there was no weight loss through the observed transition[104]. The DSC and TGA data were collected by Lloyd MacPherson of NETZSCH, while the LFA 457 measurements were performed at Caltech.

The Dulong-Petit limit of C_P was employed for SrZnSb_2 and SrZn_2Sb_2 . This likely provides an accurate description of the room temperature heat capacity, as the Debye temperature for both compounds is estimated to be 222 K, based on sound velocity data. This is likely an underestimation at higher temperatures, particularly for SrZnSb_2 due to the high electrical conductivity (implying a high electronic contribution to C_P).

Normal and shear ultrasonic measurements were performed at room temperature to extract the longitudinal and transverse sound velocities, respectively. The couplant utilized for the normal mode varied from a thin oil (mineral oil, vegetable oil) to the thick couplant utilized for shear measurements (honey or a specially purchased shear couplant). The data collected for $\text{La}_{3-x}\text{Te}_4$ were originally obtained at the Jet Propulsion Laboratory with the assistance of Jack Aldrich in the laboratory of Yoseph Bar-Cohen. These data were obtained using input from a Panametrics 5052 Pulser/Receiver with the filter at 0.03 MHz. The response was recorded via a digital oscilloscope, the Tektronic TDS 5054B-NV; the high resolution mode was employed for the longitudinal speed of sound and an averaging mode (16 waveforms) was utilized for the transverse speed of sound measurements. Raw data for the $\text{La}_{3-x}\text{Te}_4$ system are shown in Appendix G along with some additional comments. For the $\text{Ba}_8\text{Ga}_{16-x}\text{Ge}_{30+x}$ and Sr-Zn-Sb based samples, a Panametrics NDT 5800 pulser/receiver was employed with a Tektronix TDS 1012 digital oscilloscope; these measurements were performed in W. Johnson's laboratory at Caltech.

2.4 Analysis of Transport Properties

The solutions to the Boltzmann transport equation are utilized to analyze the experimental transport data. The required equations contain infinite integrals, though the upper limit can be reduced significantly to facilitate computation when necessary. These calculations were performed in Mathematica and MathCad. MathCad

Table 2.2. Experimental lattice parameter of La_3Te_4 [48], and computational lattice parameters for the relaxed La_3Te_4 , $\text{La}_3\text{Te}_3\text{Sb}$, and $\text{La}_3\text{Te}_3\text{Bi}$ cells. Reprinted with permission from *Phys. Rev. B* **81**, 125205 (2010). Copyright 2010, American Physical Society.

	Lattice Parameters (Å)			Wyckoff Positions			
	a	b	c		x	y	z
La_3Te_4 (exp)	9.634	9.634	9.634	La	0.375	0.000	0.250
				Te	0.083	0.083	0.083
La_3Te_4	9.687	9.687	9.687	La	0.375	0.000	0.250
				Te	0.076	0.076	0.076
$\text{La}_3\text{Te}_3\text{Sb}$	9.692	9.686	9.690	La	0.375	0.000	0.250
				Te	0.075	0.076	0.076
				Sb	0.080	0.081	0.081
$\text{La}_3\text{Te}_3\text{Bi}$	9.741	9.736	9.742	La	0.375	0.000	0.251
				Te	0.074	0.075	0.075
				Bi	0.079	0.080	0.080

was found to handle the larger, more complex integrations more rapidly. Mathematica was, however, utilized frequently to generate files containing tabular data for plotting the simulated transport properties.

2.5 Density Functional Calculations

This section is an adapted reproduction, with permission, from *Phys. Rev. B*, **79**, 153101 (2009) and *Phys. Rev. B*, **81**, 125205 (2010). Copyright 2009 and 2010, American Physical Society.

This primarily experimental dissertation was complemented by first-principles calculations, which provide invaluable information when examining transport in solids. These density functional theory calculations (DFT) were performed by David J. Singh[51] of Oak Ridge National Laboratory and Espen-Flage Larsen[103] of the University of Oslo.

The calculations performed by David J. Singh on La_3Te_4 employed the local-density approximation (LDA) using the linearized augmented plane-wave (LAPW) method with local orbitals[111] as implemented in WIEN2K[112]. The experimental lattice parameter of $a = 9.634$ Å from Reference [48] was used with LAPW sphere radii of 2.9 Bohr and tested basis sets. Relativistic effects, including spin-orbit were included.

Calculations of transport properties generally require knowledge regarding the relevant scattering mechanisms. However, the Hall and Seebeck coefficients do not contain a dimension of time and can often be well characterized by assuming the electronic relaxation time (τ) is independent of energy. The prior publication[51] terms this the constant relaxation time approximation (CRTA) though now we call this energy independent scattering EIS, as discussed in the Electrical Transport Theory section. The Boltzmann transport equation was utilized to calculate the Seebeck and Hall coefficients within the EIS(CRTA) using the BoltzTraP code[113].

The electronic structures of La_3Te_4 , $\text{La}_3\text{Te}_3\text{Sb}$, and $\text{La}_3\text{Te}_3\text{Bi}$ [103] were calculated by Espen Flage-Larsen within the DFT framework of the Vienna *ab-initio* simulation package (VASP)[114, 115]. Even

though these valence balanced, ternary compounds have never been synthesized and are likely to contain significant anion site disorder, these calculations serve as an approximate model to shed light on the role of the Te to Sb and Bi substitution. The calculations employed the Perdew-Burke-Ernzerhof (PBE)[116] exchange-correlation functional in the generalized gradient approximation (GGA). In the absence of experimental lattice parameters for $\text{La}_3\text{Te}_3\text{Sb}$ and $\text{La}_3\text{Te}_3\text{Bi}$, relaxations of the structures were performed using the experimental lattice parameter[48] of La_3Te_4 as input. Four out of sixteen Te atoms were exchanged for Sb or Bi within the original unit cell to obtain the $\text{La}_3\text{Te}_3\text{Sb}$ and $\text{La}_3\text{Te}_3\text{Bi}$ stoichiometry, respectively. The structures were relaxed in cell shape, volume, and atomic positions using a residual minimization, direct inversion in the iterative subspace scheme (RMM-DIIS)[117]. For comparison reasons, the relaxed La_3Te_4 structure was utilized.

An energy cutoff of 650 eV and a Γ -centered k -point sampling of $9 \times 9 \times 9$ were sufficient to converge the electronic structures. The density of states were obtained from a second run using the modified linear tetrahedron method[118].

The Te positions in the relaxed La_3Te_4 differs by 5-8% (see Table 2.2 for the diagonal lattice constants and Wyckoff positions) of the experimental structure reported in Reference [48], while the change in the La positions are within 1%. Slight distortions of the symmetry of the unit cell of $\text{La}_3\text{Te}_3\text{Sb}$ and $\text{La}_3\text{Te}_3\text{Bi}$ was observed, but was found to be less than 1% (based on the full lattice constant matrix). Hence, only the diagonal of the relaxed lattice vectors are given in Table 2.2. Wyckoff positions of $\text{La}_3\text{Te}_3\text{Sb}$ and $\text{La}_3\text{Te}_3\text{Bi}$ are strictly not valid (symmetry breaking), but are given for comparison reasons. The Sb and Bi sites change by approximately 1% with respect to the relaxed Te sites of La_3Te_4 . The discrepancy between the relaxed and experimental lattice parameters of La_3Te_4 stem from a DFT failure of properly describing the heavy elements and is most likely related to the well-known delocalization error. Due to the localization of the La f and Te d states, this error is particularly important in these systems. Relaxations of the Sb and Bi filled structures are within 1% of the relaxed La_3Te_4 structure and due to later comparisons we persist on using the relaxed La_3Te_4 parameters throughout this work. Comparisons of the band structure near the Fermi level reveal no significant change except a small shift of the La f states in the conduction band to lower energies in the relaxed La_3Te_4 structure. In addition, the band gap (of primary concern here) remains approximately constant upon relaxation. A unit cell expansion is observed upon the substitution of Sb and Bi for Te, which is expected due to size differences.

The electronic structure obtained for La_3Te_4 is consistent with that computed by David Singh[51], where a slightly smaller band gap (0.95 eV) was obtained due to the inclusion of spin-orbit coupling. The main effects of spin-orbit coupling in La_3Te_4 appear to be a small reduction in band gap and a 0.03 eV splitting of degenerate bands near the Fermi level (for the energies of interest). An additional calculation by D. Singh confirmed that spin orbit had little impact on the electron's effective mass, though it was found to be important when investigating the curvature of the valence band (p -type character).

Chapter 3

Chemical and Structural Results

3.1 Summary

The purity and composition of the synthesized compounds are discussed in this chapter. Specifically, powder x-ray diffraction data is utilized to address phase purity. The $\text{La}_{3-x}\text{Te}_4$ based compounds are all found to be phase pure. While the presence of the typical oxide La_2O_3 is difficult to rule out, these samples appear and behave (electronically) as though they are single-phase and the diffraction scans are very clean. Three of the $\text{Ba}_8\text{Ga}_{16-x}\text{Ge}_{30+x}$ samples were found to be phase pure, while two contained a very small amount of Ge impurity. The Ge impurity is common in polycrystalline $\text{Ba}_8\text{Ga}_{16-x}\text{Ge}_{30+x}$, and these samples represent some of the cleanest polycrystalline samples considered in the literature. The SrZnSb_2 compound was nearly phase pure, with a small elemental Sb impurity, while the SrZn_2Sb_2 contained a fairly large amount of ZnSb impurity.

Electron-probe microanalysis is utilized to examine sample homogeneity via backscattered electron images in $\text{La}_{3-x}\text{Te}_4$. This instrument also permits analysis of the chemical composition via wavelength dispersive spectroscopy and a detailed table is given to summarize these data for samples of nominal composition $\text{La}_{3-x}\text{Te}_4$, $\text{La}_{3-x-y}\text{Yb}_y\text{Te}_4$, and $\text{La}_3\text{Te}_{4-z}\text{Sb}_z$. The trends in composition are found to correspond to the expected changes in carrier density; the experimentally measured carrier density is the primary method of characterizing thermoelectric samples when developing physical models for transport.

A scanning electron microscope was utilized to investigate the sample homogeneity and composition in $\text{Ba}_8\text{Ga}_{16-x}\text{Ge}_{30+x}$. The chemical characterization results from energy dispersive spectroscopy are summarized in a table, and are discussed in relation to the experimental carrier concentration in the electrical transport section.

3.2 $\text{La}_{3-x}\text{Te}_4$ and Subsystems

The mechanical alloying synthesis successfully produced single phase, homogeneous samples of $\text{La}_{3-x}\text{Te}_4$, $\text{La}_{3-x-y}\text{Yb}_y\text{Te}_4$, $\text{La}_{3-x}\text{Te}_{4-z}\text{Sb}_z$ and $\text{La}_{3-x}\text{Te}_{4-z}\text{Bi}_z$. This statement is slightly less justified for the Sb

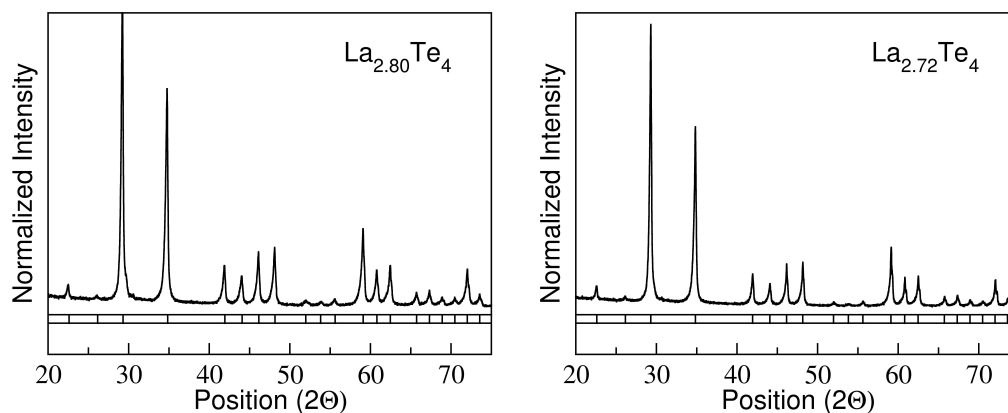


Figure 3.1. X-ray diffraction scans for two lanthanum telluride samples. The bar at the bottom demonstrates the positions of the desired peaks, and all observed peaks can be attributed to the expected Th_3P_4 structure type.

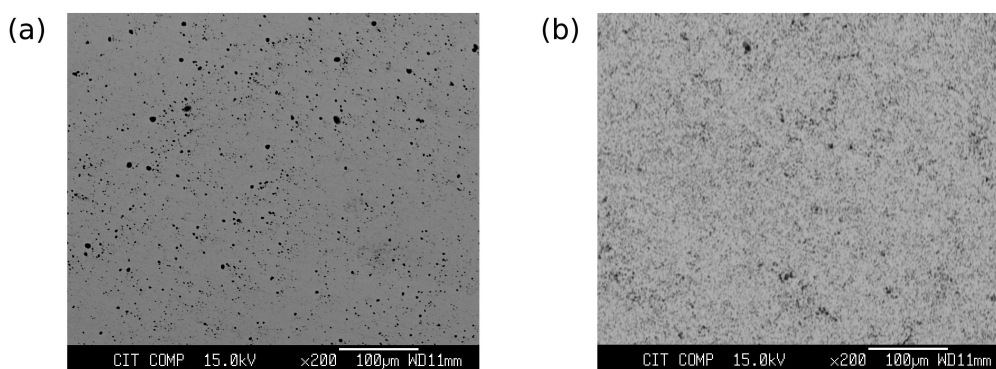


Figure 3.2. Electronprobe micrographs, taken using back scattered electron mode to reveal compositional fluctuations, indicate the samples are homogeneous with some porosity. The images shown were taken on the samples in Figure 3.1: (a) is nominal composition $\text{La}_{2.80}\text{Te}_4$ and (b) is $\text{La}_{2.72}\text{Te}_4$.

or Bi containing compounds due to the possible formation of a very difficult to identify phase (La_4Sb_3), as discussed below. However, no direct evidence for additional phases exists in these samples, and even the common oxide ($\text{La}_2\text{O}_2\text{Te}$) has been avoided in most cases.

Chemical characterization via X-ray diffraction (XRD) and electron microprobe analysis (EMPA) indicates that only the $\text{La}_{3-x}\text{Te}_4$ phase has been synthesized. This is demonstrated for two different compositions of $\text{La}_{3-x}\text{Te}_4$ in Figures 3.1 and 3.2, where the composition shown is the nominal one. The primary concern with synthesis is avoiding oxidation, which is typically observed as $\text{La}_2\text{O}_2\text{Te}$. This tetragonal phase has primary diffraction peaks near the primary diffraction peak of $\text{La}_{3-x}\text{Te}_4$; the primary peaks for $\text{La}_2\text{O}_2\text{Te}$ are at $2\theta \sim 30^\circ, 31^\circ$. The bars at the bottom of Figure 3.1 contain the desired peak positions for $\text{La}_{3-x}\text{Te}_4$, and all peaks can be assigned to the expected structure.

The micrographs shown in Figure 3.2 were taken in back scattered electron mode, which reveals compositional fluctuations or impurity phases via a change in contrast. These images correspond to the diffraction

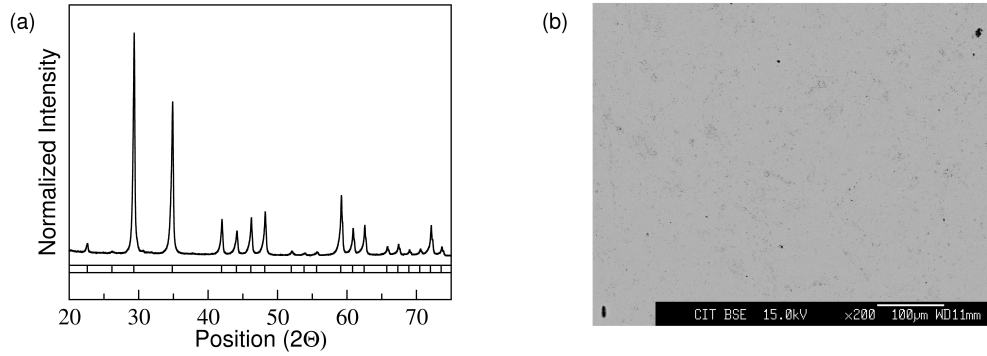


Figure 3.3. (a) X-ray diffraction scan and (b) compositional contrast image of the matrix in sample LYT107 (nominal composition $\text{La}_{2.375}\text{Yb}_{0.55}\text{Te}_4$).

data shown in Figure 3.1. Figure 3.2 reveals homogeneous samples with some porosity.

Further evidence for the synthesis of a single, stable phase was observed via thermogravimetry and differential thermal analysis, where no significant weight loss or peaks are observed up to 1375 K (not shown). This measurement reveals the sublimation rate is slightly better than that of uncoated SiGe[100], with a beginning of life (BOL) sublimation rate of $5 \times 10^{-5} \text{ g/cm}^2/\text{hr}$ compared to $8 \times 10^{-5} \text{ g/cm}^2/\text{hr}$ in uncoated SiGe. The coated SiGe, used in thermoelectric generators, has a BOL sublimation rate of $5 \times 10^{-7} \text{ g/cm}^2/\text{hr}$. The linear coefficient of thermal expansion ($\sim 19 \times 10^{-6} \text{ m/K}$ between 300 and 1200 K) was found to closely matched that of $\text{Yb}_{14}\text{MnSb}_{11}$, the *p*-type complement to $\text{La}_{3-x}\text{Te}_4$ [100]. The thermal expansion data of $\text{La}_{3-x}\text{Te}_4$ can be found in Reference [101]. A discussion of the sublimation rates and thermal expansion, as well as the reproducibility of this synthesis technique can be found in Reference [100].

The WDS data for the $\text{La}_{3-x}\text{Te}_4$ samples are summarized in Table 3.1, where the data reported for $\text{La}_{3-x}\text{Te}_4$ are an average of five point measurements which probe roughly one cubic micron. The WDS analysis leads to a lanthanum content that is not physically permitted by the crystal structure ($x < 0$). This is believed to be due to the use of LaPO_4 as the La standard, though the particular ZAF correction employed or oxidation of grain boundaries may also be the source for this deviation. Regardless of the source, the deviation between the nominal and experimentally observed compositions is relatively consistent across the entire series of samples, and the desired trend is observed. One sample contained a small inclusion of iron and chromium, presumably from the milling balls or vial; however, these elements were not found in the neighboring $\text{La}_{3-x}\text{Te}_4$ matrix. Thus, the ability to reproducibly synthesis homogeneous $\text{La}_{3-x}\text{Te}_4$ samples has been developed. Considering that this investigation is primarily concerned with thermoelectric transport, the Hall carrier density n_H is a better measure of sample character and is utilized throughout the manuscript.

The $\text{La}_{3-x-y}\text{Yb}_y\text{Te}_4$ samples were also found to be phase pure and homogeneous by X-ray diffraction and electron probe microanalysis, as observed in Figure 3.3. During EPMA, wavelength dispersive spectroscopy (WDS) revealed a changing Yb:La content that trends well with the experimental Hall carrier concentration. The WDS data summarized in Table 3.1 are an average of many (roughly 25) $20 \mu\text{m}$ WDS

Table 3.1. Summary of sample information for $\text{La}_{3-x}\text{Te}_4$ and subsystems. Wavelength dispersive spectroscopy (WDS) data and the corresponding room temperature Hall density n_H are provided.

Nominal Composition	Notebook ID	n_H (10^{21}cm^{-3})	La at. %	Te at. %	Yb at. %	Sb (Bi) at. %	WDS Formula Unit
$\text{La}_{2.99}\text{Te}_4$	LT134_34	4.07	43.3	56.7	-		$\text{La}_{3.03}\text{Te}_4$
$\text{La}_{2.92}\text{Te}_4$	LT137_3	3.90	43.4	56.6	-		$\text{La}_{3.04}\text{Te}_4$
$\text{La}_{2.86}\text{Te}_4$	LT57s_3	2.90	42.8	57.2	-		$\text{La}_{3.00}\text{Te}_4$
$\text{La}_{2.82}\text{Te}_4$	LT142_1	2.02	42.4	57.6	-		$\text{La}_{2.91}\text{Te}_4$
$\text{La}_{2.80}\text{Te}_4$	LT143_4	1.63	42.2	57.8	-		$\text{La}_{2.88}\text{Te}_4$
$\text{La}_{2.74}\text{Te}_4$	LT146_5	0.52	41.4	58.6	-		$\text{La}_{2.79}\text{Te}_4$
$\text{La}_{2.72}\text{Te}_4$	LT147_2	0.12	40.5	59.5	-		$\text{La}_{2.74}\text{Te}_4$
$\text{La}_{2.55}\text{Yb}_{0.3}\text{Te}_4$	LYT103	0.30	37.7	57.9	4.4	-	$\text{La}_{2.61}\text{Yb}_{0.30}\text{Te}_4$
$\text{La}_{2.65}\text{Yb}_{0.2}\text{Te}_4$	LYT104	0.75	39.2	57.8	2.9	-	$\text{La}_{2.71}\text{Yb}_{0.20}\text{Te}_4$
$\text{La}_{2.75}\text{Yb}_{0.1}\text{Te}_4$	LYT105	0.90	39.9	58.4	2.0	-	$\text{La}_{2.75}\text{Yb}_{0.14}\text{Te}_4$
$\text{La}_{2.325}\text{Yb}_{0.6}\text{Te}_4$	LYT106	0.06	34.0	57.4	8.6	-	$\text{La}_{2.36}\text{Yb}_{0.60}\text{Te}_4$
$\text{La}_{2.375}\text{Yb}_{0.55}\text{Te}_4$	LYT107	0.19	34.8	57.4	7.9	-	$\text{La}_{2.42}\text{Yb}_{0.55}\text{Te}_4$
$\text{La}_3\text{Te}_{3.80}\text{Sb}_{0.20}$	LTS20_1	2.94	42.6	46.0	-	11.4	$\text{La}_{3.05}\text{Te}_{3.76}\text{Sb}_{0.24}$
$\text{La}_3\text{Te}_{3.65}\text{Sb}_{0.35}$	LTS35_1	1.33	43.1	46.5	-	9.4	$\text{La}_{3.32}\text{Te}_{3.67}\text{Sb}_{0.33}$
$\text{La}_3\text{Te}_{3.40}\text{Sb}_{0.60}$	LTS60_1	0.54	43.4	46.8	-	9.8	$\text{La}_{3.06}\text{Te}_{3.31}\text{Sb}_{0.69}$
$\text{La}_3\text{Te}_{3.35}\text{Sb}_{0.65}$	LTS65_1	0.35	45.4	50.1	-	4.5	$\text{La}_{3.15}\text{Te}_{3.33}\text{Sb}_{0.67}$
$\text{La}_3\text{Te}_{3.20}\text{Sb}_{0.80}$	LTS80_3	0.08	43.3	53.3	-	3.4	$\text{La}_{3.10}\text{Te}_{3.18}\text{Sb}_{0.82}$
$\text{La}_3\text{Te}_{3.35}\text{Bi}_{0.65}$	LTB65_1	0.39	43.5	47.0	-	9.5	$\text{La}_{3.09}\text{Te}_{3.33}\text{Bi}_{0.69}$
$\text{La}_3\text{Te}_{3.20}\text{Bi}_{0.80}$	LTB80_1	0.39	43.6	45.2	-	11.2	$\text{La}_{3.10}\text{Te}_{3.20}\text{Bi}_{0.80}$

scans. Thus, it appears that Yb substitutes or fills the La position as expected, and single phase samples were produced. The expected (nominal) carrier density did not, however, trend that well with the experimental Hall density. These deviations are likely due to changing milling properties as the ratio Yb/La changes. Regardless, varying Yb/La produced a series of samples that allowed the optimization of thermoelectric efficiency to be inspected.

The samples of nominal composition $\text{La}_3\text{Te}_{4-z}\text{Sb}_z$ and $\text{La}_3\text{Te}_{4-z}\text{Bi}_z$ were found to be phase pure via X-ray diffraction. A representative set of diffraction data is shown in Figure 3.4 for the sample containing the maximum, nominal Sb content. However, the investigation of phase purity in these samples is complicated by the possible formation of La_4Sb_3 or La_4Bi_3 . These compounds possess the anti- Th_3P_4 structure types, placing La on the P site and Sb(Bi) on the Th site. The lattice constants (the diffraction scans in general), are very similar in the La_3Te_4 and La_4Sb_3 (La_4Bi_3) phases, to the extent that identifying one of these phases is nearly impossible via X-ray diffraction.

Electron probe microanalysis also suggested phase pure samples with Sb/Bi substituted on the Te site. This technique is plagued by resolution limitations, and small regions of La_4Sb_3 or La_4Bi_3 could go undetected. For instance, small portions of these phases at grain boundaries (or nanometer-scale inclusions) would be nearly impossible to identify without high resolution tunneling electron microscopy.

One strong indication of the formation of the desired phase is the absence of any additional peaks. For instance, if La_4Sb_3 or La_4Bi_3 were to form, then there would be an excess of Te which would likely form an additional phase. Thus it seems likely that these compounds form as desired, with the exception of La

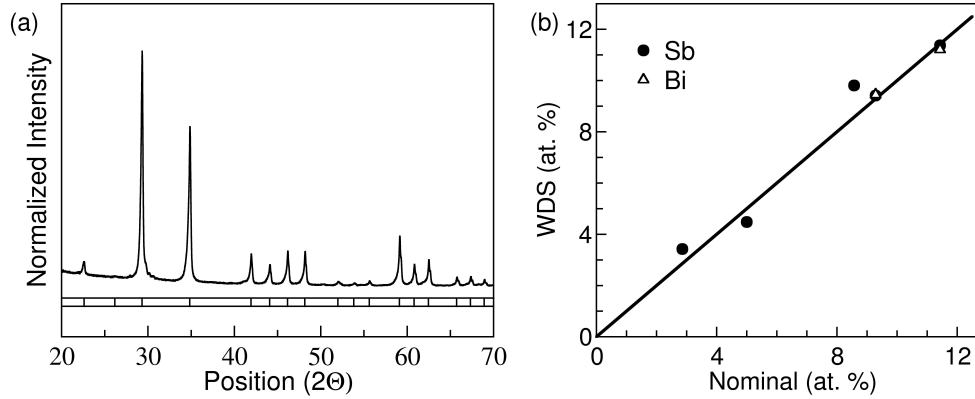


Figure 3.4. (a) X-ray diffraction scan of a sample that contains the maximum nominal Sb content ($\text{La}_3\text{Te}_{3.2}\text{Sb}_{0.8}$). (b) Wavelength dispersive spectroscopy (WDS) data for bulk atomic percent Sb versus nominal atomic percent Sb. Reprinted with permission from *Phys. Rev. B* **81**, 125205 (2010). Copyright 2010, American Physical Society.

content, which appears to be smaller than desired based on carrier concentration data. That is, La vacancies are likely present in much higher concentrations than expected from the nominally vacancy free compositions. For instance, carrier density measurements suggest $x \sim 0.10$ (assuming $\text{La}_{3-x}^{3+}\text{Te}_{4-x}^{2-}\text{Sb}_x^{3-}$). This feature is discussed in further detail in the electrical transport section. Despite the presence of some vacancies, these samples will still be referred to by their nominal compositions throughout the text.

3.3 $\text{Ba}_8\text{Ga}_{16-x}\text{Ge}_{30+x}$

This section is an adapted reproduction, with permission, from *Phys. Rev. B* **80**, 125205 (2009). Copyright 2010, American Physical Society.

The $\text{Ba}_8\text{Ga}_{16-x}\text{Ge}_{30+x}$ samples discussed in this thesis are given labels (capital letters *A* through *E*) and specific symbols are utilized to present the data, as shown in Table 3.2. Compositional data obtained via wavelength dispersive spectroscopy (WDS) are also provided in Table 3.2, and the expected changes in Ga:Ge are observed. The variation in Ba content is within the instrument resolution of ~ 0.5 at.%; Ba content is not expected to change as all samples possess the same nominal Ba concentration.

The polycrystalline samples were observed to be homogeneous via scanning electron microscopy and electron probe microanalysis. Samples *A*, *B*, and *D* were single phase via x-ray diffraction (XRD), while samples *C* and *E* contained a small amount of elemental Ge (refined to less than 1 wt.%), which is a common impurity phase in polycrystalline $\text{Ba}_8\text{Ga}_{16-x}\text{Ge}_{30+x}$ samples[89]. Phase purity is demonstrated in Figure 3.5, where a diffraction scan for the sample containing the most Ge impurity is shown (sample *E*). Figure 3.5b compares the scan shown in Figure 3.5 to a phase pure sample (*A*) in the vicinity of the Ge impurity peak.

Table 3.2. Atomic composition of $\text{Ba}_8\text{Ga}_{16-x}\text{Ge}_{30+x}$ samples assessed via wavelength dispersive spectroscopy. Reprinted with permission from *Phys. Rev. B* **80**, 125205 (2009). Copyright 2010, American Physical Society.

Sample	Symbol	Ba at.% (std dev)	Ga at.% (std dev)	Ge at.% (std dev)
A	\triangle	15.09 (0.08)	28.13 (0.14)	56.78 (0.17)
B	\square	15.31 (0.08)	28.54 (0.21)	56.15 (0.23)
C	∇	15.12 (0.06)	28.66 (0.17)	56.21 (0.18)
D	\circ	15.44 (0.16)	29.23 (0.14)	55.33 (0.18)
E	\diamond	15.10 (0.29)	29.87 (0.64)	55.03 (0.63)

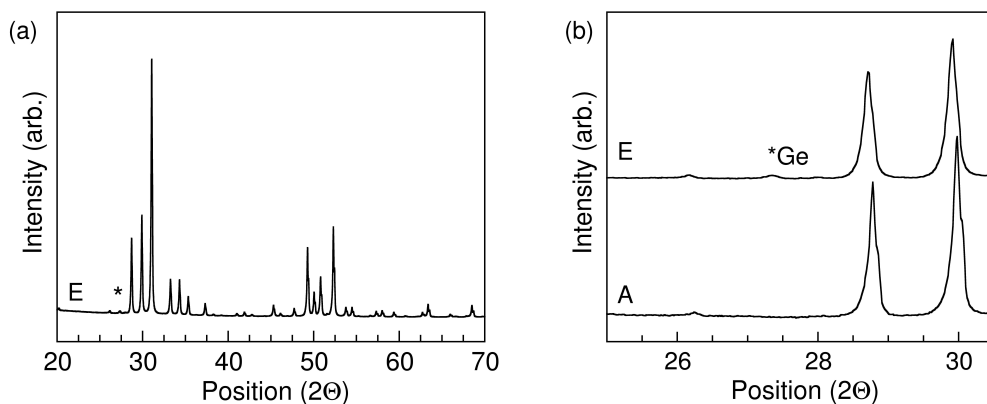


Figure 3.5. (a) X-ray diffraction scan of sample *E*, which contains the maximum Ge impurity observed in these polycrystalline samples. (b) The position around the Ge impurity is examined in detail, with a scan for sample *A* included. Reprinted (adapted) with permission from *Phys. Rev. B* **80**, 125205 (2009). Copyright 2010, American Physical Society.

3.4 SrZnSb_2 and SrZn_2Sb_2

The SrZnSb_2 samples contained a very small impurity phase of Sb. The SrZn_2Sb_2 samples contained an impurity phase of ZnSb, which was estimated to be ~ 6 volume % by Eric Toberer via Rietveld refinement. The position of the ZnSb peak is shown in Figure 3.6b. The expected (simulated) patterns are shown by the thin, gray curves in Figure 3.6. The samples also appeared relatively homogeneously under scanning electron microscopy.

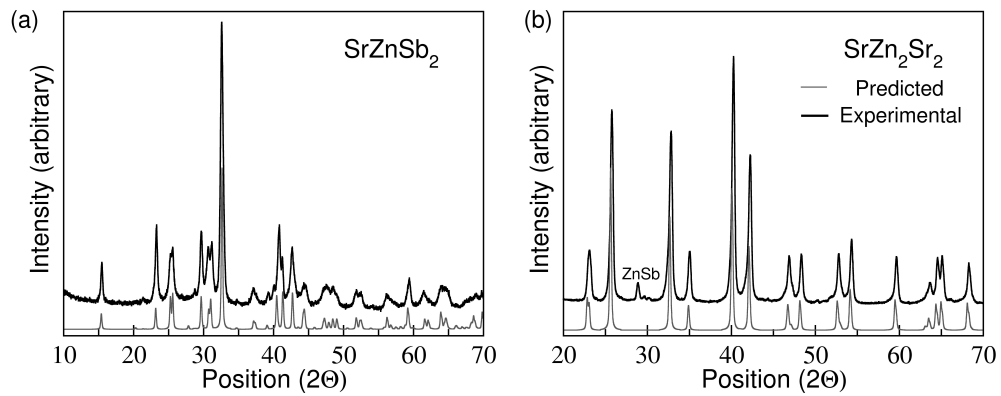


Figure 3.6. X-ray diffraction scans for (a) SrZnSb_2 and (b) SrZn_2Sr_2 . The black curves are experimental data and the thin gray curves are the simulated, expected patterns. The impurity phase of ZnSb in (b) is indicated by the included text, while Sb impurity in (a) is difficult to observe.

Chapter 4

Electrical Transport

4.1 Summary

This chapter discusses the electrical transport properties in solids, with a focus on the high-temperature thermoelectric behavior. It begins with an overview of the pertinent transport properties. In particular, expressions are given for the description of these transport properties within parabolic band models. Some discussion of the electronic relaxation times and corresponding scattering mechanisms is given. Graphs are provided to help understand the energy dependence of the more complex expressions, such as those for the Hall and Seebeck coefficients. The theoretical details discussed here are primarily concerned with the single band expressions, though bipolar or multiband effects are briefly discussed as well. A short discussion of the electronic contribution to the thermal conductivity is also provided.

The electrical transport in $\text{La}_{3-x}\text{Te}_4$ and its subsystems containing Yb, Sb, and Bi are discussed in detail. By controlling the composition, a transition from metallic to semiconducting behavior is observed. A single band model does not describe the dependence of Seebeck coefficient on carrier density for the compositions considered here. Analysis of the data suggests, and first principles calculations confirm, that the electronic structure contains multiple conduction bands in the pertinent energy range. Specifically, a light band dominates transport at low energy (low carrier density and/or high temperature) and heavy bands are important at high energies.

The substitution of Yb for La does not produce significant changes in the electronic behavior, with the exception of changing the carrier density. The substitution of Sb (Bi) for Te is found to promote activated conductivity at modest temperatures, though the high-temperature transport behavior is observed to be similar to that in $\text{La}_{3-x}\text{Te}_4$. The incorporation of Sb (Bi) also results in a reduction of the energy gap, which is confirmed via temperature-dependent Seebeck coefficient data and first principles calculations.

The electrical transport in n -type $\text{Ba}_8\text{Ga}_{16-x}\text{Ge}_{30+x}$ is found to be well described the single parabolic band model in the compositional range of interest to thermoelectric application. This is confirmed by considering previously reported first principles calculations, as well as data obtained here for a variety of carrier concentrations. Also, insulating samples have been prepared, which suggest a thermal band gap of roughly

0.4 eV.

Lastly, transport in the Sr-Zn-Sb compounds is considered. The SrZnSb₂ compound is found to be very heavily doped in a *p*-type manner, and the carrier density increases rapidly with increasing temperature. Combined with the temperature-dependent Seebeck coefficient data, this suggests a very small energy gap (or semimetallic behavior). SrZn₂Sb₂ is also *p*-type with a large number of free carriers; however, the carrier concentration is an order of magnitude lower than that of the SrZnSb₂ samples. Both compounds show the behavior expected for doped semiconductors, with the Seebeck coefficient and electrical resistivity increasing with increasing *T* before the onset of bipolar conduction.

4.2 Electrical Transport Theory

4.2.1 Introduction

Many textbooks provide detailed discussions of the following material. I have drawn significantly from Fishtul's *Heavily Doped Semiconductors*[119], which provides a detailed treatment of transport. Also, I have enjoyed Goldsmid's books, in particular the concise yet informative *Applications of Thermoelectricity*[4]. MacDonald's book *Thermoelectricity, An Introduction to the Principles*[120] provides a nice, simple discussion of thermoelectric transport. Of course, Ziman's *Electrons and Phonons. The Theory of Transport Phenomena in Solids*[29] and Ashcroft and Mermin's *Solid State Physics*[11] are invaluable resources for anyone interested in condensed matter physics. Despite the variety and thoroughness of the available texts, the aspects of electrical transport which are critical to the analysis and optimization of thermoelectric performance are now summarized.

Transport data are generally analyzed in an attempt to develop a predictive model. That is, by understanding the interactions and mechanisms governing transport one can manipulate or optimize a particular transport property. The solutions to the Boltzmann transport equation (BTE) are generally utilized to perform this task. This model for the transport properties is based on the concept of an electron distribution function, and the equilibrium Fermi-Dirac distribution function (f) is utilized as an approximation for the non-equilibrium distribution function found within the BTE. Also, it is assumed that the relaxation of the electron distribution function (back to equilibrium) can be described by a characteristic (relaxation) time τ .

The BTE is typically valid for electronic transport at high-temperatures[119]. Specifically, the relaxation time approximation is valid when scattering events are elastic in nature (energy is conserved), or when carrier scattering is isotropic[119]. These criteria are typically met, although complex dispersion relations bring the second part into question. The transport equation itself is valid when the relaxation time is much larger than the time over which the scattering events occur. This criterion is more difficult to address, though it has been suggested that it is met for systems of interest to the field of thermoelectrics[119].

The last major assumption utilized here is that the charge carrier energies are described by an isotropic,

parabolic dispersion relationship. This is equivalent to saying that the carriers have the free electron dispersion relationship. While it may appear inappropriate to exclude the impact of the atomic (ionic) lattice on the dispersion relation, this approximation often leads to very accurate models. This is due, in large part, to the periodic nature of crystalline solids which allows electrons to be treated similar to free electrons by introducing the concept of an *effective mass* (m^*)[121]. Of course, the use of semi-classical models describing local interactions (within the BTE) contributes significantly to the accuracy of the final models.

The isotropic, parabolic band dispersion relation for an electron in conduction band i is

$$E = \frac{\hbar^2 k^2}{2m_i^*} + E_{min,i}, \quad (4.1)$$

where m_i^* is the electron's effective mass and $E_{min,i}$ is the minimum energy of band i . The density of electronic states $N_i(E)$ (including spin degeneracy) in this band increases as the square root of energy:

$$N_i(E) = \frac{(2m_i^*)^{3/2}}{2\pi^2\hbar^3} \sqrt{E - E_{min,i}}. \quad (4.2)$$

For simplicity, it is assumed $E_{min,i}=0$ and that only one band contributes to conduction; this is the single parabolic band (SPB) model. For this isotropic approximation, the electron's effective mass is

$$m^* = \frac{1}{\hbar} \left(\frac{\partial^2 E(k)}{\partial k^2} \right)^{-1}. \quad (4.3)$$

The ever-increasing ease with which theorists can perform first principles calculations of electronic (band) structures requires the experimentalist to, at a minimum, qualitatively understand a band structure diagram (the 'spaghetti diagram'). The definition of m^* in Equation 4.3 facilitates this effort: the traditional way to present a band structure is to show E as a function of wavenumber k , in which case energy bands that are shallow or 'flat' are considered 'heavy' (large m^*) while bands with a sharp dispersion are 'light' (small m^*).

The following sections discuss the transport of electrons in a solid. The equations commonly utilized to analyze transport data are solutions to the linearized Boltzmann transport equation treated within the relaxation time approximation. It is assumed that itinerant conduction (non-hopping) occurs within a parabolic band(s). In this model, all electrical transport properties depend on the carrier's electrochemical potential (ζ) and relaxation time (τ), and in some cases upon the carrier's effective mass (m^*). It is common to use the reduced energy $\epsilon = E/kT$ and the reduced electrochemical potential is $\eta = \zeta/kT$, where k is Boltzmann's constant.

The electrochemical potential is utilized to describe the carrier's free energy because electrons carry a charge. The electrochemical potential (ζ) is related to the chemical potential (ξ) by $\zeta = \xi - e\phi$, where ϕ is the electrostatic potential. In this thesis, the attempt is made to only use the phrase electrochemical potential, though chemical potential is generally taken to be equivalent because the electron cannot be separated from its charge (experimentally). The term Fermi energy (E_F , or $\epsilon_F = E_F/kT$) is taken as the 0 K limit of the

electrochemical potential, and represents the highest filled energy at 0 K. In the case of electrons, which are described by the Fermi distribution function $f = (1 + \text{Exp}[\epsilon - \eta])^{-1}$, the electrochemical potential is the energy at which $f = 0.5$ for non-zero T .

The Drude model for electrical conductivity (σ) is perhaps the simplest and yet most commonly utilized model for electrical conductivity. In this model, the electrical conductivity (σ) arises as a concentration n of charged species moves in the direction of the applied field ϵ with an average velocity v_d , which is known as the drift velocity. These particles (electrons) carry a charge of magnitude e and the resulting electrical flux J_e (charge per area per time) across a plane perpendicular to ϵ is

$$J_e = nev_d. \quad (4.4)$$

Ohm's law states that

$$J = \sigma\epsilon, \quad (4.5)$$

and, therefore, the electrical conductivity is

$$\sigma = \frac{nev_d}{\epsilon}. \quad (4.6)$$

Considering electrons in a classical manner, these charged particles accelerate in the field (with force = ϵe) based on their mass m . The acceleration (a) is assumed to occur for some average time τ at which point it is interrupted by an obstacle (a scattering center). The corresponding average drift velocity is then

$$v_d = \int_0^\tau a dt = \int_0^\tau \frac{\epsilon e}{m} dt = \frac{\epsilon e}{m} \tau. \quad (4.7)$$

Utilizing this expression, a more familiar expression is obtained:

$$\sigma = ne^2\tau/m. \quad (4.8)$$

Finally, it is common to define the carrier's drift mobility μ_d ,

$$\mu_d = \frac{e\tau}{m} = \frac{v_d}{\epsilon}. \quad (4.9)$$

The concentration of charge carriers n and the relaxation time τ that describes the movement of these carriers in an electric field is therefore of great concern to those studying electrical transport. Generally, as discussed below, the carrier density is taken to correspond to all carriers in the band of interest (conduction band, for instance). However, it is the charge carriers near the electrochemical potential ζ that contribute significantly to electrical transport. This point is exemplified by the presence of $\frac{\partial f}{\partial E}$ in the transport coefficients, which is nearly a delta function about ζ when $\zeta \gg kT$.

4.2.2 Relaxation Times and Carrier Scattering

The concept of a carrier relaxation time τ is frequently utilized to model electrical transport. A broad distribution of local electron relaxation times exists, and the macroscopically observed (average) τ is the result of thousands of microscopic interactions with defects, impurities, electrons, holes, and the crystalline lattice itself. Modeling τ can be quite difficult.

In general, τ is obtained from a reciprocal sum (Eqn. 4.10) over the relaxation times associated with the various scattering mechanisms:

$$\frac{1}{\tau} = \sum_{s=1}^s \frac{1}{\tau_s}. \quad (4.10)$$

The relaxation time τ associated with a particular scattering mechanism (s) is commonly described by a power law dependence on reduced carrier energy,

$$\tau_s = \tau_{0,s} \epsilon^{\lambda-1/2}, \quad (4.11)$$

where $\tau_{0,s}$ can be a function of material parameters and temperature[28, 119, 122]. A nice review of the pertinent relaxation times is found in Reference [119].

In a few circumstances, such as in the extremes of temperature, one scattering mechanism produces much shorter relaxation times than the other scattering mechanisms, and it is said that this scattering mechanism *limits* τ . In this case, the additional scattering mechanisms can be ignored (to first order). The most common scattering mechanisms are acoustic phonon scattering and ionized impurity scattering, which tend to limit τ in the high and low temperature regimes, respectively.

When acoustic phonon scattering limits τ , the deformation potential theory provides the description of τ shown in Equation 4.12 ($\lambda = 0$, $\tau_L \propto \epsilon^{-0.5}$), where the subscript L stands for lattice scattering. This theory accounts for the presence of lattice vibrations by subjecting electrons to an alternating potential (the deformation potential). Here, v_l is the longitudinal speed of sound and the deformation potential E_{def} quantifies the change in the electronic band energy as the crystal volume changes due to the presence of a phonon[119].

$$\tau_L = \frac{\pi \hbar^4 v_l^2 d}{\sqrt{2} E_{def}^2 (m^* kT)^{3/2} \epsilon^{1/2}} \quad (4.12)$$

Ionized impurities also disturb the potential associated with the ideal lattice, and electrons are scattered by the Coulombic field associated with the randomly distributed ionized impurity. The carrier relaxation time associated with ionized impurity scattering can be described by (essentially $\lambda = 2$)[122],

$$\tau_i = \frac{16\sqrt{2} m^* \pi \chi^2 (kT)^{3/2} \epsilon^{3/2}}{N_i Z^2 e^4 g}, \quad (4.13)$$

where χ is the permittivity, Z the effective charge, N_i is the concentration of the ionized impurity, and g is

Table 4.1. Summary of energy and effective mass dependence of the carrier relaxation time due to various scattering mechanisms for carriers in a parabolic band, which are described by $\tau = \tau_{0,s} \epsilon^{\lambda-1/2}$.

Scattering Type	λ	m^* Dependence of τ_0
Acoustic Phonon	0	$(m^*)^{-3/2}$
Ionized Impurities	2	$(m^*)^{1/2}$
Neutral Impurities	0.5	$(m^*)^2$
Point Defects	0	$(m^*)^{-3/2}$

given by

$$g = \ln(1 + b) - \frac{b}{1 + b} \quad (4.14)$$

with

$$b = \frac{8m^* \epsilon kT}{\hbar^2} \frac{\chi kT F[0.5, \eta]}{n e^2 F[-0.5, \eta]}, \quad (4.15)$$

and F_j is defined by Equation 4.20.

The scattering of electrons by point defects can also be significant, and may be especially important when modeling transport in vacancy rich compounds, such as $\text{La}_{3-x}\text{Te}_4$. The relaxation time associated with point defect scattering (τ_{PD}) is described by $\lambda = 0$ as in the case for acoustic phonon scattering,

$$\tau_{PD} = \frac{\pi \hbar^4}{2^{1/2} (m^*)^{3/2} V_0 N_d (\epsilon kT)^{1/2}} \quad (4.16)$$

Energy independent scattering ($\lambda = 0.5$) is often utilized in first principles transport calculations to facilitate the computationally expensive process. This may be similar to a balance of ionized impurity and acoustic phonon scattering, which would be quite common in intermediate temperature ranges. However, the relaxation time associated with scattering by neutral impurities (τ_{NI}) of concentration N_n is also modeled in this manner (Eqn. 4.17). This is usually unimportant in heavily doped semiconductors, because the high doping concentration causes impurities (dopants) to be ionized at even very low kT . Note that scattering by optical phonons below the Debye Temperature (Θ_D) is also modeled by EIS[119].

$$\tau_{NI} = \frac{(m^* e)^2}{20 \hbar^2 \chi N_n} \quad (4.17)$$

Given the importance of the energy dependence of τ when calculating the Seebeck coefficient, as discussed below, as well as the influence of the effective mass on electrical conductivity, a summary of the key scattering mechanisms is provided in Table 4.1.

4.2.3 Carrier Concentration and Hall Coefficient

The free carrier concentration n (density) is the most critical parameter available to an experimentalist when attempting to understand and optimize thermoelectric conversion efficiency. Experimentally, the Hall effect

is utilized to probe the carrier density; this measurement provides a very accurate estimation of the carrier density in a parabolic band. The Hall effect also provides information on which type of carrier dominates electrical transport: the Hall coefficient R_H is positive in a p -type material and negative in an n -type material.

The density of carriers contributed from one parabolic band is obtained by integrating over all occupied states in the band (assuming the minimum band energy is 0),

$$n = \int_0^{\infty} N(E)f(E)dE, \quad (4.18)$$

which, upon substitution for $N(E)$ and $f(E)$, becomes

$$n = 4\pi \left(\frac{2m^*kT}{h^2} \right)^{3/2} \int_0^{\infty} \frac{\epsilon^{1/2} d\epsilon}{1 + \text{Exp}[\epsilon - \eta]}, \quad (4.19)$$

where ϵ and η are the reduced carrier energy and reduced electrochemical potential, respectively. As discussed in Appendix H, it is convenient to define the Fermi integral of order j as

$$F_j(\eta) = \int_0^{\infty} f \epsilon^j d\epsilon = \int_0^{\infty} \frac{\epsilon^j d\epsilon}{1 + \text{Exp}[\epsilon - \eta]}, \quad (4.20)$$

and thus

$$n = 4\pi \left(\frac{2m^*kT}{h^2} \right)^{3/2} F_{1/2}(\eta). \quad (4.21)$$

Clearly, a theoretical calculation of n is not sufficient when examining experimental data. Rather, n must be measured experimentally. This is accomplished via the Hall effect, which relates the voltage response to an electric current in the direction perpendicular to an applied magnetic field[123].

From the BTE, the Hall coefficient is

$$R_H = \frac{3h^3}{8\pi e(2m^*kT)^{3/2}} \frac{\int_0^{\infty} \epsilon^{3/2} \tau^2 \frac{\partial f}{\partial \epsilon} d\epsilon}{\left(\int_0^{\infty} \epsilon^{3/2} \tau \frac{\partial f}{\partial \epsilon} d\epsilon \right)^2}. \quad (4.22)$$

By relating this to the theoretical carrier density, one obtains

$$R_H = \frac{r_H}{ne} = \frac{1}{n_H e}, \quad (4.23)$$

where the Hall carrier density n_H is defined. The dimensionless Hall factor r_H accounts for scattering effects that cause deviation between n and n_H . Through comparison with Equation 4.19, which represents the *chemical* or *true* carrier density, one finds that

$$r_H = \frac{3}{2} F_{1/2}(\eta) \frac{\int_0^{\infty} \epsilon^{3/2} \tau^2 \frac{\partial f}{\partial \epsilon} d\epsilon}{\left(\int_0^{\infty} \epsilon^{3/2} \tau \frac{\partial f}{\partial \epsilon} d\epsilon \right)^2}, \quad (4.24)$$

and

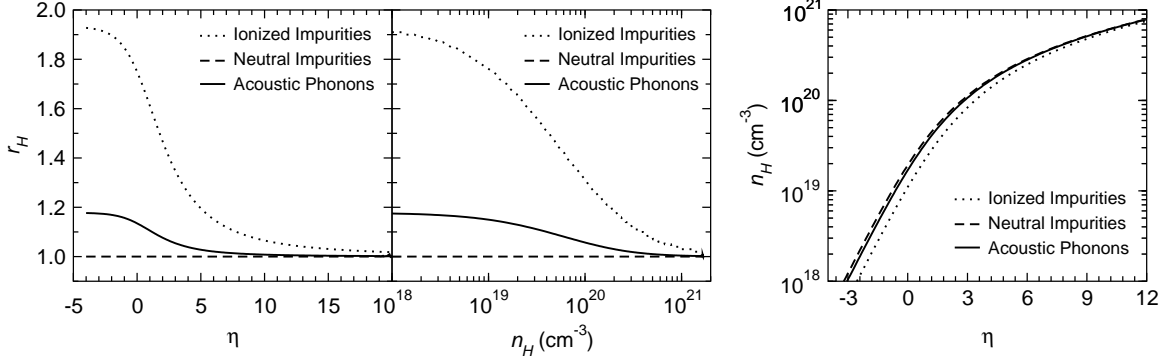


Figure 4.1. Hall factor ($r_H = n/n_H$) versus reduced electrochemical potential (left) and Hall carrier density (center). The right panel summarizes this behavior in the carrier concentration domain, where $n_H = n$ for energy independent scattering; $m^*/m_e = 1$ and 300 K have been assumed.

$$n_H = \frac{1}{R_H e} = \frac{n}{r_H} = 4\pi \left(\frac{2m^* kT}{h^2} \right)^{3/2} \frac{F_{1/2}(\eta)}{r_H}. \quad (4.25)$$

In many circumstances, the Hall factor is set to unity and n_H is treated as n . However, this is generally only valid when the electron gas is highly degenerate ($\eta \gg 0$), as shown in Figure 4.1. Indeed, for all scattering mechanisms, $r_H \rightarrow 1$ when η becomes large. In the limit of a nondegenerate electron gas, $r_H = 1.18$ when τ is limited by acoustic phonon scattering and $r_H = 1.93$ when τ is limited by ionized impurity scattering. In thermoelectric materials research, a factor ~ 2 difference between n and n_H is not that significant because the optimization of thermoelectrics generally involves examination of a very wide range of carrier densities (spanning at least an order of magnitude). However, proper modeling should account for this to avoid incorrect conclusions regarding the optimization of thermoelectric efficiency.

In general, the transport property data discussed in this text was taken at high-temperatures, where phonon scattering tends to dominate. This also means that high degeneracy is rarely obtained, and r_H and the full Fermi integrals should be utilized when modeling transport properties.

4.2.4 Electrical Conductivity and Mobility

The solution to the BTE gives the electrical conductivity of a single parabolic band as

$$\sigma = \frac{8\pi e^2 m^{1/2} (2kT)^{3/2}}{3h^3} \int_0^\infty \epsilon^{3/2} \tau \frac{\partial f}{\partial \epsilon} d\epsilon. \quad (4.26)$$

When multiple bands are present, or multiple species are conducting in parallel, the total conductivity is merely the sum of the individual conductivities.

By utilizing the Drude model (Eqns 4.6-4.9) and the equation for n , the drift mobility is obtained as

$$\mu_d = \frac{2e}{3m} \frac{\int_0^\infty \epsilon^{3/2} \tau \frac{\partial f}{\partial \epsilon} d\epsilon}{F_{1/2}(\eta)}. \quad (4.27)$$

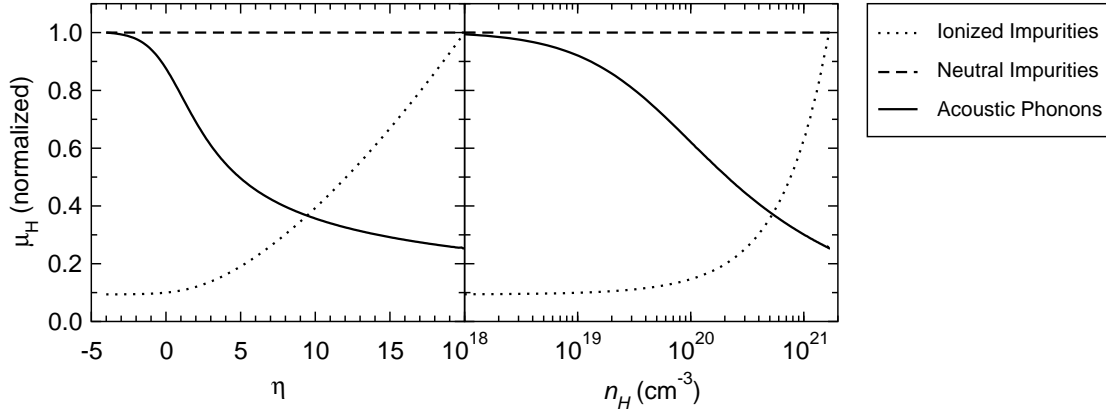


Figure 4.2. Normalized values of the Hall mobility versus reduced electrochemical potential (left) and Hall carrier density (right) (300 K, $m^*/m_e = 1$).

The Hall mobility is defined as

$$\mu_H = R_H \sigma = \frac{e \int_0^\infty \epsilon^{3/2} \tau^2 \frac{\partial f}{\partial \epsilon} d\epsilon}{m \int_0^\infty \epsilon^{3/2} \tau \frac{\partial f}{\partial \epsilon} d\epsilon}. \quad (4.28)$$

By comparing the Hall mobility to the drift mobility, it is observed that the two differ by the Hall factor r_H . As discussed above, the Hall factor is utilized to provide internal consistency when modeling transport and is necessary because the Hall coefficient is impacted by scattering events.

The energy dependence of the Hall mobility is shown in Figure 4.2, where the Hall carrier density is obtained using $m^*/m_e = 1$ and $T = 300$ K. This figure shows the drastically different behavior associated with the various scattering mechanisms. The mobility associated with ionized impurity scattering increases with increasing η (or increasing n_H) while that associated with acoustic phonon scattering decreases in this direction. This is because higher energy electrons have higher velocities and are thus less likely to be influenced by local disturbances caused by ionized impurities; this also explains the trend with increasing T shown in Eqn 4.13. The higher energy electrons are, however, scattered more strongly by acoustic phonons because a greater number of states are available for the electrons to be scattered into (number of states increase as $\epsilon^{1/2}$ and thus $1/\tau$ increases as $\epsilon^{1/2}$).

The energy dependence of τ influences the temperature-dependent μ because η is generally a function of T . The value of η tends to decrease with increasing T in thermoelectric materials because n is usually independent of T (extrinsic semiconductors, considering modest T). The mobility of highly degenerate electrons scattered by acoustic phonons decays as T^{-1} (classic metallic behavior at high T), whereas μ_H decays as $T^{-1.5}$ in a nondegenerate material (see Figure 1.4a in Section 1.4). Temperature-dependent material properties m^* , E_{def} , and v_l can modify the behavior of $\mu(T)$ dramatically.

4.2.5 Seebeck Coefficient

The Seebeck coefficient (α) is the most important thermoelectric transport property; its existence defines thermoelectricity. α determines how large of a voltage can be obtained from a temperature gradient ($V=\alpha\Delta T$), or vice versa. Clearly, large values of α are desired. Physically, the voltage produced is the difference in the electrochemical potential of the electrons (or holes) across the temperate gradient (at open circuit conditions).

For a parabolic band, the magnitude of α is a function of $\tau(\epsilon)$ and the electrochemical potential (the reduced potential η is typically utilized). Here, only the magnitude of α is considered, which is sometimes referred to as the *thermopower*. The appropriate sign is input when modeling transport data: electrons have negative α and holes have positive α (like the Hall coefficient). The Seebeck coefficient does not contain a dimension of time, and thus the magnitude of τ does not impact α . This is observed by the presence of τ in both numerator and denominator in the equation describing the Seebeck coefficient:

$$\alpha = \frac{k}{e} \left(\frac{\int_0^\infty \tau \epsilon^{3/2} (\epsilon - \eta) \frac{\partial f}{\partial \epsilon} d\epsilon}{\int_0^\infty \tau \epsilon^{3/2} \frac{\partial f}{\partial \epsilon} d\epsilon} \right). \quad (4.29)$$

Comparison of Equation 4.29 and the expression for σ (Eqn. 4.26) reveals the close relationship between α and σ . While not obvious at first, this expression essentially states that it is difficult to obtain large α and large σ simultaneously. Large α is only obtained when σ has a large energy dependence. In other words, large α is obtained when σ is highly asymmetric about the electrochemical potential (the weighting by $(\epsilon - \eta)$ in numerator). This tends to occur when the electrochemical potential is within the energy gap, and thus the conducting electrons are all located above η ; this explains the large α observed in insulators (also, see Figure 4.3a). Large σ , on the other hand, occurs when η is high in the band (a large carrier density).

The ‘‘Mott relation’’ (Eqn. 4.30) is often utilized to demonstrate the relationship between α and σ . Please see Appendix E for details of this expression.

$$\alpha = \frac{\pi^2}{3} k_b^2 T \left(\frac{\partial}{\partial E} \ln \sigma_E \right)_{E=\zeta}. \quad (4.30)$$

σ_E is the first order approximation of σ defined by

$$\sigma = \frac{e^2}{12\pi^3} \int dE \frac{\partial f}{\partial E} \int_{E=\zeta} \mathbf{v}_k \mathbf{v}_k \tau \frac{dS}{\nabla_k E} = \frac{e^2}{12\pi^3} \int dE \frac{\partial f}{\partial E} \sigma_E, \quad (4.31)$$

which becomes Equation 4.26 in the parabolic band approximation. Here, the fundamental (\mathbf{k} space) definition is utilized to reveal the generality of the Mott relation. The connection to τ is clear, and it is common to isolate the density of states $N(E)$,

$$N(E) = \frac{1}{4\pi^3} \int \frac{dS}{\nabla_k E}. \quad (4.32)$$

The Mott relation is valid for any dispersion relation (band structure) provided $\zeta \gg kT$ (degenerate

limit). For a detailed derivation and discussion of the Mott relation, please see Appendix E. It is common to assume that the velocities and relaxation times are only a function of energy in otherwise isotropic bands with the same energy minimum, in which case Equation 4.30 reduces to

$$\alpha = \frac{\pi^2 k_b^2 T m^*}{3eh^2} \left(\frac{d \ln N(E)}{dE} + \frac{d \ln v(E)^2}{dE} + \frac{d \ln \tau(E)}{dE} \right)_{E_F}. \quad (4.33)$$

The assumption required to generate this expression limits its applicability, but the direct inclusion of $N(E)$ is appealing. Thus, this expression reveals ways in which α can be enhanced beyond the traditional behavior observed when η is manipulated through n and T . For instance, the engineering of $N(E)$ for enhanced α has been demonstrated by doping PbTe with TI[30]. The energy dependence in τ is difficult to exploit at high T , where phonon scattering tends to dominate. One approach to exploit τ is to *filter* the low energy carriers by introducing energy barriers (insulating layers or particles) within a conductive matrix (this effectively turns τ into a step function in energy)[32–35].

The influence of electrochemical potential and carrier scattering is shown in Figure 4.3. In the left panel, α is plotted versus η for the three common energy dependences in τ , and the center panel shows the same data in the carrier density domain by using the free electron mass to convert between η and $n(300\text{ K})$. As expected (recall Table 4.1), ionized impurity scattering produces the largest Seebeck coefficient. Unfortunately, this scattering tends to reduce τ significantly and thus the corresponding electrical conductivity σ is generally low when τ_i limits τ . Also, ionized impurity scattering tends to dominate at low temperatures, where large α is difficult to obtain due to large η . The energy independent scattering mechanisms (EIS) also provide a larger Seebeck coefficient than does scattering by acoustic phonons. This is of particular interest because the first principles calculations typically utilize EIS and thus the predicted Seebeck coefficients are likely to be larger than observed at high-temperatures where acoustic scattering limits τ .

A large band mass is often said to be desirable because it produces a large carrier density n for a given value of η , thus allowing large electrical conductivity to be obtained for small η . This effect is shown in the right panel of Figure 4.3, where data for three different band masses are presented. The increase in m^* to m'^* moves the α curves to the right because $n' = n \times (m'^*/m^*)^{3/2}$ (for a given η, T). By inspection of the Equation 4.25, varying the temperature produces a similar effect as varying m^* . Viewed alternatively, these effects (higher m^* or T) produce larger α for a given carrier density because the corresponding value of η must be reduced to accommodate the larger m^* or T . The left panel in Figure 4.3 is valid for any T, m^* .

At first glance, it appears as though large m^* is desirable. However, large m^* actually results in lower σ (for acoustic phonon scattering) because of the relationship between mobility and effective mass, in particular due to the dependence on m^* located in τ [7]. Large effective mass does suppress the minority carrier contribution at a given n and lead to the optimization of zT at higher n (see Appendix A). Thus, it is difficult to state whether large or small m^* is preferred. Note that large *band degeneracy* (such as that found in silicon) is desirable because high band degeneracy means a large number of states contribute to conduction at a given

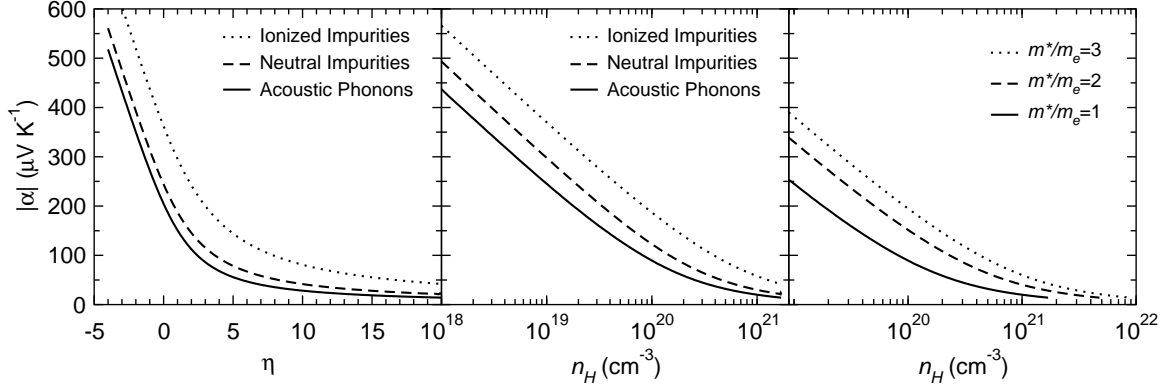


Figure 4.3. Seebeck coefficient as a function of chemical potential and scattering mechanism (left). The complementary dependence on the Hall carrier density is shown in the center panel, where $m^*/m_e = 1$ is utilized. The right panel reveals the influence of m^* , which causes the theoretical n_H curves to shift to higher values; this panel assumes acoustic scattering limits τ .

energy. Band degeneracy (an equivalence of energy states) is determined by crystallography and should not be confused with the degeneracy of an electron gas determined by η .

At high-temperatures, the scattering of electrons and/or holes is typically dominated by lattice vibrations (phonons), in which case Equation 4.12 applies ($\tau \propto \epsilon^{-1/2}$). This is equivalent to saying that the carrier's mean free path, l_σ , is energy independent because $l_\sigma = v \times \tau$, with velocity proportional to $E^{1/2}$. By inserting Equation 4.12 into Equation 4.29, the Seebeck coefficient for acoustic phonon limited τ is

$$\alpha = \frac{k}{e} \left(\frac{\int_0^\infty \epsilon^2 \frac{\partial f}{\partial \epsilon} d\epsilon}{\int_0^\infty \epsilon \frac{\partial f}{\partial \epsilon} d\epsilon} - \eta \right) = \frac{k}{e} \left(\frac{2 \int_0^\infty \epsilon f d\epsilon}{\int_0^\infty f d\epsilon} - \eta \right). \quad (4.34)$$

It is common to consider the limits of high and low degeneracy, as these provide insight into the behavior of the Seebeck coefficient. Strictly speaking, however, these limits are generally not valid when examining optimized thermoelectric materials, as they tend to produce the highest efficiency in the region of mild degeneracy ($-0.5 < \eta < 1$). However, these limits are useful when considering the general behavior of the thermoelectric phenomena.

In the limit of high degeneracy and acoustic scattering (see Appendix F for derivation), the Seebeck coefficient is

$$\alpha = \frac{\pi^2 k_b^2 T}{3e E_F} = \frac{\pi^2 k_b^2 T m^*}{3eh^2} \left(\frac{\pi}{3n} \right)^{2/3}. \quad (4.35)$$

This representation highlights the need for low chemical potential, or Fermi energy E_F , which is revealed in Figure 4.3. The connection to band mass and carrier concentration was easily drawn by substitution for the free electron E_F . A word of caution should be taken with this representation because the values of n and m^* are intimately linked via E_F . Also, this equation is only valid for large E_F and is clearly not valid for $\eta < 0$ (η within the energy gap), which is where the largest values of α are obtained (Figure 4.3). However, this

equation does provide insight into the behavior of the Seebeck coefficient, and can be utilized in simplified models to obtain a rough optimization of the thermoelectric power factor, particularly at low temperatures.

The Seebeck coefficient of a nondegenerate ($\eta \ll 0$) electron gas is

$$\alpha = \frac{k}{e}(2 + \lambda - \eta) = \frac{k}{e} \left(2 + \lambda + \ln \left[\frac{2 \left(\frac{2\pi m^* kT}{h^2} \right)^{3/2}}{n} \right] \right). \quad (4.36)$$

Thus, at low n , the Seebeck coefficient increases as $\ln[\frac{1}{n}]$ and $\ln[T]$. This ‘low density’ limit allows the relationship to entropy to be easily drawn. Consider an ideal gas, for which $pV = NkT$ and the internal energy $U = \frac{3}{2}NkT$; μ is the chemical potential. The entropy is given by

$$S = \frac{U}{T} + \frac{pV}{T} - \frac{\mu}{T} = \frac{3}{2}Nk + Nk - \frac{\mu}{T} = Nk \left(\frac{5}{2} - \frac{\mu}{kT} \right). \quad (4.37)$$

The nondegenerate electron gas is treated like an ideal gas, though the electrons carry a charge and thus their effective chemical potential includes a term associated with the electrostatic potential. Despite the inability to include a scattering related term, this simple method reveals that the Seebeck coefficient represents the electronic entropy per carrier $\alpha \approx \frac{S}{Ne}$. Of course, this is a transport property and thus the entropy of interest must be capable of flowing, hence the definition given in Section 1.2 that $\alpha = \frac{\text{entropy flux}}{\text{current density}} \Big|_{\Delta T=0}$. More detailed discussions of the relationship between α and entropy, including the necessary irreversible thermodynamics, are found in References [6, 120, 124].

4.2.6 Mixed Conduction

When both holes and electrons are present the analysis of transport data becomes significantly more complicated. In particular, the determination of the electrochemical potential is difficult, and requires knowledge of the band features of both holes and electrons, as well as the band gap E_g and the concentration of extrinsic dopants, not to mention the T dependence of band features. In an n -type semiconductor at high T , where the donor dopants are fully ionized, the charge neutrality equation states that the number of free electrons n is equal to the number of holes p plus the number of ionized donor dopants N_d [119]:

$$n = N_d + p, \quad (4.38)$$

or, upon substitution of the appropriate expressions for parabolic bands (single band degeneracy),

$$4\pi \left(\frac{2m_n^* kT}{h^2} \right)^{3/2} F_{\frac{1}{2}}(\eta) = N_d + 4\pi \left(\frac{2m_p^* kT}{h^2} \right)^{3/2} F_{\frac{1}{2}}(-\epsilon_g - \eta), \quad (4.39)$$

where $\epsilon_g = E_g/kT$ is the reduced energy gap. A similar expression can be developed when the dopant is an acceptor and the semiconductor is extrinsically doped p -type.

The solution of Equation 4.39 yields η , as well as the concentration of electrons and holes. Once η is

obtained, the transport properties of the individual species can be computed using the above expression and the realization that η be replaced by $-\epsilon_g - \eta$ in the expressions for the minority carrier. Care must be taken to utilize the appropriate sign in the expressions for the Hall and Seebeck coefficients, as electrons and holes contribute differently to these terms. The Hall and Seebeck coefficients are negative in the case of electron conduction, and positive for hole conduction.

The equations for multiband conduction are now provided. The summations are over all pertinent bands, and it is assumed that the Hall coefficients R_H and Seebeck coefficients α carrier the appropriate sign. These expressions are valid in the case of weak magnetic fields[123], the criterion for which is nearly always satisfied in thermoelectric research[119].

$$\sigma = \sum_i \sigma_i, \quad (4.40)$$

$$\alpha = \frac{\sum_i \alpha_i \sigma_i}{\sum_i \sigma_i}, \quad (4.41)$$

$$R_H = \frac{\sum_i R_{H,i} \sigma_i^2}{(\sum_i \sigma_i)^2}. \quad (4.42)$$

4.2.7 Estimation of the Band Gap

The fundamental characteristic of a semiconductor is the existence of an energy gap between the conduction and valence bands, the magnitude of which is known as the band gap E_g . Here, the conduction and valence bands are implicitly defined by their relation to an energy gap that is near the Fermi energy; core electrons do not lie in the valence band. The size of E_g determines a variety of properties, such as the number of carriers thermally activated in an ideal (valence balanced) crystal. As discussed above, a large E_g is necessary for large zT to be achieved, and the manipulation of E_g is common in thermoelectric materials research. E_g typically decreases as T increases and can be greatly affected by impurities.

A need to characterize E_g clearly exists and two methods to do so were employed in this work. The first technique involves measuring the electrical conductivity in an intrinsic sample, and the second utilizes the existence of a maximum in $|\alpha(T)|$.

In an intrinsic semiconductor, the charge neutrality expression requires $n = p$, with the exact location of η determined by T , E_g , and m_n^*/m_p^* . So long as E_g is reasonably large, the carriers are described by Boltzmann statistics, which allows η to be eliminated from Equation 4.39. Using the notation that $n = p = n_i$, this leads to

$$n_i = (np)^{0.5} = \sqrt{N_n N_p} \text{Exp} \left[\frac{-E_g}{2kT} \right], \quad (4.43)$$

where N_n and N_p are given by[121]

$$N_i = 2 \left(\frac{2\pi m_i^* kT}{h^2} \right)^{3/2}. \quad (4.44)$$

The temperature-dependence of the carrier mobility tends to cancel the factors $T^{3/2}$ in the expression for n_i , and thus the total electrical conductivity increases as

$$\sigma = \sigma_0 \text{Exp} \left[\frac{-E_g}{2kT} \right]. \quad (4.45)$$

E_g is therefore easily obtained from an Arrhenius plot of the conductivity ($\ln[\sigma]$ versus $1/T$). Obtaining a pure, intrinsic semiconductor is extremely difficult, and typically some extrinsic carrier concentration exists. However, at high T , the intrinsic carrier concentrations dominate and estimates for E_g can be obtained.

The magnitude of the Seebeck coefficient displays a maximum at high T because minority carriers reduce the thermal voltage. Sharp and Goldsmid have shown that the value of $|\alpha_{max}|$ is related to E_g via [125]

$$E_g = 2e|\alpha_{max}|T_{max}, \quad (4.46)$$

where T_{max} is the temperature at which $|\alpha_{max}|$ is observed. This is derived assuming Boltzmann statistics apply and that $m_n^*/m_p^*=1$ and $\mu_n/\mu_p=1$; the data in Appendix A confirm this expression. Significant variations can be observed when these ratios change. For instance, when the mobility of the minority carrier is ten times the mobility of the major carrier, E_g is underestimated by $\sim 35\%$ (for a particular set of properties; see Appendix A for the consideration of minority carrier effects). Similarly, if the minority carrier mobility is much less than the majority carrier mobility (or $m_{maj}^*/m_{min}^* \gg 1$), a large overestimation of E_g occurs. Thus, the characterization of E_g via $E_g = 2e|\alpha_{max}|T_{max}$ is actually very powerful because it produces an *effective band gap* that reflects the influence of the minority carrier on thermoelectric transport. The elementary charge is included to convert between Volts and Joules, and is eliminated in the conversion to electronvolts.

4.2.8 Electronic Contribution to the Thermal Conductivity

The electronic contribution to the thermal conductivity κ_e is also an electrical transport property. To state it in complete form the definition of a generic transport integral provided in Appendix E is utilized.

$$\kappa_e = \frac{1}{T} \left(K_2 - \frac{K_1^2}{K_0} \right) \quad (4.47)$$

The Wiedemann-Franz relationship is generally utilized to estimate κ_e via

$$\kappa_e = L\sigma T, \quad (4.48)$$

where L is known as the Lorenz number. In the limit of a single, parabolic band with $\tau \propto \epsilon^{\lambda-1/2}$ the Lorenz number is found to be

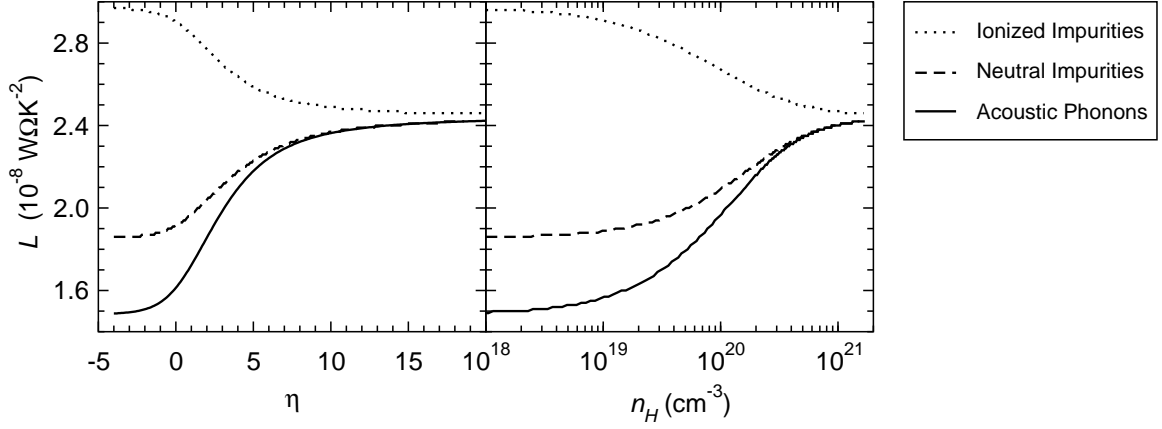


Figure 4.4. Lorenz number as a function of electrochemical potential and scattering mechanism (left). The complementary dependence on the Hall carrier density is shown in the panel on the right, where $m^*/m_e = 1$ and $T = 300$ K are utilized. The metallic limit is $2.45 \times 10^{-8} \text{ W}\Omega\text{K}^{-2}$, which is often employed at high T where it is likely to result in an underestimation of κ_L .

$$L = \frac{k^2}{e^2} \frac{(1 + \lambda)(3 + \lambda)F_\lambda(\eta)F_{\lambda+2}(\eta) - (2 + \lambda)^2 F_{\lambda+1}(\eta)^2}{(1 + \lambda)^2 F_\lambda(\eta)^2}. \quad (4.49)$$

The Lorenz number depends on η and the energy dependence of τ , which is similar to the behavior of α . The energy dependence of L is shown in Figure 4.4. The metallic limit of the Lorenz number is given by $L = \pi^2 k^2 / 3 / e^2 = 2.45 \times 10^{-8} \text{ W}\Omega\text{K}^{-2}$, and is valid at high degeneracy regardless of the carrier scattering mechanism. This limit is often utilized in transport analysis. At high-temperatures, the use of this value typically results in an overestimation of L (κ_e) and thus an underestimation of κ_L . In such cases, attention is often drawn to the “low” value of κ_L and incorrect conclusions can be drawn regarding the physics governing thermoelectric efficiency and the best methods for increasing efficiency.

When a sample has both holes and electrons contributing significantly to σ , an increase in κ_e beyond the individual electron ($\kappa_{e,n}$) and hole ($\kappa_{e,p}$) contributions is possible. This is termed the bipolar thermal conductivity, κ_b , which accounts for the transportation of the thermal energy associated with the creation/annihilation of electron-holes pairs[4].

$$\kappa_b = \frac{k^2 T}{e} \frac{\sigma_p \sigma_n}{\sigma^2} (\alpha_p - \alpha_n)^2 T \quad (4.50)$$

From this expression, it is clear that κ_b is largest when the conductivity from electrons σ_n and holes σ_p are equal. In this case, the nondegenerate equations are typically valid (provided the band gap is relatively large so that $\eta \ll 0$ can be achieved) and κ_b becomes

$$\kappa_b = \frac{k^2 T}{4e} (4 + \lambda_n + \lambda_p + \epsilon_g). \quad (4.51)$$

4.3 $\text{La}_{3-x}\text{Te}_4$

This section is an adapted reproduction, with permission, from *Phys. Rev. B*, **78** 125205 (2008) and *Phys. Rev. B*, **79**, 153101 (2009). Copyright 2008 and 2009, American Physical Society.

4.3.1 Heavily Doped $\text{La}_{3-x}\text{Te}_4$

The thermoelectric properties of interest all depend on temperature T and carrier concentration n , and thus n must be characterized as quantitatively as possible. This is accomplished via the room temperature Hall effect, which yields a Hall carrier concentration $n_H = 1/R_H e$ where R_H is the Hall coefficient and e the charge of an electron. The characterization at room temperature is generally sufficient because the free carriers are not thermally induced, though the high-temperature Hall effect is desirable for understanding the carrier mobility.

The room temperature Hall carrier concentration is shown in Figure 4.5a as a function of nominal composition, which is characterized by the carrier density ($n_{nominal}$) obtained via charge counting for $\text{La}_{3-x}\text{Te}_4$. The agreement between n_H and $n_{nominal}$ is better than that between the WDS concentration and nominal, and this demonstrates the need for a transport-based characterization of sample composition. Here, the WDS data is transformed from atomic percent into a vacancy count x_{WDS} by assuming full Te occupancy, which is then utilized to calculate a carrier density as $n_{WDS} = n_{max}(1 - 3x_{WDS})$. The scatter associated with the Hall data can be observed in Figure 4.5b, where the carrier concentration of the most resistive sample is found to be constant up to approximately 750 K, above which the data is too scattered to analyze. For large n (low resistivity), the carrier concentration is expected to be constant for all temperatures explored, as larger n is equivalent to a higher Fermi energy which effectively increases the band gap.

The room temperature Hall carrier concentration and temperature-dependent electrical conductivity (Fig. 4.8a) are utilized to estimate the temperature-dependent Hall mobility μ_H (Figure 4.6a). The μ_H values are similar to those previously reported for lanthanum telluride[40], and are slightly larger than the values reported cerium sulfide, $\text{Ce}_{3-x}\text{S}_4$ [49]. The mobility decreases with increasing temperature, which suggests phonon scattering limits μ_H .

In Figure 4.6b, the decay of μ_H (raw experimental data) for nominal $\text{La}_{2.72}\text{Te}_4$ is fit to the theory of acoustic phonon scattering using Equations 4.12 and 4.28 with $\eta(T)$ obtained from the experimental Seebeck coefficient data via Equation 4.34. An effective mass of $2.8 m_e$ was employed (based on Seebeck coefficient analysis), along with a longitudinal sound velocity of 3580 m/s (measured)[38], which produced a deformation potential of 6.1 eV. The deformation potential is generally expected to be on the order of an electronvolt[28], and is thus acceptable. The agreement between theory and experiment is good, suggesting acoustic phonon scattering does indeed limit the carrier mobility. While this is not unusual for the temperatures probed, it is somewhat surprising that the curve in Figure 4.6b was able to describe the data so well given the large number of lanthanum vacancies and complex electronic structure (see below).

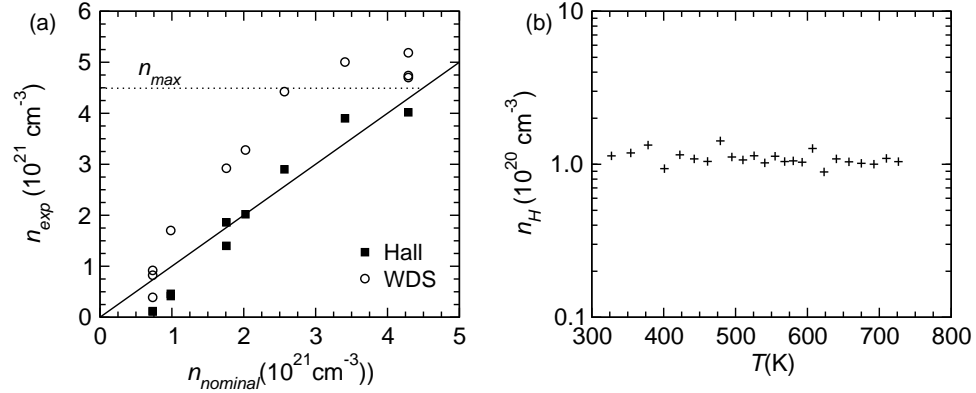


Figure 4.5. (a) Experimental carrier density as obtained from Hall effect data and compositional analysis (WDS) are plotted versus the carrier density calculated via nominal composition in $\text{La}_{3-x}\text{Te}_4$. The Hall carrier density is found to agree well with the nominal one, and is shown to be relatively independent of temperature in panel (b). The WDS data yields n values greater than the maximum allowed by crystallography and valence counting, which is likely an indication of instrumental error. Reprinted (adapted) with permission from *Phys. Rev. B*, **78** 125205 (2008). Copyright 2008, American Physical Society.

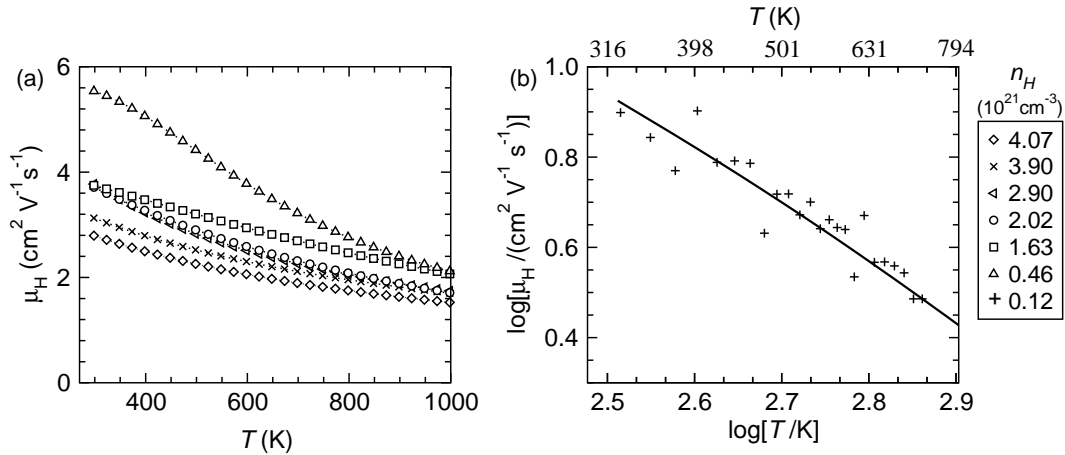


Figure 4.6. (a) The Hall mobility calculated assuming the room temperature n_H value is independent of temperature. (b) The dependence of the experimental Hall mobility is well described by the theory of acoustic phonon scattering, even in the sample with the highest vacancy concentration (nominal $\text{La}_{2.72}\text{Te}_4$). The solid line can be approximated by a simple decay of $T^{-1.28}$, representing a change from roughly $T^{-1.15}$ to $T^{-1.40}$ behavior as the temperature range of interest increases.

To further examine the effect of scattering mechanisms on the carrier mobility, we consider the carrier concentration dependence of the mobility in Figure 4.7. The room temperature Hall mobility is found to increase with decreasing n , with $\mu_H = 8.4 \text{ cm}^2/\text{V/s}$ obtained at the lowest n_H . The dependence of μ_H on n_H is consistent with the theory of acoustic phonon scattering, which is shown as the solid curve in Figure 4.7. The convergence of μ at high T is also consistent with this theory, as μ is independent of n in the non-degenerate limit (a loss of degeneracy is strongly promoted by the high T). Some deviations exist between theory and experiment, which may be caused by the electronic band structure or the presence of vacancies, both of which complicate the analysis of transport in $\text{La}_{3-x}\text{Te}_4$.

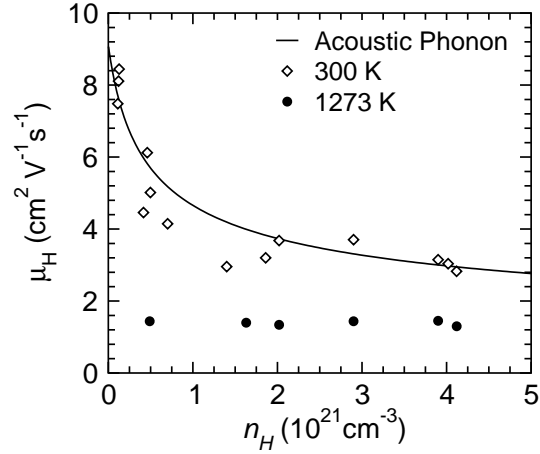


Figure 4.7. The room temperature Hall mobility is fit to a model for acoustic phonon scattering. At high temperature (1273 K), the estimated values of μ_H converge to roughly $1.5 \text{ cm}^2/\text{V}\cdot\text{s}$ due to the loss of degeneracy. Reprinted (adapted) with permission from *Phys. Rev. B*, **78** 125205 (2008). Copyright 2008, American Physical Society.

The theoretical curve in Figure 4.7 was obtained using an effective mass of $3.0 m_e$, a longitudinal sound velocity of 3580 m/s, and a deformation potential of 6.6 eV was obtained from the fit. Note, however, that smaller values of the E_{def} would be obtained if the residual resistances were accounted for. That is, if the residual resistances that reduce the mobility (independent of T) were accounted for, then a larger *thermal* mobility would be obtained which would result in a smaller E_{def} from the fit. A simplified estimate suggests E_{def} would be reduced by about 70%, and that the expected dependence on n_H is still observed (for the most part, extrapolations are difficult to make at low n). Interestingly, this trend in the thermal mobility was not observed by Cutler, who reported that the thermal mobility (unexpectedly) increased with increasing n in $\text{Ce}_{3-x}\text{S}_4$ [49].

The transport properties of $\text{La}_{3-x}\text{Te}_4$ samples display the trends typical of a heavily doped semiconductor, which is expected because the samples inherently possess $n > 10^{20} \text{ cm}^{-3}$. Recall Section 1.4 for a summary of this ‘expected’ behavior. Specifically, the electrical conductivity decreases with increasing temperature and the magnitude of the Seebeck coefficient increases with increasing temperature, as shown in Figure 4.8. The electrical conductivity decreases with increasing T due to the decrease in the mobility, which was shown in Figure 4.6. This is the classic behavior of heavily doped materials, where the carrier density is independent of T , and is often referred to as *metallic* behavior. Similarly, the Seebeck coefficient behaves as expected (Fig. 4.8b): The Seebeck coefficient of a metal should increase linearly with T , as shown in Equation 4.35 (Section 4.2 and Appendix F). For large n , the Seebeck coefficient is linear with T for all T examined, confirming the metallic behavior in the samples with largest n . As n decreases, the increase in $|\alpha|$ with T slows at high T (approaching $\log[T]$), and for the samples with lowest n the detrimental effect of minority carrier activation is observed at high T . That is, as electron-hole pairs are thermally activated, the holes produce a positive Seebeck coefficient which decreases the net voltage. In this sense, the n and T dependence of the Seebeck

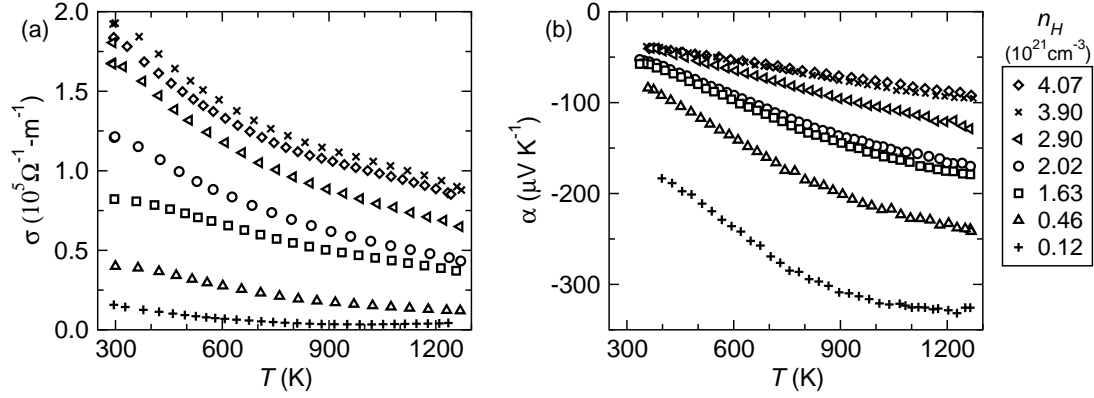


Figure 4.8. Temperature dependence of (a) electrical conductivity and (b) Seebeck coefficient in $\text{La}_{3-x}\text{Te}_4$ reveals the behavior expected for an extrinsically doped semiconductor with large n . At high T and low n_H , the effects of minority carriers are observed via the decrease in $|\alpha|$ and the increase in σ . Reprinted (adapted) with permission from *Phys. Rev. B*, **78** 125205 (2008). Copyright 2008, American Physical Society.

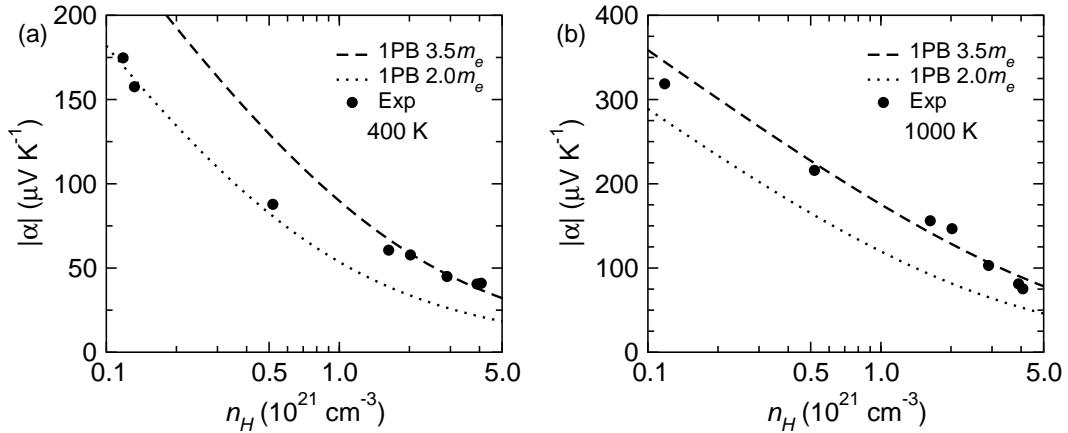


Figure 4.9. The dependence of $|\alpha|$ on n_H is found to be complex in $\text{La}_{3-x}\text{Te}_4$. Two different parabolic band masses are required to describe the data, with a light band required at low carrier density. Reprinted (adapted) with permission from *Chem. Mater.* **22**, 624 (2010). Copyright 2010 American Chemical Society.

coefficient reveals a transition from highly degenerate to non-degenerate electron gas.

The $n_H = 4.07 \times 10^{21} \text{ cm}^{-3}$ sample is expected to have a larger conductivity than the $n_H = 3.90 \times 10^{21} \text{ cm}^{-3}$ sample, and this inconsistency may be the result of many factors, including experimental error and sample inhomogeneity. For the most resistive sample, the increase in σ above $\sim 1000 \text{ K}$ indicates the activation of minority carriers. The electrical conductivity for this $n_H \sim 1.2 \times 10^{20} \text{ cm}^{-3}$ sample was difficult to verify, most likely due to the increased sensitivity to oxidation at low carrier concentration and/or the poor density ($\sim 85\%$ theoretical).

The plot of Seebeck coefficient versus carrier density, sometimes referred to as the Pisarenko Plot, is extremely valuable in the analysis of thermoelectric transport because it allows information about the band structure to be obtained. In this simplest case, the validity of the parabolic band assumption is examined. If the data lie significantly far from the parabolic band model (at a given n), then the conduction process

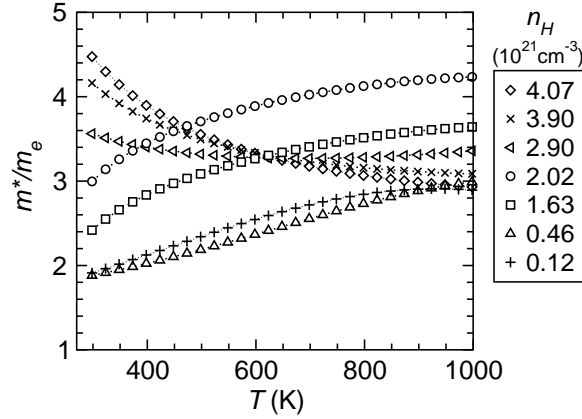


Figure 4.10. The calculated single-band effective masses in $\text{La}_{3-x}\text{Te}_4$ are found to be highly temperature-dependent. This suggests, in a manner similar to Figure 4.9, that conduction either occurs in multiple bands or in a non-parabolic band. The strong temperature dependence also suggests the band curvature(s) may be temperature-dependent, which is consistent with the behavior in Figure 4.9.

may be occurring in a non-parabolic band or multiple bands. However, a change in the dominant scattering mechanism can also lead to unexpected trends in this plot. Thus, crystallographic features and the thermal energy scale should be considered when performing such an analysis.

The Seebeck coefficient α is plotted versus the Hall carrier density n_H in Figure 4.9a,b at 400 and 1000 K, respectively. Shown along with the experimental data are two theoretical curves that assume acoustic scattering limits μ . These parabolic band (PB) models possess different effective mass m^* to describe the high and low n behavior; a reduced m^* is necessary to describe the low n data. The x-axis is plotted in log format to highlight the deviations between these two models. This analysis reveals that a single effective mass is not adequate in describing the dependence of α on n for all n . A similar deviation from simple, parabolic band conduction is observed in the temperature-dependent effective mass values shown in Figure 4.10. These values were obtained by assuming the room temperature n_H was independent of T , and $\eta(T)$ was obtained from the temperature-dependent α data.

The analysis of α data shown in Figures 4.9 and 4.10 suggests that electronic conduction occurs in either a non-parabolic band or in multiple bands. To draw such a conclusion, the influence of vacancy scattering was also considered and it appears that vacancy scattering is an unlikely source for the significant difference in m^* values required to describe all $\alpha(n)$. For starters, acoustic phonon scattering appears to limit μ , even at large vacancy concentrations (see Figure 4.6). Furthermore, if vacancy scattering were treated as ionized impurity scattering (vacancies possess an effective charge), the result would be an apparent increase in α (or m^*) at low n (large x), and not a suppressed α as observed in Figure 4.9. This is because ionized impurity scattering promotes large α through a large energy dependence of τ (see Table 4.1 and Section 4.2). Finally, vacancies might also be treated as neutral impurities, the scattering by which is modeled by the same energy dependence (n dependence) as acoustic phonon scattering and thus no change in $\alpha(n)$ would be expected in this scenario.

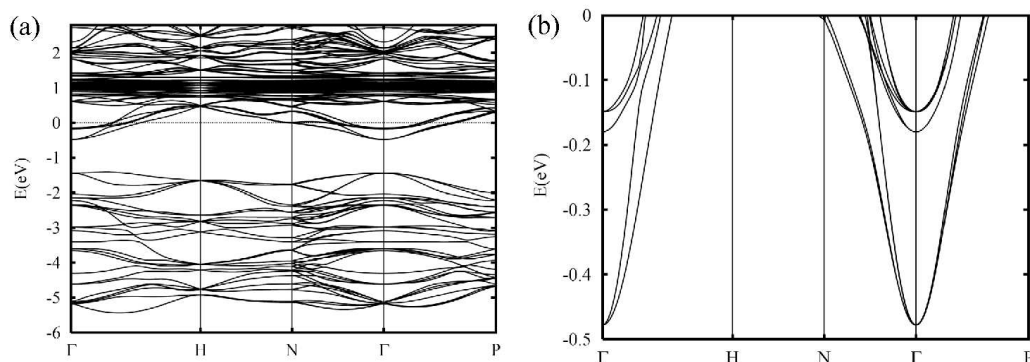


Figure 4.11. The calculated band structure in La_3Te_4 reveals a direct gap conductor with a Fermi energy well within the conduction band. (b) An examination of the pertinent bands reveals two/three bands dictate electronic transport in $\text{La}_{3-x}\text{Te}_4$. The higher energy bands possess a larger band mass, which is consistent with the analysis presented in Figure 4.9. Reprinted (adapted) with permission from *Phys. Rev. B*, **79**, 153101 (2009). Copyright 2009, American Physical Society.

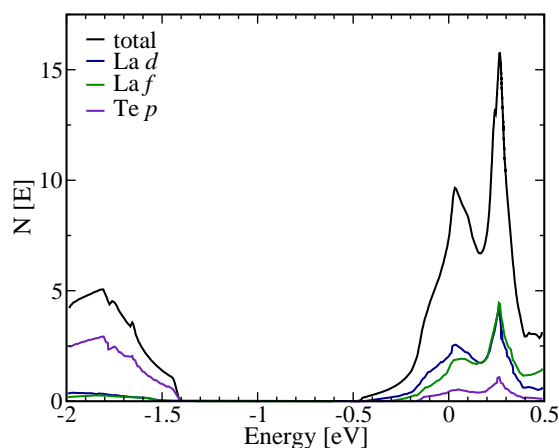


Figure 4.12. The projected density of states in La_3Te_4 reveals the conduction and valence bands are composed primarily of La and Te states, respectively. The sharp rise in $N(E)$ observed near -0.2 eV is associated with the heavy bands observed at that energy in Figure 4.11. Reprinted (adapted) with permission from *Phys. Rev. B*, **79**, 153101 (2009). Copyright 2009, American Physical Society.

To elucidate the influence of the electronic band structure on electrical transport in $\text{La}_{3-x}\text{Te}_4$, collaboration with David Singh of Oak Ridge National Laboratory was developed. David Singh performed density functional theory calculations (DFT) to obtain an electronic structure for La_3Te_4 [51]. While these calculations utilized the ideal, defect-free stoichiometry, they provide an adequate approximation to obtain invaluable information regarding the electronic structure in this system.

First principles calculations support the hypothesis that multiple bands influence electrical transport in $\text{La}_{3-x}\text{Te}_4$. The electronic band structure of La_3Te_4 is shown in Figure 4.11, where panel (b) highlights the region of interest to n -type conduction and it is revealed that the conduction band is composed of three pertinent bands. The lower energy band, corresponding to transport at low values of n , is found to have a lighter band mass (steeper curvature) than the higher energy bands.

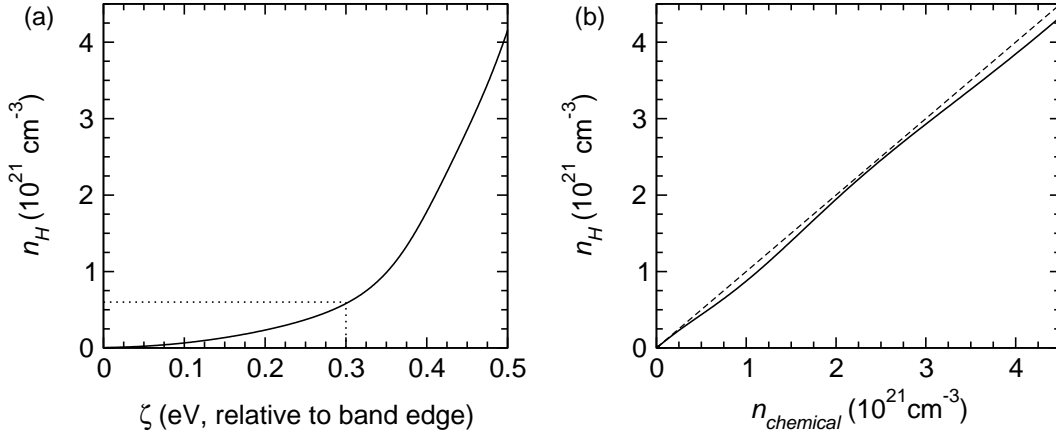


Figure 4.13. The Hall carrier density as a function of (a) Fermi energy and (b) chemical carrier density at 300 K. The Hall carrier density is always slightly less than the true carrier density due to non-parabolicity; scattering effects are not considered here and may contribute to further deviation. Reprinted (adapted) with permission from *Phys. Rev. B* **79**, 153101 (2009). Copyright 2009, American Physical Society.

The calculated band structure for La_3Te_4 has a direct gap at Γ of 0.95 eV. There is one free electron per formula unit in La_3Te_4 , and the corresponding Fermi energy E_F is 0.48 eV above the minimum conduction band edge. This position is taken as the origin in Figures 4.11a,b. The semiconducting composition corresponds to one-ninth of lanthanum atoms being vacant ($\text{La}_{2.666}\text{Te}_4$), and electrons fill conduction states as La vacancies are filled. To simulate a change in the carrier concentration, the position of the Fermi energy (and corresponding electrochemical potential as T changes) is shifted within the calculated band structure (a *rigid-band* calculation). Therefore, these calculations allow an examination of the n dependence of α in vacancy-free $\text{La}_{3-x}\text{Te}_4$, which is impossible to do experimentally.

The pertinent conduction bands are fairly parabolic in nature. The energy minima of these bands are $E_{min,1} = -0.48$ eV, $E_{min,2} = -0.18$ eV, and $E_{min,3} = -0.15$ eV (relative to E_F). The two higher energy bands would be degenerate at Γ in the absence of spin orbit coupling. These bands can be described by parabolic band effective masses of $m_1^*/m_e = 0.39$, $m_2^*/m_e = 1.05$, and $m_3^*/m_e = 1.56$. The corresponding degeneracy for each band is $g_1 = 2$, $g_2 = 1$, and $g_3 = 2$ (excluding spin degeneracy). The splitting between the heavy bands is small, and thus the system can be modeled fairly well with two bands, as suggested in Figure 4.9.

Figure 4.12 shows the total electronic density of states and projections from constituent orbitals. The conduction bands are primarily composed of La states while the valence bands are Te derived. This is expected, as the compound is primarily ionic at heart, with the empty cation states forming the conduction band and the valence band edge being composed of filled anion states. These findings are also consistent with previous calculations on La_3S_4 [126]. The coupling of n and x (vacancy concentration) thus complicates both experimental and theoretical studies of electron transport within this class of materials.

The heavy bands lead to an increase in the energy dependence of the density of states, $N(E)$, which can be observed in Figure 4.12 at approximately -0.16 eV. A similar increase in the corresponding carrier

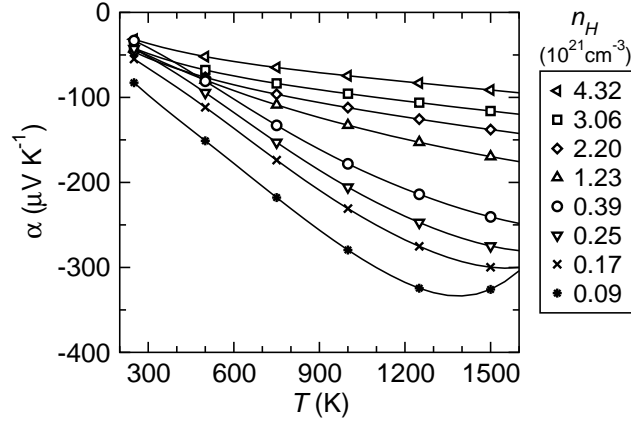


Figure 4.14. Theoretical Seebeck coefficients calculated from the first principles band structure by assuming rigid bands and a shift in the electrochemical potential as determined by the carrier concentration (legend) and the Fermi distribution function. The dependence on n_H and T is similar to that observed experimentally. The crossing of curves at low T is a clear demonstration of the multiband effects. Reprinted (adapted) with permission from *Phys. Rev. B*, **79**, 153101 (2009). Copyright 2009, American Physical Society.

density is also observed, as shown in Figure 4.13a for the theoretical n_H versus electrochemical potential ζ at 300 K. The approximate location of the heavy bands is indicated by the dashed line in Figure 4.13a. The first principles n_H values are slightly lower than the corresponding values of the chemical n due to the non-parabolic nature of the bands. The deviation is largest at high energy (high n), where a maximum difference of 4% is observed at 300 K; a larger deviation occurs at higher T . Also, the first principles calculation of n_H assumes energy independent scattering which leads to a Hall factor of unity; an inherent variation between n and n_H of up to 17% is associated with the $\tau(E)$ for acoustic phonon scattering.

The impact of band structure on α is now examined in the context of experimental results. Behavior typical of a heavily doped semiconductor is observed in both the experimental (Fig. 4.8b) and theoretical results (Figure 4.14). The theoretical results suggest the crossing of Seebeck coefficient curves at low T , which is consistent with an extrapolation of the experimental data. This is not possible within the single parabolic band framework, and such a feature is an indication of strongly energy-dependent transport. The crossing of these curves is best viewed in the Pisarenko plot. This plot of α versus n_H is shown again for clarity (Figure 4.15), as several curves have been added. For consistency with the DFT based results, the parabolic band models in Figure 4.15 have utilized an energy independent relaxation time and thus the m^* reported differs from Figure 4.9.

The theoretical n dependence of α makes sense in light of the fundamental form of the Seebeck coefficient, which suggests that the heavy, degenerate bands increase $|\alpha|$ by increasing the energy dependence of σ_E . This effect is most pronounced at lower T , but is present to some extent for all T examined. The agreement between experimental data and the *ab initio* results (labeled as DFT) is best at high T , as highlighted by Figure 4.15b, which shows data for 1000 K. This suggests that either the band masses or the assumption of energy independent scattering are more applicable at high T .

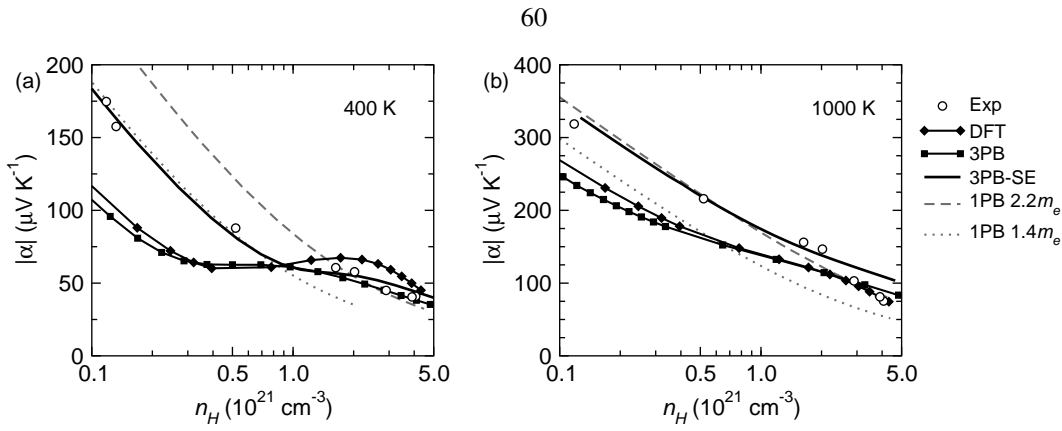


Figure 4.15. The theoretical dependence of Seebeck coefficient on Hall carrier density is compared to experimental data. First principles calculations suggest a dramatic decrease in $|\alpha|$ at low n_H . This behavior is well reproduced using a three parabolic band (3PB) model, and is improved upon when the effective mass of the light band is adjusted to match the data (3PB-SE). All theoretical curves assume an energy independent relaxation time. Reprinted (adapted) with permission from *Phys. Rev. B*, **79**, 153101 (2009). Copyright 2009, American Physical Society.

Figure 4.15 also shows multiparabolic band approximations of the first principles results (labeled as 3PB). These curves were generated using the band parameters (m_i^* , g_i) from the first principles calculations as input. The multiparabolic band approximation of $|\alpha|$ agrees very well with the full calculation, indicating minor asymmetries and band splitting do not have significant impact on α while multiband effects have dramatic impact on α .

The final curve shown in Figure 4.15 is a semi-empirical, multiparabolic band model (labeled as 3PB-SE). The semi-empirical models allow the value of m_1^* to be adjusted for a better description of the low n_H data; all other band parameters remained as calculated by first principles. The agreement between the semi-empirical model and the experimental data is quantitative at low T . However, a larger m_1^* is required to describe the low n data at 1000 K. It is difficult to know if this is a real feature of the material or if it simply represents a failure of the model, but it is consistent with the increasing m^* for low n shown in Figure 4.10.

If vacancies scatter electrons like ionized impurities, then the energy dependence of τ would vary with T and one would expect energy independent scattering to be more accurate at high T (where phonon scattering dominates). While this is consistent with the results presented here, the electrical resistivity seems to suggest μ_H is dominated by phonon scattering at all T examined, and the general trend in $\alpha(n_H)$ also suggests impurity scattering is not present, though it could be hidden by band features (a very light band with ionized impurity scattering). At this level of analysis, it is most appropriate to say that either the density functional band masses or the scattering assumption are not valid for all n and T examined.

4.3.2 Near-Insulating $\text{La}_{3-x}\text{Te}_4$

The production of insulating $\text{La}_{3-x}\text{Te}_4$ is complicated by the La-Te phase diagram, as well as the high vapor pressure associated with Te. The use of mechanical alloying allowed for the production of such samples near

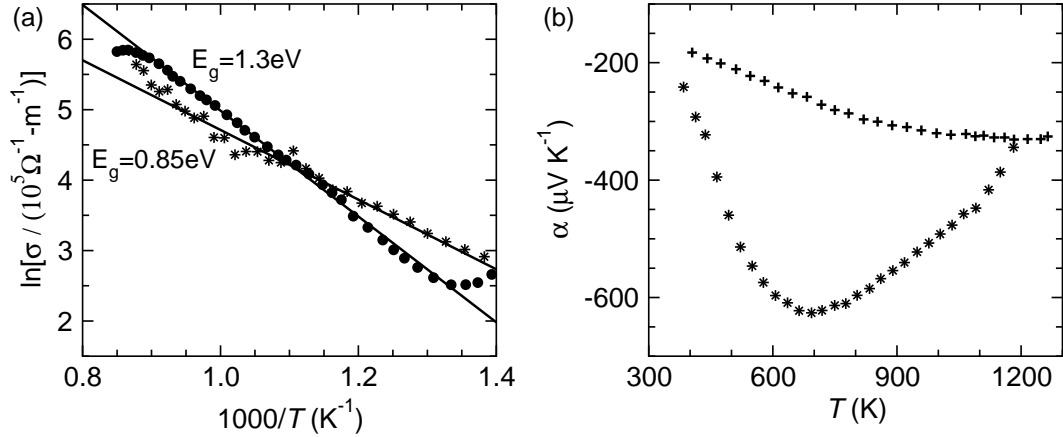


Figure 4.16. (a) Electrical conductivity of near insulating lanthanum telluride samples in an Arrhenius plot. Data for two samples are fit to obtain the thermal band gap (see Eqn. 4.45). (b) The Seebeck coefficient of the near insulating sample ‘*’ is much larger than that for the sample with $n_H \sim 1.2 \times 10^{20} \text{ cm}^{-3}$ ‘+’. The clear peak in the Seebeck coefficient for ‘*’ suggests a thermal band gap of 0.84 eV, consistent with the corresponding electrical conductivity data. Reprinted (adapted) with permission from *Phys. Rev. B*, **78** 125205 (2008). Copyright 2008, American Physical Society.

room temperature. An exact characterization of the electrical properties of these samples is also difficult, in particular due the extreme sensitivity to oxidation.

The electrical conductivity for the near insulating samples is plotted in Arrhenius format in Figure 4.16a. The data shown correspond to 800 K to 1100 K, and the band gaps of 0.85 eV and 1.3 eV are obtained from the linear fits. At room temperature, the sample with data indicated by ‘*’ possessed a Hall carrier density near $5 \times 10^{16} \text{ cm}^{-3}$; this value is meaningless in a truly intrinsic sample but some extrinsic carriers are inferred from the Seebeck coefficient data. The existence of some vacancies is expected, thus the presence of some free carriers is not surprising. At high T , however, the intrinsic carrier concentration likely dominates and leads to the traditional activated T dependence observed for σ in semiconductors. Two different data sets are shown: the ‘*’ data were collected using the Van der Pauw technique while the filled symbols were obtained via a four-point bar method (JPL System 2). This latter method uses a 1 cm tall sample, as opposed to a disk. The linear behavior observed at high T is lost at low T , presumably due to the presence of some extrinsic carriers, though hopping conduction may be present at these low n values[52].

The Seebeck coefficient for the near insulating sample (‘*’) is compared to that of the sample with $n_H \sim 1.2 \times 10^{20} \text{ cm}^{-3}$ (‘+’) in Figure 4.16b. The Seebeck coefficient in this near insulating sample is much larger than that of the high n_H sample; note that this ‘high’ n_H sample has the lowest n_H of the previously-discussed, heavily doped samples.

The band gap estimated via $E_g = 2e\alpha_{max}T_{max}$ is approximately 0.84 eV. This value is in agreement with that obtained from the fitting of electrical conductivity data at high T . Also, while the Seebeck coefficient of the $n_H \sim 1.2 \times 10^{20} \text{ cm}^{-3}$ sample does not demonstrate a clear maximum, one is essentially implied at the highest temperature, from which a similar value is obtained. These values are also consistent with the

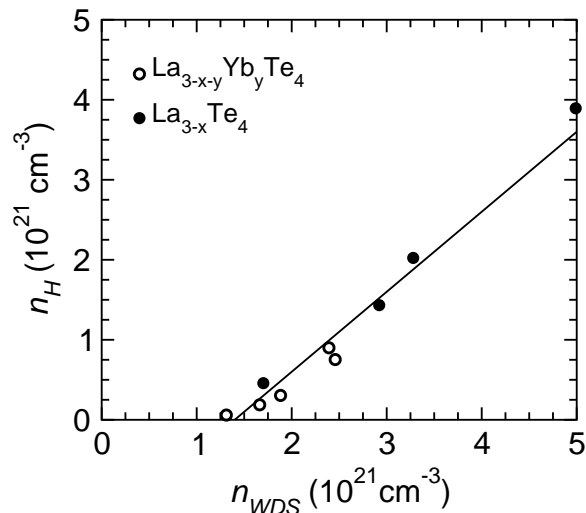


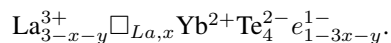
Figure 4.17. Wavelength dispersive spectroscopy (WDS) data are presented along with the room temperature Hall concentration n_H . The expected correlation between n_H and WDS compositions is qualitatively demonstrated by using valence counting to obtain a carrier density n_{WDS} . The solid curve represents this simple theory but is shifted in n to match the data; it is the consistent slope that provides strong evidence that simple valence counting applies. Reprinted with permission from *Chem. Mater* **22**, 2995 (2010). Copyright 2010 American Chemical Society.

density functional calculations on La_3Te_4 , which revealed $E_g \sim 0.95 \text{ eV}$; the theoretical band gap would likely decrease if the high defect concentration at $\text{La}_{2.667}\text{Te}_4$ were taken into account.

4.3.3 $\text{La}_{3-x-y}\text{Yb}_y\text{Te}_4$

This Section is reprinted with permission from *Chem. Mater* **22**, 2995 (2010). Copyright 2010 American Chemical Society.

It is believed that primarily Yb^{2+} exists in the lanthanum telluride matrix, and the following environment is expected:



The variation of rare earth content results in the desired control over carrier density, which is assessed via the Hall carrier density n_H , as observed in Figure 4.17. The values of n_{WDS} were obtained from the experimental atomic compositions using the outlined valence counting ($n \propto (1 - 3x - y)$). As with the pure $\text{La}_{3-x}\text{Te}_4$ samples[38], WDS overestimates the rare earth content and quantitative agreement between n_H and n_{WDS} is not obtained. The expected trends are observed, however, and the samples with and without Yb fall on the same line indicating the desired chemical behavior has been achieved. The observation of larger than expected rare earth content is believed to be an instrumental error associated with the use of oxide standards for La and Yb, though minor oxidation may be present at grain boundaries (not observed experimentally).

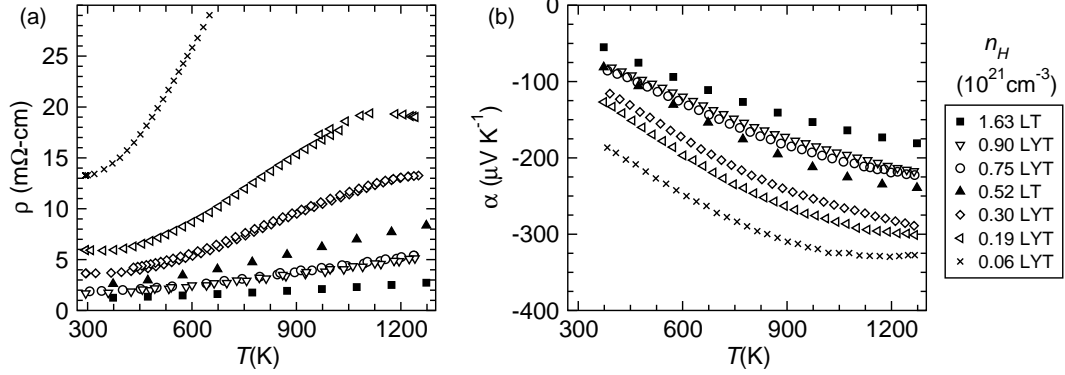


Figure 4.18. The temperature dependence of the (a) electrical resistivity and (b) Seebeck coefficient in $\text{La}_{3-x-y}\text{Yb}_y\text{Te}_4$ is found to be similar to that in $\text{La}_{3-x}\text{Te}_4$. Reprinted with permission from *Chem. Mater* **22**, 2995 (2010). Copyright 2010 American Chemical Society.

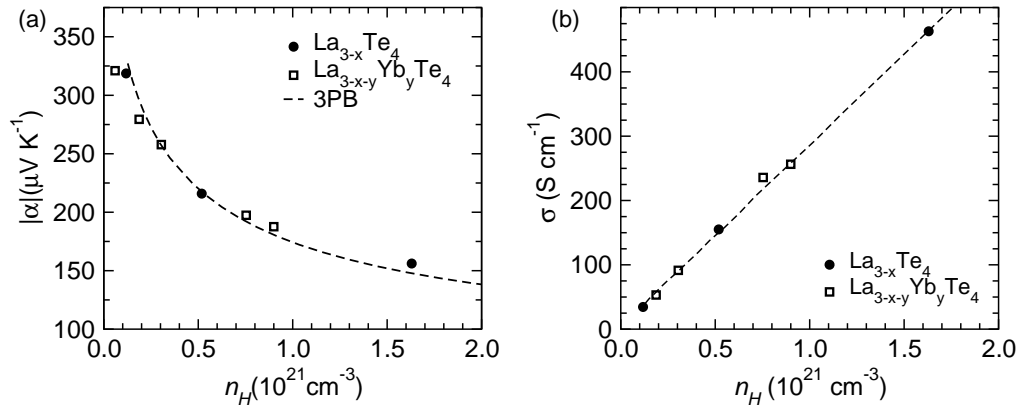


Figure 4.19. The electrical transport properties at 1000 K in $\text{La}_{3-x-y}\text{Yb}_y\text{Te}_4$ and $\text{La}_{3-x}\text{Te}_4$ are well described by simple models. The fit to α is a three parabolic band model (3PB-SE) taken from Figure 4.15 and σ is described by a linear fit. Reprinted with permission from *Chem. Mater* **22**, 2995 (2010). Copyright 2010 American Chemical Society.

The temperature dependence of the electrical resistivity and Seebeck coefficient is shown in Figure 4.18. As with $\text{La}_{3-x}\text{Te}_4$ samples, an increase in the magnitudes of α and ρ is observed with increasing T and decreasing n_H (increasing Yb content). For samples with the largest n_H , $|\alpha|$ increases linearly with increasing T , while those with low n_H manifest the detrimental effects of minority carrier activation at high T . Similar behavior is observed in the electrical resistivity, where the more heavily doped samples behave more like metals (linear increase with T) and those with lower doping act more like heavily doped semiconductors (ρ increases as $\sim T^{1.5}$ until minority carrier activation is observed). Note the data for ρ of the most resistive sample was very difficult to obtain due to rapid oxidation and poor quality contacts at this carrier concentration; efforts to obtain the high-temperature ρ data were abandoned upon realization that this sample has a non-optimal carrier density.

To examine the influence of Yb on thermoelectric performance other than by changing n_H , the n_H dependence of α and the electrical conductivity ($\sigma = 1/\rho$) is examined in Figure 4.19, which shows data at

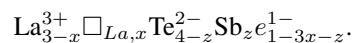
1000 K. The dependence of α and σ on n_H is found to be similar in samples with and without Yb. Also, the thermal band gap, estimated from the maximum in the Seebeck coefficient $E_g \sim 2e\alpha_{max}T_{max}$, is found to be ~ 0.8 eV in both types of samples[38]. These results suggest that the addition of Yb changes the transport properties through a modification of the carrier density alone, and not through a change in the electronic structure. As discussed in Section 4.3, a single band model fails to capture the full n dependence of α in $\text{La}_{3-x}\text{Te}_4$ and thus the solid curve in Figure 4.19a is a three parabolic band (3PB) model taken from Section 4.3 (or Reference [51]), where it is termed the semiempirical multiparabolic band model (3PB-SE).

Previous work on $\text{La}_{3-x}\text{S}_4$ revealed an increase in the thermoelectric power factor ($\alpha^2\sigma$) with substitutions of the form $\text{La}_{3-y}\text{RE}_y\text{S}_4$, where $\text{RE} = \text{Sm}, \text{Eu}, \text{and Yb}$ [44]. This observed improvement was attributed primarily to enhancements in the Seebeck coefficient, which can be understood as changes in the effective mass. This is physically plausible, as the conduction band is dominated by lanthanum states[51, 126] and thus a substitution for lanthanum may change the conduction band curvature (mass). If a similar change were to occur in the tellurium based system, $\text{La}_{3-x-y}\text{Yb}_y\text{Te}_4$, a deviation from the 3PB model in Fig. 4.19a would have been observed. The absence of any obvious change to band structure indicates the Yb f-states reside below the valence band edge in lanthanum telluride. This generalization is consistent with the Yb-Te phase diagram, where only YbTe is observed, whereas the Yb-S phase diagram is complex and contains phases with Yb^{3+} (one unfilled f-state). Thus, the improvement in electrical properties of $\text{La}_{3-y}\text{Yb}_y\text{S}_4$ may be related to a valence fluctuation that places f-states near the conduction band edge and promotes a larger effective mass. This may be viewed as similar to Tl doping in PbTe, which promotes an enhanced hole effective mass through resonant states near the valence band edge[30].

4.3.4 $\text{La}_{3-x}\text{Te}_{4-z}\text{Sb}_z$ and $\text{La}_{3-x}\text{Te}_{4-z}\text{Bi}_z$

This section is an adapted reproduction, with permission, *Phys. Rev. B* **81**, 125205 (2010). Copyright 2010, American Physical Society.

The (ideal) non-isoelectronic anionic substitution of Sb (or Bi) for Te produces a chemical environment that can be described by



As shown in Table 4.2, the magnitudes of the Seebeck coefficients and electrical resistivity increase with increasing Sb or Bi content, and the Hall carrier density $n_H = 1/R_H e$ decreases with increasing Sb content. This is expected for the substitution of 3^- anion (Sb, Bi) for a 2^- anion (Te) in an n -type semiconductor.

As shown in Figure 4.20, the experimental values of n_H are consistently lower than expected from valence counting assuming nominal composition, and the deviation is greatest at large Sb (Bi) content. The primary source for reduced n_H is likely to be the presence of lanthanum vacancies, which remove electrons from the system and thus reduce n_H . Vacancy formation may be promoted by the presence of Sb or Bi in the crystal. However, simple valence counting would suggest that the sample with the most Sb is not the

Table 4.2. Nominal composition and sample label for nominal $\text{La}_3\text{Te}_{4-z}\text{Sb}_z$ and $\text{La}_3\text{Te}_{4-z}\text{Bi}_z$ are provided along with Hall carrier density and electrical resistivity at 300 K, and Seebeck coefficient at 400 K; a few $\text{La}_{3-x}\text{Te}_4$ samples are also given labels for convenience. Reprinted with permission from *Phys. Rev. B* **81**, 125205 (2010). Copyright 2010, American Physical Society.

Sample ID	Nominal Composition	n_H (10^{21}cm^{-3})	ρ ($\text{m}\Omega\text{-cm}$)	α ($\mu\text{V/K}$)
<i>Sb1</i>	$\text{La}_3\text{Te}_{3.80}\text{Sb}_{0.20}$	2.9	0.53	-45
<i>Sb2</i>	$\text{La}_3\text{Te}_{3.65}\text{Sb}_{0.35}$	1.3	1.1	-53
<i>Sb3</i>	$\text{La}_3\text{Te}_{3.40}\text{Sb}_{0.60}$	0.54	9.0	-74
<i>Sb4</i>	$\text{La}_3\text{Te}_{3.35}\text{Sb}_{0.65}$	0.35	18	-91
<i>Sb5</i>	$\text{La}_3\text{Te}_{3.20}\text{Sb}_{0.80}$	0.08	43	-148
<i>Bi1</i>	$\text{La}_3\text{Te}_{3.35}\text{Bi}_{0.65}$	0.39	7.1	-71
<i>Bi2</i>	$\text{La}_3\text{Te}_{3.20}\text{Bi}_{0.80}$	0.39	10	-76
<i>LT1</i>	$\text{La}_{2.99}\text{Te}_4$	4.1	0.61	-41
<i>LT2</i>	$\text{La}_{2.74}\text{Te}_4$	0.52	2.7	-88
<i>LT3</i>	$\text{La}_{2.72}\text{Te}_4$	0.12	8.8	-175

sample with the largest vacancy concentration, and thus the driving force for vacancy formation does not seem to be proportional to Sb or Bi content. It is possible that the presence of Sb or Bi modifies the mechanical alloying synthesis and promotes the loss of one species (or some binary compound) over another. In general, the mechanical alloying synthesis may have a systematic loss of one species over another due to differences in brittleness or ductility (elements may preferentially stick to vial) or reactivity. The vacancy count in $\text{La}_{3-x}\text{Te}_4$ can reach $x = \frac{1}{3}$, and $x \sim 0.12$ is the maximum x required to satisfy the electron count in the Sb or Bi systems (found in *Sb2*); the x values needed to explain these trends are quite reasonable. Note that cationic Sb substitution for La does not provide an explanation for the observed trend in carrier concentration. Vacancy formation may be promoted by the formation of La_4Sb_3 (anti- Th_3P_4 structure type), though identifying this phase is extremely difficult due to the similar lattice parameters and atomic masses. One interesting possibility is anionic (acceptor) Sb sitting on a La site in $\text{La}_{3-x}\text{Te}_4$, which would reduce the carrier concentration and could certainly manipulate electronic transport. Note that anionic Sb does exist in the thermoelectric material Sb_2Te_3 .

Scattering mechanisms can also produce a variation between n_H and the chemical n , which is the n associated with charge counting. The influence of scattering effects are manifested in the Hall factor, $r_H = n/n_H$, which is discussed in Section 4.2. As will be shown below, large Sb (Bi) addition modifies electron conduction, and thus likely leads to a change in r_H relative to the pure $\text{La}_{3-x}\text{Te}_4$ samples (or samples with low Sb content). The influence of r_H is relatively small compared to stoichiometry, as $r_H=1.93$ and 1.18 are the upper limits of r_H when the carrier mobility is limited by ionized impurity scattering and acoustic phonon scattering, respectively[119].

The temperature dependence of the Seebeck coefficients is shown in Figure 4.21. The magnitude and temperature dependence of α in the Sb containing (filled circles, panel (a)) and Bi containing samples (open triangles, panel (b)) are similar to that of pure $\text{La}_{3-x}\text{Te}_4$ samples (gray curves). However, at high temperatures a suppression of the magnitude of α is observed in the Bi containing samples and those with high Sb

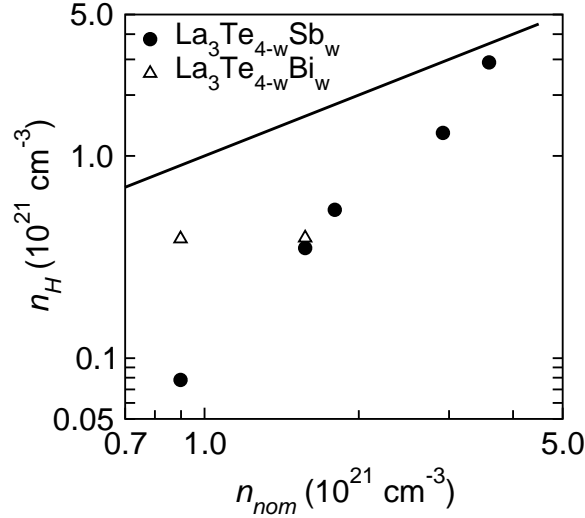


Figure 4.20. The experimental Hall carrier density $n_H = 1/R_H e$ at room temperature is plotted versus the theoretical carrier density obtained from charge counting for nominal $\text{La}_3\text{Te}_{4-z}\text{Sb}_z$ and $\text{La}_3\text{Te}_{4-z}\text{Bi}_z$. The experimental carrier density is always less than the expected value (solid line) and the discrepancy is likely due to the presence of La vacancies. Reprinted with permission from *Phys. Rev. B* **81**, 125205 (2010). Copyright 2010, American Physical Society.

content due to the thermal activation of minority carriers.

At moderately high temperatures, where acoustic phonon scattering should limit the carrier relaxation time regardless of sample composition, the dependence of the Seebeck coefficient on carrier density is found to be similar for all samples. This is shown in Figure 4.22a, where the magnitude of α at 1000 K is plotted versus the room temperature n_H . The minor changes in α imply that the conduction band does not change significantly upon Sb or Bi substitution for Te, which is consistent with the DFT results presented below. However, it is possible the effective mass is lower in the Sb or Bi substituted compounds, as suggested by the slight suppression of the Seebeck coefficient at low n_H . The single parabolic band model shown in Figure 4.22a (solid curve) is generated utilizing an effective mass of $m^* = 2.8m_e$ and the assumption that acoustic phonon scattering limits μ [119].

Less variation in the electronic properties of these samples is observed when $|\alpha|$ is plotted as a function of $\ln(\sigma)$ at 1000 K, see Figure 4.22b. This implies any reduction in $|\alpha|$ (for a given n) associated with band mass is compensated for by an increase in μ . Such a trend is consistent with the relationship between mobility and effective mass, $\mu \propto 1/m^*$; scattering effects can cause an even stronger variation in μ as m^* changes (see Eqn. 4.12). The apparent increase in $|\alpha|$ for pure $\text{La}_{3-x}\text{Te}_4$ samples near $2 \times 10^{21} \text{ cm}^{-3}$ is likely related to the electronic structure (heavy bands are found at $\sim 0.3 \text{ eV}$ above the low-mass, minimum energy bands)[51], although experimental error must also be acknowledged.

The primary effect of Sb or Bi substitution on α is a compensation of α at high T and large z , which is caused by the thermal excitation of minority carriers. This is evidence for a reduced band gap in samples with high Sb or Bi content, as $\text{La}_{3-x}\text{Te}_4$ samples showed this feature at lower n and higher T . The thermal gap can

be estimated by the maximum in $|\alpha|$ versus T , $E_g = 2e\alpha_{max}T_{max}$ [125], which yields $E_g \sim 0.46$ eV for the two Bi containing samples, $E_g \sim 0.63$ eV for sample *Sb5*, and $E_g \sim 0.84$ eV was obtained for $\text{La}_{3-x}\text{Te}_4$ [38]. A reduced energy gap is also inferred, in a similar manner, from the ρ and κ data.

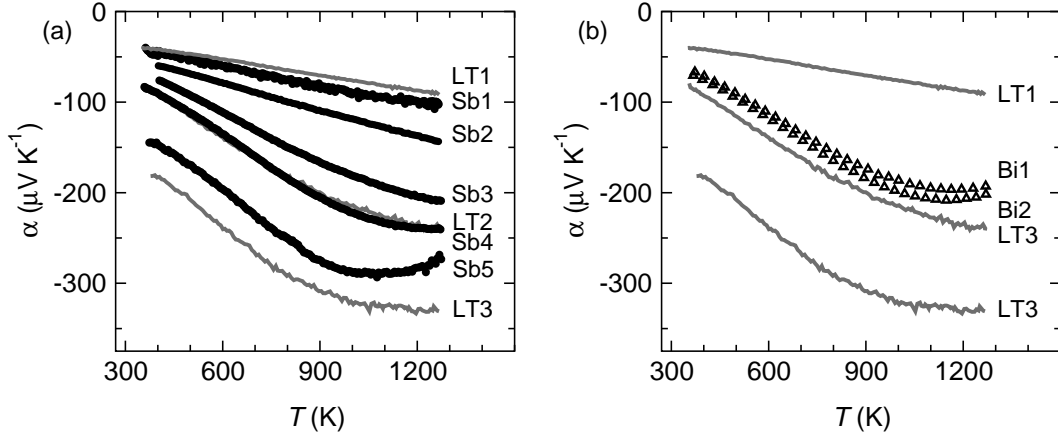


Figure 4.21. Temperature dependence of Seebeck coefficients for nominal (a) $\text{La}_3\text{Te}_{4-z}\text{Sb}_z$ (closed circles) and (b) $\text{La}_3\text{Te}_{4-z}\text{Bi}_z$ (open triangles) are similar to those of the pure $\text{La}_{3-x}\text{Te}_4$ samples[38] (solid gray curves). The maximum value of $|\alpha|$ and the corresponding temperature suggest that the band gap is reduced by Sb addition, and is further reduced with Bi addition. Reprinted (adapted) with permission from *Phys. Rev. B*, **81**, 125205 (2010). Copyright 2010, American Physical Society.

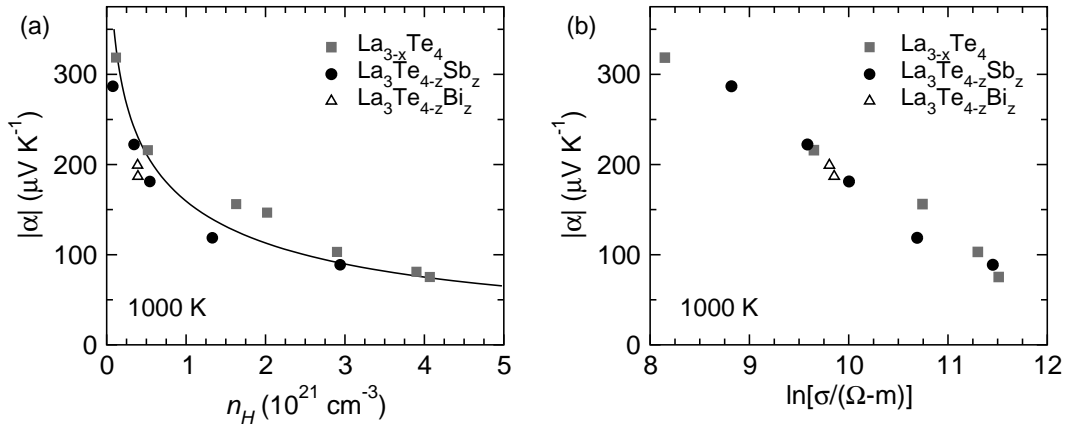


Figure 4.22. (a) The dependence of Seebeck coefficient at 1000 K on the room temperature Hall carrier concentration is similar for $\text{La}_3\text{Te}_{4-z}\text{Sb}_z$, $\text{La}_3\text{Te}_{4-z}\text{Bi}_z$, and pure $\text{La}_{3-x}\text{Te}_4$ samples[38], implying little change to the conduction band occurs upon substitution. Also shown is a single parabolic band model (solid curve). (b) Seebeck coefficient as a function of the natural logarithm of the electrical conductivity (at 1000 K) demonstrates similarity of electrical transport in all samples at high T , where it is assumed acoustic phonon scattering limits the carrier mobility in all samples. Reprinted with permission from *Phys. Rev. B*, **81**, 125205 (2010). Copyright 2010, American Physical Society.

The experimental observation of reduced energy gap upon Sb or Bi substitution is consistent with the density functional theory (DFT) calculations. The DFT calculations on the idealized La_3Te_4 , $\text{La}_3\text{Te}_3\text{Sb}$, and $\text{La}_3\text{Te}_3\text{Bi}$ compounds suggest the primary effect of Sb or Bi substitution is to raise the energy of the valence

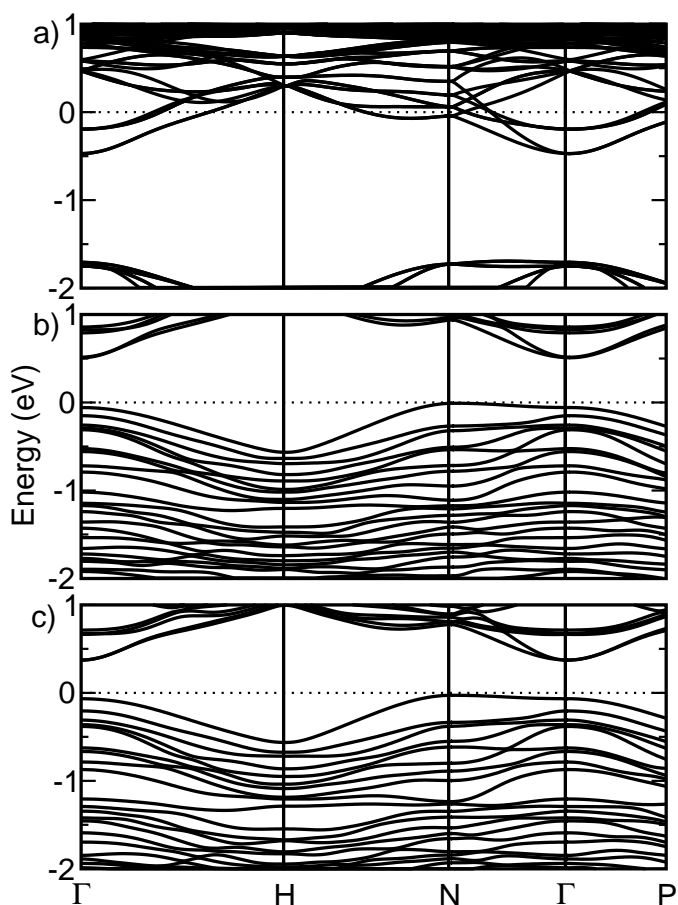


Figure 4.23. The calculated electronic structures of (a) La_3Te_4 , (b) $\text{La}_3\text{Te}_3\text{Sb}$ and (c) $\text{La}_3\text{Te}_3\text{Bi}$ shown for the relevant energy range. Reprinted with permission from *Phys. Rev. B* **81**, 125205 (2010). Copyright 2010, American Physical Society.

band, where the majority of Te, Sb, and Bi states are located, and thus the substitutions result in a reduction of the energy gap (see Figure 4.23). The most noticeable change to the conduction band with Sb (Bi) substitution is the splitting of heavy, degenerate bands at the Γ point near 0.3 eV above the minimum conduction energy. The substitutions also flatten these bands somewhat, and thus an increased band mass may be expected at high doping levels. However, these changes in electronic structure are predicted for high Sb or Bi concentration, and it is thus not surprising that the samples with low Sb content and high n_H do not show an increased band mass. Therefore, a dramatic change in the Seebeck coefficient (n -type) is not expected with these anionic substitutions (at moderate T), which is in agreement with the experimental data. These results imply cation substitutions are required to significantly modify the conduction bands in $\text{La}_{3-x}\text{Te}_4$ (primarily composed of La states) and provide large changes in the Seebeck coefficient.

The DFT energy gaps are most easily observed in the density of states (Figure 4.24), where E_g of 1.22, 0.51, and 0.38 eV are calculated for La_3Te_4 , $\text{La}_3\text{Te}_3\text{Sb}$, and $\text{La}_3\text{Te}_3\text{Bi}$, respectively. To further validate these trends, the band structure of isostructural La_3S_4 was calculated and an energy gap of 2.07 eV was observed;

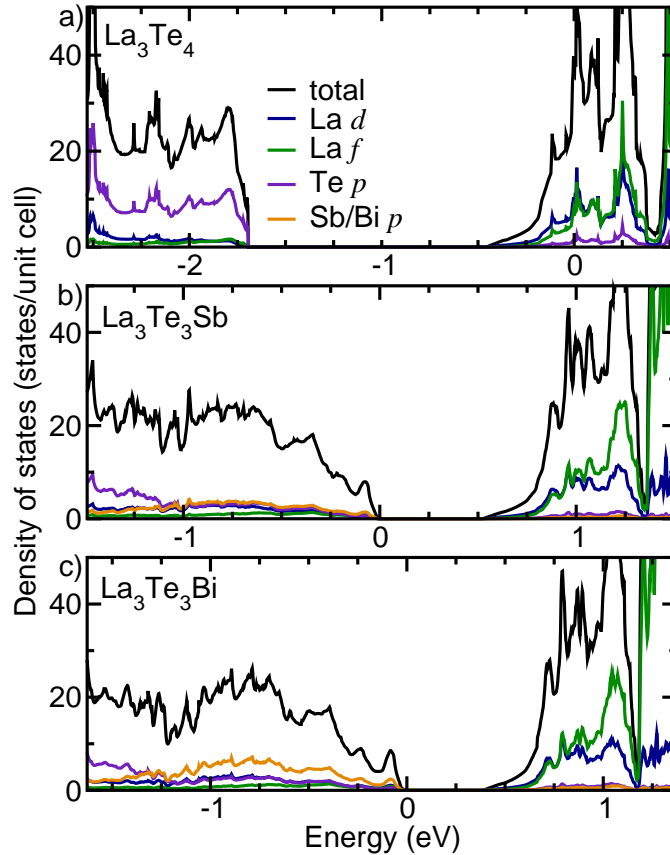


Figure 4.24. The projected density of states (DOS) reveals a decreasing energy gap in the compounds (a) La_3Te_4 , (b) $\text{La}_3\text{Te}_3\text{Sb}$ and (c) $\text{La}_3\text{Te}_3\text{Bi}$. A total of 3 eV is shown for all panels. Reprinted with permission from *Phys. Rev. B*, **81**, 125205 (2010). Copyright 2010, American Physical Society.

the larger gap of La_3S_4 is consistent with prior calculations[126] and the increasing electronegativity as one moves from Te to S. Note the Fermi level (0 eV) is placed within the conduction band for La_3Te_4 because it has one free electron per formula unit, and the Fermi level for $\text{La}_3\text{Te}_3\text{Sb}$ and $\text{La}_3\text{Te}_3\text{Bi}$ is at the top of the valence band because these are valence balanced compositions.

In Figure 4.25a, the electrical resistivity of Sb containing compounds (filled circles) are compared to that of sample *LT3* (gray curve), which has the highest resistivity of the heavily doped $\text{La}_{3-x}\text{Te}_4$ samples. In Figure 4.25b, the less resistive samples are examined in further detail, along with samples containing Bi (open triangles) and the two less resistive $\text{La}_{3-x}\text{Te}_4$ samples (gray curves). At low Sb content (and low Bi content, not shown), electrical conduction is very similar to that in $\text{La}_{3-x}\text{Te}_4$, which makes physical sense because these samples have high carrier concentrations and similar composition. The linear increase in ρ with increasing T implies acoustic phonon scattering limits the carrier mobility, which is consistent with the data for $\text{La}_{3-x}\text{Te}_4$ (even for large x).

In Figure 4.25a, the electrical resistivity of Sb containing compounds (filled circles) are compared to that of sample *LT3* (gray curve), which has the highest resistivity of the heavily doped $\text{La}_{3-x}\text{Te}_4$ samples.

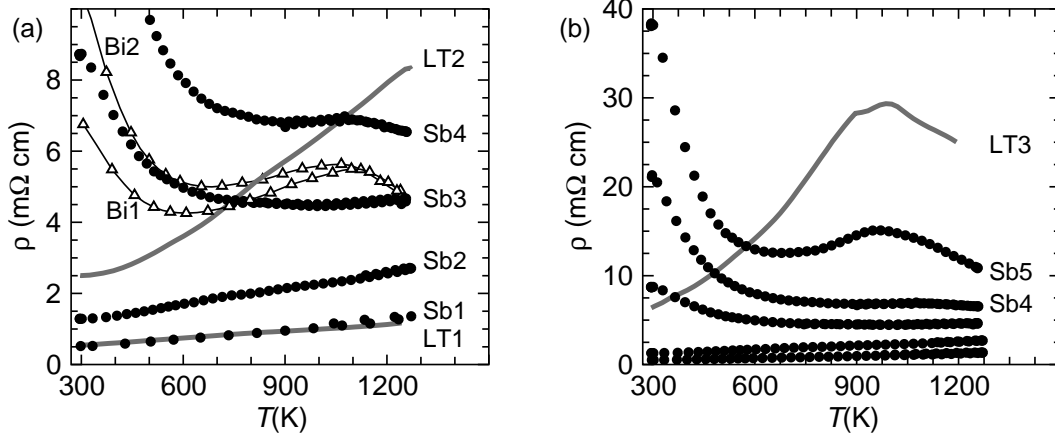


Figure 4.25. The resistivity of nominal $\text{La}_3\text{Te}_{4-z}\text{Sb}_z$ at low Sb content is similar to that of pure $\text{La}_{3-x}\text{Te}_4$ samples, and as Sb content increases an activated process emerges. Panel (a) also includes nominal $\text{La}_3\text{Te}_{4-z}\text{Bi}_z$ samples, which display similar behavior. Reprinted with permission from *Phys. Rev. B*, **81**, 125205 (2010). Copyright 2010, American Physical Society.

In Figure 4.25b, the less resistive samples are examined in further detail, along with samples containing Bi (open triangles) and the two less resistive $\text{La}_{3-x}\text{Te}_4$ samples (gray curves). At low Sb content (and low Bi content, not shown), electrical conduction is very similar to that in $\text{La}_{3-x}\text{Te}_4$, which makes physical sense because these samples have high carrier concentrations and similar composition. The linear increase in ρ with increasing T implies acoustic phonon scattering limits the carrier mobility, which is consistent with the data for $\text{La}_{3-x}\text{Te}_4$ (even for large x).

The expected heavily doped behavior (positive $d\rho/dT$ at moderate T) is lost at large Sb or Bi content, and activated conduction is observed at moderate T for $z \geq 0.6$. This transition is shown in Figure 4.25b, where the resistivity decreases with increasing T for large z and moderate T . The source for activated conduction is unclear; it could be caused by the substitution of Sb for Te which promotes local variations in the electric potential associated with the randomly distributed anions, or defects or impurities which may be promoted by large Sb (Bi) concentrations. The decrease in ρ with increasing T is primarily associated with a change in the carrier mobility, not carrier density, as demonstrated by the temperature dependences of n_H and μ_H in Figures 4.26a and 4.26b, respectively.

Above $\sim 550 \text{ K}$, the mobility in the Sb containing sample (*Sb5*) is larger than the mobility in the $\text{La}_{3-x}\text{Te}_4$ (*LT3*) sample (Fig. 4.26b). The larger mobility in *Sb5* at high T may be related to the reduction in La vacancies, which are likely scattering sources in $\text{La}_{3-x}\text{Te}_4$ when x is large. The Seebeck coefficient data in Figure 4.22a implies a minor reduction in effective mass, which would also promote an increased mobility (consider Eqn. 4.12 and the classic definition $\mu = e\tau/m$). Note the similar n_H in *Sb5* and *LT3*.

Activated conduction is inferred from the $\mu_H(T)$ shown in Figure 4.26b. However, due to the small temperature range over which the activated behavior is observed in this high-temperature study, a variety of models are found to adequately fit the data. In particular, small polaron and variable range hopping (three

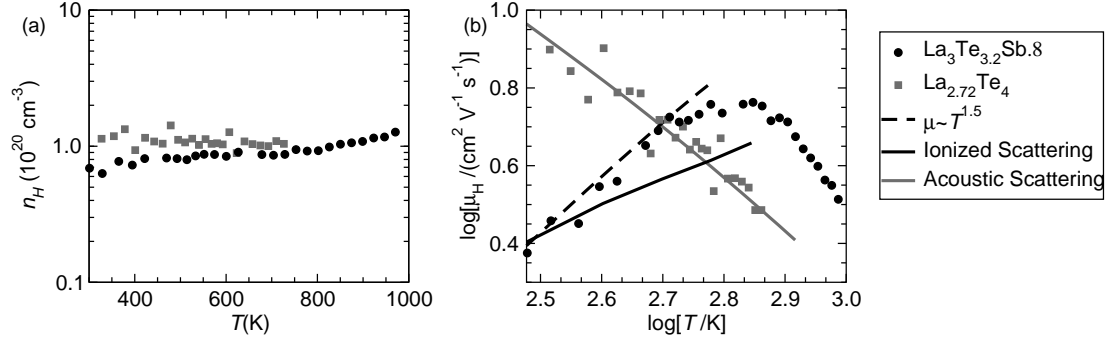


Figure 4.26. Temperature dependence of (a) Hall carrier concentration and (b) the Hall mobility for the samples containing the most Sb (solid markers) and highest vacancy content (*LT3*). The Hall mobility of the $\text{La}_{3-x}\text{Te}_4$ sample (gray markers) decays with increasing temperature as expected for simple acoustic phonon scattering, the theoretical description of which is shown by the solid gray curve. The mobility of the nominal $\text{La}_3\text{Te}_{3.2}\text{Sb}_{0.8}$ sample (*Sb5*) increases with increasing T for moderate T , and decreases with increasing T at high T . The theoretical temperature dependence for ionized impurity scattering is represented by the black curve; the dashed curve shows $T^{3/2}$ behavior (see Eqn. 4.13). Fit to generic activation in *Sb5* at moderate T yields an activation energy of 0.06 eV. Reprinted with permission from *Phys. Rev. B*, **81**, 125205 (2010). Copyright 2010, American Physical Society.

dimensional) both provide a reasonable description of the data in Figure 4.26b. For the sake of simplicity, a generic activated mechanism ($\mu_H \propto \exp[E_a/kT]$) is considered for the data in Figure 4.26b. In the range 300 to 600 K, an activation energy of $E_a = 0.06$ eV is obtained.

Anderson localization is a type of activated conduction studied by Cutler and Mott in $\text{Ce}_{3-x}\text{S}_4$ [52], which is another rare-earth chalcogenide possessing the Th_3P_4 structure type. In their study, Cutler and Mott concluded that the random distribution of Ce vacancies promotes Anderson localization[52]. However, in $\text{Ce}_{3-x}\text{S}_4$, localization was only observed at low temperatures and/or very low n ($x \rightarrow \frac{1}{3}$). For instance, the most conductive $\text{Ce}_{3-x}\text{S}_4$ sample to display this behavior had a room temperature resistivity of ~ 25 m Ω -cm, and displayed predominantly itinerant conduction down to ~ 100 K where the onset of localization was observed. Localization was not observed in phase pure $\text{La}_{3-x}\text{Te}_4$ samples for the temperatures ($T > 300$ K) and doping levels considered here[38]; low temperature studies have yet to be performed. Activated $\rho(T)$ was observed near room temperature in two samples that were not phase pure, though this effect was not present past 400 K and was very minor in comparison to the behavior observed in the Sb (Bi) doped samples. The behavior in these impurity containing samples was not reproducible in phase pure $\text{La}_{3-x}\text{Te}_4$, whereas activated behavior was reproduced by multiple synthetic efforts and procedures (for instance additional annealing time was considered) in the Sb (Bi) containing samples. Recall the Sb or Bi doped samples are phase pure by the same characterization techniques that identified the impurities believed responsible for the observation of small deviations from itinerant conduction (assumed due to “dirty” grain boundaries) in $\text{La}_{3-x}\text{Te}_4$.

The temperature dependence of μ_H for sample *Sb5* may be explained by the conventional theory of itinerant electron conduction with multiple scattering sources. In this framework, the increase in μ_H with increasing T at moderate T is due to ionized impurity scattering (by Sb or Bi anions), and the decrease in

μ_H at high T is caused by acoustic phonon scattering. To utilize the equations describing μ_H presented in Section 4.2, the carrier relaxation time τ must be obtained via appropriate summation of all contributing scattering times τ_s (see Eqn. 4.10). Difficulty treating multiple scattering mechanisms arises due to the dependence of μ_H on η , as well as the functional forms of the various τ_s (the prefactor $\tau_{0,s}$ is not always independent of energy). In general, the experimentalist obtains an approximate temperature-dependent η from the temperature dependence of the Seebeck coefficient utilizing Equation 4.29. The values of $\eta(T)$ are difficult to obtain when multiple scattering mechanisms are present, and an additional measurement is generally required to allow a more complete solution to be obtained. As discussed, in the limit of high or low T , a single scattering mechanism may limit μ_H , which allows $\eta(T)$ to be obtained more easily. Clearly, the reliability of such a treatment rests heavily on the electronic structure, which is assumed to be well described by a parabolic band. The samples analyzed here (*LT3* and *Sb5*) have relatively low doping levels and transport is likely to be determined by only the minimum energy conduction band, which is, to first order, parabolic.

First recall the temperature dependence of μ_H for the $\text{La}_{3-x}\text{Te}_4$ sample (*LT3*) in Figure 4.26b (from Figure 4.6b). The decay of μ_H in *LT3* with increasing T is well described by the theory of acoustic phonon scattering, which is shown by the solid gray curve in Figure 4.26b and was discussed in Section 4.3. The temperature dependence of μ_H for sample *LT3* in Figure 4.26b differs from the $T^{-3/2}$ decay implied by Equation 4.12 because the decrease in η with increasing T impacts μ_H via the integrals in Equation 4.28. Temperature-dependent m^* , v_l , and E_{def} can also effect the magnitude or temperature dependence of μ_H significantly. A change in one or all of these material properties with Sb substitution may explain the difference between the μ_H for samples *Sb5* and *LT3* at high T , where acoustic phonon scattering likely limits μ_H regardless of composition.

For illustrative purposes, the moderate T behavior of μ_H for sample *Sb5* is compared to a theoretical curve (solid black line) generated by assuming ionized impurity scattering limits τ . The relevant equations are Equations 4.13-4.15 and 4.29. The theoretical curve is generated assuming the nominal composition $\text{La}_3\text{Te}_{3.2}\text{Sb}_{0.8}$ is valid to obtain N_i , and again $m^*=2.8m_e$. Then $\chi=27\epsilon_0$ is obtained by fitting to the room temperature data (ϵ_0 is the permittivity of free space). The deviation from this theoretical curve and the experimental data can be easily explained by temperature-dependent m^* or χ , though other sources of error include the single band approximation, temperature independent $n=8\times 10^{19}\text{ cm}^{-3}$, and the inclusion of only one type of scattering. In this case, a temperature-dependent m^* could result from the multiband features and the increased occupation of states associated with thermal broadening (recall this is a parameterized, single-band effective mass). The dashed black line in Figure 4.26b demonstrates $T^{3/2}$ behavior commonly associated with ionized impurity scattering in the non-degenerate limit.

4.4 $\text{Ba}_8\text{Ga}_{16-x}\text{Ge}_{30+x}$

This section is an adapted reproduction, with permission, from *Phys. Rev. B*, **80**, 125205 (2009). Copyright 2009, American Physical Society.

As discussed in the Section 1.5.2 of the Introduction, the charge counting in type I clathrates leads to a flexible system that enables an inherent optimization of thermoelectric performance. The strict relationship between composition and carrier density is illustrated in Figure 4.27a, where Hall carrier concentrations are plotted versus experimental composition. The experimental x values were obtained from the WDS data assuming no vacancies on the framework: $\frac{30+x}{16-x} = \frac{\text{Ge at.}\%}{\text{Ga at.}\%}$. The results agree well with the theoretical n versus x (solid curve), which is obtained by simple charge counting that reveals x free electrons per formula unit (holes are formed for $x < 0$). Note there is a small difference between the chemical n and n_H due to scattering effects, which are discussed below.

The agreement between experiment and theory suggests that valence counting rules are strictly obeyed in n -type $\text{Ba}_8\text{Ga}_{16-x}\text{Ge}_{30+x}$ (for the compositions of interest to thermoelectric applications). Note the same conclusion is drawn from both EDS and WDS data, due to the similar slope, though the EDS data is shifted to excess Ge by roughly $x = 0.4$. The use of standards during WDS measurements typically yields higher accuracy than in EDS measurements. The atomic percent Ba obtained from WDS reveals greater Ba content than allowed by the crystal structure (8/54=14.8 at.%); this assumes no framework vacancies. The error in Ba content may be related to the use of an oxide for the Ba standard, as similar errors in WDS data were observed for the $\text{La}_{3-x}\text{Te}_4$ system, where LaPO_4 was utilized for the La standard and La content was found to be greater than that allowed by the crystal structure (the same conditions were employed)[38]. However, this may also be due to the presence of a barium rich oxide at the grain boundaries, or Ge/Ga vacancies.

While simple charge counting rules appear to apply assuming no vacancies, the role of vacancies (both framework and filler) remains unclear[127–129]. Ba vacancies have been suggested by refinement of diffraction data[128], and the literature also contains studies which fit diffraction data to $\text{Ba}_8\text{Ga}_y\text{Ge}_z$ where $y+z < 46$, as well as the fully occupied $\text{Ba}_8\text{Ga}_{16-x}\text{Ge}_{30+x}$ [129–131]. The formation of vacancies in n -type clathrates appears to be most important when compositions lie far from the charge balanced composition[129, 132]. Vacancies remove electrons from the system and thus move the Fermi energy (and carrier concentration) towards more reasonable levels, as seen in $\text{K}_8\text{Si}_{46-x}$ and $\text{Rb}_8\text{Sn}_{46-x}$ (for n -type systems)[90].

The growth of single crystal samples with nominal composition near $\text{Ba}_8\text{Ga}_{16}\text{Ge}_{30}$ frequently results in n -type samples[73, 74], which could be due to greater Ge content than expected. Energetic arguments have been made to suggest $\text{Ba}_8\text{Ga}_{15}\text{Ge}_{31}$ may be more stable than $\text{Ba}_8\text{Ga}_{16}\text{Ge}_{30}$ due to a reduction in Ga-Ga repulsion[69].

The $\text{Ba}_8\text{Ga}_{16-x}\text{Ge}_{30+x}$ samples produced for this investigation were found to be unstable upon measurement to 1050 K[107]. The pertinent data and a discussion of this issue and its resolution are provided in Appendix C. In summary, a decrease in the electrical resistivity was observed after samples were measured

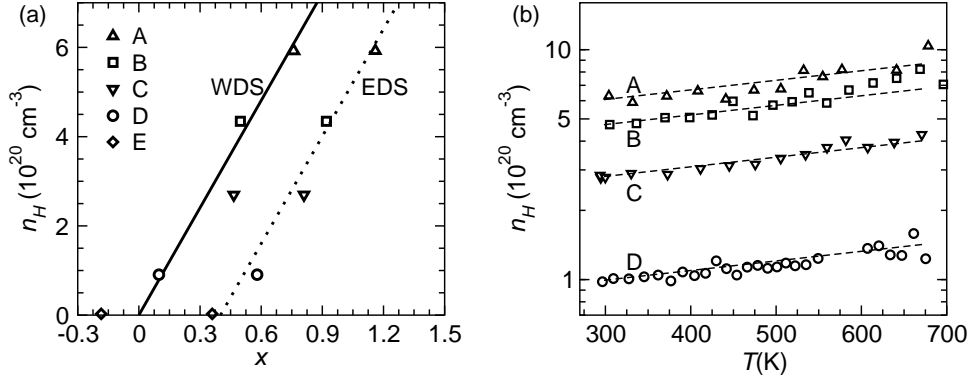


Figure 4.27. (a) Room temperature Hall density in $\text{Ba}_8\text{Ga}_{16-x}\text{Ge}_{30+x}$ as a function of elemental composition x , as determined from wavelength dispersive spectroscopy (WDS) and energy dispersive spectroscopy (EDS). The solid line is generated from electron counting assuming $\text{Ba}_8\text{Ga}_{16-x}\text{Ge}_{30+x}$ stoichiometry, and the dashed line possesses the same slope but contains a shift in x of 0.4. (b) The Hall carrier density increases slightly with increasing T ; the dashed lines are visual guides. Reprinted (adapted) with permission from *Phys. Rev. B*, **80**, 125205 (2009). Copyright 2009, American Physical Society.

Table 4.3. Room temperature properties of $\text{Ba}_8\text{Ga}_{16-x}\text{Ge}_{30+x}$ samples, where the calculated r_H and m^* are obtained assuming acoustic phonon scattering limits μ . Reprinted with permission from *Phys. Rev. B*, **80**, 125205 (2009). Copyright 2009, American Physical Society.

Sample	Symbol	n_H (10^{20} cm^{-3})	r_H -	μ_H ($\text{cm}^2/\text{V/s}$)	α ($\mu\text{V/K}$)	m^* (m_e)
A	\triangle	5.9	1.02	11.6	-52	1.82
B	\square	4.3	1.04	12.8	-65	1.86
C	∇	2.7	1.05	14.4	-81	1.74
D	\circ	0.9	1.11	12.1	-159	2.02
E	\diamond	0.03	1.18	7.2	-143	-

to $T > 1000$ K in the JPL high-temperature Hall effect station. This was found to be due to an increase in the carrier density. No such behavior was observed after measurement in the Seebeck coefficient or thermal diffusivity systems. This issue was resolved by determining a temperature to which the data/samples remained stable (1000 K).

The change in carrier density (composition) produces the expected change in transport properties. This is readily observed at room temperature, as summarized in Table 4.3.

The temperature dependence of n_H is shown in Figure 4.27b. While a slight increase with increasing T is observed, the values of n_H are dominated by extrinsic doping, which is consistent with the valence counting. The increase in n_H with T cannot be explained by temperature-dependent r_H when only acoustic phonon scattering is present (r_H would increase with T and $n_H = n/r_H$ should decrease if n originates from a valence imbalance associated with framework composition). A temperature-dependent r_H may explain some, though not all, of the T dependence of n_H if there are competing scattering mechanisms. If ionized impurity scattering is important at low T , the values of r_H would be larger than those shown in Table 4.3, and r_H would decrease with increasing T as acoustic phonon scattering becomes more important.

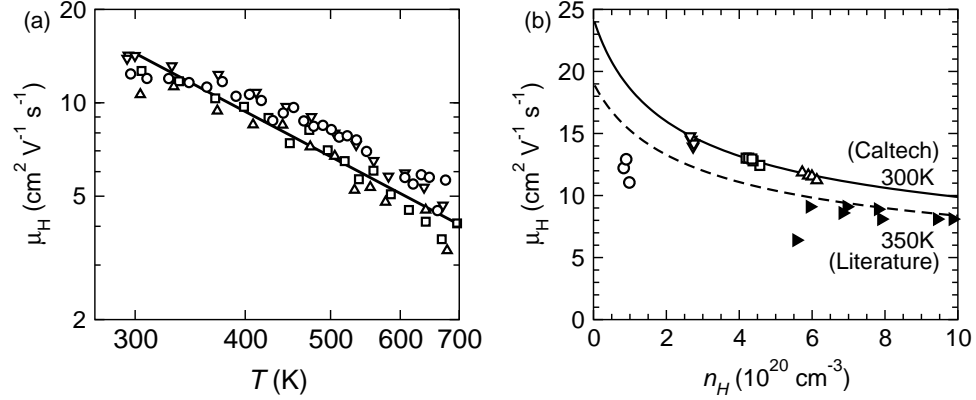


Figure 4.28. (a) Temperature dependence of the Hall mobility in log-log format, with a $T^{-1.5}$ decay (solid curve) shown for comparison (see Eqn. 4.12). (b) Room temperature Hall mobility versus carrier concentration for samples from this study (open markers with symbols as in Table 3.2), as well as data at 350 K from Martin (filled markers). The experimental data are compared to theoretical curves generated assuming the carrier mobility is limited by acoustic phonon scattering (solid curve for 300 K, dashed curve at 350 K). The data symbols are consistent with those in Table 4.3. Reprinted with permission from *Phys. Rev. B*, **80**, 125205 (2009). Copyright 2009, American Physical Society.

As shown in Figure 4.28a, μ_H decreases with increasing T for samples *A-D*. The temperature dependence of μ_H in a heavily doped semiconductor can usually be modeled by a power law $\mu_H \propto T^{-p}$ when one scattering mechanism dominates μ_H for the temperature range of interest. Examining the μ_H data in this manner, we find that the empirically observed parameter p for samples *A – D* changes with increasing temperature. Such deviations from power law behavior are best observed in a log-log plot, hence the axis selection in Figure 4.28a. The failure of a single power law to fit the mobility data is likely due to the presence of multiple scattering mechanisms. However, the theoretical dependence of μ_H on T for charge carriers scattered by acoustic phonons is more complex than initially observed via Equations 4.12 and 4.28, and $p > 1.5$ can be explained via Equation 4.12 when v_l , m^* , and E_{def} depend on T . Of course, at high T the single carrier description fails and an underestimated μ_H is obtained. The n_H and α data imply m^* does increase with increasing T .

As can be inferred from Figure 4.28a, the empirical p is found to increase as the T range of interest increases. This is consistent with competing scattering mechanisms, where the influence of acoustic phonon scattering becomes increasingly important as T rises. A single p value describes the data much better if it is obtained using $n_H(T) = n_H(T = 300 \text{ K})$. The carrier density is believed to originate from a valence imbalance associated with the framework composition, and should thus be independent of temperature at moderate T . Thus, it is possible that the unexpected temperature dependence of n_H leads to an incorrect $\mu_H(T)$. At high temperatures, $p > 1.5$ is observed, which suggests temperature-dependent band mass (consistent with the α and n_H).

The dependence of μ_H on T and n_H is complex, particularly in materials where multiple scattering mechanisms limit the carrier mean free path. A proper treatment of μ_H data requires allowance for all

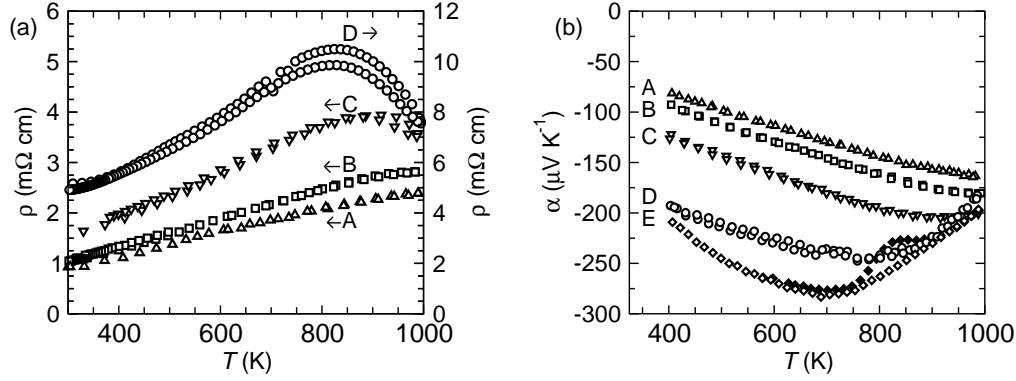


Figure 4.29. (a) Electrical resistivity and (b) Seebeck coefficient versus temperature in $\text{Ba}_8\text{Ga}_{16-x}\text{Ge}_{30+x}$ (open markers with symbols as in Table 4.3). Reprinted (adapted) with permission from *Phys. Rev. B*, **80**, 125205 (2009). Copyright 2009, American Physical Society.

relevant scattering mechanisms, including residual resistances associated with grain boundaries and defects. At moderate temperatures, the mobility of a heavily doped semiconductor is typically limited by acoustic phonon scattering and/or ionized impurity scattering. The effect of ionized impurities is greatest at lower temperatures, and acoustic phonon scattering tends to dominate at higher temperatures. Alloy scattering, which has been considered in the $\text{Ba}_8\text{Ga}_x\text{Cu}_y\text{Ge}_{46-x-y}$ system[133], may also be present and would be most influential at lower temperatures (also modeled with $\lambda=0$). At high temperatures we expect μ_H to be limited by acoustic phonon scattering, and this assumption ($\lambda=0$) is utilized in the subsequent analysis.

The variation of μ_H with n_H is shown in Figure 4.28b, where room temperature data from this study and data at 350 K reported by Martin et al.[89] are compared to theoretical curves based on Equations 4.25, 4.12 and 4.28. We note the μ_H values are in agreement with the literature[71, 73]. The dependence of μ_H on n_H is found to be in fair agreement with the theoretical description of acoustic scattering, though only a small concentration window is examined and relatively little variation with n_H is observed. The effect of residual resistance (via grain boundaries and defects) is to decrease μ_H , although this alone does not appear to explain the deviation from theory for sample *D*. In the traditional view of ionized impurity scattering, a reduced carrier concentration eventually leads to a lower mobility due to decreased screening of the ionized impurities (unlikely to be the case). The suppression of μ_H in sample *D* may be associated with an additional scattering mechanism, or a processing related feature, and thus no conclusion can be drawn at this time.

The curves in Figure 4.28b were generated using temperature-dependent values of C_{11} from the literature[86], which are related to v_l via the density d by $v_l = \sqrt{(C_{11}/d)}$. A value of $m^* = 1.86m_e$ is selected based on similar analysis of the room temperature Seebeck coefficients (4.31a). The theoretical curves in Figure 4.28a were generated using a deformation potential of $E_{def} = 8.3$ eV, which is a reasonable value for a doped semiconductor[28, 119].

The electrical resistivity increases with decreasing n and increasing temperature for samples *A* – *D*, as expected for a heavily doped semiconductor (see Figure 4.29a). The increase in ρ with increasing T

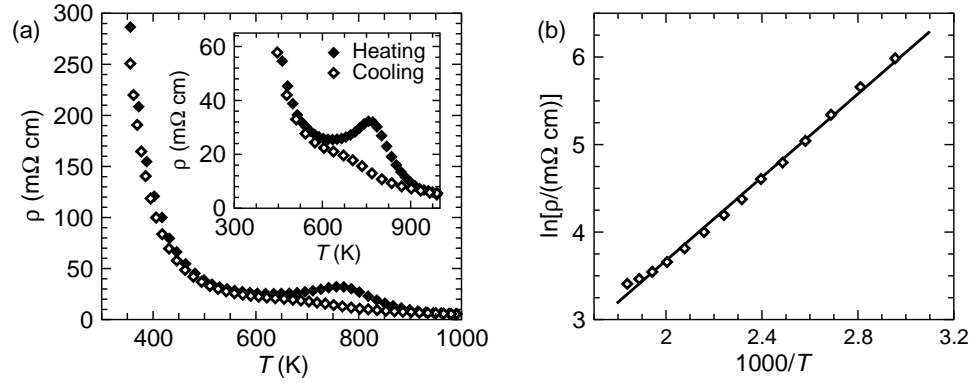


Figure 4.30. (a) Electrical resistivity of near-insulating sample E decreases rapidly with increasing temperature. The inset examines an interesting event that occurs upon heating; the source of this event has not been isolated. (b) An Arrhenius plot of the resistivity demonstrates this behavior between 340 and 540 K, where an energy gap of $E_g = 0.41$ eV is obtained from the linear fit shown. Reprinted (adapted) with permission from *Phys. Rev. B*, **80**, 125205 (2009). Copyright 2009, American Physical Society.

corresponds to the decrease in μ_H shown in Figure 4.28a. The effect of thermally activated minority carriers can be observed at high temperature where the resistivity begins to decrease for samples C and D .

The resistivity of sample E displays the temperature dependence commonly observed for an intrinsic semiconductor, as shown in Figure 4.30a,b. If the decrease in ρ is assumed to be due to the thermal excitation of charge carriers across the energy gap, yielding $\rho \propto \text{Exp}(E_g/2kT)$, a band gap E_g of 0.41 eV is obtained from the fit (solid line) in Figure 4.30b. The high-temperature behavior of this sample is examined in the inset of Figure 4.30a, where an event is observed upon heating. This event is also observed in the Seebeck coefficient (α) at high temperatures, where a decrease in the magnitude of α is observed at high temperature (see Fig. 4.29b). The event (increase in ρ) observed in sample E occurred upon consecutive heating cycles for both ρ and α , and was not observed upon cooling. This behavior is not understood, and high-temperature diffraction measurements have been undertaken to elucidate the role of structure on transport; these measurements are being conducted by Bo B. Iversen's group (University of Aarhus, Denmark). See Appendix C for related discussion.

As shown in Figure 4.29b, the Seebeck coefficients have the expected sign and temperature dependence for heavily doped, n -type semiconductors. Consistent with the behavior of ρ in Figure 4.29a, the magnitudes of the Seebeck coefficients of the low n samples display maxima at high temperature, where the thermally activated holes reduce the thermoelectric voltage. By utilizing $E_g \sim 2e\alpha_{max}T_{max}$ [125], a thermal band gap of ~ 0.39 eV is observed for samples C , D , and E , which is consistent with E_g obtained from electrical resistivity data for sample E . The values of E_g reported here are consistent with *ab initio* electronic structure calculations reported by Blake et al. ($E_g \sim 0.5$ eV)[134], while calculations by Madsen et al. predicted a larger value ($E_g \sim 0.9$ eV)[135].

In Figure 4.31a, the room temperature data for $|\alpha|$ from this study and the literature are compared to two theoretical calculations, while Figure 4.31b examines the behavior observed at 600 K for the Caltech

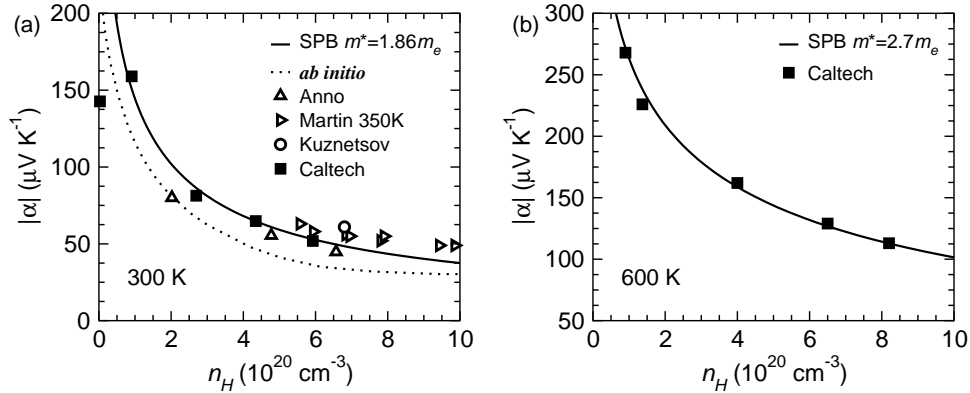


Figure 4.31. Absolute value of the Seebeck coefficient versus Hall carrier density at (a) 300 K and (b) 600 K. At 300 K, data from this study and the literature are compared to a single parabolic band (SPB) model, as well as the *ab initio* calculation by Madsen et al[135]. Note the data from Martin et al. is reported at 350 K. The experimental data were taken from References [71, 73, 89]. The effective mass required to model the data is found to increase with increasing temperature. Panel (a) is reprinted with permission from *Phys. Rev. B*, **80**, 125205 (2009). Copyright 2009, American Physical Society.

samples. The dashed curve in Figure 4.31a is the result of *ab initio* calculations previously reported by Madsen et al[135]. The experimental data are well described by the SPB model (solid curves), the curvature of which also agrees well with the *ab initio* results, though a small change in curvature exists at high n .

The agreement between theory and experiment strongly justifies the use of a single parabolic band model during the analysis of electronic transport, particularly for the $\text{Ba}_8\text{Ga}_{16-x}\text{Ge}_{30+x}$ compositions of interest for thermoelectric application. The solid curve in Figure 4.31a is generated using a single parabolic band (SPB) model, with an effective mass of $m^*=1.86m_e$, while in Figure 4.31b an effective mass of $2.7m_e$ was necessary to describe the data at 600 K. We note the *ab initio* results shown here were extracted from the published report, which was originally presented as a function of electrons per formula unit (chemical n), and is thus not a direct comparison with the Hall data and contains minor error associated with data extraction.

4.5 SrZnSb_2 and SrZn_2Sb_2

This section is an adapted reproduction, with permission, from *J. Appl. Phys.*, **106** 013706 (2009). Copyright 2009, American Institute of Physics.

SrZnSb_2 and SrZn_2Sb_2 were found to be p -type conductors with room temperature Hall carrier concentrations of $5 \times 10^{20} \text{ cm}^{-3}$ and $1.5 \times 10^{19} \text{ cm}^{-3}$, respectively. As shown in Figure 4.32b, the value of n_H for SrZnSb_2 increases quickly with increasing temperature, which is indicative of a small band gap semiconductor or a semimetal. At high temperatures, the single-carrier description yields an exaggerated n_H due to the excitation of electrons into the conduction band. Without knowledge regarding the mobility of holes and electrons (as a function of temperature) it is impossible to calculate the true hole concentration and mobility at high T in materials with small E_g .

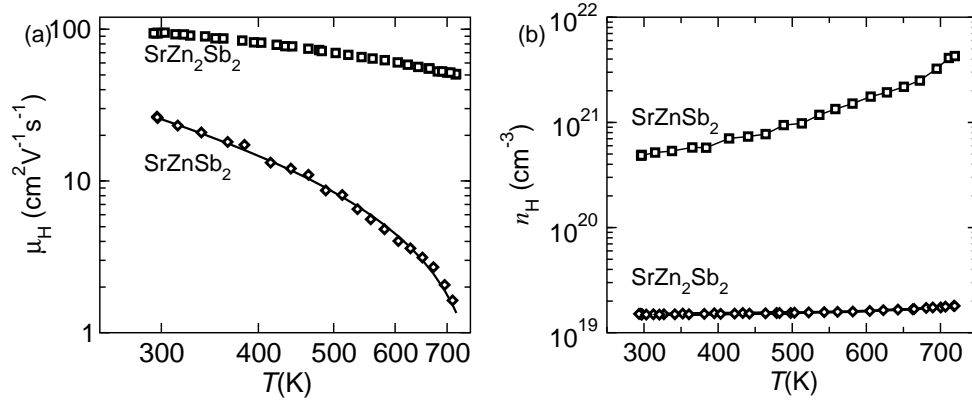


Figure 4.32. The Hall effect data reveals a decrease in the carrier mobility with increasing T for both samples. (b) The carrier density is relatively temperature independent in SrZn_2Sb_2 , but increases strongly with increasing T in SrZnSb_2 which indicates a very small energy gap. Reprinted with permission, from *J. Appl. Phys.*, **106** 013706 (2009). Copyright 2009, American Institute of Physics.

The electrical resistivity (ρ) of SrZnSb_2 and SrZn_2Sb_2 increases with increasing temperature, as shown in Figure 4.33a. For SrZnSb_2 , ρ increases less than linearly with temperature due to the thermal excitation of carriers. The corresponding Hall mobility (μ_H) decreases with increasing temperature (Fig. 4.32a), presumably due to scattering by acoustic phonons, and at high temperatures multi-carrier effects yield an underestimated μ_H . See Appendix A for a discussion of multi-carrier effects.

The higher mobility in SrZn_2Sb_2 is explained by the change in carrier density and the reduced effective mass (see Seebeck coefficient analysis below). Specifically, the reduced carrier density in SrZn_2Sb_2 acts to push the chemical potential closer to the band edge, thus promoting a larger μ_H when acoustic scattering limits τ as discussed in Section 4.2. However, the deformation potential is observed to be fairly different in these materials, with $E_{def} = 14.7$ eV in SrZn_2Sb_2 and $E_{def} = 9.7$ eV in SrZnSb_2 . These values were obtained at room temperature, using $m^*/m_e=0.55$ (SrZn_2Sb_2) and 0.92 (SrZnSb_2) as discussed below; values for v_l are given in Table 5.2. The temperature dependence of μ_H is not well described by the theory presented in Section 4.2 when temperature independent properties are utilized. This is likely due to the changing effective mass, speed of sound, and/or deformation potential, though additional scattering mechanisms may also be important. Note that if additional scattering mechanisms were included, the calculated values of E_{def} would decrease. Also, multi-carrier effects may cause significant deviations from the true carrier properties.

Seebeck coefficient (α) measurements support p -type conduction, with positive α obtained for all temperatures (Fig. 4.33b). The Seebeck coefficient of SrZnSb_2 is small, likely due to the high doping level, and the observed temperature dependence is similar to that of a heavily doped semiconductor. Similarly, the Seebeck coefficient of SrZn_2Sb_2 is relatively large, due to the low doping level.

A thermal band gap of $E_g=0.07$ eV is estimated for SrZnSb_2 , while $E_g\sim 0.3$ eV is obtained for SrZn_2Sb_2 . The small energy gap estimated for SrZnSb_2 is consistent with the sharp increase in n_H observed in Figure 4.32b. These estimates are obtained using the maximum value of α and the corresponding T : $E_g \sim$

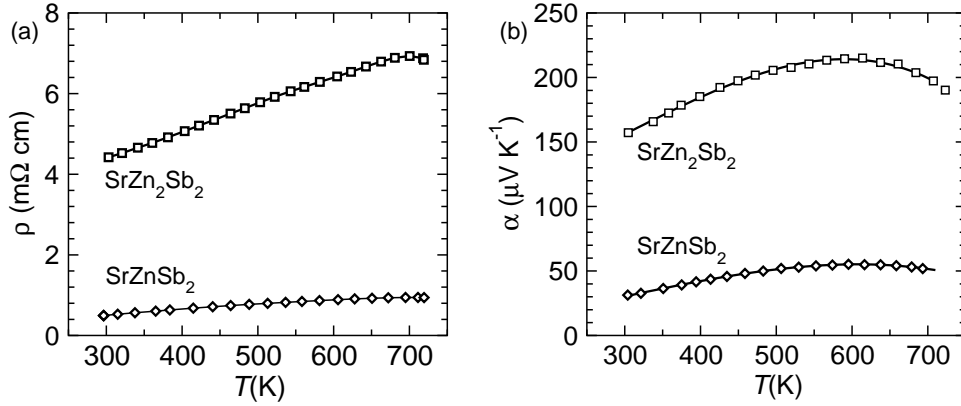


Figure 4.33. (a) Electrical resistivity and (b) Seebeck coefficient in the Sr-Zn-Sb systems. The behavior of SrZn_2Sb_2 is best described as a doped, small band gap semiconductor, while a significantly smaller energy gap (nearly semimetallic) is inferred from the electrical transport properties in SrZnSb_2 . Reprinted with permission, from *J. Appl. Phys.*, **106** 013706 (2009). Copyright 2009, American Institute of Physics.

$2e\alpha_{max}T_{max}$ [125]. The effective mass of SrZnSb_2 is calculated to be $0.92 m_e$ at room temperature, while that of $\text{SrZn}_2\text{Sb}_2=0.55m_e$. The effective mass is calculated from the room temperature n_H and α using a single parabolic band model with carrier mobility limited by acoustic phonon scattering. The Hall factor was not taken into account in this case.

The transport properties of other $A\text{Zn}_2\text{Sb}_2$ ($A = \text{Ca}, \text{Yb}, \text{Eu}$) were previously reported[95–97] and are summarized here. The nominally stoichiometric compounds were found to be extrinsically doped, p -type semiconductors with 3.0×10^{19} to 1.5×10^{20} holes per cm^3 at 300 K[97]. Using the same approach as above, $E_g \sim 0.3 \text{ eV}$ and $m^* \sim 0.6 m_e$ have been calculated for these compounds[97], with $m^* = 0.57 m_e$ obtained at 300 K for EuZn_2Sb_2 from the data in Reference [96]. The carrier mobility of all $A\text{Zn}_2\text{Sb}_2$ ($A = \text{Sr}, \text{Ca}, \text{Yb}, \text{Eu}$) is found to be larger than in SrZnSb_2 , probably due to the reduced effective mass and lower carrier density. While the various $A\text{Zn}_2\text{Sb}_2$ compounds have similar m^* , the variation in μ does not follow any trend with carrier concentration and the Yb and Eu compounds have surprisingly large μ . The difference in m^* , μ , and E_g between these compounds and SrZnSb_2 suggests the layer of infinite Sb chains impacts the electronic structure of SrZnSb_2 near the top of the valence band. We have recently published a more-detailed account of these $A\text{Zn}_2\text{Sb}_2$ compounds, which included first principles calculations, and the reader is pointed to that body of work for a complete discussion[97].

Chapter 5

Thermal Transport

5.1 Summary

This chapter begins with a general discussion of the thermal conductivity κ of solids. The importance of the distribution of phonon group velocities is highlighted. Specifically, it is not appropriate to assume that all phonon modes move at the highest velocity (the sound velocity, or the velocity of acoustic phonons). As such, the classic result obtained from kinetic theory must be reconsidered or used cautiously. A few expressions for κ at high temperatures in insulating materials are given, along with some expressions for the corresponding minimum κ .

The thermal conductivity, in the materials discussed here, generally behaves as expected for doped semiconductors. That is, κ decreases as the carrier density decreases due to a decreasing electronic contribution, and decreases with increasing temperature due to increased phonon-phonon scattering. A few exceptions to these trends are observed, however, when the influence of point-defect scattering or phonon group velocity changes dramatically with composition.

In $\text{La}_{3-x}\text{Te}_4$, the high defect concentration at large x promotes a very low lattice thermal conductivity κ_L . By considering samples with low carrier concentration and low vacancy concentration (nominal $\text{La}_3\text{Te}_{4-z}\text{Sb}_z$), the influence of an increasing group velocity is observed as it produces a higher lattice thermal conductivity at higher defect concentrations. Also, these Sb containing samples regain the expected decay in κ_L with increasing temperature, which is suppressed in the presence of high concentrations of point defects.

The lattice thermal conductivity of $\text{Ba}_8\text{Ga}_{16-x}\text{Ge}_{30+x}$ is found to be approximately 1 W/m/K at 300 K. This low lattice thermal conductivity is likely not due to the presence of a Ba “filler” atom that promotes phonon scattering; κ_L decays as expected for simple phonon-phonon scattering. Rather, the large number of atoms per unit cell promotes a large number of optical phonon modes, which have low group velocity and thus do not contribute significantly to the thermal conductivity. This behavior is also inferred by considering the two Sr-Zn-Sb compounds, where the large unit cell compound contains a smaller lattice thermal conductivity and the trends can be explained by simple consideration of the number of atoms per unit cell.

5.2 Thermal Transport Theory

The formulations reviewed here are discussed by a number of authors. I have found the papers by P. G. Klemens to provide a significant amount of detail and discussion.[36, 37] Of course, several books discuss thermal transport in detail, and of particular interest to those studying thermoelectrics are the books by Bhandari and Rowe[136] and Drabble and Goldsmid,[137, 138], though traditional texts such as Ziman's are also very useful.[29]

5.2.1 Lattice Thermal Conductivity

Kinetic theory relates the thermal conductivity κ for a system of particles to their specific heat C (per unit volume), mean velocity v , and a mean free path l characterizing the distance traveled between random scattering events:

$$\kappa = \frac{1}{3}Cvl. \quad (5.1)$$

In an electrically insulating, crystalline material, the flow of heat is through lattice vibrations that are quantified as phonons, which are often treated by kinetic theory. In this case, the above expression defines an average phonon mean free path l . However, this approach comes with several shortfalls because, in general, a variety of vibrational modes exists and thus a more appropriate expression is

$$\kappa = \frac{1}{3} \sum_i C_i v_i l_i. \quad (5.2)$$

It is common to consider the frequency dependent properties; if C , v , and l depend on the frequency of the lattice vibrations in a continuous manner, then

$$\kappa = \frac{1}{3} \int C(\omega)v(\omega)l(\omega)d\omega = \frac{1}{3} \int_0^{\omega_{max}} C(\omega)v(\omega)^2\tau(\omega)d\omega. \quad (5.3)$$

The difficulty in using Equation 5.3 arises primarily in the description of $v(\omega)$ and $\tau(\omega)$, as several reasonable theories for C exist. The frequency-dependent velocity of phonons is essentially impossible to measure. However, the velocity of the long wavelength vibrations can be approximated by the material's sound velocity, v_s . These phonons are termed acoustical phonons, and the maximum frequency associated with acoustical phonons is here termed $\omega_{D,A}$. The velocity of all acoustical phonons is generally close to v_s , though some change in $v(\omega)$ is expected at large ω (typically a reduction of v). For $\omega > \omega_{D,A}$, the vibrational modes are termed optical phonons, and the Debye frequency, ω_D is the upper limit of ω for these modes and thus the upper limit in Equation 5.3. The Debye frequency is related to the Debye temperature Θ_D by $\omega_D = k\Theta_D/\hbar$, and Θ_D can be readily estimated from the mean sound velocity v_m from

$$\Theta_D = \frac{v_m \hbar}{k_b} \left(\frac{6\pi^2}{V} \right)^{1/3}, \quad (5.4)$$

where the average v_m of the longitudinal v_l and transverse v_t sound velocities is

$$v_m = 3^{1/3}(v_l^{-3} + 2v_t^{-3})^{-1/3}. \quad (5.5)$$

Optical phonons generally have (very) low group velocity and, to simplify models, it is common to ignore the heat they transport. In general, this approximation becomes more valid in materials that contain atoms with high mass contrast, as well as a variety of chemical bonds, as these features promote a large energy gap between the acoustic and optical modes (which often leads to lower group velocities as well).[36, 139] Also, optical modes can promote thermal resistance through the annihilation of acoustic phonons: *acoustic + acoustic* \rightarrow *optic*.[140] Therefore, some of the heat carried by optical phonons may be offset by an increased scattering of the acoustical modes.

When the majority of heat is transported by acoustical phonons, the macroscopic phonon mean free path l is more physical if it is considered to be the mean free path of acoustic phonons l_{ac} :

$$\kappa_L = \frac{1}{3} C_{ac} v_{ac} l_{ac}, \quad (5.6)$$

where $C_{ac} = C/N_a$ is the contribution of the acoustic phonons to the volumetric specific heat for a primitive cell containing N_a atoms. The specific heat is scaled by N_a because acoustic phonons are associated with 3 of the $3N_a$ degrees of freedom in a crystal, with the remaining $(3N_a - 3)$ modes being associated with the optical phonons. The total C in a crystal is often cited as $3R/V_m$, where R is the ideal gas constant and V_m is the molar volume; this is known as the Dulong-Petit limit of C and is actually quite accurate at $T > \Theta_D$ where all modes are thermally accessible.[11] To perform an equivalent calculation using Equation 5.3, the upper limit of the integration is taken to be $\omega_D = \omega_{D,A} = \omega_D/N_a^{1/3}$. This is (mathematically) equivalent to setting the velocity of all optical phonons to zero.

A value for v_{ac} is required to obtain an estimate for l_{ac} from Equation 5.6. This is obtained fairly easily from measurements of the sound velocity, which are discussed in Appendix G. Equation 5.6 implies the three acoustic branches have the same velocity, and thus the average v_m must be utilized.

Use of Equation 5.6 generally leads to a more reasonable value of l than would be obtained from Equation 5.1, which assumed the optical phonons also travel at v_m . The concept that acoustic phonons dominate transport and the corresponding mean free paths are longer than otherwise thought can help optimize thermoelectric materials by allowing phonon scattering to be considered within a more physically realistic model (especially for large N_a).

The equations expressed above are generally useful for analyzing transport data, rather than for predicting it. Clearly, v_{ac} can be estimated from ultrasonic measurements and C_{ac} can be estimated by considering the

Dulong-Petit limit. Therefore, a predictive theory of κ_L (at high T) must estimate the value of the mean free path or phonon relaxation time ($l_{ac} = v_{ac}\tau_{ac}$). Similar to the relaxation times of electrons, theories have been developed to estimate τ for phonons when they are scattered by various sources. In general, the phonon relaxation times depend on temperature and frequency. Phonon-phonon interactions tend to limit τ at high temperatures where phonon populations are large. Phonon populations are determined by the Bose-Einstein distribution function, and the phonon occupations (and thus interactions) increase linearly with T at high T . This, in turn, produces the $\kappa_L \propto T^{-1}$ behavior commonly observed in crystalline materials at high T . [37]

To obtain a more rigorous treatment of κ , one must consider the frequency dependence of C , v , and τ . Typically, the Debye model is utilized to estimate $C(\omega)$ and theoretical model development focused on obtaining $\tau(\omega)$. Estimating $v(\omega)$ is extremely difficult, and it is common to utilize the speed of sound as an estimate for all $v(\omega)$, though this drastically overestimates v for optical phonons (large ω). The details of such considerations are provided in several texts and the reader is referred to References [11, 36, 37, 139].

The high temperature limit leads to a simplification of the integrand in Equation 5.3 when the Debye model for C is combined with the theory of τ derived for phonon-phonon interactions. Klemens shows this limit to be [37]

$$\kappa_L \approx \frac{\pi}{2\gamma^2} \left(\frac{k}{h}\right)^3 Ma \frac{\Theta_D^3}{T}, \quad (5.7)$$

where a is the lattice parameter, M the mass, and the Grüneisen parameter γ is defined as

$$\gamma = - \left(\frac{d \ln \omega_D}{d \ln V_m} \right)_T = \frac{3\alpha_T B_T V_m}{C}. \quad (5.8)$$

γ can be obtained from the linear coefficient of thermal expansion (α_T) and the isothermal bulk modulus, $B_T = B_s / (1 + \alpha_T \gamma T)$ where B_s is the adiabatic bulk modulus.

Slack's model, which only considers the contribution from acoustic phonons, leads to a slightly different high temperature limit, [139]

$$\kappa_L = \frac{B \bar{M} V^{1/3} \Theta_D^3}{N_a^{2/3} \gamma^2 T}, \quad (5.9)$$

where \bar{M} is the average atomic mass, and H is a function of γ equal to

$$H = \frac{4.86 \times 10^7}{2(1 - 0.514\gamma^{-1} + 0.228\gamma^{-2})} \approx 3 \times 10^7 s^{-3} K^{-3}. \quad (5.10)$$

This formulation suggests that the lattice thermal conductivity decreases with increasing N_a , which can be understood as reducing the relative contribution of the acoustic phonons. Increasing N_a results in a larger number of optical phonons, and these phonons generally possess low (group) velocities. These trends have been discussed in a recent review article produced by the Snyder Group. [27] The main conclusion is that complex materials with large unit cells are likely to have low κ_L , and are thus promising starting points in

the search for novel thermoelectric materials.

5.2.2 Minimum Lattice Thermal Conductivity

Theories for the minimum thermal conductivity of a solid are often useful to consider when analyzing thermal transport data. The simplest models revolve around the idea of a minimum mean free path l_{min} that is on the order of the interatomic distance. This assumption presents a difficult situation, as now the phonon wavelength is much longer than its mean free path, and the concept of a phonon tends to break down.

Cahill's formulation is developed for amorphous materials and is an extension of Einstein's model ("a random walk of energy between localized oscillators of varying size and frequencies").[141] This approach assumes the minimum phonon mean free path is one-half of its wavelength, which yields[141]

$$\kappa_{min} = \left(\frac{\pi}{6}\right)^{1/3} kV^{-2/3} \sum_i v_i \left(\frac{T}{\Theta_i}\right)^2 \int_0^{\Theta_i/T} \frac{x^3 e^x}{(e^x - 1)^2} dx, \quad (5.11)$$

where the summation is over the one longitudinal and two transverse modes, V represents the average volume per atom, $\Theta_i = v_i(\hbar/k_b)(6\pi^2/V)^{1/3}$, and v_i is the sound velocity for the longitudinal and transverse modes.

The high temperature limit of this expression is easily calculated to be

$$\kappa_{min} = \frac{1}{2} \left(\frac{\pi}{6}\right)^{1/3} kV^{-2/3} (2v_t + v_l). \quad (5.12)$$

Slack's model for the minimum thermal conductivity in crystalline materials assumes the minimum mean free path of a phonon is equal to its wavelength, as he believes this is the lower limit for a phonon to be considered a wave. [139, 141] Slack gives the minimum thermal conductivity for acoustic modes at high temperatures as[142]

$$\kappa_{min,Acoustic} = \frac{3}{2} \left(\frac{4\pi}{3}\right)^{1/3} \left(\frac{vk}{V^{2/3}N^{2/3}}\right). \quad (5.13)$$

5.2.3 Electronic Contribution to the Thermal Conductivity

The treatment of the electronic contribution (κ_e) to the total thermal conductivity was covered in Section 4.2. However, the important details are briefly reviewed here along with some general discussion.

In general, the electronic contribution is the sum of three terms: $\kappa_{e,n}$ being the contribution from electrons, $\kappa_{e,p}$ the contribution from holes, and the bipolar contribution κ_b arises when holes and electrons contribute a similar portion to the total electrical conductivity.

$$\kappa_e = \kappa_{e,n} + \kappa_{e,p} + \kappa_b. \quad (5.14)$$

While the values of $\kappa_{e,n}$ or $\kappa_{e,p}$ can be obtained relatively accurately in a heavily doped semiconductor by use of the Wiedemann-Franz relationship, it is very difficult to isolate these values in an intrinsic semicon-

ductor at high T . However, at moderate T , $\kappa_{e,n}$ and $\kappa_{e,p}$ are typically low in this case (σ is small), and thus a measure of κ in an intrinsic semiconductor provides a good, direct estimate for κ_L . At high temperatures, where minority carrier activation influences transport, the electronic contributions are difficult to address. The bipolar contribution κ_b is especially difficult to characterize because it is influenced by the Seebeck coefficient and electrical conductivity of both carrier types. Thus, at high temperatures, the electronic contribution is difficult to obtain and the commonly employed single band model (majority carrier κ_e only) results in an artificially high value of κ_L (an apparent increase in κ_L at high T). For this reason, it is best to discuss the estimated κ_L in the region where the single band Lorenz number L , as obtained from $\alpha(T)$, is decreasing (assuming τ is limited by acoustic phonon scattering).

For convenience, the primary equations of interest are restated now. The Wiedemann-Franz relationship states that the electronic contribution from species i is related to the electrical conductivity of species i (σ_i), temperature T , and the corresponding Lorenz number L_i via

$$\kappa_{e,i} = L_i \sigma_i T, \quad (5.15)$$

where, for carriers in a parabolic band experiencing a carrier relaxation time of the form $\tau \propto \epsilon^{\lambda-1/2}$,

$$L = \frac{k^2 (1 + \lambda)(3 + \lambda) F_\lambda(\eta) F_{\lambda+2}(\eta) - (2 + \lambda)^2 F_{\lambda+1}(\eta)^2}{e^2 (1 + \lambda)^2 F_\lambda(\eta)^2}. \quad (5.16)$$

The reader is reminded that $\lambda = 0$ describes acoustic phonon scattering of carriers. The bipolar thermal conductivity is

$$\kappa_b = \frac{\sigma_h \sigma_e}{\sigma} (\alpha_h - \alpha_e)^2 T. \quad (5.17)$$

5.3 $\text{La}_{3-x}\text{Te}_4$

This section is an adapted reproduction, with permission, from *Phys. Rev. B*, **78** 125205 (2008). Copyright 2008, American Physical Society.

The thermal transport in $\text{La}_{3-x}\text{Te}_4$ samples is similar to that in many other heavily doped semiconductors. Specifically, the thermal conductivity is heavily influenced by an electronic contribution κ_e and the lattice contribution κ_L is clearly important. The magnitude of κ_e is directly linked to sample composition because the carrier density is a function of lanthanum content. However, this inherent link between lanthanum vacancy concentration and carrier density results in an additional influence of composition on κ via κ_L , as the crystallographic defects scatter phonons. In this manner, the thermal transport in $\text{La}_{3-x}\text{Te}_4$ is actually rather complex.

The thermal diffusivity of $\text{La}_{3-x}\text{Te}_4$ samples is shown in Figure 5.1a. The values of D_T decrease with increasing T above ~ 600 K for all compositions. An increase in D_T at moderate T is observed in samples with relatively large n_H . While this is not typical of crystalline materials, it can be explained by considering the temperature independent, residual (electronic) resistance.

The calculated values of the specific heat C_P are shown in Figure 5.1b. The specific heat increases with increasing temperature due to an increase in both the anharmonic contributions and the electronic contribution. The compositional dependence shown in Figure 5.1b is due to differences in the electronic contribution C_e . The values of C_e for $\text{La}_{3-x}\text{Te}_4$ were estimated by scaling a calculated value for C_e in La_3Te_4 by the ratio of room temperature Hall carrier density. In the limit of a free electron gas, C_e increases linearly with increasing T and is proportional to the carrier density divided by the Fermi energy[11]. The values of $C_e(T)$ for La_3Te_4 utilized here were taken from Reference [101], where they were calculated from the first-principles band structure reported in Reference [51] and shown in Section 4.3. Low temperature specific heat data confirmed the trend in C_e utilized here to obtain C_P for a range of x values[101].

The assumption that the only compositional dependence in C_P arises due to C_e is not strictly valid. For instance, considering the $3R/\bar{M}$ limit of C_P known as the Dulong-Petit limit, it is observed that a small change in the mean atomic weight \bar{M} occurs as x ranges from zero to one-third. However, this factor only results in a decrease in C_P by $\sim 0.2\%$, and is thus of little concern.

An interesting feature in the $\text{La}_{3-x}\text{Te}_4$ system is a change in the phonon density of states ($pDOS$) with composition. The specific nature of this relationship was discussed at length in Reference [101], and the most critical feature is reviewed here. The phonon density of states were found to *stiffen* with increasing vacancy content. This means that the phonon dispersion shifted to higher energies, and the corresponding Debye temperature increased as x increased. The decrease in carrier density is believed to be responsible for this stiffening. Specifically, a large carrier density (or large $N(E_F)$) reduces the impact of ion displacements by screening the force felt on neighboring ions. As the carrier density decreases, the energy to produce a given displacement increases, and thus the $pDOS$ becomes stiffer. The change in average phonon energy

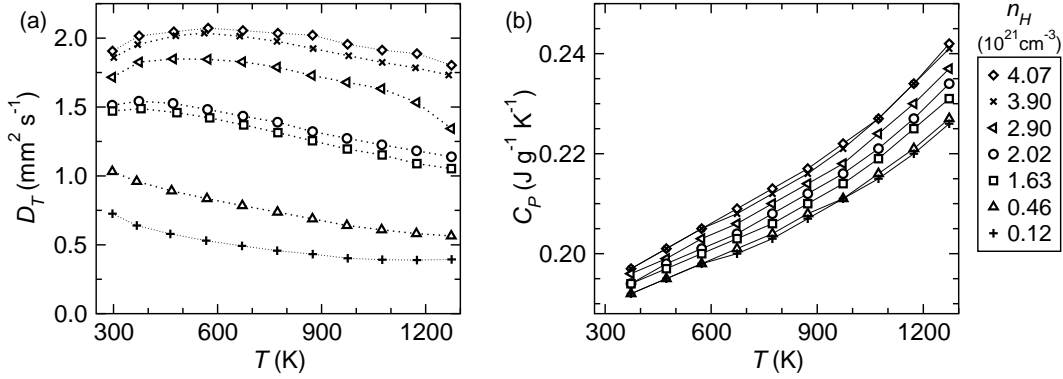


Figure 5.1. Temperature dependence of the (a) experimental thermal diffusivity and (b) calculated heat capacity in $\text{La}_{3-x}\text{Te}_4$ as estimated from data taken on La_3Te_4 [101]. Panel (a) is reprinted (adapted) with permission from *Phys. Rev. B*, **78** 125205 (2008). Copyright 2008, American Physical Society.

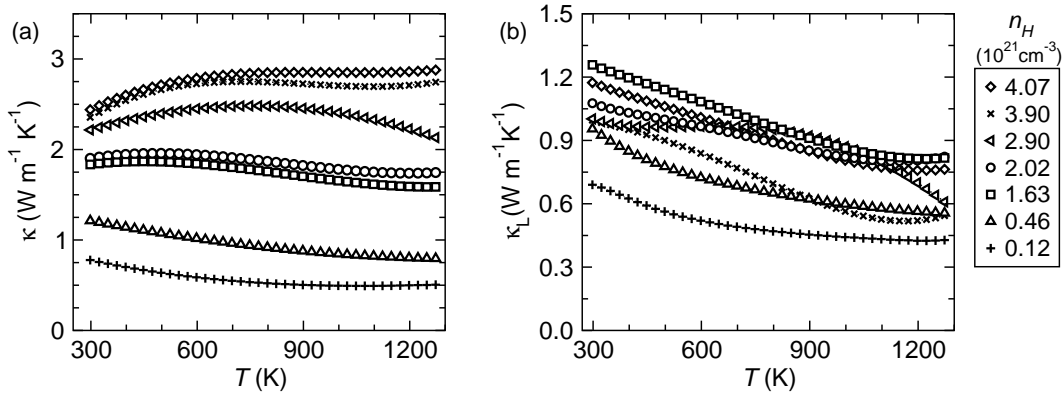


Figure 5.2. Temperature dependence of the (a) total and (b) lattice thermal conductivity in La_3Te_4 . The decrease with increasing T is due to phonon-phonon scattering, while the decrease in κ_L with decreasing n_H is due to increased point defect scattering associated with La vacancies.

with composition does not significantly alter C_P at high temperatures. Therefore, to first order, the values of C_P shown in Figure 5.1b provide an accurate description of the true C_P .

The total thermal conductivity is shown in Figure 5.2a, and the corresponding lattice contribution is shown in Figure 5.2b. In general, both κ and κ_L decrease with increasing T and increasing x . The decrease in κ_L with increasing T is expected for crystalline materials due to increased phonon-phonon interactions as temperature increases. This feature was discussed in Section 5.2. The decrease in κ with increasing x is expected, as this is primarily due to a decrease in the electronic contribution κ_e . The Lorenz values utilized to obtain κ_e are shown in Figure 5.3. It was shown that using the metallic limit (dashed line) results in negative κ_L at high temperatures for $\text{La}_{3-x}\text{Te}_4$ [38].

The decrease in κ_L with decreasing n is not common in semiconductors. In classic semiconductors, such as Si or GaAs, the free carriers are introduced via point defects (dopants) and thus a higher n typically implies a higher level of defects and lower κ_L . Point defects scatter phonons due to a combination of mass contrast and lattice strain. The effect of mass contrast (an additional ΔM of mass above or below matrix

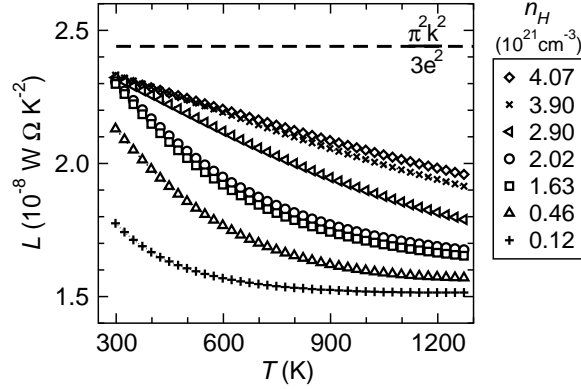


Figure 5.3. Temperature dependence of the calculated Lorenz number in $\text{La}_{3-x}\text{Te}_4$. These values were obtained from the temperature-dependent Seebeck coefficient assuming single parabolic band behavior with electron mobility limited by acoustic phonon scattering. The dashed line indicates the metallic limit, and negative values of κ_L are obtained when this value is employed for data analysis in the $\text{La}_{3-x}\text{Te}_4$ system[38]

atom mass M) is easier to address than is lattice strain. The phonon relaxation time associated with mass contrast scattering is proportional to the mole fraction of impurity atoms (x_I) and the square of the relative mass difference; for a one atom system this simplifies to[143]

$$\frac{1}{\tau_{mass}} = \left(\frac{\Delta M}{M} \right)^2 \frac{V}{x_I} \frac{\omega^2}{4\pi v^3}. \quad (5.18)$$

In $\text{La}_{3-x}\text{Te}_4$, a high defect concentration corresponds to a low carrier density, and thus one expects κ_L to decrease as x increases (n decreases). This phonon scattering is strong due to the large mass contrast associated with the vacancy point defect, as implied by the behavior of τ_{mass} in Equation 5.18. Also, large mol fractions of vacancies are possible, as up to one-ninth of lanthanum atoms can be vacant. The decrease of κ_L with decreasing n is observed in Figure 5.2b. Some irregularities are observed, likely due to small errors in measuring the three properties required to obtain κ_L , though the single band model is not strictly valid. Recall $\alpha(T)$ is utilized to obtain the temperature-dependent chemical potential, and $\kappa(T)$ and $\sigma(T)$ are also used in the calculation as well. Also, some of the unusual behavior in Figure 5.2b is associated with the estimation of C_P , which possesses error due to the complicated electronic and vibrational spectrums in this system. Regardless, the expected trends are observed as κ_L generally decreases with both T and n_H .

The stiffening of the $pDOS$ discussed above can also have significant impact on κ_L . The increase in Θ_D with decreasing n_H implies an increase in the speed of sound with increasing vacancy concentration. The value of κ_L is greatly influenced by the speed of sound, as discussed in Section 5.2. The expected increase in κ_L due to increasing Θ_D may be offset by the decrease in κ_L associated with point defect scattering. Thus, the contributions of these two factors are extremely difficult to estimate. The phonon density of states did reveal significant peak broadening at high x , which is likely due to the scattering of phonons by vacancies[101].

The scattering of phonons by electrons is common in metals at low temperatures. Isolating this interaction

is very difficult, and generally requires low temperature thermal conductivity data. In the case of $\text{La}_{3-x}\text{Te}_4$, this scattering seems plausible due to the large carrier density that can be achieved, as well as the transition to a superconducting state at low T . The presence of superconductivity at large n implies strong electron-phonon coupling, which is enhanced by the large effective mass (large $N(E_F)$). However, the presence of defect scattering by vacancies and the stiffening in the $pDOS$ severely complicates the study of electron-phonon coupling in $\text{La}_{3-x}\text{Te}_4$. This feature is discussed in more detail in Section 5.3.2 where nominally vacancy free samples were utilized to probe the possibility of electron-phonon interactions at high T .

5.3.1 $\text{La}_{3-x-y}\text{Yb}_y\text{Te}_4$

This Section is reprinted with permission from *Chem. Mater* **22**, 2995 (2010). Copyright 2010 American Chemical Society.

The thermal diffusivity and thermal conductivity of Yb containing lanthanum telluride samples are shown in Figure 5.4. The thermal conductivity decreases with increasing temperature and decreasing n_H (Fig. 5.4b), as was observed in the $\text{La}_{3-x}\text{Te}_4$ samples. This is generally due to the increasing phonon-phonon interactions and the decreasing electronic contribution to κ , respectively.

The dependence of thermal conductivity on n_H is shown in Figure 5.5 (at 1000 K). The decrease in κ with decreasing n_H is common for semiconductors due to the decrease in the electronic contribution κ_e , which is proportional to the electrical conductivity. However, it is once again observed that even the lattice thermal conductivity κ_L decreases with decreasing n_H . The decrease in κ_L for $\text{La}_{3-x}\text{Te}_4$ is due to increasing point defect scattering as the La vacancy concentration increases.[38] The Yb substitution results in an additional point defect scattering, albeit with the filling of some vacancies, and thus the dependence of κ_L on n_H is similar in the Yb containing samples.

As before, the lattice thermal conductivity was obtained by using a single parabolic band model to estimate the Lorenz number under the assumption that acoustic phonon scattering limits the carrier mobility. The Wiedemann-Franz relationship is then utilized to estimate κ_e , which is subtracted from κ to obtain κ_L . [38]

The data shown in Figures 5.4 and 5.5 thus confirms that Yb can be utilized to control the carrier density in $\text{La}_{3-x}\text{Te}_4$ while maintaining the desirably low κ_L that makes $\text{La}_{3-x}\text{Te}_4$ a prime candidate for thermoelectric application.

5.3.2 $\text{La}_{3-x}\text{Te}_{4-z}\text{Sb}_z$ and $\text{La}_{3-x}\text{Te}_{4-z}\text{Bi}_z$

This section is an adapted reproduction, with permission, *Phys. Rev. B*, **81**, 125205 (2010). Copyright 2010, American Physical Society.

The thermal diffusivity and conductivity of nominal $\text{La}_{3-x}\text{Te}_{4-z}\text{Sb}_z$ and $\text{La}_{3-x}\text{Te}_{4-z}\text{Bi}_z$ are shown as a function of temperature in Figure 5.6. For moderate temperatures, all samples behave similarly and D_T and κ generally decrease with increasing T and decreasing n_H . At high temperatures, D_T and κ rise in the

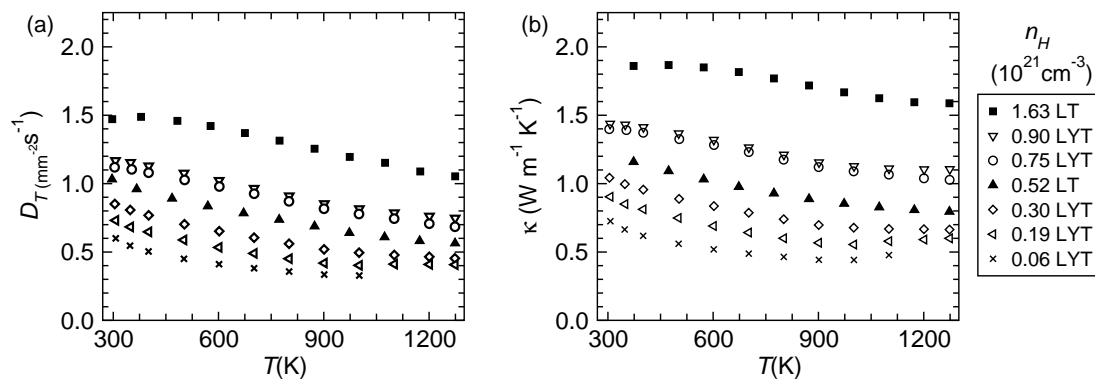


Figure 5.4. Temperature dependence of the (a) thermal diffusivity and (b) thermal conductivity in $\text{La}_{3-x-y}\text{Yb}_y\text{Te}_4$ (LYT, open markers), and two $\text{La}_{3-x}\text{Te}_4$ (LT, filled markers) data sets are shown for comparison. The legend provides the room temperature Hall carrier concentrations.

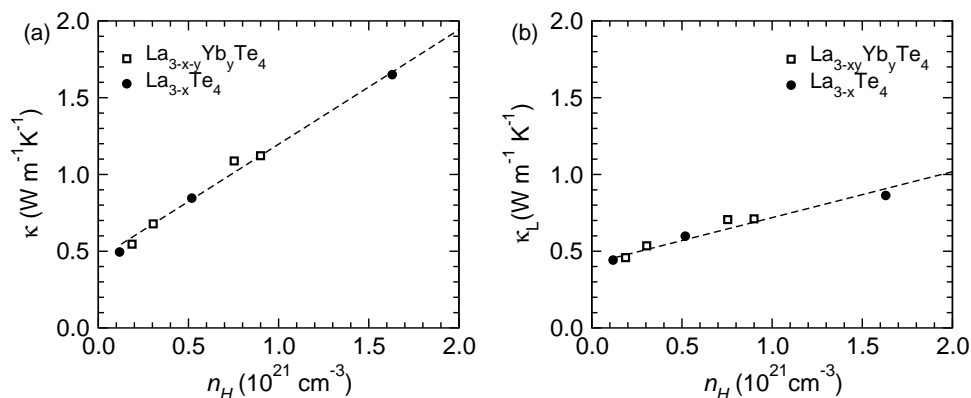


Figure 5.5. The dependence of thermal conductivity at 1000 K on room temperature Hall carrier density in $\text{La}_{3-x-y}\text{Yb}_y\text{Te}_4$ samples is similar to that $\text{La}_{3-x}\text{Te}_4$ samples. Total thermal conductivity is shown in panel (a), and (b) shows the lattice thermal conductivity. The decrease of κ_L represented by the visual guide (dotted line) is associated with point defect scattering (increasing vacancy or Yb concentration). Reprinted with permission from *Chem. Mater* **22**, 2995 (2010). Copyright 2010 American Chemical Society.

samples containing Bi (open triangles) or large amounts of Sb. This is due to the thermal excitation of charge carriers across the energy gap, which is facilitated by Sb (Bi) substitution due to the reduction of the energy gap. The heat capacity utilized to obtain κ increases (nearly linearly) with increasing T , and thus κ mimics D_T . In the absence of heat capacity data for all compositions, the values of C_P were taken from Reference [101] for La_3Te_4 and recalculated to account for reduced electronic contribution, as done for $\text{La}_{3-x}\text{Te}_4$ and $\text{La}_{3-x-y}\text{Yb}_y\text{Te}_4$. While some changes in C_P with elemental substitution are expected due to changes in average atomic mass, these effects are estimated to be less than 7% for the Bi compounds (a decrease in C_P is expected), and less than 1% for the Sb compounds (an increase in C_P is expected) for complete substitution ($z = 1$).

As discussed in Sections 4.2 and 5.2, the lattice thermal conductivity (κ_L) is estimated via the Wiedemann-Franz relationship within the limitations of a single band approximation, from which the Lorenz number L

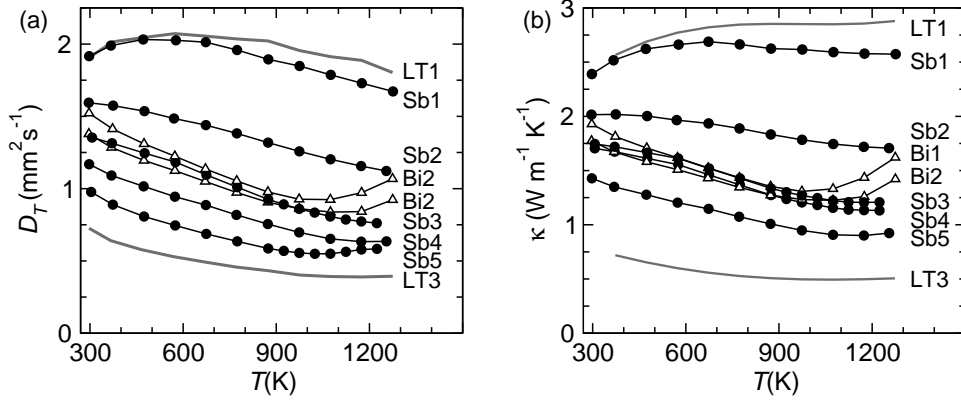


Figure 5.6. The (a) thermal diffusivity and (b) thermal conductivity decreases with decreasing carrier concentration (increasing Sb content) and increasing temperature. The thermal activation of carriers increases D_T and κ at high temperature, and is observed in the Sb and Bi containing samples because these elemental substitutions lead to a reduced energy gap. Reprinted (adapted) with permission from *Phys. Rev. B*, **81**, 125205 (2010). Copyright 2010, American Physical Society.

is obtained via common solution to the Boltzmann transport equation. This approach assumes the energy dependence of τ can be modeled by simple power law ($\tau \propto \epsilon^{\lambda-1/2}$), which is typically most valid when one scattering mechanism limits the carrier mobility. Acoustic phonon scattering ($\lambda = 0$) appears to limit μ for low Sb content. For large Sb content, one could argue that ionized impurity scattering limits the carrier mobility at low or moderate T . Fortunately, at large Sb content, κ_e is small regardless of the scattering assumption and thus the trends observed are not strongly dependent on the choice of scattering mechanism. To demonstrate the minor influence of λ on κ_L , the values of κ_L obtained from the limiting assumptions of $\lambda = 0$ ($L \leq 2.44 \times 10^{-8} \text{ V}^2 \text{ K}^{-2}$) and $\lambda = 2$ ($L \geq 2.44 \times 10^{-8} \text{ V}^2 \text{ K}^{-2}$) are compared in Figures 5.7a,b. Due to the small influence of L for the low σ compounds, the calculation of L for the case of ionized impurity scattering has been simplified by assuming that b defined by Equation 4.15 is independent of carrier energy and thus $\lambda = 2$ can be utilized in Equation 4.49. Recall the necessary $\eta(T)$ is obtained from $\alpha(T)$.

The lattice thermal conductivity is plotted versus the electrical conductivity in Figure 5.7a, where data at 573 K are shown. The increase in κ_L as σ decreases may be linked to a decrease in electron-phonon interactions, the strength of which increase with increasing carrier mass[144, 145]. According to Pippard[145], when perfectly free electrons scatter acoustic phonons, the phonon mean free path l_{e-p} scales as

$$l_{e-p} \propto \frac{dv_s^2}{nm^*v_f}, \quad (5.19)$$

where d is the density and v_f and v_s are the Fermi and mean sound velocities, respectively. This suggests that, if electron-phonon interactions limit κ_L , the value of κ_L should decrease as carrier density n increases. For the current system, a decrease in n generally leads to a decrease in m^* due to the multiband features shown in Figure 4.11. Pippard's theory differs somewhat from that presented by Ziman for l_{e-p} , though the same n dependence is observed in the $T \rightarrow \infty$ limit[144]. In general, these theories do not predict the scattering of

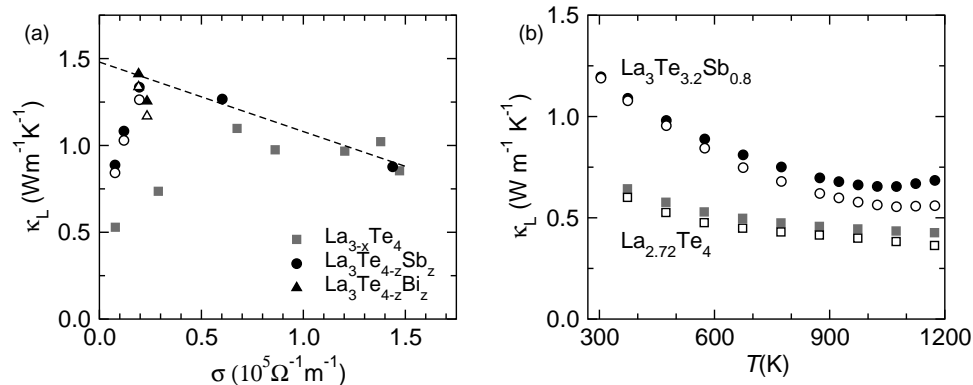


Figure 5.7. (a) The lattice thermal conductivity as a function of electrical conductivity at 573 K in pure and Sb(Bi) containing lanthanum telluride. For moderately large σ , κ_L increases as σ decreases (dashed line is a visual guide). This may be evidence for electron-phonon coupling, though the phonon group increases as σ decreases. At low σ , κ_L is reduced by point defect scattering, where the ability of vacancies to scatter phonons is highlighted. (b) The lattice thermal conductivity as a function of temperature reveals the temperature dependence expected for crystalline materials in *Sb5*, which is consistent with the reduced number of vacancies. The high concentration of vacancies in *LT3* promotes a lower κ_L with less temperature dependence. In both panels, the filled symbols represent data obtained assuming acoustic phonon scattering limits μ and open symbols are for data obtained assuming ionized impurity scattering limits μ . Reprinted (adapted) with permission from *Phys. Rev. B*, **81**, 125205 (2010). Copyright 2010, American Physical Society.

phonons by electrons at moderate or high T , where the energy scales are unfavorably, and thus this effect is expected to be small compared to Umklapp scattering (based on traditional theory).

Electron-phonon interactions are not the only explanation for the trends observed in Figure 5.7a. Calorimetry and inelastic neutron scattering have suggested the Debye temperature in $\text{La}_{3-x}\text{Te}_4$ increases by roughly 20% from $x=0$ to $x = \frac{1}{3}$ [101]. This is believed to be due to the decrease in carrier concentration and the corresponding decrease in density of states at the Fermi level (reduction in ion displacement screening), and thus this effect should be relatively similar in the $\text{La}_3\text{Te}_{4-z}\text{Sb}_z$ compounds where carrier concentration is reduced with Sb substitution. This feature is likely to be hidden in $\text{La}_{3-x}\text{Te}_4$ samples due to the strong scattering of phonons by vacancies as n decreases.

From kinetic theory, the lattice thermal conductivity is proportional to v_s (which is proportional to the Debye temperature) and thus the 20% change in Debye temperature can explain much of the change in κ_L shown in Figure 5.7a. Approximately a 4% reduction in C_P is expected when z increases from 0 to 1 due to a reduction in the electronic contribution (at 573 K), and less than a 1% increase is expected from the reduction in average atomic mass (for the Sb containing compounds).

In Figure 5.7a, it is observed that point defect scattering significantly reduces κ_L at low σ . This makes physical sense, as low σ samples have large La vacancy content (for pure $\text{La}_{3-x}\text{Te}_4$) or high Sb concentrations. In $\text{La}_{3-x}\text{Te}_4$, an $\sim 50\%$ reduction in κ_L occurs as x increases from roughly 0 to 0.3, which demonstrates the strong scattering of phonons by vacancies. The reduction in κ_L at low σ and large Sb content appears faster than expected for point defect scattering by Sb ions alone (very little mass contrast to scat-

tering phonons), and thus the data suggests an additional scattering source is present. Additional phonon scattering may arise due to local inhomogeneity or differences in microstructure that are related to changes in the synthesis due at high Sb (Bi) concentration. Also, if La_4Sb_3 forms or anionic Sb sits on cationic La sites, additional phonon scattering would likely be observed. We note that the vacancy concentration inferred from Hall data and electron counting (assuming complete Sb substitution) suggests the vacancy concentration is fairly independent of Sb content, and thus vacancy formation is not utilized to explain the results at high Sb content.

The strong scattering of phonons by lanthanum vacancies leads to a nearly temperature independent κ_L in sample *LT3* (nominal $\text{La}_{2.72}\text{Te}_4$), see Figure 5.7b. In nominal $\text{La}_3\text{Te}_{3.2}\text{Sb}_{0.8}$, the reduced number of vacancies increases the effective crystallinity (reduces point defect scattering of phonons), thereby increasing κ_L and promoting the usual decrease in κ_L with increasing T ($\sim T^{-1}$) expected for a crystalline material at high T . The temperature dependence of κ_L for the samples containing Sb leads to low κ_L at high T , thus allowing large thermoelectric performance to be achieved.

5.4 $\text{Ba}_8\text{Ga}_{16-x}\text{Ge}_{30+x}$

This section is an adapted reproduction, with permission, from *Phys. Rev. B*, **80**, 125205 (2009). Copyright 2009, American Physical Society.

The thermal diffusivity for n -type $\text{Ba}_8\text{Ga}_{16-x}\text{Ge}_{30+x}$ is shown in Figure 5.9a. The values of D_T decrease with decreasing n and temperature, for $T < 800$ K. An unusual (sudden) decrease in D_T is observed in samples *A* – *C*, which is most readily observed in sample *A* near 650 K. Additional D_T data were taken for sample *A* using 10 K increments, and the event appears to occur continuously.

The high-temperature specific heat capacity is shown in Figure 5.9c. The C_P data reported here are consistent with low temperature data from in the literature[79], an estimate of which is shown as a solid line in Figure 5.9c below 300 K. Also, the room temperature specific heat is found to be approximately equal to the value obtained using the method of Dulong-Petit (dashed line, 0.3065 J/g/K), and thus the C_P reported is physically reasonable. At moderate T , C_P increases linearly with increasing temperature, presumably due to an increase in the anharmonic and/or electronic contributions. The linear temperature dependence is lost at roughly 650 K, where an event occurs and C_P increases abruptly. Above this event, C_P appears to be independent of temperature, and a value of 0.361 J/g/K is utilized to draw the solid line in Figure 5.9c between 675 and 1000 K. The exact high T behavior and the compositional dependence of this ‘transition’ are unknown. These features are not addressed in the literature, and their origin remains unknown. The linear fit from 300 to 675 K ($C_P = 7.8 \times 10^{-5} T + 0.28$ in J/g/K) followed by a constant value of 0.361 J/g/K was utilized to calculate κ for all compositions.

The temperature dependence of $\kappa = D_T C_P d$ is shown in Figure 5.9c. The decrease in κ with decreasing n and increasing T is expected for a doped, crystalline semiconductor. A clear increase in κ associated

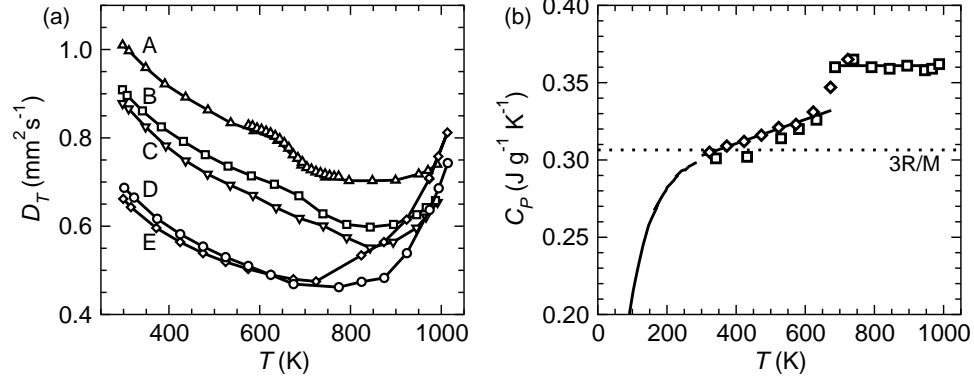


Figure 5.8. (a) The thermal diffusivity of n -type $\text{Ba}_8\text{Ga}_{16-x}\text{Ge}_{30+x}$ shows the expected temperature dependence at moderate T . Above 650 K, sudden decreases in D_T are observed. This is most readily seen in the data for sample A, where D_T was collected in smaller T intervals to examine this behavior. (b) The temperature-dependent specific heat also reveals a transition. At moderate T , the data collected for this study (markers) are consistent with the low temperature C_P reported by Sales et al.[79] and the simple Dulong-Petit model ($3R/M$). Reprinted (adapted) with permission from *Phys. Rev. B*, **80**, 125205 (2009). Copyright 2009, American Physical Society.

with the event in C_P is observed near 675 K, which is indicated by the dashed line in Figures 5.9. At high temperatures, the thermal excitation of charge carriers leads to an increase in κ via an increased electronic contribution. The electronic component of the thermal conductivity (κ_e) has contributions from electrons, holes, and the bipolar conductivity (κ_b).

The lattice contribution to the thermal conductivity is shown in Figure 5.9b, where no compositional dependence is observed. As discussed in Section 4.2.8, the values of κ_L are calculated from $\kappa_L = \kappa - \kappa_e$, where κ_e is estimated via the Wiedemann-Franz relationship ($\kappa_e = LT/\rho$). The Lorenz number L is calculated by employing a single parabolic band model, and the carrier mobility is assumed to be limited by acoustic phonon scattering ($\lambda=0$). The values of L obtained from this method are most accurate for moderate temperatures (before intrinsic carrier activation is observed), which is the region in Figure 5.9b where L decreases with increasing T . At higher T , this approximation breaks down and the estimated κ_L begins to increase because κ_b is not included in the single band definition of L .

Here, the carrier mobility is assumed to be limited by acoustic phonon scattering ($\lambda=0$) and the reduced Fermi energy η is obtained as a function of temperature from the experimental Seebeck coefficients using Equation 4.29.

Also shown in Figure 5.9b is the theoretical value of the minimum lattice thermal conductivity, κ_{min} . Consistent with the observed κ_L , the theoretical κ_{min} shows little compositional dependence (the calculation is for samples A and E). At moderate temperatures, κ_L approaches κ_{min} . Thus, even though $\text{Ba}_8\text{Ga}_{16-x}\text{Ge}_{30+x}$ demonstrates crystalline-like thermal conductivity, the absolute value of κ_L appears to approach the amorphous limit at high temperatures (in the absence of κ_b). The values of κ_{min} were obtained using Cahill's formulation[141], which is shown in Equation 5.11.

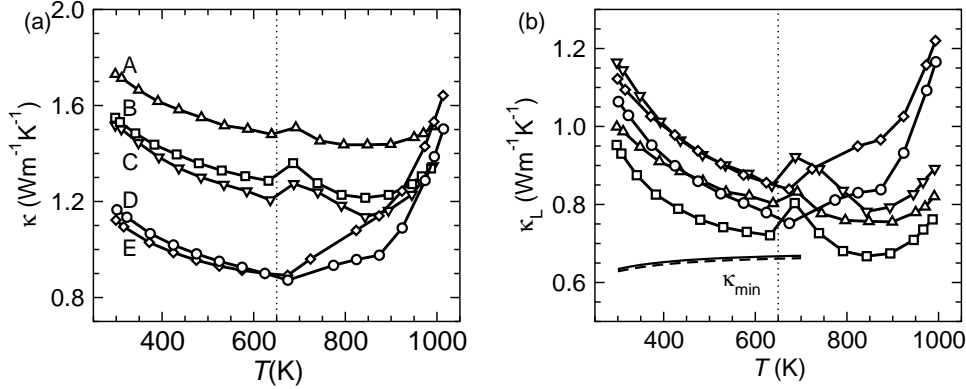


Figure 5.9. a) Total thermal conductivity and (b) lattice thermal conductivity versus temperature. κ_L does not reveal any trend with composition, and approaches the theoretical κ_{min} (solid and dashed curves for samples A and E) before the estimated κ_L begins to increase due to the unaccounted bipolar contribution at high T (the increase is an artifact of the analysis). A clear increase in κ associated with the abrupt increase in C_P can be observed (marked by dotted curve). Reprinted (adapted) with permission from *Phys. Rev. B*, **80**, 125205 (2009). Copyright 2009, American Physical Society.

The lattice thermal conductivity decreases with increasing T for moderate temperature, suggesting κ_L decreases due to an increase in phonon-phonon scattering with rising temperature. In a crystalline material, κ_L should decay as T^{-1} when phonon-phonon scattering limits the phonon mean free path, but κ_L remains finite at high temperatures (hence κ_{min}). Thus, for phonon-phonon scattering alone, the physical description of high-temperature thermal transport in a crystalline material is $\kappa_L = \kappa_{min} + \kappa_0/T$ and the κ_{min} term is important when it is comparable to κ_0/T . The data shown in Figure 5.9b are well described by such behavior (before the onset of bipolar conduction at high T), and fitting results in $\kappa_{min} \sim 0.56(0.06) \text{ Wm}^{-1}\text{K}^{-1}$ and $\kappa_0 = 150(30) \text{ Wm}^{-1}$ with standard deviations given in parenthesis. Note the good agreement between the value of κ_{min} obtained via this method and that from Equation 5.11 ($\sim 0.66 \text{ Wm}^{-1}\text{K}^{-1}$). Therefore, the high-temperature κ_L behavior in $\text{Ba}_8\text{Ga}_{16-x}\text{Ge}_{30+x}$ is likely determined by phonon-phonon interactions (assuming the bipolar thermal conductivity is accounted for). The low temperature thermal transport is in agreement with this conclusion, as κ_L of n -type $\text{Ba}_8\text{Ga}_{16-x}\text{Ge}_{30+x}$ increases with decreasing T to roughly 10 K.

It has been shown[83] that the classic definition of the phonon mean free path l is inconsistent with the phonon lifetimes measured via inelastic neutron scattering. The phonon mean free paths are generally obtained via $\kappa_L = (1/3)C_P v l$ (Equation 5.1); note this C_P is in units of J/K/m^3 . Indeed, this equation suggests that l is on the order of 6\AA , which would mean the phonon lifetimes are a fraction of a picosecond ($\sim 0.2 \text{ ps}$). In the case of thermal transport dominated by acoustic phonons, as in κ_L for the $\text{Ba}_8\text{Ga}_{16-x}\text{Ge}_{30+x}$ system, a more appropriate mean free path to consider is that of the acoustic phonons, as these carry most of the heat. In this case, the appropriate definition is $\kappa_L = (1/3)C_{ac} v_{ac} l_{ac}$ (Equation 5.6), where l_{ac} is the mean free path of acoustic phonons and the volumetric specific heat of acoustic phonons is $C_{ac} = C_P/N_a$, where N_a is the number of atoms per primitive cell. Using this equation, and the data shown in Table 5.1, it appears that the

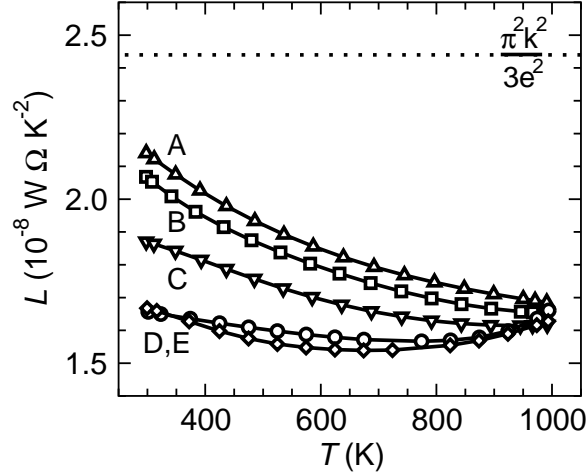


Figure 5.10. The calculated Lorenz numbers versus T in $\text{Ba}_8\text{Ga}_{16-x}\text{Ge}_{30+x}$ are significantly lower than the metallic limit, which is represented by the dashed line. Data were generated assuming acoustic phonon scattering limits μ . Reprinted (adapted) with permission from *Phys. Rev. B*, **80**, 125205 (2009). Copyright 2009, American Physical Society.

Table 5.1. Room temperature ultrasonic data and calculated properties of $\text{Ba}_8\text{Ga}_{16-x}\text{Ge}_{30+x}$ samples. Reprinted with permission from *Phys. Rev. B*, **80**, 125205 (2009). Copyright 2009, American Physical Society.

Sample	v_L m/s	v_t m/s	v_m m/s	$\kappa_{L,exp}$ W/m/K	$\kappa_{L,theory}$ W/m/K	Θ_D K	γ -
A	4500	2690	2970	1.0	2.1	311	1.62
E	4510	2630	2920	1.1	1.9	306	1.55

low κ_L in $\text{Ba}_8\text{Ga}_{16-x}\text{Ge}_{30+x}$ is largely a result of the suppression of the volumetric specific heat of acoustic phonons due to the large unit cell. This formalism leads to $l_{ac} \sim 300 \text{ \AA}$, which corresponds to phonon lifetimes near 10 ps, which are larger than those obtained via neutron scattering. Clearly, as discussed in Reference [83], the microscopic representation of the kinetic theory (Equation 5.3) should be utilized.

At high temperature, κ_L appears to increase, but this is an artifact of the above analysis because the bipolar thermal conductivity (κ_b) is not included. The bipolar thermal conductivity arises when both holes and electrons are present and contributing significantly to the electrical conductivity [138]; the common expression for κ_b is shown in Equation 4.50. In Figure 5.9a, the increase of κ at high T is observed to be most significant for samples with lower n_H . This is in agreement with the basic theory for κ_b and thus we believe κ_b is the primary source for increased κ at high T , as opposed to a contribution from optical phonons.

Alternatively, κ_L can be estimated from a plot of κ versus $1/\rho$ for various samples at a particular temperature. This method assumes $\kappa = \kappa_L + LT/\rho$. Performing this task yields $\kappa_L = 1.1 \text{ Wm}^{-1}\text{K}^{-1}$ and $L = 1.78 \times 10^{-8} \text{ W}\Omega\text{K}^{-2}$ at 300 K, and the change with increasing temperature occurs as expected: at 500 K this approach yields $\kappa_L = 0.88 \text{ Wm}^{-1}\text{K}^{-1}$ and $L = 1.73 \times 10^{-8} \text{ W}\Omega\text{K}^{-2}$.

In Table 5.1, speed of sound corresponding to the longitudinal (v_L) and transverse (v_t) modes are provided for samples A and E. The similarity in v_L for the two different samples suggests the elastic constant C_{11}

does not vary much with composition, and thus a composition-dependent C_{11} cannot explain the lower than expected Hall mobility in sample D (see Section 4.4). Also shown in Table 5.1 are experimental and theoretical values for κ_L , as well as the calculated Debye temperatures (Θ_D) and Grüneisen parameters (γ) for these samples (at 300 K, calculated using equations in Reference [142]). The theoretical κ_L is calculated utilizing Slack's formulation (Equation 5.9)[142]. The moderate agreement between experimental and theoretical κ_L is acceptable for such a simple theory, which only considers thermal resistance from Umklapp processes. To calculate the Grüneisen parameter[142], a thermal expansion coefficient of $1.5 \times 10^{-5} K^{-1}$ is selected, which is an average of the reported values[75, 86]. The Debye temperatures in Table 5.1 are consistent with those in the literature[79, 83].

As shown in Figure 5.10, the Lorenz numbers utilized to determine κ_L are significantly smaller than the metallic limit of $2.44 \times 10^{-8} W\Omega K^{-2}$, which is shown as the dashed line in Figure 5.10. As expected, the calculated L values decrease with increasing temperature (due to decreasing η), and at high temperatures L rises due to the failure of a single band model (the calculated η rises). The simplest analysis for κ_e utilizes the metallic limit for L , which commonly overestimates the electronic contribution and leads to reduced κ_L . For example, at ~ 800 K the value of κ_L for sample A is ~ 0.49 W/m/K using the metallic limit of L and ~ 0.76 W/m/K using $L \sim 1.75 \times 10^{-8} W\Omega K^{-2}$ (obtained from single band analysis). Of course, there are cases where L is greater than the metallic limit, but this generally requires the carrier mobility to be limited by ionized impurity scattering. Therefore, the literature values for κ_L are often an underestimation of the true values, which can lead to improper conclusions regarding appropriate methods for further optimization of thermoelectric efficiency.

5.5 SrZnSb₂ and SrZn₂Sb₂

This section is an adapted reproduction, with permission, from *J. Appl. Phys.*, **106** 013706 (2009). Copyright 2009, American Institute of Physics.

The thermal conductivity shown in Figure 5.11a is calculated as the product of the density d , thermal diffusivity D_T , and heat capacity C_P , the latter of which is estimated using the method of Dulong-Petit. $C_P=0.252$ J/g/K for SrZnSb₂, and $C_P=0.270$ J/g/K for SrZn₂Sb₂. As seen in Figure 5.11a, the thermal conductivity of SrZnSb₂ is relatively independent of temperature. Specifically, the value of κ initially decreases with increasing temperature, and then rises for $T > 500$ K. The lattice contribution shown in Figure 5.11b is estimated by $\kappa_L = \kappa - \kappa_e$. The electronic contribution is obtained from the Wiedemann-Franz relationship, $\kappa_e = L\sigma T$, where the Lorenz number L is calculated using a single band model with carrier mobility limited by acoustic phonon scattering[4]. For SrZnSb₂, the calculation of L yields values between 2.35 and $2.19 \times 10^{-8} W\Omega K^{-2}$ for T between 300 and 675 K, respectively, which is consistent with the 'metallic' nature of SrZnSb₂.

The estimation of κ_L reveals a significant contribution to κ from κ_e , as expected for materials with low

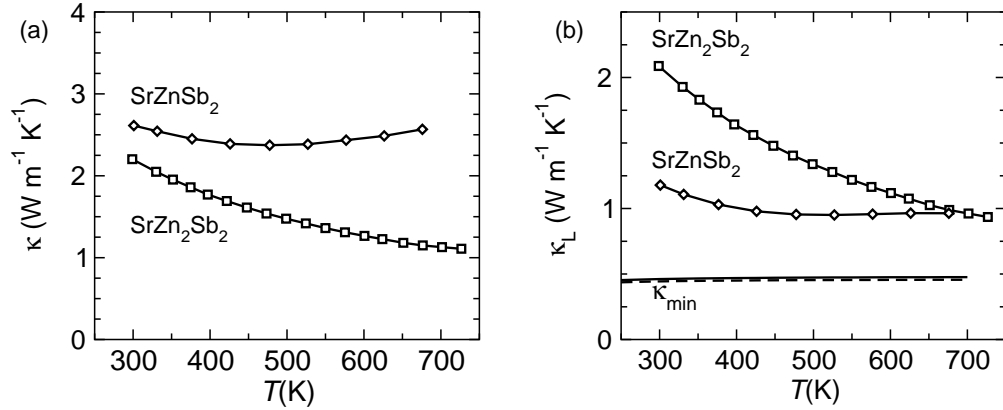


Figure 5.11. Temperature dependence of the (a) total and (b) lattice thermal conductivity in the Sr-Zn-Sb systems. κ_L is significantly lower in SrZnSb₂ at moderate temperature, likely due to the larger number of atoms per unit cell promoting the formation of low-velocity, optical phonons. Both compounds are found to have a similar minimum thermal conductivity due to their similar sound velocities, as observed in Table 5.2. Reprinted (adapted) with permission from *J. Appl. Phys.*, **106** 013706 (2009). Copyright 2009, American Institute of Physics.

ρ . In Figure 5.11b, the value of κ_L for SrZnSb₂ is observed to decrease with increasing temperature up to roughly 500 K, where it remains at ~ 1 W/m/K. A decrease in κ_L with increasing temperature is expected for crystalline materials (T^{-1} decay due to an increase in phonon-phonon scattering for the acoustic modes), while temperature independent κ_L is typically observed in disordered systems.

The plateau above 500 K does not suggest that SrZnSb₂ has glass-like thermal conductivity at high T . At high temperatures, κ_e possesses additional contributions due to the thermal excitation of charge carriers across the band gap. In particular, the bipolar thermal conductivity (κ_b) can occur when both holes and electrons are present. The value of κ_b cannot be determined without knowledge of the electronic properties of both carrier types. We expect κ_b to be significant at high temperature in SrZnSb₂ due to the large increase in n_H , which suggests holes and electrons are thermally activated. The net result is an overestimation of κ_L , particularly at high temperatures, and thus the temperature independent κ_L estimated in Figure 5.11b is likely an artifact of the analysis.

As shown in Figure 5.11b, the lattice thermal conductivity of SrZnSb₂ is roughly one-half that of SrZn₂Sb₂ at 300 K. For most of the temperatures examined, κ_L for SrZnSb₂ is significantly lower than that of SrZn₂Sb₂. The values of κ_L converge at high T , likely due to the crystalline-like decay (T^{-1}) of κ_L in SrZn₂Sb₂ and the presence of κ_b in SrZnSb₂. Due to the complexity of transport at high T in SrZnSb₂, only the room temperature properties are considered in further detail. Furthermore, significant variations from the estimated values of C_P are not expected at room temperature.

Sound velocities are utilized to estimate the mean phonon group velocity (v_m), Debye temperature (Θ_D), and average acoustic phonon mean free path (l_{ac}), which is discussed below. The room temperature data is summarized in Table 5.2, where it is shown that the two compounds have very similar v_m and Θ_D , which was estimated via Equation 5.4. The values of v_l and v_t are also used to estimate the minimum value of the

thermal conductivity (κ_{min}) with Cahill's formulation for amorphous materials (Eqn. 5.11)[141].

Within Cahill's model, both compounds are predicted to have very similar κ_{min} (lower curves in Figure 5.11b), which is roughly one-half of the κ_L observed at high T . The values of V employed here are obtained from References [146, 147]. When utilizing Slack's formulation for κ_{min} (including the optical contribution)[142], a smaller $\kappa_{min} = 0.28 \text{ Wm}^{-1}\text{K}^{-1}$ is calculated for SrZnSb_2 while $\kappa_{min} = 0.45 \text{ Wm}^{-1}\text{K}^{-1}$ for SrZn_2Sb_2 ; the difference is due to a smaller acoustic contribution for SrZnSb_2 (related to number of atoms per unit cell).

When thermal transport is governed by acoustic phonons, such as implied by the temperature dependence of κ_L , it is more appropriate to consider average properties of the acoustic modes. The mean free path of acoustic phonons is then obtained from Equation 5.6.

From this formulation, and the summary of results in Table 5.2, it is observed that the ratio of the specific heat of acoustic phonons (in J/gm^3) is

$$\frac{(C_{ac})_{\text{SrZnSb}_2}}{(C_{ac})_{\text{SrZn}_2\text{Sb}_2}} \approx 0.3,$$

but the ratio of (acoustic) mean free paths is

$$\frac{l_{ac, \text{SrZnSb}_2}}{l_{ac, \text{SrZn}_2\text{Sb}_2}} \approx 1.9.$$

Therefore, the reduced κ_L in SrZnSb_2 is likely associated with a decrease in the relative ability of acoustic phonons to carry heat, or the increased number of optical modes, which have low group velocity. If the classic definition of a average phonon mean free path is utilized (C_P in place of C_{ac} , Eqn. 5.1), the average mean free path of SrZnSb_2 would be calculated to be roughly a factor of two smaller than that of SrZn_2Sb_2 and both mean free paths would be roughly an order of magnitude smaller than those reported in Table 5.2.

From a structural point of view, the larger unit cell of SrZnSb_2 results in reduced κ_L via a reduction in the volumetric specific heat of heat carrying phonons. According to Slack, when only acoustic phonons contribute to the thermal transport, the thermal conductivity is proportional to $N_a^{-2/3}$ (Eqn 5.9)[139]. The trends observed here are in agreement with this theoretical prediction, provided γ does not vary much between the two compounds. Specifically, when $\gamma = 2$ is assumed, Equation 5.9 yields $\kappa_L = 1.78 \text{ Wm}^{-1}\text{K}^{-1}$ for SrZnSb_2 and $\kappa_L = 3.56 \text{ Wm}^{-1}\text{K}^{-1}$ for SrZn_2Sb_2 . The main difference is the value of N_a , with a ratio suggested by Slack's model of $(N_{a, \text{SrZnSb}_2}/N_{a, \text{SrZn}_2\text{Sb}_2})^{-2/3} = (16/5)^{-2/3} = 0.46$, and thus unit cell size can explain the observed trends in κ_L . The relationship between κ_L and unit cell size (a loose description of the number of atoms per unit cell) in Sb-containing compounds was discussed in a recent review article[27].

The role of optical phonons complicates this comparison some, as the increased number of atoms per unit cell in SrZnSb_2 leads to more optical modes than in SrZn_2Sb_2 . Optical phonons may carry heat, however in these compounds the mass ratios are greater than one (between 1.3 and 1.9) and thus optical modes are not expected to contribute significantly to thermal transport[139]. Also, optical modes can promote thermal resistance through the annihilation of acoustic phonons: *acoustic* + *acoustic* \rightarrow *optic*[140]. Therefore, the

Table 5.2. Room temperature properties of SrZnSb₂ and SrZn₂Sb₂. Reprinted (adapted) with permission from *J. Appl. Phys.*, **106** 013706 (2009). Copyright 2009, American Institute of Physics

compound	n_a at./cell	κ_L W/m/K	v_l m/s	v_t m/s	v_m m/s	Θ_D K	l_{ac} Å	C_{ac} J/g/K
SrZnSb ₂	16	1.2	3540	2040	2270	222	170	0.0157
SrZn ₂ Sb ₂	5	2.1	3750	2010	2240	222	91	0.0540

small amount of heat carried by the optical phonons may be offset by an associated scattering of the acoustical modes.

Structural features must also be considered as a source for low κ_L in SrZnSb₂. The infinite chains of Sb may be flexible and/or have large thermal parameters that promote phonon scattering. Also, the similarity in a and b lattice parameters may allow the frequent production of twin boundaries, which would also promote phonon scattering. This feature is currently being investigated by transmission electron microscopy via collaboration with Øystein Prytz of the University of Oslo. The point defects (vacancies) associated with hole production are most likely not responsible for reduced κ_L in SrZnSb₂ because large changes in defect concentrations would be expected between SrZn₂Sb₂ and YbZn₂Sb₂ (based on the values of n_H), and these compounds have similar κ_L . The presence of Sb impurity in SrZnSb₂ is not believed to be the source of low κ_L as the SrZn₂Sb₂ samples contained a fairly large quantity of ZnSb impurity. Finally, the scattering of phonons via charge-carriers was determined to be insignificant based on the theory by Ziman. Furthermore, scattering effects are unlikely to be the source for reduced κ_L as l_{ac} for SrZnSb₂ is larger than l_{ac} for SrZn₂Sb₂, which suggests less phonon scattering in SrZnSb₂.

The data reported in Reference [96] suggests a significantly lower κ_L for EuZn₂Sb₂ at high T , but this is calculated using $L = 2.45 \times 10^{-8} \text{ W}\Omega\text{K}^{-2}$, which is the metallic limit that generally overestimates κ_e . Using the same single band model discussed here, κ_L is estimated to be slightly lower in EuZn₂Sb₂ than in SrZn₂Sb₂: κ_L of EuZn₂Sb₂ $\sim 1.8 \text{ Wm}^{-1}\text{K}^{-1}$ at 314 K and $\kappa_L \sim 0.7 \text{ Wm}^{-1}\text{K}^{-1}$ at 713 K (these values correspond to $L = 1.82 \times 10^{-8} \text{ W}\Omega\text{K}^{-2}$ and $1.65 \times 10^{-8} \text{ W}\Omega\text{K}^{-2}$, respectively).

Chapter 6

Thermoelectric Efficiency

6.1 Summary

This chapter examines the thermoelectric performance of the following compounds: the $\text{La}_{3-x}\text{Te}_4$ based materials, the type-I clathrate $\text{Ba}_8\text{Ga}_{16-x}\text{Ge}_{30+x}$, and the layered materials SrZnSb_2 and SrSn_2Sb_2 .

Before discussing the various compounds, a brief review of thermoelectric efficiency is given. The importance of the carrier concentration is discussed, as well as some simple methods for determining if the carrier concentration should be increased or decreased to improve a material's figure of merit zT . This concludes with zT written as a function of one material dependent parameter (β) and three energy-dependent parameters, and a short discussion of how this expression is utilized to obtain a plot of zT versus carrier density is given.

The thermoelectric figure of merit zT in optimized $\text{La}_{3-x}\text{Te}_4$ is found to be greater than that in SiGe alloys, the competing high-temperature material, with $zT \sim 1.2$ achieved at 1273 K. The chemical manipulations considered (Yb, Sb, Bi addition) were not found to significantly modify thermoelectric efficiency at high temperatures, with the exception of Bi addition which reduced zT due to a significant reduction in the band gap. Lower zT is observed in $\text{Ba}_8\text{Ga}_{16-x}\text{Ge}_{30+x}$, with zT near 0.85 at 1000 K. Still lower zT is observed in the Sr-Zn-Sb compounds, which are not candidates for thermoelectric application.

Later in the chapter, the relationship between zT and device efficiency is considered. Here, the importance of the material's thermoelectric compatibility factor s is highlighted. This feature is particularly important when generating segmented devices, as can be observed when comparing the efficiency of segmented legs based on $\text{La}_{3-x}\text{Te}_4$ with those based on SiGe alloys. The theoretical efficiency in a $\text{La}_{3-x}\text{Te}_4$ -PbTe leg is found to approach 20% of the Carnot efficiency, or about 14% total efficiency.

6.2 Review of Thermoelectric Efficiency

The primary measure of a material's thermoelectric performance is the dimensionless figure of merit,

$$zT = \frac{\alpha^2 \sigma T}{\kappa}, \quad (6.1)$$

which is determined by the Seebeck coefficient α , the electrical conductivity σ , and the thermal conductivity $\kappa = \kappa_L + \kappa_e$ which is the sum of the lattice and electronic contributions, respectively. Thermoelectric compatibility also influences thermoelectric conversion efficiency, as discussed in Section 6.6.

For a given material, zT is generally optimized via the free carrier density. A few effortless approaches can be utilized to estimate the optimum carrier density for a given system. In general, the most important thing for an experimentalist to recognize is whether the carrier density needs to be increased or reduced. The Seebeck coefficient is perhaps the best thermoelectric property to consider for this initial approach. Of course, if the resistivity is far too large (say, hundreds of $\text{m}\Omega\text{-cm}$) then it is clear that the carrier density is too low (unless $\kappa_L=0$). As discussed in the Introduction, the limit of zT when $\kappa_L=0$ is very informative:

$$zT = \frac{\alpha^2}{L}, \quad (6.2)$$

where a Lorenz number of $L \approx 2 \times 10^{-8} \text{W}\Omega\text{K}^{-2}$ is a reasonable estimation to consider. This reveals that $|\alpha| = 141 \mu\text{V}/\text{K}$ is required for $zT = 1$ in the ideal limit of $\kappa_L = 0$. The functional form of α is well understood, and has been demonstrated in Section 4.2, where it is shown that $|\alpha|$ increases with decreasing n . Thus, if the experimental values of α are less than $\sim 150 \mu\text{V}/\text{K}$, the carrier density must be decreased for attractive zT to be achieved. This also reveals that obtaining large $|\alpha|$ is critical for obtaining large zT . Furthermore, this suggests that when smaller values of κ_L are achieved, a concurrent decrease in n can be performed to maximize zT ; low κ_L allows for larger α to be utilized.

The field of thermoelectrics is rich with history, and many of our ‘Giants’ have discussed the optimization of thermoelectric materials[3, 4]. For instance, the famous text by Ioffe cites that n_{opt} increases with increasing m^* and T as[3]

$$n_{opt} = \frac{2(2\pi m^* k_b T)^{3/2}}{h^3}. \quad (6.3)$$

This simple model is developed assuming Boltzmann statistics hold, and is actually an optimization of the power factor ($\alpha^2 \sigma$). However, it does provide an initial guideline for the optimization of thermoelectric efficiency. The ease with which complex integrations can be computed has certainly changed since Ioffe’s day, and thus a more *complete* optimization can be readily achieved using a program such as Mathematica.

From the theory of electrical transport outlined in Section 4.2, the dependence of zT on carrier concentration can be readily computed for a given set of material parameters. The key thermoelectric parameters are the lattice thermal conductivity κ_L , and the carrier’s effective mass m^* and mobility μ . To generate a theoretical $zT(n_H)$, one must assume something about the behavior of μ (the behavior of the carrier relaxation time τ). Generally, at high temperatures, μ decreases with increasing T due to scattering by phonons. Therefore,

it is common to assume phonon scattering limits μ . First principles calculations often utilize the assumption that μ is independent of energy, as this facilitates computation and is a reasonable approximation.

The figure of merit zT can be written as a function of the carrier's (reduced) electrochemical potential η and the key material properties:

$$zT = \frac{\alpha^2}{L + (\psi\beta)^{-1}}, \quad (6.4)$$

where

$$\beta = \frac{\mu_0(m^*)^{3/2}T^{5/2}}{\kappa_L}, \quad (6.5)$$

and

$$\psi = \frac{8\pi e}{3} \left(\frac{2k}{h^2} \right)^{3/2} (1 + \lambda)F_\lambda(\eta). \quad (6.6)$$

The values of μ_0 , m^* , and κ_L must be obtained at the temperature of interest, and are consistent with the type of carrier scattering assumed (λ). The values of α and L are calculated using Equations 4.29 and 4.49, and the corresponding carrier density is calculated using Equation 4.25.

The zT expression is developed using the drift mobility, $\mu_d = \mu_H/r_H$, and the value of μ_0 is obtained from Equation 4.28 by taking $\mu_0 = e\tau_0/m^*$. For $\lambda=0$ (acoustic phonon scattering), $\mu_0 > \mu_H$, while for $\lambda = 0.5$ (energy independent scattering) $\mu_0 = \mu_H$. All of the necessary expressions can be found in Reference [119] or Section 4.2.

These equations are utilized to estimate the optimum carrier density for a particular value of β . This method is based on the single, parabolic band assumption and is simply a convenient expression for zT that is a restatement of the previously shown expressions for α , σ , and κ . Therefore, in some cases (such as $\text{Ba}_8\text{Ga}_{16-x}\text{Ge}_{30+x}$), this method is very accurate, while in others modifications must be made to account for multiband behavior (such as $\text{La}_{3-x}\text{Te}_4$). Despite this limitation, they are very useful in determining how to maximize zT or increase the maximum zT . For instance, reductions in κ_L or increases in μ_H can be simulated and are often very informative. The validity of these predictions certainly decreases as the amount of data is reduced and the applicability of the parabolic band approximation or a particular scattering assumption becomes unclear.

6.3 $\text{La}_{3-x}\text{Te}_4$

The temperature-dependent zT values for $\text{La}_{3-x}\text{Te}_4$ are shown in Figure 6.1a, and similar behavior is observed in the $\text{La}_{3-x-y}\text{Yb}_y\text{Te}_4$ samples (Figure 6.1b). zT increases with increasing temperature, primarily due to the direct dependence of zT on T and the increase in $\alpha^2\sigma$, though the decrease in κ also contributes. The zT values are generally increasing with increasing T for all temperatures considered because the large band gap of $\text{La}_{3-x}\text{Te}_4$ prohibits the detrimental effects of minority carriers, even at 1273 K (for most com-

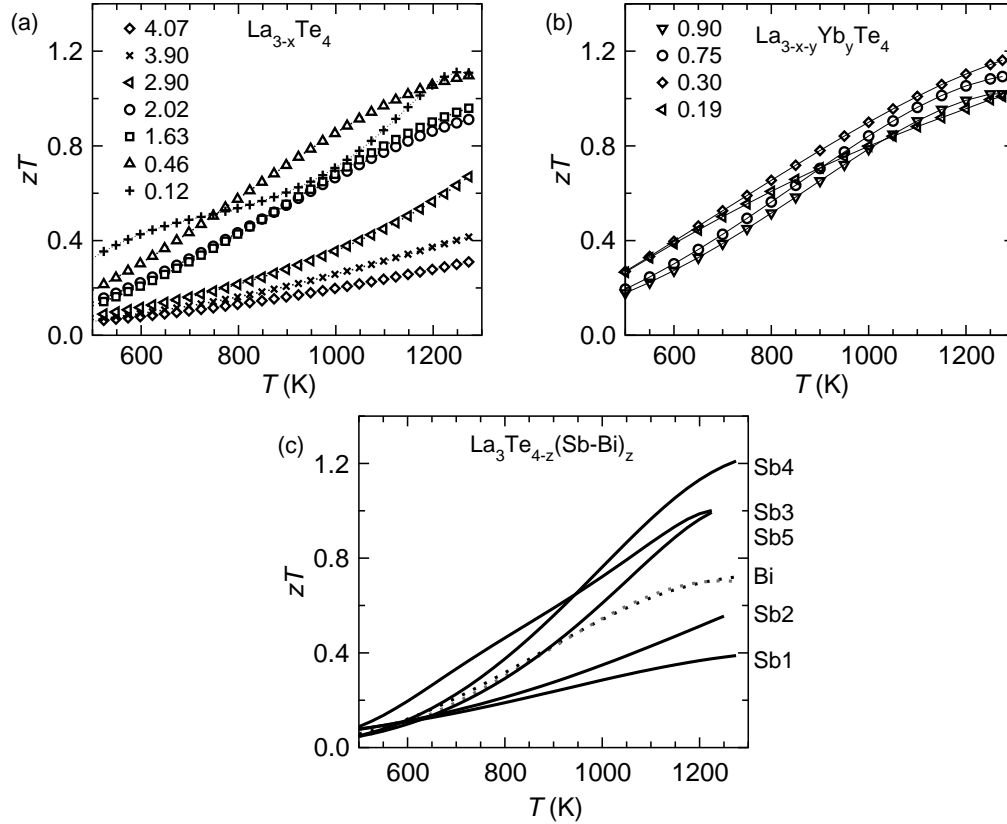


Figure 6.1. The temperature dependent zT in $La_{3-x}Te_4$ and its subsystems reveals a maximum of $zT \sim 1.2$ at 1273 K. The distribution of zT is small in the Yb containing samples due to the narrow range of carrier densities examined (shown in the legends of (a) and (b)). In Sb (Bi) containing samples, zT increases slowly due to the activated nature of the electrical conductivity. Reprinted (adapted) with permission from *Phys. Rev. B*, **78** 125205 (2008) and *Phys. Rev. B*, **81**, 125205 (2010). Copyright 2008 (panel a) and 2010 (panel b), American Physical Society.

positions). The samples with large n_H do not possess large zT due to small $|\alpha|$ and large κ .

The Sb containing samples have lower zT at moderate T due to the reduced σ . However, large zT is observed at high T due to the increased carrier mobility. Unlike $La_{3-x}Te_4$ or $La_{3-x-y}Yb_yTe_4$ samples, the zT values display a maximum at high T and high Sb (Bi) content. This is due to the reduction of the energy gap with Sb (Bi) substitution for Te. Specifically, zT is reduced due to a compensation of α and a small increase in κ_e occurs due to the excitation of minority carriers across the energy gap.

The carrier concentration dependence of $zT(T = 1000 \text{ K})$ is shown in Figure 6.2, where data for Yb containing samples are included in panel (a) and for the Sb(Bi) containing samples in panel (b). The largest zT is observed in samples with relatively low n_H , and a maximum is predicted at $n = 3 \times 10^{20} \text{ cm}^{-3}$. This is primarily associated with a large $|\alpha|$ and the reduced κ_L observed at low n_H and high defect concentrations. The low κ_L is also relatively independent of T in the $La_{3-x}Te_4$ or $La_{3-x-y}Yb_yTe_4$ samples, which promotes large zT over a wide temperature range. The data for Sb/Bi containing samples in Figure 6.2b reveals lower zT than found in $La_{3-x}Te_4$ due to the reduced σ . However, an increase in σ occurs at high T , and thus large

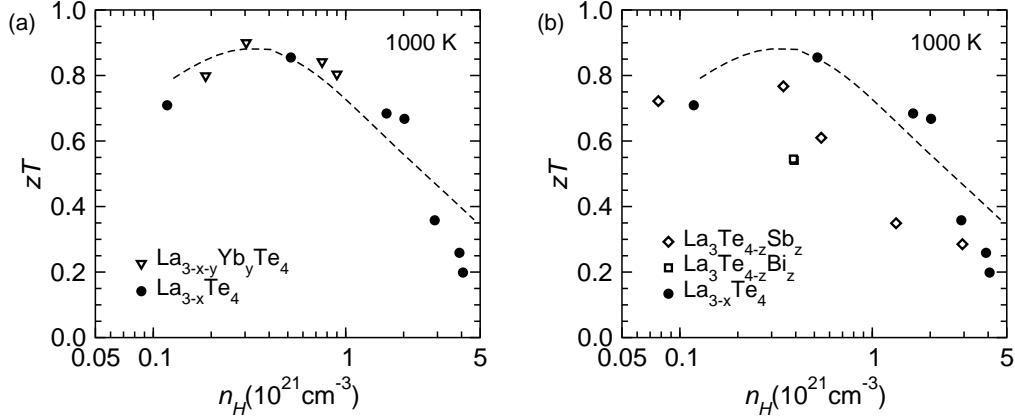


Figure 6.2. The carrier density dependence of zT for $\text{La}_{3-x}\text{Te}_4$ and its subsystems reveals an optimum carrier density near $n_H \sim 3 \times 10^{20} \text{ cm}^{-3}$ (at 1000 K). The Sb(Bi) containing samples have lower than predicted zT due to the suppression of σ at moderate T . The theoretical curve is generated using the fits to α , σ , and κ shown in Figures 4.19 and 5.5; linear models for σ and κ are combined with a three parabolic bands model for α . The model predicts larger than observed α at high n_H , which leads to the overestimation of zT .

zT is observed above 1000 K in the Sb-containing samples.

The heavy bands at high energy influence the thermoelectric performance of $\text{La}_{3-x}\text{Te}_4$ by modifying the electrical transport, in particular through changes in the Seebeck coefficient. At 1000 K, the optimum carrier density is predicted to be $n=3 \times 10^{20} \text{ cm}^{-3}$ from semi-empirical models, and this is confirmed by experiment as well. However, there is a wide range of compositions with large zT . This feature is highlighted in Figure 6.3, where the carrier density is plotted versus the theoretical electrochemical potential (both from parabolic band(s) and from DFT). The orange area corresponds to the room temperature n_H for samples that obtain $zT > 1$ at 1273 K. The heavy band location is indicated by the gray region, and the offset of these bands from the light band (edge of the conduction band) results in the large zT at relatively high n . Thus, while the absolute optimization appears to occur near the band edge, which is consistent with traditional theory, the presence of nested bands leads to a wide range of samples with large thermoelectric performance because they introduce a large density of states beyond what would be observed if only the light band existed (this is shown for n by the ‘1PB light’ curve). Of course, the effects of κ must also be considered; the decrease in κ_L as n decreases would typically lead to the optimization of zT at even lower n [9].

6.4 $\text{Ba}_8\text{Ga}_{16-x}\text{Ge}_{30+x}$

This section is an adapted reproduction, with permission, from *Phys. Rev. B*, **80**, 125205 (2009). Copyright 2009, American Physical Society.

The thermoelectric figure of merit zT in n -type $\text{Ba}_8\text{Ga}_{16-x}\text{Ge}_{30+x}$ is shown as a function of temperature in Figure 6.4a. The values of zT are calculated using polynomial fits to the α , ρ , and D_T data, as well as the two-part fit for C_P shown in Figure 5.9b. As observed in Figure 6.4a, the maximum zT is found to be ~ 0.86

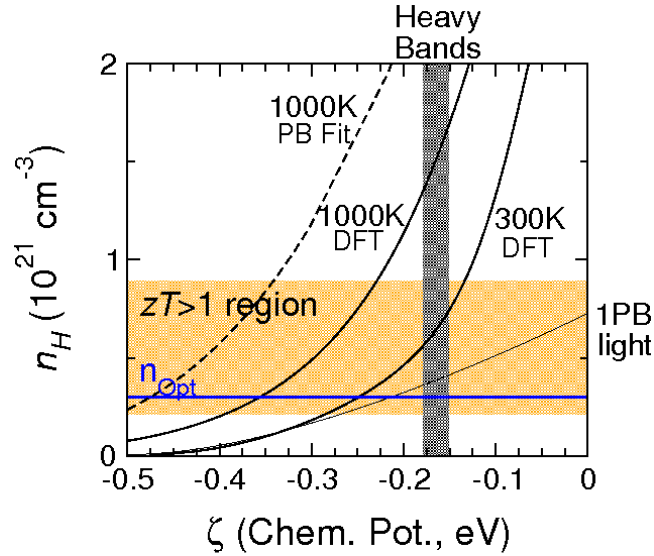


Figure 6.3. A representation of the theoretical relationship between chemical potential and carrier concentration in $\text{La}_{3-x}\text{Te}_4$. The optimum carrier concentration corresponds to the edge of the light band, for the semi-empirical model developed in Figure 4.15b, as expected for a typical semiconductor. However, the nested, heavy bands lead to a wide range of carrier concentrations with $zT > 1$ at 1273 K. This theoretical n versus ζ is influenced by the choice of scattering mechanism, and the energy independent scattering assumed here likely leads to lower band masses than expected and thus larger ζ for a given n, T .

at 950 K, and occurs in samples with $n = 2.7$ and $4.4 \times 10^{20} \text{cm}^{-3}$ at 300 K (C and B , respectively). Samples with lower doping levels (D, E) display smaller zT due to higher ρ , and possess a maximum in $zT(T)$ at lower T . This temperature dependence is expected because samples with a lower n_H possess a greater compensation (reduction by minority carriers) of the Seebeck coefficient and a larger increase in κ due to κ_b (for a given T). Sample A , which has the largest n_H at 300 K, displays a lower value of zT for all T , likely due to the lower value of $|\alpha|$. Note that permanent changes in the material properties of $\text{Ba}_8\text{Ga}_{16-x}\text{Ge}_{30+x}$ were observed upon characterization to 1050 K [107], and thus thermoelectric operation above 1000 K is unlikely (see Appendix C). The optimum n_H values are found to be consistent with the simple theory outlined by Ioffe [3], which predicts an optimum carrier density near $4 \times 10^{20} \text{cm}^{-3}$ for $\text{Ba}_8\text{Ga}_{16-x}\text{Ge}_{30+x}$ operation at 950 K (based on room temperature m^*).

Also shown in Figure 6.4a is the zT curve generated for sample B (B_{DP}) using the Dulong-Petit heat capacity ($C_P = 0.3065 \text{ J/g/K}$). This calculation reveals that zT reaches unity at 950 K for the common C_P assumption; this curve provides a direct comparison with literature data utilizing $C_P = 3R/\text{bar}M = 0.3065 \text{ J/g/K}$. Note the zT values presented here do not account for thermal expansion effects. It has been shown that including the effects of thermal expansion in ρ and D_T leads to an $\sim 3\%$ reduction in zT for $\text{Ba}_8\text{Ga}_{16-x}\text{Ge}_{30+x}$ [75]. The zT values shown here are consistent with those presented for polycrystalline samples [75, 89], and are lower than those reported by Saramat et al. for single crystal samples ($zT \sim 1.3$ at 935 K) [74]. The C_P used by Saramat et al. is lower than that utilized here, but this difference alone does not explain the observed

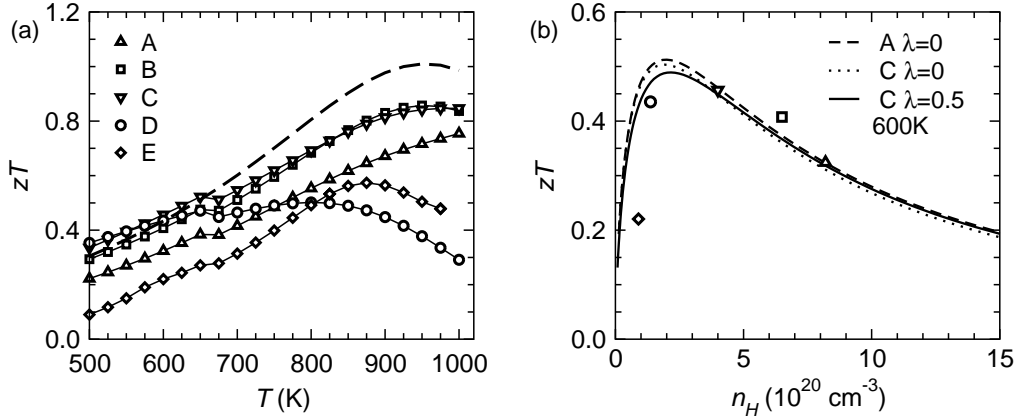


Figure 6.4. (a) The temperature-dependent zT in n -type $\text{Ba}_8\text{Ga}_{16-x}\text{Ge}_{30+x}$ reveals a maximum near 950 K for samples B and C . The value of zT obtained using the Dulong-Petit estimate of C_P is provided by the curve labeled B_{DP} . For sample E , fits to the cooling data for α and ρ were utilized to generate zT , for all other samples both heating and cooling were utilized to obtain zT . (b) The experimental zT is plotted versus n_H with all parameters obtained at 600 K. Also shown are three single band models, which demonstrate the expected dependence of zT on n_H at 600 K. The curves for $\lambda=0$ are generated assuming acoustic phonon scattering limits the carrier mobility, and $\lambda=0.5$ implies an energy independent mobility. The input parameters for these curves are given in Table 6.1. Reprinted with permission from Phys. Rev. B **80**, 125205 (2009). Copyright 2009, American Physical Society.

discrepancy and thus the larger zT may be related to increased mobility in single crystals.

The carrier concentration dependence of zT is well described by conventional theory, as shown in Figure 6.4b. In Figure 6.4b, the experimental zT at 600 K is plotted versus n_H (at 600 K) and is compared to single parabolic band models, the details of which are described below. The experimental data are well described by the rigid band models, which show a maximum zT of 0.5 near $2 \times 10^{20} \text{cm}^{-3}$ (at 600 K). This corresponds to roughly $\text{Ba}_8\text{Ga}_{15.75}\text{Ge}_{30.25}$.

The predicted carrier dependence is believed to be accurate because the Seebeck coefficients are well described by a single band model (Fig.4.31b) and the value of κ_L did not demonstrate any trend with composition (Fig.5.9b). Also, the data presented in Figure 6.4b is for ~ 600 K, where the single carrier description should be valid. It is possible the theoretical curves underestimate zT at high n_H ($> 8 \times 10^{20} \text{cm}^{-3}$), as the first principles Seebeck coefficient curve in Fig. 4.31b has less n dependence than expected from a single band description. The theoretical curves are plotted as a function of n_H at 600 K, and thus a shift to lower room temperature n_H is expected. However the samples are extrinsically doped and n_H varies only slightly with temperature (Figure 4.27b). The optimum doping level estimated in Figure 6.4b is likely applicable to high temperatures, although the effect of minority carriers must be considered.

The theoretical curves in Figure 6.4b are calculated using Equations 6.4–6.5 and Equation 4.25, as discussed in Section 6.2. The input parameters are summarized in Table 6.1.

Consistent with rigid band conduction, similar optimum doping level and maximum zT are obtained regardless of which data set (which sample) is utilized to generate the input parameters. The selection of

Table 6.1. Parameters for theoretical zT ($T = 600$ K) versus n_H shown in Figure 6.4. Reprinted with permission from *Phys. Rev. B*, **80**, 125205 (2009). Copyright 2009, American Physical Society.

Sample	λ	μ_0 (cm ² /V/s)	m^* (m_e)	κ_L (W/m/K)
<i>A</i>	0	7.6	2.7	0.81
<i>C</i>	0	8.3	2.7	0.87
<i>C</i>	0.5	5.9	1.8	0.80

dominant scattering mechanism (within reason) also has little impact on the optimum doping level and maximum zT . When energy independent scattering is assumed ($\lambda = 0.5$), the theoretical zT is very similar to that from the assumption of acoustic phonon scattering, as observed by the similarity between the solid and dashed black curves.

Perhaps the simplest way to enhance zT in this system is to reduce κ_L via alloying. In fact, substituting Yb on the Ba site has shown to reduce κ_L [85], although the carrier density was found to increase with increasing Yb content suggesting the framework composition was not fixed. The theoretical zT for a given κ_L is easily calculated within the model presented here, and given the agreement between theory and experiment the values obtained are expected to be fairly accurate. Assuming a 20% decrease in κ_L at 600 K, and using the input parameters for sample *A* from Table 6.1, a maximum zT of 0.61 is obtained at $T=600$ K. This corresponds to a minor reduction (8%) in optimum doping level, as expected for a simple semiconductor [3, 9]. It therefore seems reasonable that the zT of a polycrystalline, n -type Ba₈Ga_{16-x}Ge_{30+x}-based compound could exceed unity at high temperatures.

6.5 SrZnSb₂ and SrZn₂Sb₂

The thermoelectric performance in SrZn₂Sb₂ greatly exceeds that in SrZnSb₂, as observed in Figure 6.5a. This is due to both the high carrier density in SrZnSb₂, which promotes a low Seebeck coefficient and large κ , as well as the small energy gap which also promotes reduced α and increased κ at high T . The zT value obtained for SrZn₂Sb₂ is similar to that obtained in other AZn₂Sb₂ compounds (where $A = Sr, Ca, Yb, Eu$). However, the performance is lower in the $A = Sr$ compound [97]. This is despite the existence of near optimum carrier density in the SrZn₂Sb₂ compound.

The theoretical dependence of zT on n_H is shown in Figure 6.5b, where it has been assumed that acoustic phonon scattering limits μ . The SrZn₂Sb₂ is found to have near optimal carrier density for the given set of m^* , T , μ and κ_L . SrZnSb₂, on the other hand, is too heavily doped, as expected from the large n_H and low α . The single band model estimates a zT of 0.3 at 500 K in SrZnSb₂, though this value would be difficult to achieve due to the small band gap in SrZnSb₂; the single band model is not accurate in SrZnSb₂ at high T . Thus, SrZnSb₂ is unlikely to achieve large zT and is not a candidate for thermoelectric application. Similarly, the relatively low zT in SrZn₂Sb₂ prohibits further development of this material, despite the fact that it possesses the optimum carrier density for its material properties. In particular, the YbZn₂Sb₂ and

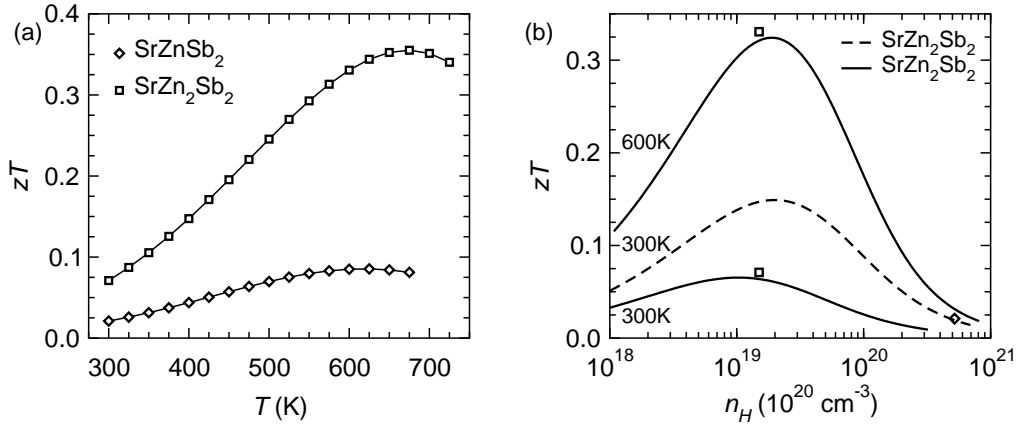


Figure 6.5. (a) The temperature dependent zT reveal a maximum in zT near 600 and 650 K in SrZnSb_2 and SrZn_2Sb_2 , respectively. (b) The SrZnSb_2 sample possesses too large of a carrier density to obtain large zT , while the SrZn_2Sb_2 sample has the optimum carrier density for that material's transport parameters.

Table 6.2. Parameters for theoretical zT versus carrier density in SrZnSb_2 and SrZn_2Sb_2

Sample	T	μ_0 ($\text{cm}^2/\text{V/s}$)	m^* (m_e)	κ_L (W/m/K)
SrZnSb_2	300	78.6	0.92	1.17
SrZn_2Sb_2	300	133.8	0.55	2.20
SrZn_2Sb_2	600	76.5	0.51	1.12

EuZn_2Sb_2 compounds are promising materials due to their abnormally large μ . This feature is not well understood, and has been discussed in a preliminary manner in Reference [97].

The curves at 300 K and 600 K were generated using the values in Table 6.2. The curves were generated assuming acoustic phonon scattering limits the hole mobility. A model is not generated for SrZnSb_2 at 600 K due to its small band gap

6.6 Thermoelectric Compatibility and Device Efficiency

6.6.1 Overview of Device Efficiency

The efficiency (η) of a thermoelectric energy conversion leg is given by $\eta = \eta_C \eta_r$, where $\eta_C = \frac{T_H - T_C}{T_H}$ is the Carnot efficiency and η_r is a reduced efficiency that depends on the material properties. For a single thermoelectric element (one leg of a thermoelectric 'couple') with constant α, σ , and κ , the optimized leg efficiency is [39]

$$\eta = \eta_C \frac{\sqrt{1 + Z\bar{T}} - 1}{\sqrt{1 + Z\bar{T}} + T_C/T_H}, \quad (6.7)$$

and thus $\eta \rightarrow \eta_C$ as $Z\bar{T} \rightarrow \infty$; \bar{T} is the average of the hot (T_H) and cold (T_C) side temperatures. This expression defines a device level figure of merit Z , which then depends on the material properties and op-

erating temperatures. The theoretical maximum efficiency (for temperature dependent material properties) occurs when the optimum reduced current density u is achieved across the entire temperature gradient[39]. The reduced current density u is defined as the ratio of the electric current density J to the heat flux by conduction[39]:

$$u = \frac{J}{\kappa \nabla T}. \quad (6.8)$$

The optimum reduced current density is defined as the thermoelectric compatibility factor s , which is[39]

$$s = \frac{\sqrt{1 + zT} - 1}{|\alpha|T}. \quad (6.9)$$

The parameter s is an intrinsic materials property, like zT , and has units of inverse volts. Conversion efficiency decreases when $u \neq s$, and thus efficiency decreases when s changes strongly across a thermoelectric couple (the value of u is constant). The change in s can be caused by the presence of multiple types of materials (segmentation), or simply the change in s across one material (a strong temperature dependence in s). Therefore, when forming a segmented couple, it is best to match the s values of adjoining materials (at the temperature of the joint). It is also desirable to have a self-compatible material, where s is relatively independent of T . The interested readers are recommended to review References [39, 148, 149].

6.6.2 Efficiency in $\text{La}_{3-x}\text{Te}_4$ and Subsystems

This section reveals the predicted (optimized), single-leg conversion efficiencies for the lanthanum telluride based materials. Data for SiGe are also provided, as lanthanum telluride is a candidate material to replace SiGe in high temperature power generation. A program developed by G. J. Snyder was utilized to compute the optimized, single leg efficiency of the materials considered. This code utilizes the temperature dependent thermoelectric properties and performs a full calculation of device efficiency, including the effects of compatibility. The transport data for materials not discussed in this text were taken from the internal JPL data set.

The calculated efficiency of single leg thermoelectric generators is shown in Figure 6.6. The hot side is taken to be 1273 K, and the efficiency is plotted versus the temperature drop. The temperature drop in NASA's traditional, SiGe based thermoelectric generators is 700 K (from a 1273 K hot side)[150]. The thermoelectric efficiency of these devices is about 8%, though an additional $\sim 1-2\%$ is lost at the device level. In Figure 6.6, SiGe is shown to have a single leg efficiency over 9% at this ΔT , and the theoretical device efficiency quoted here is reduced by the poor performance of the p -type SiGe leg. The actual system power output is reduced by $\sim 1.6\%$ each year, and only roughly 0.33% of this is due to degradation of the thermoelectric materials over time; the majority is associated with reduced thermal flux and temperature[150].

The efficiency of the optimized $\text{La}_{3-x-y}\text{Yb}_y\text{Te}_4$ sample (LaYbTe) is greater than that of SiGe for all temperature drops. In nearly optimized $\text{La}_{3-x}\text{Te}_4$ (LaTe), the efficiency is similar to SiGe for a single-

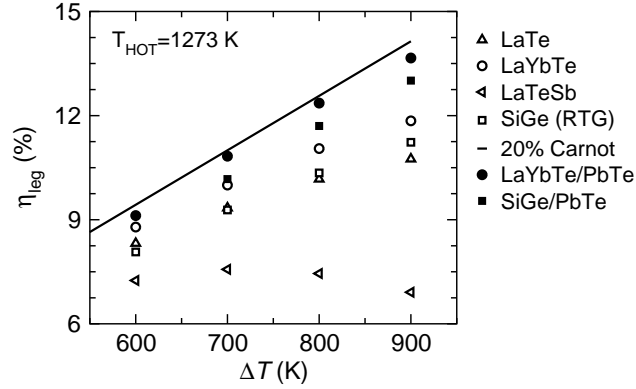


Figure 6.6. Optimized, single leg conversion efficiencies are plotted versus temperature drop for a hot side of $T = 1273$ K. The open markers represent single material (non-segmented) legs, while the closed markers represent segmentation with PbTe (the ‘3N’ data, internal JPL reference). The solid line indicates 20% of the Carnot efficiency. The samples with the highest zT were selected for these calculations, with ‘LaTe’ representing pure $\text{La}_{3-x}\text{Te}_4$, ‘LaYbTe’ representing the substitution of Yb for La, and ‘LaTeSb’ the substitution of Sb for Te.

material leg. At low ΔT , this $\text{La}_{3-x}\text{Te}_4$ provides higher efficiency because the zT of SiGe is higher at low T . In Sb containing samples, $\text{LaTeSb} = \text{La}_3\text{Te}_{4-z}\text{Sb}_z$, the conversion efficiency is low for all ΔT due to the decreased zT at low T associated with the activated behavior of the electrical conductivity.

The efficiency of these legs is increased by segmenting with PbTe. The segmented leg efficiencies are shown by the filled markers in Figure 6.6. For the case of optimized lanthanum telluride (optimized with the aid of Yb addition), the segmented leg efficiency breaks 14% for a cold side temperature of 373 K. For small ΔT , the benefits of segmentation are minor and do not outweigh the complications associated with segmenting two materials together (mechanical failure due to thermal expansion, chemical reactivity).

The amount of increase in efficiency upon segmentation is dictated by the thermoelectric compatibility. In Figure 6.7a, the compatibility factors of the optimized $\text{Ba}_8\text{Ga}_{16-x}\text{Ge}_{30+x}$ and $\text{La}_{3-x-y}\text{Yb}_y\text{Te}_4$ from this thesis (filled markers) are compared to data for PbTe, SiGe, and CoSb_3 , the latter of which is a contender for low T power generation. It is observed that the compatibility factor of $\text{La}_{3-x-y}\text{Yb}_y\text{Te}_4$ matches those of PbTe and CoSb_3 better than SiGe does, and thus a larger increase in net efficiency is expected (in segmented legs) Also, the $\text{Ba}_8\text{Ga}_{16-x}\text{Ge}_{30+x}$ compound is found to have a highly favorable compatibility, and s is very independent of T (except for the drastic change associated with the spike in C_P). This aspect of $\text{Ba}_8\text{Ga}_{16-x}\text{Ge}_{30+x}$ was discussed in detail by Toberer et al. in Reference [75].

The effect of composition on s in $\text{La}_{3-x}\text{Te}_4$ is shown in Figure 6.7b. In this system, the change in s with composition is complex. The extremes of high and low carrier density are both found to have the lowest s . However, the change in s is relatively small (take note of the axis), particularly when varying composition near the maximum zT . Therefore, the maximum conversion efficiency is likely to be dictated by zT alone. However, the changes in mechanical properties must certainly be considered when performing device development.

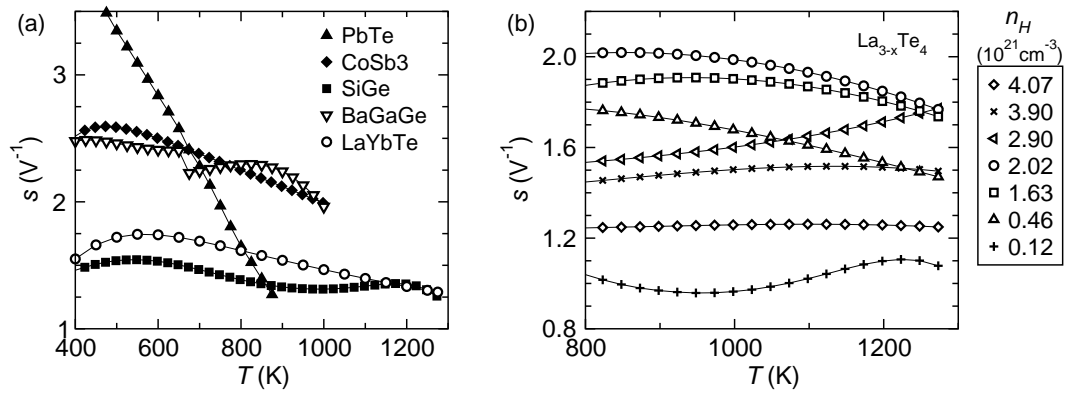


Figure 6.7. The compatibility factors s of low temperature materials PbTe and CoSb₃ are compared to those of the high temperature materials SiGe and $\text{La}_{3-x-y}\text{Yb}_y\text{Te}_4$. A constant value of s is desired across the entire ΔT , and thus segmentation with $\text{La}_{3-x-y}\text{Yb}_y\text{Te}_4$ results in larger increase in conversion efficiency than does segmentation with SiGe. Reprinted (adapted) with permission from *Phys. Rev. B*, **78** 125205 (2008). Copyright 2008, American Physical Society.

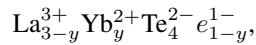
Chapter 7

Future Studies

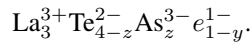
The work discussed in this thesis provides an excellent baseline for future studies attempting to improve the thermoelectric performance in the $\text{La}_{3-x}\text{Te}_4$ and $\text{Ba}_8\text{Ga}_{16-x}\text{Ge}_{30+x}$ systems. To perform a scientific study examining the influence of modifications on performance, the interested researcher(s) should perform baseline experiments on these systems and compare the thermoelectric performance at specific Hall carrier concentrations. This is particularly important, as small changes in processing can affect the thermoelectric performance of a material. Also, given the difficulty in measuring the thermoelectric properties, it is important to isolate the effects of differing experimental apparatuses.

Continued efforts to understand and optimize transport in $\text{La}_{3-x}\text{Te}_4$ should focus on enhancing the electrical properties while maintaining low lattice thermal conductivity. Specifically, $\text{La}_{3-x}\text{Te}_4$ is a low mobility compound and an enhancement in the mobility should be targeted. A fundamental change to the band structure may be favorable for increased mobility, and may also benefit the Seebeck coefficient. Specifically, decreasing the energy offset between the light and heavy bands would likely promote larger thermoelectric efficiency (all things remaining equal).

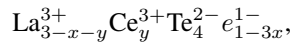
Chemical manipulations are likely to enhance performance by allowing scattering and carrier concentration to be tuned independently, and will be necessary to modify the electronic structure. Some specific compositions to consider include the vacancy free compositions, such as



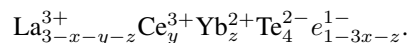
and perhaps the anionic substitution



The influence of other trivalent rare earth compounds on the electronic structure should be considered, through compositions such as



and



Measurements on the transport properties at low temperature are likely to be beneficial when attempting to improve performance in lanthanum telluride and understand the role of chemical manipulation. These measurements may also elucidate the temperature dependence of the band features (curvature, band energy offsets) and would provide additional information about the scattering of electrons and phonons via vacancies that would allow scattering mechanisms to be avoided and/or exploited.

The $\text{Ba}_8\text{Ga}_{16-x}\text{Ge}_{30+x}$ system has been studied for some time now, with a large emphasis on the low temperature transport. While these compounds are unlikely to achieve very large zT , it is likely that zT greater than unity can be achieved through either (i) alloying to reduce the thermal conductivity or (ii) chemical modification to increase the energy gap and suppress the bipolar contribution at high T . To achieve (i), samples containing both Yb and Ba may be considered; this would most likely increase zT at lower temperatures and promote a larger average zT . For approach (ii), the energy gap in other Type-I clathrates should be considered to allow chemical modifications to be selected appropriately.

Appendix A

Minority Carrier Properties and Transport

A.1 General Trends

This appendix examines the influence of minority carrier properties and band gap, on the observed thermoelectric properties in a simple semiconductor. Holes are taken to be the majority carriers, and electrons the minority carriers (simply so that all coefficients are positive). The calculations assumed an acceptor density of $5 \times 10^{20} \text{cm}^{-3}$, with complete filling of these states (complete ionization). It was assumed that acoustic phonon scattering limits the relaxation times of both holes and electrons. The baseline calculation assumed identical material properties for holes and electrons: $m^*/m_e=1$, $E_{def}=3 \text{ eV}$, $E_g=0.5 \text{ eV}$, $v_l=3000 \text{ m/s}$, and a material density 6 g/cm^3 . These parameters lead to moderate zT .

The baseline properties were maintained for the majority carrier in all calculations. The ratios provided in the legend correspond to changes in minority carrier properties and *thus the single band model represents the limit of thermoelectric performance*. Results of the baseline calculation (Equal Props) are shown by the solid curves in the following figures.

When the mass of the majority carrier is increased relative to the minority carrier (dashed curves), the number of minority carriers decreases and thus the influence of the minority carriers is weakened. However, when the mass of the minority carrier increases (dotted curves), the detrimental effects of minority carriers are noticed more profoundly. This process is complicated the relation of the carrier mass to its mobility ($\mu \propto (m^*)^{-5/2}$), and the net change in zT with the effective mass ratio is not that significant.

An increasing minority carrier mobility results in a significant decrease in zT due to a large bipolar thermal conductivity and a large decrease in the Seebeck coefficient. A similar effect is observed for a reduced band gap. The opposite is true for an increased band gap or a reduced minority carrier mobility. Clearly a large energy gap is desired. Indeed, the minority carrier effects consistently lead to reduced zT . Note that the $E_g=0.7 \text{ eV}$ data set is nearly equivalent to a single band model (for the baseline carrier properties)

One approach for increasing zT at high T is to increase the energy gap. This allows low n samples to be utilized, thus promoting large zT via a large α , as well as the reduced electronic contribution to the thermal conductivity. However, an equally valid approach is to modify the band properties of the minority carrier.

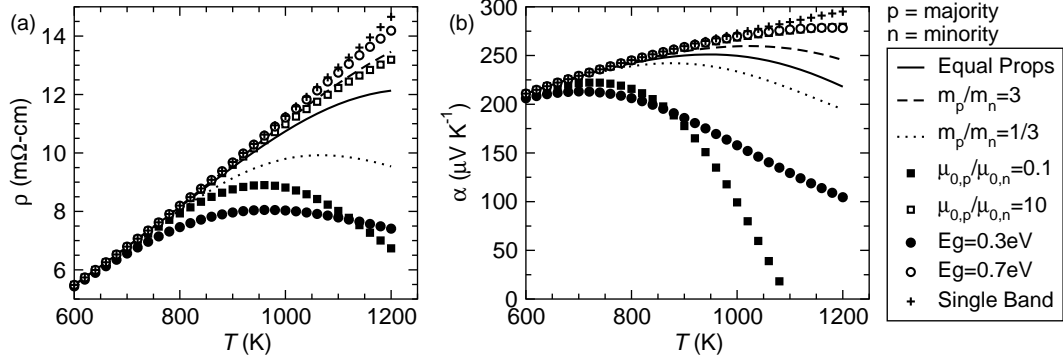


Figure A.1. The influence of minority carrier band properties, and energy gap, on (a) the electrical resistivity and (b) the Seebeck coefficient as a function of temperature. ‘Equal Props’ stands for $E_g=0.5$ eV and carrier property ratios of unity.

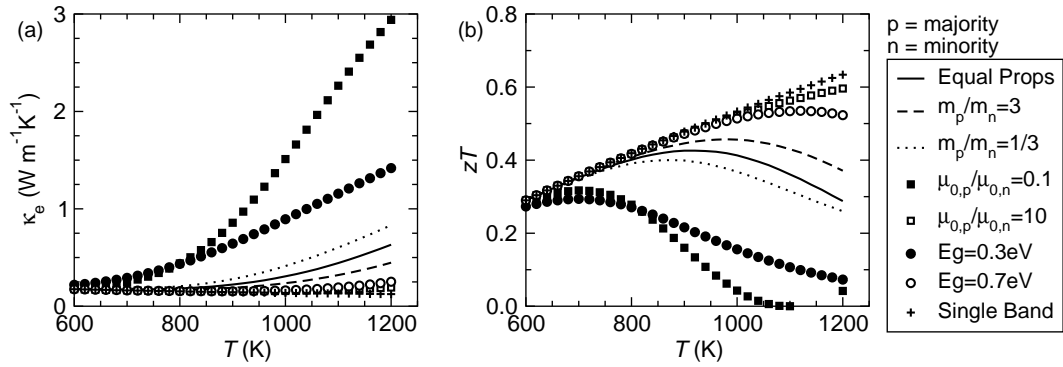


Figure A.2. The influence of minority carrier band properties, and energy gap, on the temperature-dependent (a) the electronic contribution to the thermal conductivity and (b) the thermoelectric figure of merit. ‘Equal Props’ stands for $E_g=0.5$ eV and carrier property ratios of unity.

Sometimes, this can be achieved through the introduction of heavy states that result in localization of carriers (significant reduction in the mobility). This must be done with care, as an increased band mass does lead to increased minority carrier effects when all else remains constant. Of course, the individual band masses are closely linked to the band gap itself, and thus the manipulation of minority carrier effects is very complicated.

The variation of minority carrier properties, and energy gap, also effects the maximum zT obtained at a particular temperature and the corresponding optimum carrier density n_{opt} . When the band gap or majority carrier mass or mobility are increased (relative to the minority carrier), the value of zT_{max} and the corresponding n_{opt} increases and n_{opt} decreases as both approach the single band limit. Recall that the above analysis utilized a constant majority carrier property set, and thus the increase in mobility ratio does not result in an increase in zT .

The above discussed is complicated, though only slightly, by the interrelation of these transport properties and the electrochemical potential. The effective mass ratio and the energy gap influence the chemical potential via the charge neutrality expression (see Figure A.4). Therefore, the temperature dependent Seebeck coefficients of the individual carriers (functions of energy alone) also change (and not just the weighted sum

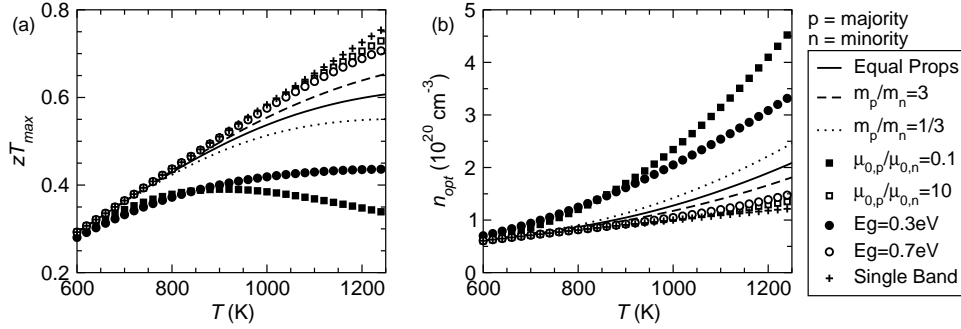


Figure A.3. The influence of minority carrier band properties and energy gap on the (a) maximum zT obtained at the (b) optimum carrier density n_{opt} , both of which are functions of temperature. Note that the majority carrier properties are fixed (minority carrier properties are varied), and thus the increased mobility ratio does not produce zT greater than that in the single band limit. ‘Equal Props’ stands for $E_g = 0.5$ eV and carrier property ratios of unity.

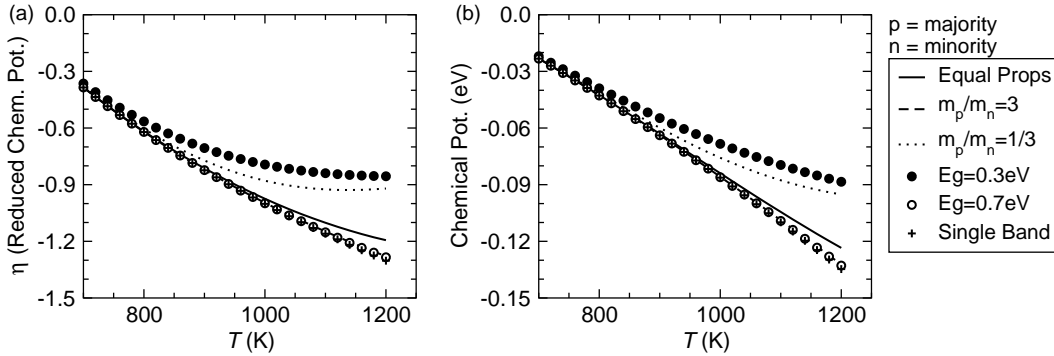


Figure A.4. The influence of minority carrier band properties, and energy gap, on (a) the reduced electrochemical potential and (b) the electrochemical potential in units of eV (relative to the band edge, negative implies η is in the band gap). Only the band masses and energy gap influence this behavior, which arises from a solution of the charge neutrality equation. ‘Equal Props’ stands for $E_g = 0.5$ eV and carrier property ratios of unity.

of these properties). However, this effect is relatively small.

A.2 Experimental Hall Carrier Concentration and Mobility

The presence of multiple carrier types leads to difficulty analyzing Hall effect data. This behavior is particularly important to understand because the temperature dependent Hall carrier density n_H and mobility μ_H is one of the most useful data sets in thermoelectric research. Generally, a single band model is assumed and thus the observed values of n_H and μ_H are not strictly valid. That is, the values of n_H and μ_H are derived from the Hall coefficient, which has contributions from both holes and electrons. The deviation between these observed (single band) values and the true values is greatest at high T , low E_g , $\mu_{majority} < \mu_{minority}$, and $m_{majority}^* \gg m_{minority}^*$.

The multi-carrier effects lead to an overestimation of the majority carrier concentration, and an underesti-

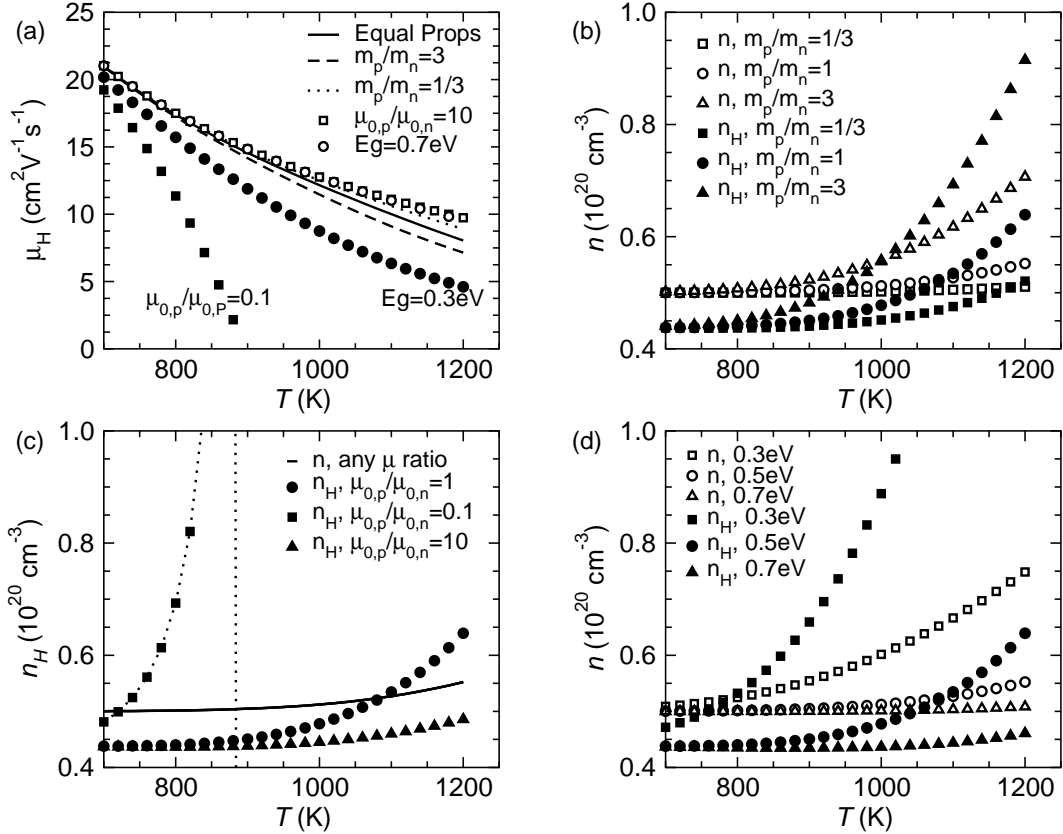


Figure A.5. Demonstration of the variation in Hall properties obtained using a single band assumption as carrier properties change; these are the values an experimentalist would obtain from measurement if the data were analyzed using a single carrier model. At high T , the net result of large minority carrier contribution to the electrical conductivity is an overestimation of the Hall carrier density and an underestimation of the Hall mobility. The variation between this n_H and the actual n is also shown. At low T , the Hall carrier concentration is generally less than the actual carrier density because in this single carrier regime, the scattering effects must be considered and $n = 1/R_h e$ is not strictly valid (see Section 4.2).

mation of the majority carrier mobility. However, it should be noted that this statement is only valid at high T where the minority carrier has a significant contribution to the total electrical conductivity. At low T , where only one carrier type is present, the Hall density underestimates the actual carrier density due to scattering effects (assuming acoustic phonon scattering, recall the Hall factor r_H). Only when these are considered, and the Hall factor is calculated, does the Hall effect produce an accurate characterization of the true n value. Of course, when n is very large, the Hall factor approaches unity and even at low n this error is generally less than 20%. This intricate relationship between n and n_H is observed in Figure A.5b-d. Also, non-parabolic band effects are not being considered here, but can be important.

It should be stressed that Figure A.5 represents the data that would be obtain from a Hall effect measurement if the single band model were employed when multiple carrier types were contributing to conduction. The data shown correspond to the actual majority carrier properties in the limit of large E_g or small μ_{min} .

Appendix B

Pressure-Assisted Sintering

In an argon glove box, the materials to be sintered are loaded into a high density graphite die, which was obtained from POCO. This step may appear trivial, but it can have significant impact on the sample's properties. In particular, the loading procedure can determine whether or not a mechanically stable sample is formed, and can also lead to oxidation. Before the powder can be poured into the die, a circular piece of graphoil and an anvil (spacer) are inserted into the base of the die. The powder is then poured into the die. Typically, 7-10 g of material are loaded, and a series of dumping/settling stages is often required. The poured powder is settled by tapping on the side of the die or tapping the die on the glove box floor. The author tended to tap the die while rotating for about ten seconds. The settled powder is then compressed by hand using a long graphite plunger, after which the final graphoil, spacers, and (shorter) plunger are inserted. The prepressed configuration should have about one inch of plunger exposed. The prepared die is generally inserted into a plastic bag and transported to the hot press. Upon removal from the bag, the die should be loaded as quickly as possible. Note that simple steps, such as examining the condition of the hot press before removing the die from the glove box, can easily save a sample.

Hot pressing was completed at JPL on the "Old Press," which allows for a stress-free anneal after sintering. The hot press employs industrial argon flow and mechanical pump vacuum capable of ~ 60 mTorr. It

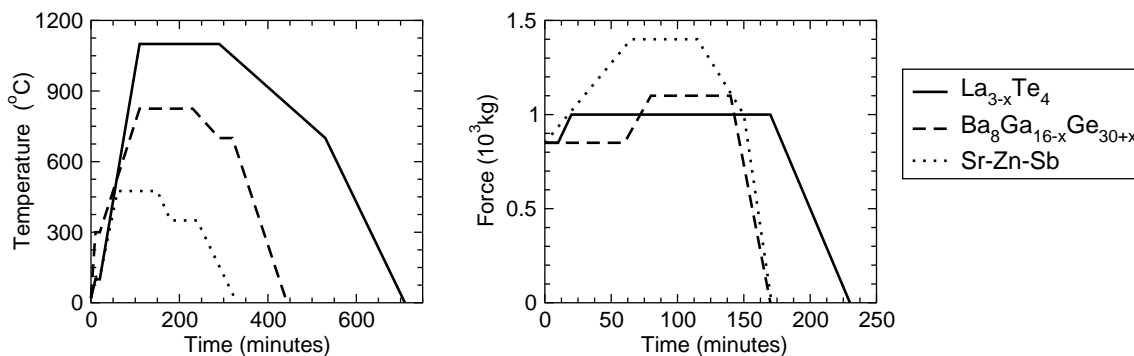


Figure B.1. Representative *press profiles* of the samples considered in this thesis. The complete release of force is usually an important step in the production of mechanically stable, refractory materials. In the legend, Sr-Zn-Sb stands for the SrZnSb₂ and SrZn₂Sb₂ samples.

possesses a minimum load of roughly 0.9 metric tons when the hydraulics are engaged and the force controller is running in “Auto”; this is the minimum force applied to a sample at the beginning of a hot-press run. Thus a value of 0 metric tons in Table B.1 at the onset of a press run refers to 0.8 to 0.9 metric tons. However, programming for 0 metric tons at the end of a press run does correspond to a complete removal of force when an interlock is utilized to switch the hydraulics off and to turn the vacuum on (with argon off). The press profiles shown in Figure B.1 illustrate this point.

Table B.1. Programming details for the sintering of selected compounds in the “Old Press.” The programming times are specified as R=Ramp and D=Dwell.

Stage	La ₃ Te ₄		Ba ₈ Ga _{16-x} Ge _{30+x}		SrZnSb ₂ , SrZn ₂ Sb ₂	
	Temperature (°C, min)	Force (10 ³ kg, min)	Temperature (°C, min)	Force (10 ³ kg, min)	Temperature (°C, min)	Force (10 ³ kg, min)
1	(100, 10R)	(0, 10D)	(300, 10R)	(0, 60D)	(110, 10R)	(0, 50D)
2	(100, 10D)	(1, 10R)	(300, 10D)	(1.1, 20R)	(110, 10D)	(1.4, 15R)
3	(1100, 90R)	(1, 150D)	(825, 90R)	(1.1, 60D)	(475, 40R)	(1.4, 50D)
4	(1100, 180D)	(0, 60R)	(825, 120D)	(0, 30R)	(475, 90D)	(1, 35R)
5	(700, 240R)	-	(700, 60R)	-	(350, 30R)	(1, 35D)
6	(700, 1D)	-	(700, 30D)	-	(350, 60D)	(0, 20R)
7	(25, 180R)	-	(20, 120R)	-	(0, 90R)	-
8	(25, 1D)	-	(20, 1D)	-	(0, 1D)	-

The loading of the die into the chamber can be difficult for a new or out-of-practice user. As such, this step can cause oxidation of the sample if the user is not careful. The die is placed into the chamber and a thermocouple is inserted near the bottom of the die. The condition of the thermocouple should be examined prior to removing the die from the argon bag to minimize exposure to oxygen. The dies were typically 12.3 mm inner diameter, and a graphoil sheet (0.15 mm thick) was utilized to isolate the sample from the die (and plunger). Generally, vacuum was pulled and the system was purged with Ar three or four times. A nice procedure is to pull vacuum to 400 mTorr, purge, then 300 mTorr, purge, then 200 mTorr, purge then for about 10 minutes with the force and temperature profiles running for the last 5. This should allow the temperature to reach 100 °C while vacuum is still being pulled, thus promoting the removal of water. Also, this procedure may allow a significant concentration of oxygen to be removed from the chamber before the lower level vacuum is reached, which will cause the evacuation of the argon trapped within the powder matrix.

Generally, the temperature and force profiles are entered into the controllers while the vacuum/purge procedure is being performed. The details required for the controller are given in Table B.1, where the format chosen is to benefit the user of the “Old Press” at JPL.

Appendix C

Thermal Stability in $\text{Ba}_8\text{Ga}_{16-x}\text{Ge}_{30+x}$

Data collection on $\text{Ba}_8\text{Ga}_{16-x}\text{Ge}_{30+x}$ samples originally occurred to 1050 K. This was believed justified by the high melting point of $\text{Ba}_8\text{Ga}_{16-x}\text{Ge}_{30+x}$ (> 1270 K) and the hot pressing of these samples near 1100 K. However, this characterization procedure resulted in changing electrical transport properties, and thus an adequate temperature needed to be identified. These features are discussed in Reference [107].

The characterization of electrical resistivity to 1050 K resulted in a decreasing electrical resistivity with increasing measurement number, as shown in Figure C.1a. Upon lowering the upper limit to $T = 1000$ K, the data were found to be stable and reproducible, as observed in Figure C.1b.

The decrease in electrical resistivity upon characterization to 1050 K is due to an increase in carrier density, as shown in Figure C.2. The data shown in Figure C.2 was taken at Caltech between high temperature runs performed at JPL. These lower temperature data did not show any difference between heating and cooling, and thus the difference observed is due to the repeated runs to 1050 K.

No change in transport was observed upon characterization to 1050 K in the Seebeck coefficient or thermal diffusivity systems. However, some *bleeding* was observed from the sample surface after Seebeck coefficient measurement to 1050 K. Thus, the extrusion of Ga from the sample may be the source for this behavior; rearrangement on the clathrate framework would be required for Ga loss to occur, and this seems unlikely in the measurement timeframe. However, Ga extrusion was observed via high resolution X-ray data taken at SPRING-8 in Japan on the samples discussed in this text. These data were taken by Bo Iversen, and the data are currently being considered in detail. The initial refinement revealed the formation of Ge at high T . A linear increase in the lattice constant was observed (consistent with preliminary data obtained at Caltech), and no irregular changes in the crystallographic data were inferred. It seems possible that this transformation occurs at the grain boundaries, leaving the primary diffraction pattern of the bulk matrix to be observed. The partnership with Bo Iversen was developed in hopes of explaining the transition event observed in the transport properties, though no explanation of that behavior has been developed. Therefore, the stability of this phase remains unclear.

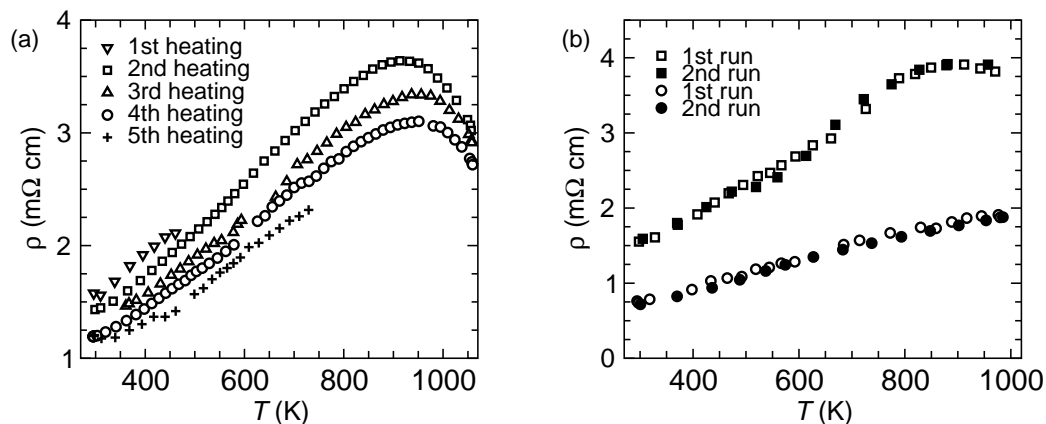


Figure C.1. Repeated high temperature measurements resulted in a decreasing electrical resistivity for $\text{Ba}_8\text{Ga}_{16-x}\text{Ge}_{30+x}$ when characterization occurred to $T \sim 1050$ K. However, characterization to ~ 1000 K resulted in consistent properties, as shown in panel (b). The lower curve in panel (b) is for a sample with ~ 2 wt.% Ge impurity, and thus the Ge impurity did not influence this thermal stability property. With kind permission from Springer Science+Business Media: *Journal of Electronic Materials*, Thermal Stability and Phase Purity in Polycrystalline $\text{Ba}_8\text{Ga}_x\text{Ge}_{46-x}$, vol. 38, 2009; A. Saramat, E. S. Toberer, A. F. May, and G. J. Snyder, Fig. 3.

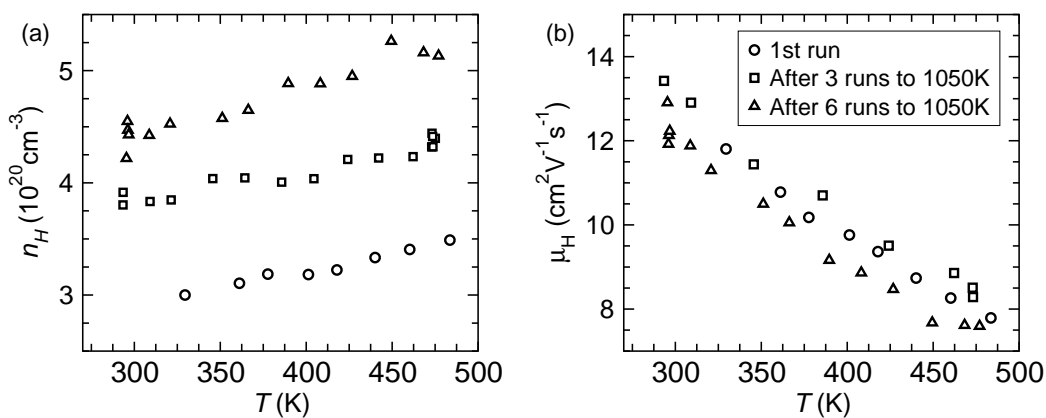


Figure C.2. Moderate temperature data collected between the runs to 1050 K to demonstrate the high temperature measurements resulted in an increase in carrier density. Little change in the mobility was observed. With kind permission from Springer Science+Business Media: *Journal of Electronic Materials*, Thermal Stability and Phase Purity in Polycrystalline $\text{Ba}_8\text{Ga}_x\text{Ge}_{46-x}$, vol. 38, 2009; A. Saramat, E. S. Toberer, A. F. May, and G. J. Snyder, Fig. 4.

Appendix D

Transport Coefficients in Single Scattering Limit

The following equations are valid when the carrier relaxation time can be described by $\tau = \tau_0 \epsilon^{\lambda-1/2}$. In this representation, $\lambda = 0$ implies acoustic phonon scattering or point defect scattering, $\lambda = 0.5$ implies energy independent scattering (such as neutral impurity scattering), and $\lambda = 2$ characterizes ionized impurity scattering. This is only an approximation for ionized impurity scattering, as shown by 4.13 which contains $g(\epsilon)$ and thus the simple power law description is not entirely accurate. This additional energy dependence causes τ to decrease more rapidly with decreasing η (increasing T), though the effect is not major.

The Hall factor is

$$r_H = \frac{3}{2} F_{1/2}(\eta) \frac{(1/2 + 2\lambda) F_{2\lambda-1/2}(\eta)}{(1 + \lambda)^2 F_{\lambda}^2(\eta)}. \quad (\text{D.1})$$

Using $\mu_0 = e\tau_0/m^*$, the Hall mobility is

$$\mu_H = \mu_0 \frac{(1/2 + 2\lambda) F_{2\lambda-1/2}(\eta)}{(1 + \lambda) F_{\lambda}(\eta)}. \quad (\text{D.2})$$

The magnitude of the Seebeck coefficient is

$$\alpha = \frac{k}{e} \left(\frac{(2 + \lambda) F_{\lambda+1}(\eta)}{(1 + \lambda) F_{\lambda}(\eta)} - \eta \right). \quad (\text{D.3})$$

The electrical conductivity is

$$\sigma = \frac{8\pi e^2 m^{1/2} (2kT)^{3/2}}{3h^3} \int_0^{\infty} (1 + \lambda) F_{\lambda}(\eta). \quad (\text{D.4})$$

Recall that the Fermi integrals are

$$F_j(\eta) = \int_0^{\infty} \frac{\zeta^j d\zeta}{1 + \text{Exp}[\zeta - \eta]}. \quad (\text{D.5})$$

Appendix E

The Mott Relation

This appendix derives the *Mott relationship* (Eqn. E.1, also 4.30), which is a common expression for the Seebeck coefficient. No assumptions regarding the electronic structure are required to obtain Eq. E.1. However, an assumption that the electron gas is highly degenerate (that the Fermi distribution is nearly a step function) is required; specifically, the electrochemical potential ζ is large with respect to the thermal energy kT in which case the expansion utilized converges quickly.[29]

$$\alpha = \frac{\pi^2}{3} k_b^2 T \left(\frac{\partial}{\partial E} \ln \sigma_E \right)_{E=\zeta}, \quad (\text{E.1})$$

σ_E is the zeroth-order approximation for the electrical conductivity, and is defined by Equation E.3. The Mott relation is equivalent to saying that only electrons with $E = \zeta$ contribute to σ (the width of $\frac{\partial f}{\partial E}$ is not considered). Interestingly, in the formal definition of α , electrons with $E = \zeta$ do not contribute to the Seebeck coefficient.

The electrical conductivity σ is

$$\sigma = \frac{e^2}{12\pi^3} \int dE \frac{\partial f}{\partial E} \int \mathbf{v}_k \mathbf{v}_k \tau(E_k) \frac{dS}{\nabla_k E}, \quad (\text{E.2})$$

and

$$\sigma_E = \int \mathbf{v}_k \mathbf{v}_k \tau \frac{dS}{\nabla_k E}. \quad (\text{E.3})$$

These expressions are equivalent to Equation 4.26 in the parabolic band approximation. Here, the \mathbf{k} space definitions are utilized to reveal the generality of the Mott relation.

The basic expression for α as obtained from the Boltzmann transport equation is

$$\alpha = \frac{1}{eT} \frac{K_1}{K_0}, \quad (\text{E.4})$$

where

$$K_n = -\frac{1}{12\pi^3} \int \frac{\partial f}{\partial E} dE \int_{E=\zeta} \mathbf{v}_k \mathbf{v}_k \tau (E_k - \zeta)^n \frac{dS}{\nabla_k E}, \quad (\text{E.5})$$

and when reduced energies ($\epsilon = E/kT$ and $\eta = \zeta/kT$) are utilized, the Seebeck coefficient can be expressed as

$$\alpha = \frac{k}{e} \frac{\int \sigma_E (\epsilon - \eta) \frac{\partial f}{\partial \epsilon} d\epsilon}{\int \sigma_E \frac{\partial f}{\partial \epsilon} d\epsilon}. \quad (\text{E.6})$$

In this fundamental expression, it is clear that large α is only obtained when the quantity σ_E is asymmetric about η . The Mott relation is simply an extension of this definition, with the goal of obtaining a simple expression that is easily interpreted.

The innermost integration in K_n is performed over all states \mathbf{k} making up the Fermi surface that is described by a differential skin dS . Therefore, an assumption regarding the dispersion relationship must be made if K_n is to be evaluated. The evaluation of the integral over the Fermi surface eliminates the dependence on \mathbf{k} and results in a function of energy. One can thus consider the evaluation of a generic integral

$$Int = - \int \Phi(E) \frac{\partial f}{\partial E} dE. \quad (\text{E.7})$$

This generic integral can be estimated using the first few terms of the Sommerfeld expansion, which is accurate when the system is highly degenerate ($\eta \gg 0$). The integrand is approximated by a Taylor expansion about $E = \zeta$, leading to

$$Int = - \int \left(\Phi(\zeta) + (E - \zeta) \frac{\partial \Phi(E)}{\partial E} \Big|_{E=\zeta} + (E - \zeta)^2 \frac{\partial^2 \Phi(E)}{\partial E^2} \Big|_{E=\zeta} + \dots + (E - \zeta)^j \frac{\partial^j \Phi}{\partial E^j} \Big|_{E=\zeta} \right) \frac{\partial f}{\partial E} dE. \quad (\text{E.8})$$

The first term in the solution of our generic integral simply becomes $\Phi(\zeta)$, and the odd-order terms do not contribute because $\frac{\partial f}{\partial E}$ is even in $(E - \zeta)$. [11] The even order terms evaluate as

$$\int (E - \zeta)^{2n} \frac{\partial^{2n} \Phi}{\partial E^{2n}} \Big|_{E=\zeta} \frac{\partial f}{\partial E} dE = 2C_{2n} (k_b T)^{2n} \frac{\partial^{2n} \Phi}{\partial E^{2n}} \Big|_{E=\zeta}, \quad (\text{E.9})$$

Thus the generic integral is given as [11, 29]

$$Int \approx \Phi(\zeta) + 2 \sum_{n=1}^{\infty} C_{2n} (k_b T)^{2n} \frac{\partial^{2n} \Phi}{\partial E^{2n}} \Big|_{E=\zeta}, \quad (\text{E.10})$$

where, in the words of Ziman, the integrations to obtain the constant C_{2n} utilize elegant mathematics that yield

$$C_{2n} = \sum_{s=1}^{\infty} \frac{(-1)^{s+1}}{s^{2n}}, \quad (\text{E.11})$$

for which

$$C_2 = \frac{\pi^2}{12}, \text{ and } C_4 = \frac{7\pi^4}{720}.$$

The necessary expressions K_n are thus approximated to zeroth order as

$$K_0 = \frac{1}{12\pi^3} \left(\int_{E=\zeta} \mathbf{v}_k \mathbf{v}_k \tau \frac{dS}{\nabla_k E} \right), \quad (\text{E.12})$$

and the first non-vanishing term for K_1 is second order in kT :

$$K_1 = \frac{1}{12\pi^3} \frac{\pi^2}{3} k_b^2 T^2 \frac{\partial}{\partial E} \left(\int_{E=\zeta} \mathbf{v}_k \mathbf{v}_k \tau \frac{dS}{\nabla_k E} \right). \quad (\text{E.13})$$

Placing these expressions back into Equation E.4,

$$\alpha = \frac{\pi^2}{3} k_b^2 T \left(\frac{\frac{\partial}{\partial E} \left(\int_{E=\zeta} \mathbf{v}_k \mathbf{v}_k \tau \frac{dS}{\nabla_k E} \right)}{\int_{E=\zeta} \mathbf{v}_k \mathbf{v}_k \tau \frac{dS}{\nabla_k E}} \right), \quad (\text{E.14})$$

and thus we have obtained Equation E.1 (Eqn. 4.30).

The trick is to then utilize this expression to gain insight into the behavior of α . To perform this task, we recognize that we have been considering the movement of electrons on a Fermi surface—the integrations in \mathbf{k} space are said to be performed at $E = \zeta$. Thus, we are concerned with the behavior of τ and \mathbf{v}_k at $E = \zeta$. Considering the definition of the group velocity \mathbf{v}_k ,

$$\mathbf{v}_k = \frac{1}{\hbar} \nabla_k E(\mathbf{k}). \quad (\text{E.15})$$

It is clear that this quantity will depend on \mathbf{k} for an arbitrary surface S . Equation 4.30 is therefore the only form of the Mott relation that is valid for all dispersion relations $E(\mathbf{k})$. Indeed, discussions of manipulating the band structure for enhanced α can only call upon this form where sharp changes in \mathbf{v}_k are permitted. However, it is a nice demonstration of the fact that when σ has strong energy dependence at the chemical potential $E = \zeta$ the Seebeck coefficient is large.

To proceed further and provide a simplified version of the Mott Relation, we must therefore make an assumption about τ and \mathbf{v}_k . The simplest case to consider is that of a cubic material, where $k_x = k_y = k_z$ and thus $\mathbf{v}^2 = \frac{1}{3}(v_x^2 + v_y^2 + v_z^2)$. It is then assumed that τ is only a function of E , or only depends on \mathbf{k} via $E(\mathbf{k})$ and can thus be removed from the integral over dS . Also, it is recognized that the density of electronic states at $E = \zeta$ is defined as

$$N(\zeta) = \frac{1}{4\pi^3} \int_{E=\zeta} \frac{dS}{\nabla_k E}. \quad (\text{E.16})$$

Therefore, for cubic (isotropic) materials the Mott relation becomes

$$\alpha = \frac{\pi^2}{3} k_b^2 T \left(\frac{\partial}{\partial E} \ln v(E)^2 \tau(E) N(E) \right)_{E=\zeta} = \frac{\pi^2}{3\zeta} k_b^2 T \left(\frac{\partial}{\partial \ln E} \ln v(E)^2 \tau(E) N(E) \right)_{E=\zeta}, \quad (\text{E.17})$$

where $v(E)$, $\tau(E)$ and $N(E)$ are all functions of energy. Again, to make any additional simplifications one must assume something regarding the electronic structure. In general $v^2 \propto E$ and $\tau \propto E^{\lambda-1/2}$, in which case

$$\alpha = \frac{\pi^2}{3\zeta} k_b^2 T \left(\frac{1}{2} + \lambda + \frac{\partial \ln N(E)}{\partial \ln E} \right)_{E=\zeta}, \quad (\text{E.18})$$

and for parabolic bands $N(E) \propto E^{1/2}$, which leads to the expression discussed in Appendix F.

To utilize the carrier mobility in place of τ , we recognize that $\mu = \frac{e\tau}{m^*}$ and thus this leads to the same expression as Eqn. E.18 provided that m^* is not a function of energy. To include the carrier density n and mobility μ one must use the free electron model (or similar, simple expression). For free electrons, the electron density n is related to the Fermi energy E_F and corresponding density of states $N(E_F)$ via $n = \frac{2}{3} E_F N(E_F)$; the Fermi velocity is $v_F^2 = \frac{2E_F}{m^*}$. Recognizing that $v_F^2 \tau(E_F) e / 2E_F = \mu(E_F)$ is the mobility of electrons at E_F , we find

$$\alpha = \frac{\pi^2}{3E_F} k_b^2 T \left(\frac{\partial \ln \mu(E)}{\partial \ln E} + \frac{\partial \ln n(E)}{\partial \ln E} \right)_{E=E_F}. \quad (\text{E.19})$$

Therefore, to utilize the carrier density n and mobility μ in the Mott relation requires the assumption of a parabolic band (or some other simple dispersion relationship). Furthermore, this expression is derived for (and only strictly valid at) $T=0$ K because the simple relationship between n and $E_F N(E_F)$ was utilized.

Clearly, additional assumptions make Equation E.1 more and more user friendly. However, each assumption limits the validity of this expression, and it is best to utilize this expression solely for insight into the behavior of α . That said, similar insight can be obtained from the basic relationship for α (Eqn. E.6), which clearly shows that a large Seebeck is possible only when there is a large asymmetry in σ about $E = \zeta$.

Appendix F

Degenerate Limit of the Seebeck Coefficient

A common expression for the Seebeck coefficient is

$$\alpha = \frac{\pi^2 k_b^2 T m^*}{3e h^2} \left(\frac{\pi}{3n} \right)^{2/3} (1 + \lambda). \quad (\text{F.1})$$

This is the metallic or high-degeneracy limit of α for a parabolic conductor. This expression is clearly simplified when acoustic phonon scattering limits τ , in which case $\tau \propto E^{-1/2}$ and $\lambda = 0$. Saying acoustic phonon scattering limits the mobility or relaxation time is equivalent to saying the carrier mean free path $l = v \times \tau$ is energy independent ($v = \sqrt{2E/m}$ and $\tau \propto E^{-1/2}$).

Here two methods of obtaining this equation are discussed. The first approach utilizes the fundamental equation for a parabolic band conductor as obtained from the Boltzmann transport equation. The second utilizes the ‘‘Mott relation,’’ which is already a degenerate limit equation for the Seebeck coefficient.

F.1 From the Boltzmann Transport Equation

Repeating from the Electrical Transport Theory section, the magnitude of the Seebeck coefficient for a single, parabolic band conductor is

$$\alpha = \frac{k}{e} \left(\frac{\int_0^\infty \epsilon^{5/2} \tau \frac{\partial f}{\partial \epsilon} d\epsilon}{\int_0^\infty \epsilon^{3/2} \tau \frac{\partial f}{\partial \epsilon} d\epsilon} - \eta \right). \quad (\text{F.2})$$

Upon assuming that a single scattering mechanism modeled with a relaxation time $\tau \propto \epsilon^{\lambda-1/2}$, the above equation can be integrated by parts (see Appendix H) to yield an equation composed of the Fermi integrals $F_j = \int_0^\infty \epsilon^j f d\epsilon$:

$$\alpha = \frac{k}{e} \left(\frac{(2 + \lambda)F_{\lambda+1}(\eta)}{(1 + \lambda)F_\lambda(\eta)} - \eta \right). \quad (\text{F.3})$$

In the limit of high degeneracy ($\eta \gg 0$), the Fermi integrals can be approximated to second order as[119]

$$F_j(\eta) = \frac{(\eta)^{j+1}}{j+1} + \frac{j\pi^2}{6}(\eta)^{j-1}. \quad (\text{F.4})$$

Utilizing this approximation, and after some algebraic manipulation, we obtain

$$\alpha = \frac{k}{e} \left(\frac{(1+\lambda)\frac{\pi^2}{6}}{\eta(1+(1+\lambda)^2\frac{\pi^2}{6}\eta^{-2})} \right). \quad (\text{F.5})$$

Thus, in this representation we see that an additional criterion for using this high degeneracy Seebeck equation is

$$\eta^2 \gg (1+\lambda)^2, \quad (\text{F.6})$$

which, when true, leads to

$$\alpha = \frac{k}{e} \left(\frac{(1+\lambda)\pi^2}{6\eta} \right). \quad (\text{F.7})$$

Recalling that η is the reduced electrochemical potential, which is nearly equivalent to E_F/kT for the case of high degeneracy, we obtain

$$\alpha = \frac{k^2T(1+\lambda)}{6eE_F}. \quad (\text{F.8})$$

And by inserting the relationship between E_F and n, m^* we obtain

$$\alpha = \frac{\pi^2 k_b^2 T m^*}{3eh^2} \left(\frac{\pi}{3n} \right)^{2/3} (1+\lambda). \quad (\text{F.9})$$

F.2 From the Mott Relation

This same result can also be obtained by utilizing the commonly cited ‘‘Mott Relationship’’ (see App. E), which describes the Seebeck coefficient of a free electron metal at low temperatures (another high degenerate limit):

$$\alpha = \frac{\pi^2 k_b^2 T}{3eh^2} \left(\frac{d \ln \sigma_E}{dE} \right)_{E_F} = \frac{\pi^2 k_b^2 T m^*}{3eh^2 E_F} \left(\frac{d \ln \sigma_E}{d \ln E} \right)_{E_F}. \quad (\text{F.10})$$

Following MacDonald[120], we expand this to include the density of states $N(E)$, carrier velocity v and τ :

$$\alpha = \frac{\pi^2 k_b^2 T}{3eh^2 E_F} \left(\frac{d \ln N(E)}{d \ln E} + \frac{d \ln v(E)^2}{d \ln E} + \frac{d \ln \tau(E)}{d \ln E} \right)_{E_F}. \quad (\text{F.11})$$

Now, taking $E = \frac{1}{2}mv^2$, $\tau \propto \epsilon^{\lambda-1/2}$, and assuming a parabolic band where $N(E) \propto E^{0.5}$, one obtains

$$\alpha = \frac{\pi^2 k_b^2 T}{3eh^2 E_F} \left(\frac{1}{2} + 1 + \lambda - \frac{1}{2} \right) = \frac{\pi^2 k_b^2 T(1 + \lambda)}{3eh^2 E_F}. \quad (\text{F.12})$$

Appendix G

Sound Velocity: Measurement and Use

Knowledge of a material's speed of sound (v) allows an easy estimation of the material's Debye temperature, Θ_D . Ultrasonic measurements are a relatively simple method of obtaining v . This appendix describes the general methods utilized for this thesis and shows a representative example within the $\text{La}_{3-x}\text{Te}_4$ system. The instrument settings utilized to obtain quality data will depend on the material of interest. The measurement of longitudinal (normal) and transverse (shear) sound velocities requires a couplant between the sample and transducer, and thus care should be taken to not harm the material surface during measurement. That is, when possible, use a non-aqueous couplant and/or perform the tests quickly.

The first task is to record ultrasonic response data. The quality of the data generally depends on the quality of the sample, with both surface defects and internal defects reducing the quality of the data. Due to this effect, and the transient nature of this data, it is best to obtain similar data several times to obtain some sense for the error in the simple analysis. Thus, it is common to take data over both a wide range (as shown in Figure G.1) and over smaller ranges (ones that include only two peaks).

After obtaining data similar to that in Figure G.1, the distance (in time) between peaks is determined. In general, it is best to perform this task for a variety of conditions (first maximum, first minimum, etc.) and then combine these results for an average. The velocity is then obtained from $v = \frac{\text{length}}{\text{time}}$, where the length associated with the time between two (nearest) peaks is twice that of the sample length. In some cases, the velocity is simply too low to allow a large number of responses to be recorded. Also, the data often contains multiple peaks and thus preliminary knowledge of the sound velocity is useful.

With the sound velocity data, an estimation of the Debye temperature can be performed via [137]

$$\Theta_D = \frac{v_m \hbar}{k_b} \left(\frac{6\pi^2}{V} \right)^{1/3}, \quad (\text{G.1})$$

where V is the average volume per atom and v_m is calculated from the longitudinal v_l and transverse v_t speeds of sound by

$$v_m = 3^{1/3} (v_l^{-3} + 2v_t^{-3})^{-1/3}. \quad (\text{G.2})$$

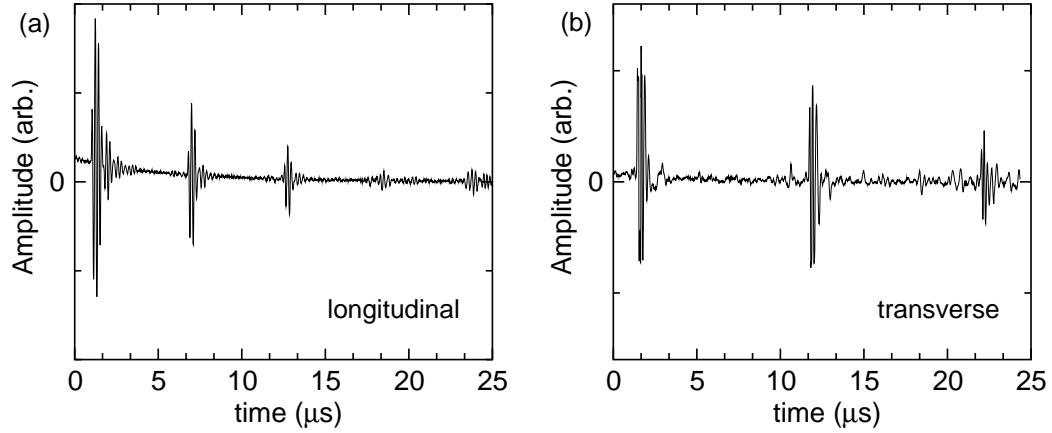


Figure G.1. (a) Longitudinal and (b) transverse response in an ultrasonic pulse/response experiment. These curves are taken for a sample of nominal composition $\text{La}_{2.8}\text{Te}_4$, using a digital oscilloscope system at JPL.

The sound velocities are also utilized in the estimation of the minimum thermal conductivity, κ_{min} , via Cahill's formulation for amorphous materials[141],

$$\kappa_{min} = \left(\frac{\pi}{6}\right)^{1/3} k_b V^{-2/3} \sum_i v_i \left(\frac{T}{\Theta_i}\right)^2 \int_0^{\Theta_i/T} \frac{x^3 e^x}{(e^x - 1)^2} dx, \quad (\text{G.3})$$

where the summation is over the one longitudinal and two transverse modes with $\Theta_i = v_i(\hbar/k_b)(6\pi^2/V)^{1/3}$. The high temperature limit is

$$\kappa_{min} = \frac{1}{2} \left(\frac{\pi}{6}\right)^{1/3} k_b V^{-2/3} (2v_t + v_l). \quad (\text{G.4})$$

If the linear thermal expansion coefficient is known, the bulk modulus and Grüneisen parameter γ can be estimated for isotropic crystals; for instance, see Reference [142]. Also, these materials parameters are combined in Slack's model[142] to estimate the lattice thermal conductivity when only acoustic phonons contribute to κ_L (Eqn. 5.9 in Section 5.2).

Appendix H

The Transport Integral

Integrals of the type

$$\int_0^{\infty} k^3 \tau \frac{\partial f}{\partial k} dk \quad (\text{H.1})$$

are very common in the solutions to the Boltzmann transport equation, and are appropriately termed the transport integrals. To this point, we have not made an assumption regarding the relationship between E and k (the energy or band dispersion relationship). We have, however, assumed that there exists a band of energies which are a continuous function of position and that the motion of electrons has a characteristic time τ . To proceed further, the experimentalist needs a relationship between E and k . We shall see that when the expression $\frac{\partial f}{\partial k}$ is transformed into the energy domain via a parabolic band approximation, this term acts to weight the contributions from various energies to the transport property at hand. Effectively, by weighting the energy dependence with the derivative of the Fermi distribution only energies near the electrochemical potential contribute significantly to the transport. This makes physical sense, as those states well below the chemical potential are subject to the Pauli exclusion principles, and those well above the chemical potential are rarely accessible.

Assuming a parabolic band of index i , the energy is given by $E = \frac{\hbar^2 k^2}{2m_i^*} + E_{min,i}$ where m_i^* is the density of states effective mass of band i and $E_{min,i}$ is the minimum energy of the band. In a single band system, it is convenient to set $E_{min,i} = 0$, so that

$$k^3 = \left(\frac{E 2m_i^*}{\hbar^2} \right)^{3/2}, \quad (\text{H.2})$$

and

$$\frac{\partial f}{\partial k} dk = \frac{\partial f}{\partial E} dE, \quad (\text{H.3})$$

thus,

$$\int_0^\infty k^3 \tau \frac{\partial f}{\partial k} dk = \int_0^\infty \left(\frac{E 2m^*}{\hbar^2} \right)^{3/2} \tau \frac{\partial f}{\partial E} dE. \quad (\text{H.4})$$

For a parabolic band the integrals of concern generally have the form

$$\int_0^\infty E^{3/2} \tau \frac{\partial f}{\partial E} dE = \int_0^\infty -E^{3/2} \tau \frac{\text{Exp}[\frac{E-\zeta}{kT}]}{(1 + \text{Exp}[\frac{E-\zeta}{kT}])^2} dE, \quad (\text{H.5})$$

where

$$\frac{\partial f}{\partial E} = \frac{-1}{kT} \frac{\text{Exp}[\frac{E-\zeta}{kT}]}{(1 + \text{Exp}[\frac{E-\zeta}{kT}])^2}. \quad (\text{H.6})$$

It is common to utilize the dimensionless energies $\epsilon = \frac{E}{kT}$ and $\eta = \frac{\zeta}{kT}$, which leads to integrals of the form

$$(kT)^{3/2} \int_0^\infty -\epsilon^{3/2} \tau \frac{\partial f}{\partial E} dE. \quad (\text{H.7})$$

We are thus concerned with the form of τ . The common assumption is that the relaxation time τ associated with a particular scattering mechanism (s) is described by a power law, $\tau_s = \tau_{0,s}(T)\epsilon^{\lambda-1/2}$. In general, multiple scattering mechanisms influence the carrier relaxation time, and τ is obtained from

$$\frac{1}{\tau} = \sum_{s=1}^s \frac{1}{\tau_s}. \quad (\text{H.8})$$

In a few circumstances, such as in the extremes of temperature, one scattering mechanism leads to much shorter characteristic relaxation time and this in turn limits the absolute τ . In this case, the additional scattering mechanisms can be ignored (to first order), and the integrals will take the form

$$-\tau_{0,s} \int_0^\infty \epsilon^{3/2} \epsilon^{\lambda-1/2} \frac{\partial f}{\partial E} dE = -\tau_{0,s} \int_0^\infty \epsilon^{\lambda+1} \frac{\partial f}{\partial E} dE. \quad (\text{H.9})$$

Therefore, the generic integral of interest is

$$-\int_0^\infty \epsilon^j \frac{\partial f}{\partial E} dE, \quad (\text{H.10})$$

which, when integrated by parts, gives

$$\int_0^\infty f j \epsilon^{j-1} dE. \quad (\text{H.11})$$

The Fermi integrals $F_j(\eta)$ are thus commonly encountered

$$F_j(\eta) = \int_0^\infty f \epsilon^j d\epsilon = \int_0^\infty \frac{\epsilon^j d\epsilon}{1 + \text{Exp}[\epsilon - \eta]}. \quad (\text{H.12})$$

Bibliography

- [1] A. Angrum, Nasa and JPL website, Voyager spacecraft lifetime summary, <http://voyager.jpl.nasa.gov/spacecraft/spacecraftlife.html> (Accessed March 2010).
- [2] L. Bell, Cooling, heating, generating power, and recovering waste heat with thermoelectric systems, *Science* **321**, 1457 (2008).
- [3] A. F. Ioffe, *Semiconductor Thermoelements and Thermoelectric Cooling* (Infosearch Ltd, London, 1957).
- [4] H. J. Goldsmid, *Applications of Thermoelectricity* (Butler & Tanner Ltd, London, 1960).
- [5] I. V. Cadoff and E. Miller, *Thermoelectric Materials and Devices* (Reinhold Publishing Corporation, New York, 1960).
- [6] R. R. Heikes and J. R. W. Ure, *Thermoelectricity: Science and Engineering* (Interscience Publishers, New York, 1961).
- [7] C. Wood, Materials for thermoelectric energy conversion, *Reports on Progress in Physics* **51**, 459 (1988).
- [8] G. D. Mahan, *Solid State Physics*, vol. 51 (Academic Press, New York, 1998).
- [9] E. S. Toberer and G. J. Snyder, Complex thermoelectric materials, *Nature Materials* **7**, 105 (2008).
- [10] H. Littman and B. Davidson, Theoretical bound on the thermoelectric figure of merit from irreversible thermodynamics, *Journal of Applied Physics* **32**, 217 (1961).
- [11] N. W. Ashcroft and N. D. Mermin, *Solid State Physics* (Thomson Learning Inc, United States of America, 1976).
- [12] J. O. Sofo and G. D. Mahan, Optimum band gap of a thermoelectric material, *Physical Review B* **49**, 4565 (1994).
- [13] G. J. Snyder, Caltech thermoelectrics group website, <http://www.thermoelectrics.caltech.edu/> (2010).

- [14] B. Abeles, D. S. Beers, G. D. Cody, and J. P. Dismukes, Thermal conductivity of Ge-Si alloys at high temperatures, *Physical Review* **125**, 44 (1962).
- [15] J. P. Dismukes, L. Ekstrom, E. F. Steigmeier, I. Kudman, and D. S. Beers, Thermal and electrical properties of heavily doped Ge-Si alloys up to 1300 K, *Journal of Applied Physics* **35**, 2899 (1964).
- [16] A. J. Minnich, M. S. Dresselhaus, Z. F. Ren, and G. Chen, Bulk nanostructured thermoelectric materials: Current research and future prospects, *Energy & Environmental Science*, **2**, 466 (2009).
- [17] M. S. Dresselhaus, G. Chen, M. Y. Tang, R. G. Yang, H. Lee, D. Z. Wang, Z. F. Ren, J.-P. Fleurial, and P. Gogna, New directions for low-dimensional thermoelectric materials, *Advanced Materials* **19**, 1043 (2007).
- [18] J. R. Sootsman, D. Y. Chung, and M. G. Kanatzidis, New and old concepts in thermoelectric materials, *Angewandte Chemie International Edition* **48**, 8616 (2009).
- [19] P. Pichanusakorn and P. Bandaru, Nanostructured thermoelectrics, *Materials Science and Engineering: R* **67**, 19 (2010).
- [20] S. K. Bux, et al., Nanostructured bulk Si as an effective thermoelectric material, *Advanced Functional Materials* **19**, 2445 (2009).
- [21] G. Joshi, et al., Enhanced thermoelectric figure-of-merit in nanostructured *p*-type silicon germanium bulk alloys, *Nano Letters* **8**, 4670 (2008).
- [22] A. J. Minnich, H. Lee, X. W. Wang, G. Joshi, M. S. Dresselhaus, Z. F. Ren, G. Chen, and D. Vashaee, Modeling study of thermoelectric SiGe nanocomposites, *Physical Review B* **80**, 155327 (2009).
- [23] B. Poudel, et al., High-thermoelectric performance of nanostructured bismuth antimony telluride bulk alloys, *Science* **320**, 634 (2008).
- [24] J. C. Caylor, K. Coonley, J. Stuart, T. Colpitts, and R. Venkatasubramanian, Enhanced thermoelectric performance in PbTe-based superlattice structures from reduction of lattice thermal conductivity, *Applied Physics Letters* **87**, 023105 (2005).
- [25] J. R. Sootsman, R. J. Pcionek, H. Kong, C. Uher, and M. G. Kanatzidis, Strong reduction of thermal conductivity in nanostructured PbTe prepared by matrix encapsulation, *Chemistry of Materials* **18**, 4993 (2006).
- [26] T. Ikeda, E. S. Toberer, V. A. Ravi, S. M. Haile, and G. J. Snyder, Lattice thermal conductivity of self-assembled PbTe-Sb₂Te₃ composites with nanometer lamellae, *Proceedings of the Twenty Sixth International Conference on Thermoelectrics* p. 1 (2007).

- [27] E. S. Toberer, A. F. May, and G. J. Snyder, Zintl chemistry for designing high efficiency thermoelectric materials, *Chemistry of Materials* **22**, 624 (2010).
- [28] A. H. Wilson, *The Theory of Metals* (The Syndics of the Cambridge University Press, London, 1953).
- [29] J. M. Ziman, *Electrons and Phonons. The Theory of Transport Phenomena in Solids* (Oxford University Press, London, 1963).
- [30] J. P. Heremans, V. Jovovic, E. S. Toberer, A. Saramat, K. Kurosaki, A. Charoenphakdee, S. Yamanaka, and G. J. Snyder, Enhancement of thermoelectric efficiency in PbTe by distortion of the electronic density of states, *Science* **321**, 554 (2008).
- [31] L. D. Hicks and M. S. Dresselhaus, Thermoelectric figure of merit of a one-dimensional conductor, *Physical Review B* **47**, 16631 (1993).
- [32] D. Vashaee and A. Shakouri, Improved thermoelectric power factor in metal-based superlattices, *Physical Review Letters* **92**, 106103 (2004).
- [33] A. Shakouri and J. E. Bowers, Heterostructure integrated thermionic coolers, *Applied Physics Letters* **71**, 1234 (1997).
- [34] J. M. O. Zide, D. Vashaee, Z. X. Bian, G. Zeng, J. E. Bowers, A. Shakouri, and A. C. Gossard, Demonstration of electron filtering to increase the Seebeck coefficient in $\text{In}_{0.53}\text{Ga}_{0.47}\text{As}/\text{In}_{0.53}\text{Ga}_{0.28}\text{Al}_{0.19}\text{As}$ superlattices, *Physical Review B* **74**, 205335 (2006).
- [35] J. Martin, L. Wang, L. Chen, and G. S. Nolas, Enhanced Seebeck coefficient through energy-barrier scattering in PbTe nanocomposites, *Physical Review B* **79**, 115311 (2009).
- [36] M. Roufosse and P. G. Klemens, Thermal conductivity of complex dielectric crystals, *Physical Review B* **7**, 5379 (1973).
- [37] P. G. Klemens, *Solid State Physics*, vol. 7 (Academic Press, New York, 1958).
- [38] A. F. May, J.-P. Fleurial, and G. J. Snyder, Thermoelectric performance of lanthanum telluride produced via mechanical alloying, *Physical Review B* **78**, 125205 (2008).
- [39] G. J. Snyder, *Thermoelectrics Handbook: Macro to Nano, Chapter 9* (CRC Press, New York, 2005).
- [40] L. Danielson, M. Alexander, C. Vining, R. Lockwood, and C. Wood, Thermoelectric properties of latey, *Proceedings Seventh International Conference on Thermoelectric Energy Conversion* p. 71 (March 1988).
- [41] C. Vining, C. Wood, J. Parker, A. Zoltan, L. Danielson, and M. Alexander, Electrical and thermal transport in lanthanum telluride, *Proceedings Seventh International Conference on Thermoelectric Energy Conversion* p. 9 (March 1988).

- [42] C. Wood, A. Lockwood, J. Parker, A. Zoltan, and D. Zoltan, Thermoelectric properties of lanthanum sulfide, *Journal of Applied Physics* **58**, 1542 (1985).
- [43] G. G. Gadzhiev, S. M. Ismailov, M. M. Khamidov, K. K. Abdullaev, and V. V. Sokolov, Thermophysical properties of sulfides of lanthanum, praseodymium, gadolinium, and dysprosium, *High Temperature, Translated from Teplofizika Vysokikh Temperatur Vol 38, p910 (2000)* **38**, 875 (2000).
- [44] J. F. Nakahara, T. Takeshita, M. J. Tschetter, B. J. Beaudry, and J. K. A. Gschneidner, Thermoelectric properties of lanthanum sulfide with Sm, Eu, and Yb additives, *Journal of Applied Physics* **63**, 2331 (1988).
- [45] K. Westerholt, H. Bach, R. Wendemuth, and S. Methfessel, Superconducting $\text{La}_{3-x}\text{Te}_4$ compounds, *Journal of Physics F—Metal Physics*, **10**, 2459 (1980).
- [46] R. M. Bozorth, F. Holtzberg, and S. Methfessel, Superconducting lanthanum chalcogenides, *Physical Review Letters* **14**, 952 (1965).
- [47] W. L. Cox, H. Steinfink, and W. F. Bradley, The structure refinement of La_2Te_3 , a Th_3P_4 type structure, *Inorganic Chemistry* **5**, 318 (1966).
- [48] J. Flahaut, M. Guittard, M. Patrie, M. P. Pardo, S. M. Golabi, and L. Domange, Phases cubiques type Th_3P_4 dans les sulfures, les seleniures et les tellurures L_2X_3 et L_3X_4 des terres rares, et dans leurs combinaisons ML_2X_4 avec les sulfures et seleniures MX de calcium, strontium et baryum. Formation et propriétés cristallines, *Acta Crystallographica* **19**, 14 (1965).
- [49] M. Cutler, J. Leavy, and R. Fitzpatrick, Electron transport in semimetallic cerium sulfide, *Physical Review* **133**, A1143 (1964).
- [50] M. Cutler and J. Leavy, Electron transport in high-resistivity cerium sulfide, *Physical Review* **133**, A1153 (1964).
- [51] A. F. May, D. J. Singh, and G. J. Snyder, Influence of band structure on the large thermoelectric performance of lanthanum telluride, *Physical Review B* **79**, 153101 (2009).
- [52] M. Cutler and N. F. Mott, Observation of anderson localization in an electron gas, *Physical Review* **181**, 1336 (1969).
- [53] A. A. Eliseev, E. I. Yarembash, Y. G. Kuznetsov, E. S. Vigileva, A. A. Reshchikova, and L. I. Anotonoa, Lanthanum tellurides, *Russian Journal of Inorganic Chemistry* **9**, 482 (1964).
- [54] T. H. Ramsey, H. Steinfink, and E. J. Weiss, The phase equilibria and crystal chemistry of the rare earth-group VI systems. IV. lanthanum-tellurium, *Inorganic Chemistry* **4**, 1154 (1965).
- [55] V. P. Zhuze, V. M. Sergeeva, and O. A. Golikova, *Soviet-Physics Solid State* **11**, 2071 (1970).

- [56] L. R. Danielson, V. Raag, and C. Wood, *Proceedings Intersociety Energy Conversion Engineering Conference (Society of Automotive Engineers, Miami)* p. 531 (1985).
- [57] S. R. Brown, S. M. Kauzlarich, F. Gascoin, and G. J. Snyder, $\text{Yb}_{14}\text{MnSb}_{11}$: New high efficiency thermoelectric material for power generation, *Chemistry of Materials* **18**, 1873 (2006).
- [58] J. F. Shackelford, *Introduction to Materials Science for Engineers* (Prentice Hall, Upper Saddle River, New Jersey, 2000).
- [59] R. D. Shannon, Revised effective ionic radii and systematic studies of interatomic distances in halides and chalcogenides, *Acta Crystallographica* **A32**, 751 (1976).
- [60] K. A. Gschneidner, On the valences of europium and ytterbium in compounds, *Journal of the Less Common Metals* **17**, 13 (1969).
- [61] N. K. Abrikosov, K. A. Zinchenko, and A. A. Eliseev, Phase Diagram of the System Yb-Te, *Inorganic Materials (Engl. Transl.)* **6**, 1021 (1970).
- [62] N. N. Greenwood and A. Earnshaw, *Chemistry of the Elements* (Pergamon Press, New York, 1984).
- [63] W. M. Temmerman, L. Petit, A. Svane, Z. Szotek, M. Lders, P. Strange, J. B. Staunton, I. D. Hughes, and B. L. Gyorffy, *Handbook on the Physics and Chemistry of Rare Earths*, vol. 39 (Elsevier, Oxford, 2009).
- [64] B. D. Padalia, W. C. Lang, P. R. Norris, L. M. Watson, and D. J. Fabian, X-ray photoelectron core-level studies of the heavy rare-earth metals and their oxides, *Proceedings of the Royal Society A* **354**, 269 (1977).
- [65] F. Hulliger, New ternary anti- Th_3P_4 -type europium compounds, *Materials Research Bulletin* **14**, 259 (1979).
- [66] D. L. Partin, Lead telluride doped with rare-earth elements, *Journal of Applied Physics* **57**, 1997 (1985).
- [67] Z. Golacki and M. Heinonen, Valency of Yb in PbS and PbTe determined by XPS, *Acta Physica Polonica, A* **91**, 775 (1997).
- [68] B. Eisenmann, H. Schaefer, and R. Zagler, Die verbindungen $A_8B_{16}C_{30}$ ($A = \text{Sr, Ba}$; $B = \text{Al, Ga}$; $C = \text{Si, Ge, Sn}$), *Journal of the Less Common Metals* **118**, 43 (1986).
- [69] M. Christensen and B. B. Iversen, Host structure engineering in thermoelectric clathrates, *Chemistry of Materials* **19**, 4896 (2007).

- [70] H. Anno, M. Hokazono, M. Kawamura, J. Nagao, and K. Matsubara, Thermoelectric properties of $\text{Ba}_8\text{Ga}_x\text{Ge}_{46-x}$ clathrate compounds, *Proceedings of the Twenty First International Conference on Thermoelectrics* pp. 77 (2002).
- [71] H. Anno, M. Hokazono, M. Kawamura, and K. Matsubara, Effect of transition element substitution on thermoelectric properties of semiconductor clathrate compounds, *Proceedings of the Twenty Second International Conference on Thermoelectrics* pp. 121 (2003).
- [72] M. A. Avila, K. Suekuni, K. Umeo, and T. Takabatake, Carrier-tuning of single-crystalline $\text{Ba}_8\text{Ga}_{16}\text{Ge}_{30}$, *Physica B* **383**, 124 (2006).
- [73] V. L. Kuznetsov, L. A. Kuznetsova, A. E. Kaliazin, and D. M. Rowe, Preparation and thermoelectric properties of $\text{A}_8^{\text{II}}\text{B}_{16}^{\text{III}}\text{B}_{30}^{\text{IV}}$ clathrate compounds, *Journal of Applied Physics* **87**, 7871 (2000).
- [74] A. Saramat, et al., Large thermoelectric figure of merit at high temperatures in czochralski-grown clathrate $\text{Ba}_8\text{Ga}_{16}\text{Ge}_{30}$, *Journal of Applied Physics* **99**, 023708 (2006).
- [75] E. S. Toberer, M. Christensen, B. B. Iversen, and G. J. Snyder, High temperature thermoelectric efficiency in $\text{Ba}_8\text{Ga}_{16}\text{Ge}_{30}$, *Physical Review B* **77**, 075203 (2008).
- [76] G. S. Nolas, J. L. Cohn, G. A. Slack, and S. B. Schujman, Semiconducting Ge clathrates: Promising candidates for thermoelectric applications, *Applied Physics Letters* **73**, 178 (1998).
- [77] J. L. Cohn, G. S. Nolas, V. Fessatidis, T. H. Metcalf, and G. A. Slack, Glasslike heat conduction in high-mobility crystalline semiconductors, *Physical Review Letters* **82**, 779 (1999).
- [78] G. S. Nolas, T. J. R. Weakley, J. L. Cohn, and R. Sharma, Structural properties and thermal conductivity of crystalline Ge clathrates, *Physical Review B* **61**, 3845 (2000).
- [79] B. C. Sales, B. C. Chakoumakos, R. Jin, J. R. Thompson, and D. Mandrus, Structural, magnetic, thermal, and transport properties of $X_8\text{Ga}_{16}\text{Ge}_{30}$ ($X = \text{Eu}, \text{Sr}, \text{Ba}$) single crystals, *Physical Review B* **63**, 245113 (2001).
- [80] S. Paschen, W. Carrillo-Cabrera, A. Bentien, V. H. Tran, M. Baenitz, Y. Grin, and F. Steglich, Structural, transport, magnetic, and thermal properties of $\text{Eu}_8\text{Ga}_{16}\text{Ge}_{30}$, *Physical Review B* **64**, 214404 (2001).
- [81] A. Bentien, M. Christensen, J. D. Bryan, A. Sanchez, S. Paschen, F. Steglich, and G. D. Stucky, Thermal conductivity of thermoelectric clathrates, *Physical Review B* **69**, 045107 (2004).
- [82] A. Bentien, S. Johnsen, and B. B. Iversen, Strong phonon charge carrier coupling in thermoelectric clathrate, *Physical Review B* **73**, 094301 (2006).

- [83] M. Christensen, A. B. Abrahamsen, N. B. Christensen, F. Juranyi, N. H. Andersen, K. Lefmann, J. Andreasson, C. R. H. Bahl, and B. B. Iversen, Avoided crossing of rattler modes in thermoelectric materials, *Nature Materials* **7**, 811-815 (2008).
- [84] M. Christensen, A. B. Abrahamsen, N. B. Christensen, F. Juranyi, N. H. Andersen, K. Lefmann, J. Andreasson, C. R. H. Bahl, and B. B. Iversen, $\text{Ba}_8\text{Ga}_{16}\text{Sn}_{30}$ with Type-I clathrate structure: Drastic suppression of heat conduction, *Applied Physics Letters* **92**, 041901 (2008).
- [85] X. Tang, P. Li, S. Deng, and Q. Zhang, High temperature thermoelectric transport properties of double-atom-filled clathrate compounds $\text{Yb}_x\text{Ba}_{8-x}\text{Ga}_{16}\text{Ge}_{30}$, *Journal of Applied Physics* **104**, 013706 (2008).
- [86] N. L. Okamoto, T. Nakano, K. Tanaka, and H. Inui, Mechanical and thermal properties of single crystals of the Type-I clathrate compounds $\text{Ba}_8\text{Ga}_{16}\text{Ge}_{30}$ and $\text{Sr}_8\text{Ga}_{16}\text{Ge}_{30}$, *Journal of Applied Physics* **104**, 013529 (2008).
- [87] N. L. Okamoto, K. Kishida, K. Tanaka, and H. Inui, Effect of in additions on the thermoelectric properties of the Type-I clathrate compound $\text{Ba}_8\text{Ga}_{16}\text{Ge}_{30}$, *Journal of Applied Physics* **101**, 113525 (2007).
- [88] S. Deng, X. Tang, P. Li, and Q. Zhang, High temperature thermoelectric transport properties of *p*-type $\text{Ba}_8\text{Ga}_{16}\text{Al}_x\text{Be}_{30-x}$, *Journal of Applied Physics* **103**, 073503 (2008).
- [89] J. Martin, H. Wang, G. S. Nolas, Optimization of the thermoelectric properties of $\text{Ba}_8\text{Ga}_{16}\text{Ge}_{30}$, *Applied Physics Letters* **92**, 222110 (2008).
- [90] G. J. Miller, *Structure and Bonding at the Zintl Border, in Chemistry, Structure, and Bonding of Zintl Phases and Ions* (VCH Publishers, New York, 1996).
- [91] E. S. Toberer, C. A. Cox, S. R. Brown, T. Ikeda, A. F. May, S. M. Kauzlarich, and G. J. Snyder, Traversing the metal-insulator transition in a Zintl phase: Rational enhancement of thermoelectric efficiency in $\text{Yb}_{14}\text{Mn}_{1-x}\text{Al}_x\text{Sb}_{11}$, *Advanced Functional Materials* **18**, 2795 (2008).
- [92] X.-J. Wang, M.-B. Tang, J.-T. Zhao, H.-H. Chen, and X.-X. Yang, Thermoelectric properties and electronic structure of Zintl compound BaZn_2Sb_2 , *Applied Physics Letters* **90**, 232107 (2007).
- [93] S.-J. Kim, S. Hu, C. Uher, and M. G. Kanatzidis, $\text{Ba}_4\text{In}_8\text{Sb}_{16}$: Thermoelectric properties of a new layered Zintl phase with infinite zigzag Sb chains and pentagonal tubes, *Chemistry of Materials* **11**, 3154 (1999).
- [94] S.-J. Kim, S. Hu, C. Uher, T. Hogan, B. Huang, J. D. Corbett, M. G. Kanatzidis, Structure and thermoelectric properties of $\text{Ba}_6\text{Ge}_{25-x}$, $\text{Ba}_6\text{Ge}_{23}\text{Sn}_2$, and $\text{Ba}_6\text{Ge}_{22}\text{In}_3$: Zintl phases with a chiral clathrate structure, *Journal of Solid State Chemistry* **153**, 321 (1999).

- [95] F. Gascoin, S. Ottensmann, D. Stark, S. M. Haile, and G. J. Snyder, Zintl phases as thermoelectric materials: Tuned transport properties of the compounds $\text{Ca}_x\text{Yb}_{1-x}\text{Zn}_2\text{Sb}_2$, *Advanced Functional Materials* **15**, 1860 (2005).
- [96] H. Zhang, J.-T. Zhao, Y. Grin, X.-J. Wang, M.-B. Tang, Z.-Y. Man, H.-H. Chen, and X.-X. Yang, A new type of thermoelectric material, EuZn_2Sb_2 , *Journal of Chemical Physics* **129**, 164713 (2008).
- [97] E. S. Toberer, A. F. May, B. Melot, E. Flage-Larsen, and G. J. Snyder, Electronic structure and transport in thermoelectric compounds $A\text{Zn}_2\text{Sb}_2$, ($A = \text{Sr}, \text{Ca}, \text{Yb}, \text{Eu}$), *Dalton Transactions* **39**, 1046 (2010).
- [98] G. K. H. Madsen, Automated search for new thermoelectric materials: The case for LiZnSb , *Journal of the American Chemical Society* **128**, 12140 (2006).
- [99] J. K. Burdett and G. J. Miller, Fragment formalism in main-group solids: Applications to AlB_2 , CaAl_2Si_2 , BaAl_4 , and related materials, *Chemistry of Materials* **2**, 12-26 (1990).
- [100] A. May, J. Snyder, and J.-P. Fleurial, Lanthanum telluride: Mechanochemical synthesis of a refractory thermoelectric material, *AIP Conv. Proc., STAIF 2008* **969**, 672 (2008).
- [101] O. Delaire, A. F. May, M. A. McGuire, W. D. Porter, D. L. Abernathy, V. A. Ravi, S. A. Firdosi, and G. J. Snyder, Phonon density of states and heat capacity of $\text{La}_{3-x}\text{Te}_4$, *Physical Review B* **80**, 184302 (2009).
- [102] A. F. May, J.-P. Fleurial, and G. J. Snyder, Optimization of thermoelectric efficiency in $\text{La}_{3-x-y}\text{Yb}_y\text{Te}_4$, *Chemistry of Materials* **22**, 2995 (2010).
- [103] A. F. May, E. Flage-Larsen, and G. J. Snyder, Electron and phonon scattering in the high temperature thermoelectric $\text{La}_3\text{Te}_{4-z}\text{M}_z$, $M = \text{Sb}, \text{Bi}$, *Physical Review B* **81**, 125205 (2010).
- [104] A. F. May, E. S. Toberer, A. Saramat, and G. J. Snyder, Characterization and analysis of thermoelectric transport in n -type $\text{Ba}_8\text{Ga}_{16-x}\text{Ge}_{30+x}$, *Physical Review B* **80**, 125205 (2009).
- [105] A. F. May, E. S. Toberer, and G. J. Snyder, Transport properties of the layered Zintl compound SrZnSb_2 , *Journal of Applied Physics* **106**, 013706 (2009).
- [106] E. S. Toberer, A. F. May, C. Scanlon, and G. J. Snyder, Thermoelectric properties of p -type LiZnSb : Assessment of *ab initio* calculations, *Journal of Applied Physics* **105**, 063701 (2009).
- [107] A. Saramat, E. S. Toberer, A. F. May, and G. J. Snyder, Thermal stability and phase purity in polycrystalline $\text{Ba}_8\text{Ga}_x\text{Ge}_{46-x}$, *Journal of Electronic Materials* **38**, 1423 (2009).
- [108] P. Shemon, *Diffusion in Solids* (The Minerals, Metals & Materials Society, U.S.A., 1989).
- [109] W. M. Deen, *Analysis of Transport Phenomena* (Oxford University Press, New York, 1998).

- [110] C. Wood, D. Zoltan, and G. Stapfer, Measurement of Seebeck coefficient using a light pulse, *Reviews of Scientific Instruments* **56**, 719 (1985).
- [111] D. J. Singh and L. Nordstrom, *Planewaves, Pseudopotentials and the LAPW Method* (Springer, Berlin, 2006).
- [112] P. Blaha, K. Schwarz, G. Madsen, D. Kvasnicka, and J. Luitzand, <http://www.wien2k.at/>.
- [113] G. K. H. Madsen and D. J. Singh, Boltztrap. A code for calculating band-structure dependent quantities, *Computer Physics Communications* **175**, 67 (2006).
- [114] G. Kresse and J. Hafner, *Ab initio* molecular dynamics for open-shell transition metals, *Physical Review B* **48**, 13115 (1993).
- [115] G. Kresse and J. Furthmüller, Efficient iterative schemes for *ab initio* total-energy calculations using a plane-wave basis set, *Physical Review B* **54**, 11169 (1996).
- [116] J. P. Perdew, K. Burke, and M. Ernzerhof, Generalized gradient approximation made simple, *Physical Review Letters* **77**, 3865 (1996).
- [117] P. Pulay, Convergence acceleration in iterative sequences: The case of SCF iteration, *Chemical Physics Letters* **73**, 393 (1980).
- [118] P. E. Blöchl, O. Jepsen, and O. K. Andersen, Improved tetrahedron method for brillouin-zone integrations, *Physical Review B* **49**, 16223 (1994).
- [119] V. I. Fistul, *Heavily Doped Semiconductors* (Plenum Press, New York, 1969).
- [120] D. K. C. MacDonald, *Thermoelectricity: An introduction to the principles* (John Wiley & Sons, New York, 1962).
- [121] R. F. Pierret, *Advanced Semiconductor Fundamentals* (Prentice Hall, Upper Saddle River, New Jersey, 2003).
- [122] D. Chattopadhyay and H. J. Queisser, Electron scattering by ionized impurities in semiconductors, *Reviews of Modern Physics* **53**, 745 (1981).
- [123] E. H. Putley, *The Hall Effect and Related Phenomena* (Butterworths, London, 1960).
- [124] A. L. Rockwood, Relationship of thermoelectricity to electronic entropy, *Physical Review A* **30**, 2843 (1984).
- [125] H. J. Goldsmid and J. W. Sharp, Estimation of the thermal band gap of a semiconductor from Seebeck measurements, *Journal of Electronic Materials* **28**, 869 (1999).

- [126] J. H. Shim, K. Kim, B. I. Min, and J. S. Kang, Electronic structures of La_3S_4 and Ce_3S_4 , *Physica B* **328**, 148 (2003).
- [127] J. D. Bryan, N. P. Blake, H. Metiu, G. D. Stucky, B. B. Iversen, R. D. Poulsen, and A. Bentien, Nonstoichiometry and chemical purity effects in thermoelectric $\text{Ba}_8\text{Ga}_{16}\text{Ge}_{30}$ clathrate, *Journal of Applied Physics* **92**, 7281 (2002).
- [128] J. D. Bryan, V. I. Srđanov, G. D. Stucky, and D. Schmidt, Superconductivity in germanium clathrate $\text{Ba}_8\text{Ga}_{16}\text{Ge}_{30}$, *Physical Review B* **60**, 3064 (1999).
- [129] N. L. Okamoto, K. Kishida, K. Tanaka, and H. Inui, Crystal structure and thermoelectric properties of Type-I clathrate compounds in the BaGaGe system, *Journal of Applied Physics* **100**, 073504 (2006).
- [130] M. Christensen, N. Lock, J. Overgaard, and B. B. Iversen, Crystal structures of thermoelectric *n*- and *p*-type $\text{Ba}_8\text{Ga}_{16}\text{Ge}_{30}$ studied by single crystal, multitemperature, neutron diffraction, conventional x-ray diffraction and resonant x-ray diffraction, *Journal of the American Chemical Society* **128**, 15657-15665 (2006).
- [131] W. Carrillo-Cabrera, R. C. Gil, S. Paschen, Y. Grin, and Y. N. Hrin, Crystal structure of $\text{Ba}_8\text{Ga}_{4.44}\text{Ge}_{39.14}(\text{vac})_{2.42}$, $\text{Ba}_8\text{Ga}_{8.62}\text{Ge}_{36}(\text{vac})_{1.38}$, and $\text{Ba}_8\text{Ga}_{12.35}\text{Ge}_{33.27}(\text{vac})_{0.38}$, three clathrate-I variants., *Zeitschrift fuer Kristallographie–New Crystal Structures* **217**, 183 (2002).
- [132] E. Alleno, G. Maillet, O. Rouleau, E. Leroy, and C. Godart, Germanium vacancies and charge transport properties in $\text{Ba}_8\text{Zn}_x\text{Ge}_{46-x-y}\text{vac}_y$, *Chemistry of Materials* **21**, 1485 (2009).
- [133] M. Hokazono, H. Anno, and K. Matsubara, Effect of Cu substitution on thermoelectric properties of Ge clathrates, *Materials Transactions* **46**, 1485 (2005).
- [134] N. P. Blake, S. Lattner, J. D. Bryan, G. D. Stucky, and H. Metiu, Band structures and thermoelectric properties of the clathrates $\text{Ga}_8\text{Ga}_{16}\text{Ge}_{30}$, $\text{Sr}_8\text{Ga}_{16}\text{Ge}_{30}$, $\text{Ba}_8\text{Ga}_{16}\text{Si}_{30}$, and $\text{Ba}_8\text{In}_{16}\text{Sn}_{30}$, *Journal of Chemical Physics* **115**, 8060 (2001).
- [135] G. K. H. Madsen, K. Schwarz, P. Blaha, and D. J. Singh, Electronic structure and transport in Type-I and Type-VIII clathrates containing strontium, barium, and europium, *Physical Review B* **68**, 125212 (2003).
- [136] C. M. Bhandari and D. M. Rowe, *Thermal Conduction in Semiconductors* (John Wiley & Sons, New York, 1988).
- [137] J. R. Drabble and H. J. Goldsmid, *Thermal Conduction in Semiconductors* (Pergamon Press, New York, 1961).
- [138] H. J. Goldsmid, *The Thermal Properties of Solids* (Dover Publications, New York, 1965).

- [139] G. A. Slack, *Solid State Physics*, vol. 34 (Academic Press, New York, 1979).
- [140] G. P. Srivastava, Role of optical phonons in the high temperature thermal conductivity of semiconductors, *Physica Status Solidi B* **90**, K125 (1978).
- [141] D. G. Cahill, S. K. Watson, and R. O. Pohl, Low limit to the thermal conductivity of disordered crystals, *Physical Review B* **46**, 6131 (1992).
- [142] G. A. Slack and V. G. Tsoukala, Some properties of semiconducting IrSb₃, *Journal of Applied Physics* **76**, 1665 (1994).
- [143] P. G. Klemens, The scattering of low-frequency lattice waves by static imperfections, *Proceedings of the Physical Society* **A68**, 1113 (1955).
- [144] J. M. Ziman, The effect of free electrons on lattice conduction, *Philosophical Magazine* **1**, 191 (1956).
- [145] A. B. Pippard, Ultrasonic attenuation in metals, *Philosophical Magazine* **46**, 1104 (1955).
- [146] E. Brechtel, G. Cordier, and H. Schaefer, Zur darstellung und kristallstruktur des SrZnSb₂, *Zeitschrift fuer Naturforschung, Teil B. Anorganische Chemie, Organische Chemie* **34**, 251 (1979).
- [147] A. Mewis, AB₂X₂-verbindungen im CaAl₂Si₂-type, IV (1) zur struktur der verbindungen CaZn₂Sb₂, CaCd₂Sb₂, SrZn₂Sb₂ und SrCd₂Sb₂, *Zeitschrift fuer Naturforschung, Teil B. Anorganische Chemie, Organische Chemie* **33**, 382 (1978).
- [148] G. J. Snyder, Application of the compatibility factor to the design of segmented and cascaded thermoelectric generators, *Applied Physics Letters* **84**, 2436 (2004).
- [149] G. J. Snyder and T. S. Ursell, Thermoelectric efficiency and compatibility, *Physical Review Letters* **91**, 148301 (2003).
- [150] J. Yang and T. Caillat, Thermoelectric materials for space and automotive power generation, *MRS Bulletin* **31**, 224 (2006).